UNIVERSIDADE DE LISBOA
INSTITUTO SUPERIOR TÉCNICO

Nuclear technology and engineering studies on reflectometry systems for ITER and DEMO

Yohanes Setiawan Nietiadi

Supervisor: Doctor Bruno Miguel Soares Gonçalves

Co-supervisors: Doctor Catarina Isabel Silva Vidal

Doctor Raul Fernandes Luís

Thesis approved in public session to obtain the PhD Degree in

Technological Physics Engineering

Jury Final Classification: Pass with Distinction and Honour

2022

UNIVERSIDADE DE LISBOA
INSTITUTO SUPERIOR TÉCNICO

Nuclear technology and engineering studies on reflectometry systems for ITER and DEMO

Yohanes Setiawan Nietiadi

Supervisor: Doctor Bruno Miguel Soares Gonçalves

Co-supervisors: Doctor Catarina Isabel Silva Vidal

Doctor Raul Fernandes Luís

Thesis approved in public session to obtain the PhD Degree in

Technological Physics Engineering

Jury Final Classification: Pass with Distinction and Honour

Jury

Chairperson:
Doctor Luís Paulo da Mota Capitão Lemos Alves, *Instituto Superior Técnico, Universidade de Lisboa*

Members of the Committee:
Doctor Fernando Jorge Ventura Antunes, *Faculdade de Ciências e Tecnologia, Universidade de Coimbra*
Doctor Lorenzo Virgilio Boccaccini, *Institute of Neutron Physice and Reactor Technology, Karlsruhe Institute of Technology (KIT), Germany*
Doctor Artur Jorge Louzerio Malaquias, *Instituto Superior Técnico, Universidade de Lisboa*
Doctor Raul Fernandes Luís, *Instituto Superior Técnico, Universidade de Lisboa*

Funding Institution – Fundação para a Ciência e Tecnologia

2022

Acknowledgments

This thesis would not have been successfully completed without the support from my supervisors, family, and friends during these 4 years. I am deeply grateful to each of them. I would like to thank some of them in particular:

To Doctor Raul Luís, without whose feedback, advice, guidance, encouragement and support, it would have been difficult to push myself through all the process of this PhD. I also appreciate the opportunity that he gave me to learn new things and work on the integration of various diagnostics, which broadened my vision. Above all, I am indebted to him for all his kindness and patience while guiding me through all the process.

To Doctor Bruno Gonçalves, for giving me the opportunity to work at Instituto de Plasmas e Fusão Nuclear (IPFN) of Instituto Superior Técnico, his trust on my work, and all his support during this period.

To Doctor Catarina Vidal, for all her knowledge in finite-element and mechanical analysis, which helped me to understand it better. I would also like to thank her support and advice.

I would like to thank all my colleagues from IPFN, in particular from the Group of Engineering and System Integration (GESI), for all their help and the work environment they granted me. I would like thank Doctor Paulo Varela for his support, advice and collaboration on the ITER PPR project. I would also like to thank Doctor António Silva, Doctor Alberto Vale, and Doctor Jorge Belo for their advice, support and collaboration on the development of the multi-reflectometer system for DEMO.

I would like to acknowledge the financial support from the following institutions:

- Fundação para a Ciência e Tecnologia (FCT), for the PhD fellowship PD/BD/135230/2017
- Instituto de Plasmas e Fusão Nuclear, for the fellowship BL6/2022

I wish to thank my friends from the same cohort of the APPLAuSE program, with whom I strove together, Joana Alves, Duarte Nina, and Ruggero Giampaoli, for their companionship and friendship during the last 5 years.

I also thank the people from Embaixada da República da Indonésia and Associação de Estudantes da Indonésia em Portugal, for being a family for me in Portugal.

Finally, the people without whom this work would not be possible – my family and my wife, Pamela. It was because of their unwavering support, encouragement, love and patience that I was able to go through these 5 years without actually giving up. To them I dedicate this thesis.

Abstract

Controlled nuclear fusion is one of the most promising solutions to address the world's increasing demand for sustainable and clean energy sources. In the path towards commercial electricity produced from fusion energy, DEMO is foreseen in the EUROFusion roadmap as an intermediate step between ITER (under construction) and commercial power plants. Large tokamaks like ITER and DEMO will require extensive networks of diagnostics, able to provide reliable plasma control over extended operation periods. Among these, microwave reflectometry has been proven as an alternative control technique, by measuring and monitoring the plasma density, position and shape with high spatial and temporal resolutions.

This Doctoral Thesis presents an engineering assessment and design studies for two diagnostics developed by IPFN/IST: the ITER Plasma Position Reflectometry (PPR) system and a multi-reflectometer system for DEMO. Due to the nature of reflectometry measurements, some front-end components will be directly exposed to the plasma, subjected to fluxes of high-energy neutrons (14 MeV) that will contribute to the thermal loads in the systems and may change the material properties, which can compromise the integrity of the components during the reactor lifetime. Therefore, complex design studies (involving neutronics, thermo-mechanical analyses and electromagnetic simulations) are crucial to ensure that these diagnostics survive in the harsh radiation environments of ITER and DEMO without serious compromise to their performance.

For the ITER PPR system, ANSYS Mechanical was used to estimate the operation temperatures of the in-vessel components in two different positions, known as gaps 4 and 6. In the studied configurations, results showed that the plasma-facing antennas of the PPR system would operate above the temperature limit for stainless steel under irradiation, even after several optimization attempts. In face of these results, different materials were suggested for the front-ends of gaps 4 and 6. Even though the ITER Organization decided to descope the PPR system in 2019, the lessons learned on the design activities are still valid for the development of the reflectometry system proposed for DEMO.

For the latter, a previously proposed integration concept – the Diagnostics Slim Cassette (DSC) – was designed and evaluated. CATIA V5, MCNP, and ANSYS were used to design the system and estimate the neutron and gamma fluxes, heat loads and operation temperatures, as well as and their impact on the performance of the reflectometry measurements. The nuclear and thermo-mechanical analyses presented in this work demonstrate the feasibility of the concept and the ability of the system to operate under the harsh irradiation environment of DEMO, by comparing the results with the standards of the RCC-MR code. This is achieved with a simple cooling system design, possible to manufacture using conventional techniques. The results and simulation workflow presented in this thesis can be used as guidelines for other diagnostics, namely the ones that consider the DSC as a possible integration solution.

Keywords: ITER and DEMO diagnostics, Thermo-mechanical analysis, Microwave reflectometry, Neutronics, Diagnostic integration

Resumo

A fusão nuclear controlada é umas das soluções mais promissoras para o aumento da procura por formas mais sustentáveis de produção de energia eléctrica à escala global. No caminho a percorrer até à comercialização de energia eléctrica produzida através da fusão, o reactor DEMO, desenvolvido pelo consórcio EUROFusion, é um passo intermédio entre o ITER (em construção) e os reactores comerciais do futuro. *Tokamaks* de grandes dimensões como o ITER e o DEMO requerem redes complexas de sistemas de diagnóstico, que permitam controlar o plasma de forma fiável por longos períodos de operação. Entre estes, a reflectrometria de microondas já demonstrou ser uma forma alternativa de controlo, capaz de monitorizar a densidade, a posição e a forma do plasma com elevada resolução espacial e temporal.

Esta tese apresenta estudos de *design* e engenharia para dois sistemas de diagnóstico desenvolvidos pelo IPFN/IST: o sistema de reflectometria de posição de plasma (PPR) do ITER e um sistema com múltiplos reflectómetros proposto para o DEMO. Devido à natureza das medições, alguns dos componentes destes sistemas estarão expostos directamente ao plasma, sujeitos a elevados fluxos de neutrões de alta energia (14 MeV) que contribuirão para as cargas térmicas nos componentes e poderão ter como efeito alterar as propriedades dos materiais, pondo em risco a sua integridade mecânica durante os períodos de funcionamento dos reactores. Por esta razão, estudos complexos de *design* (envolvendo neutrónica, análises termo-mecânicas e simulações electromagnéticas) são cruciais para garantir que os diagnósticos sobrevivem aos ambientes de radiação do ITER e do DEMO sem comprometer o seu desempenho.

Para o sistema PPR do ITER, o software ANSYS Mechanical foi usado para estimar as temperaturas de operação dos componentes mais expostos, em duas posições distintas, conhecidas como *gaps* 4 e 6. Nas configurações estudadas, os resultados mostram que as antenas do sistema PPR estariam sujeitas a temperaturas superiores ao limite estabelecido pelo ITER para o aço inoxidável sob irradiação, mesmo após várias tentativas de optimização. Tendo em conta estes resultados, diferentes materiais foram propostos para as antenas. Apesar de a Organização ITER ter descontinuado o desenvolvimento do sistema PPR, o conhecimento adquirido durante os estudos de integração e desenvolvimento continua a ser válido para o desenho do sistema de reflectometria proposto para o DEMO.

Para este sistema, um conceito de integração proposto previamente – *Diagnostics Slim Cassette* (DSC) – foi desenhado e avaliado. Os códigos CATIA V5, MCNP e ANSYS foram usados para desenhar o sistema e estimar fluxos de neutrões e radiação gama, cargas térmicas e temperaturas de operação, assim como o impacto que essas condições de operação terão nas medições de reflectometria. As análises nucleares e termo-mecânicas apresentadas neste trabalho demonstram a viabilidade do conceito e a capacidade do sistema para operar no ambiente de radiação do reactor DEMO, de acordo com os padrões estabelecidos pelo código RCC-MR. Este resultado é obtido com uma configuração simplificada do sistema de arrefecimento, possível de fabricar com técnicas convencionais. Os resultados e as metodologias implementadas nesta tese podem servir como directizes para outros sistemas de diagnóstico, nomeadamente aqueles em que a DSC possa servir como possível solução de integração.

Palavras-chave: ITER, DEMO, Análise termo-mecânica, Reflectometria de microondas, Neutrónica, Integração de diagnósticos

Contents

List of Figures

List of Tables

Acronyms

APDL	ANSYS Parametric Design Language
AUG	ASDEX Upgrade
BB	Breeding Blanket
BM	blanket module
BP	Back Plate
BROND	Biblioteka Rekomendovannykh Ocenennykh Nejtronnykh Dannykh
BSL	Baseline
BSS	Back Supporting Structure
BU	Breeding Unit
BZ	Breeding Zone
CAD	Computer Aided Design
CAS	Chinese Academy of Sciences
cdf	cumulative distribution function
CFD	Computational Fluid Dynamic
CGS	Constructive Solid Geometry
CJD	Centr po Jadernym Dannym
CO_2	Carbon Dioxide
COBS	Centre OutBoard Segment
CP	Contact Point
CSEWG	Cross Section Evaluation Working Group
CTS	Collective Thomson Scattering
CXRS	Charge eXchange Recombination Spectroscopy
CY	calendar year
D.O.F	Degree of Freedom
DBTT	Ductile to Brittle Transition Temperature
DC	Diagnostics and Control

DEMO	DEMOnstration power station
DNS	Direct Numerical Simulation
dpa	displacements per atom
DSC	Diagnostics Slim Cassette
DTM	Discrete Transfer Model
DWT	Double-Walled Tubes
EC	Electron Cyclotron
ECE	Electron Cyclotron Emission
EDF	Electricité de France
ELM	Edge-Localized Mode
EM	Electromagnetic
ENDF	Evaluated Nuclear Data File
EP	Equatorial Port
EPP	Equatorial Port Plug
F4E	Fusion for Energy
FB	Fill Block
FDTD	Finite-Difference Time-Domain
FE	Finite Element
FEA	Finite Element Analysis
FEM	Finite Element Method
FENDL	Fusion Evaluated Nuclear Data Library
FLUKA	FLUktuierende KAskade
FM-CW	Frequency Modulation of a Continuous Wave
FNG	Frascati Neutron Generator
FPY	full power years
FSI	Fluid-Solid Interaction
FVM	Finite Volume Method

FW	First Wall
Geant4	GEometry ANd Tracking
HCD	Heating and Current Drive
HCLL	Helium Cooled Lithium Lead
HCPB	Helium-Cooled Pebble Blanket
HF	Heat Fluxes
HFS	high-field side
HIP	Hot Isostatic Pressing
HKM	Hybrid Kinematic Mechanism
IAEA	International Atomic Energy Agency
IB	Inboard Blanket
IBS	Inboard Blanket Segment
IML	Inboard Midplane Limiter
IO	ITER Organization
IPC	Immediate Plastic Collapse
IPFL	Immediate Plastic Flow Localization
IPFN/IST	Instituto de Plasmas e Fusão Nuclear
IPI	Immediate Plastic Instability
ITER	International Thermonuclear Experimental Reactor
IVC	In-Vessel Component
JAEA	Japan Atomic Energy Agency
JEFF	Joint Evaluated Fission and Fusion File
JENDL	Japanese Evaluated Nuclear Data Library
JET	Joint European Torus
KIT	Karlsruhe Institute of Technology
LED	light emitting diode
LES	Large Eddy Simulation

LFS	low-field side
LIBS	Left InBoard Segment
LOBS	Left OutBoard Segment
LP	Lower Port
MCAM	Multi-Physics Coupling Analysis Modelling
MCNP	Monte Carlo N-Particle Code
MMS	Multi-Module Segment
MPC	Mechanical Pipe Connection
MSE	Motional Stark Effect
MW	microwave
NEA	Nuclear Energy Agency
NH	Nuclear Heat loads
OB	Outboard Blanket
OBS	Outboard Blanket Segment
OLL	Outboard Lower Limiter
OML	Outboard Midplane Limiter
PDE	Partial Differential Equation
pdf	probability distribution function
PF	Poloidal Field
PFC	Poloidal Field Coil
PHTS	Primary Heat Transfer System
ppf	percent point function
PPR	Plasma Position Reflectometry
PWR	Pressurised Water Reactor
RANS	Reynolds-averaged Navier Stokes equation
RH	Remote Handling
RIBS	Right InBoard Segment

RM	Remote Maintenance
RNC	Radial Neutron Camera
ROBS	Right OutBoard Segment
RR	Research Reactor
SFR	Sodium Fast Reactor
SL	Stress Linearization
SMS	Single Module Segment
SP	Stiffening Plate
SST	Shear Stress Transport
SW	Side Wall
TBM	Test Blanket Module
TF	Toroidal Field
TFC	Toroidal Field Coil
TS	Tore Supra
UDF	User-defined function
UL	Upper Limiter
UP	Upper Port
VNC	Vertical Neutron Camera
VV	Vacuum Vessel
WCLL	Water-Cooled Lithium Lead
WG	waveguide
WPBB	Work Package Breeding Blankets
WPDC	Work Package Diagnostics & Control
WPRM	Work Package Remote Maintenance

Part I

Introduction

Chapter 1

Introduction

1.1 Overview of the world energy consumption

The world energy demand has been increasing steadily over the past 100 years. The Industrial Revolution changed irrevocably the energy consumption pattern, from the direct use of wood and coal for heating to engine power generation and later electricity [1]. Today, fossil fuels account for 80% of the energy consumption worldwide [2], as shown in Figure 1.1. Fossil fuels (Oil, Coal, and Gas) have limited reserves, and their use releases Carbon Dioxide (CO_2), methane (CH_4) and nitrous oxide (N_2O) to the atmosphere, which are the primary cause of climate change by trapping the heat in the atmosphere [3]. This is illustrated by Figure 1.2, which shows the fossil fuel reserves in years (a), the rising trend of the average land-sea temperature (b), and the global atmospheric concentrations of CO_2, (CH_4) and nitrous oxide (c and d).

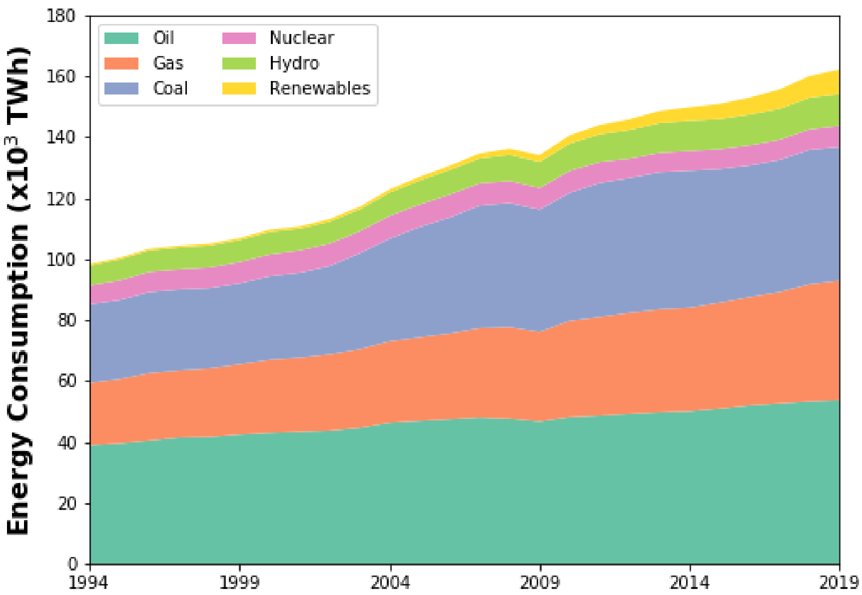

Figure 1.1: Global energy consumption by sources [4].

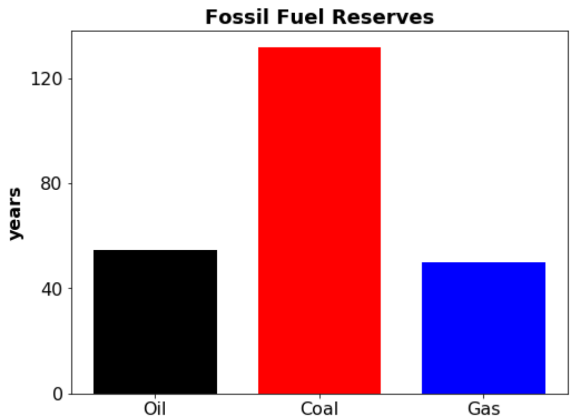

(a) Fossil fuel reserves (years) [4]

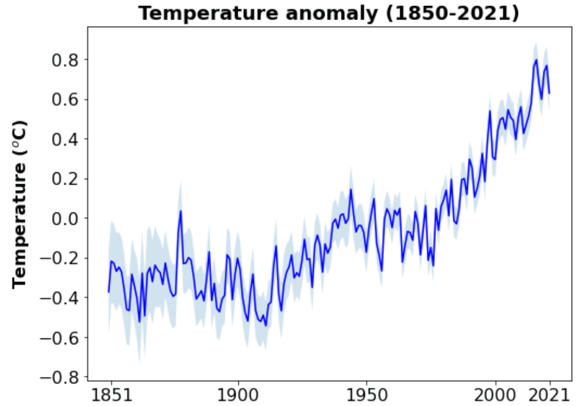

(b) Global average land-sea temperature anomaly relative to the 1961-1990 average temperature (1850-2021) [5]

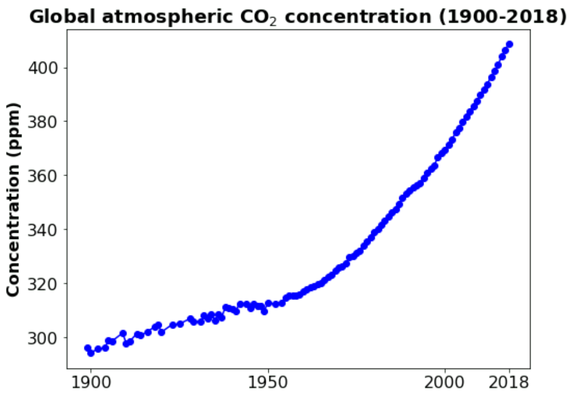

(c) Global mean annual concentration of CO_2, measured in parts per million (ppm) [6]

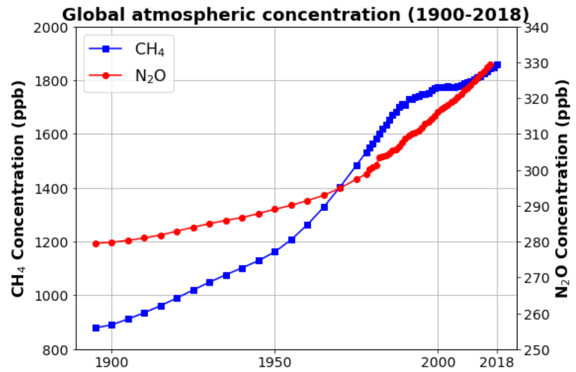

(d) Global annual averaged atmospheric concentration of methane and nitrous oxide, measured in parts per billion (ppb) [6]

Figure 1.2: Fossil fuel reserves and their impact on the climate change.

These issues worsen with the rise of the world population [7], estimated to reach 10 billion by the middle of the century, as illustrated in Figure 1.3. Therefore, it is important to find new clean energy sources which can supply the increasing energy demand while preventing the catastrophic consequences of global warming.

Although alternative energy sources (hydroelectricity, nuclear fission, solar, wind, and geothermal) are already replacing fossil fuels to some extent, hydroelectricity and geothermal energy depend on the geographic location, while the production of solar and wind energy is intermittent. Though nuclear fission might produce energy with higher efficiency and lower cost than the other alternative energy sources, it raises questions, mainly regarding the long-lived radioactive waste and nuclear proliferation. Thus, nuclear fusion is a promising option to fulfil the energy demand while reducing the energy production cost and its impact on the environment.

1.2 Nuclear Fusion

Nuclear fusion, which powers the stars [8], is a reaction in which two light, high energetic particles overcome the repulsive Coulomb force and fuse into a heavier nucleus, with subatomic particles as by-

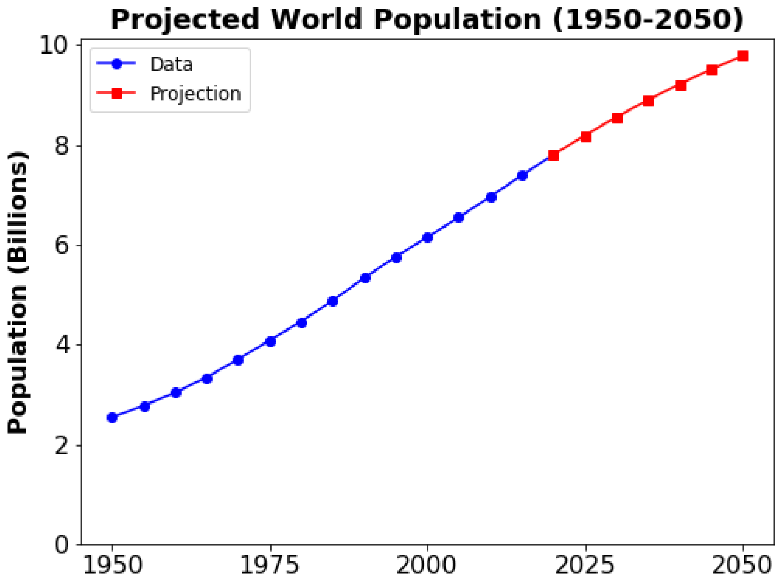

Figure 1.3: Projected world population (1950-2050) [7].

products. Though the elements in the periodic table were produced by chains of nuclear fusion reactions, not all of these reactions are exothermic and in most cases extreme conditions are required to make them happen. Therefore, when the objective is energy production, the focus is on exothermic reactions, which occur when the nuclei are lighter than $^{56}_{26}$Fe or $^{62}_{28}$Ni [9] (where the binding energy per nucleon is maximized, as shown in Figure 1.4). From the reactions listed in Table 1.1, it is evident that D–$^{3}_{2}$He and D–T are the ones that produce more energy.

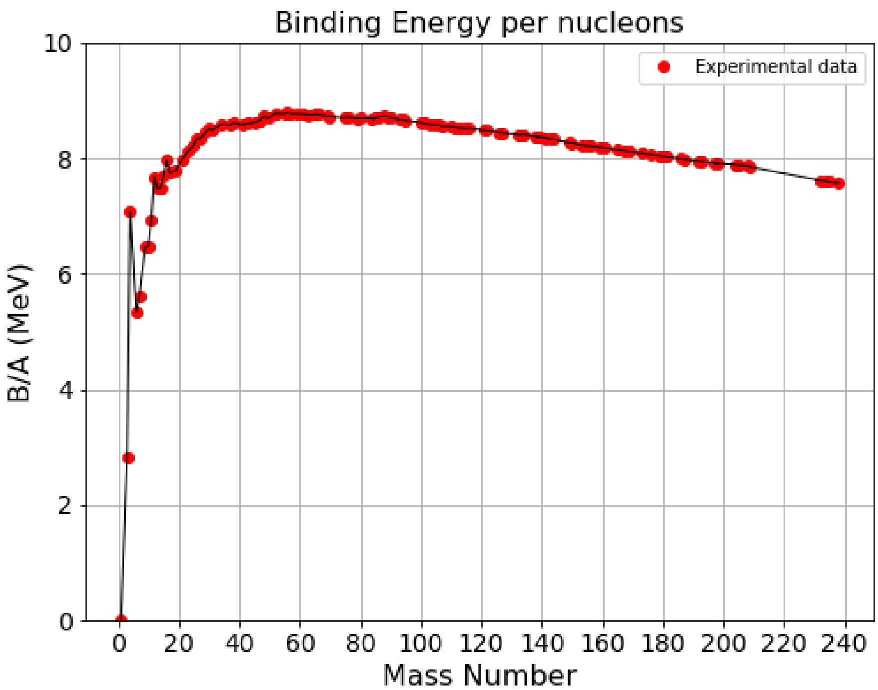

Figure 1.4: Binding energy per nucleons [10].

To optimize the reaction probability (presented by the nuclear cross-section, see Figure 1.5), the nucleus needs to be at some specific energy that is related to the peak of the curve. This energy can be achieved inside a fusion reactor by accelerating the nucleus before colliding it with the target. Therefore, it is important to maximize the reaction probability with the least amount of energy, since this increases the output to input power ratio. The preferred reaction for fusion reactors is the D–T reaction, because it has the highest cross section at a lower input energy. Furthermore, the relative degree of reactivity, $\langle \sigma v \rangle$, presented in Figure 1.5, shows that the D–T reaction is favourable since it reaches the peak at the lowest temperature.

Table 1.1: Most favourable fusion reactions [11].

Reaction			Released energy
${}^{2}_{1}\mathrm{D} + {}^{3}_{1}\mathrm{T}$	$\rightarrow$	${}^{4}_{2}\mathrm{He}\,(3.52\,\mathrm{MeV}) + {}^{1}_{0}\mathrm{n}\,(14.06\,\mathrm{MeV})$	17.58 MeV
${}^{2}_{1}\mathrm{D} + {}^{2}_{1}\mathrm{D}$	$\rightarrow$	${}^{3}_{1}\mathrm{T}\,(1.01\,\mathrm{MeV}) + {}^{1}_{1}\mathrm{p}\,(3.02\,\mathrm{MeV})\ (50\%)$	4.03 MeV
	$\rightarrow$	${}^{3}_{2}\mathrm{He}\,(0.82\,\mathrm{MeV}) + {}^{1}_{0}\mathrm{n}\,(2.45\,\mathrm{MeV})\ (50\%)$	3.27 MeV
${}^{2}_{1}\mathrm{D} + {}^{3}_{2}\mathrm{He}$	$\rightarrow$	${}^{4}_{2}\mathrm{He}\,(3.6\,\mathrm{MeV}) + {}^{1}_{1}\mathrm{p}\,(14.7\,\mathrm{MeV})$	18.3 MeV
${}^{3}_{1}\mathrm{T} + {}^{3}_{1}\mathrm{T}$	$\rightarrow$	${}^{4}_{2}\mathrm{He} + 2\,{}^{1}_{0}\mathrm{n} + (11.3\,\mathrm{MeV})$	11.3 MeV
${}^{3}_{2}\mathrm{He} + {}^{3}_{2}\mathrm{He}$	$\rightarrow$	${}^{4}_{2}\mathrm{He} + 2\,{}^{1}_{1}\mathrm{p}$	
${}^{3}_{2}\mathrm{He} + {}^{3}_{1}\mathrm{T}$	$\rightarrow$	${}^{4}_{2}\mathrm{He} + {}^{1}_{1}\mathrm{p} + {}^{1}_{0}\mathrm{n} + 12.1\,\mathrm{MeV}\ (51\%)$	12.1 MeV
	$\rightarrow$	${}^{4}_{2}\mathrm{He}\ (4.8\,\mathrm{MeV}) + {}^{2}_{1}\mathrm{D}\ (9.5\,\mathrm{MeV})\ (43\%)$	14.3 MeV
	$\rightarrow$	${}^{4}_{2}\mathrm{He}\ (0.5\,\mathrm{MeV}) + {}^{1}_{0}\mathrm{n}\ (1.9\,\mathrm{MeV}) + {}^{1}_{1}\mathrm{p}\,(11.9\,\mathrm{MeV})\ (6\%)$	12.1 MeV
${}^{1}_{1}\mathrm{p} + {}^{6}_{3}\mathrm{Li}$	$\rightarrow$	${}^{4}_{2}\mathrm{He}\ (1.7\,\mathrm{MeV}) + {}^{3}_{2}\mathrm{He}\ (2.3\,\mathrm{MeV})$	4.0 MeV
${}^{3}_{2}\mathrm{He} + {}^{6}_{3}\mathrm{Li}$	$\rightarrow$	$2\,{}^{4}_{2}\mathrm{He} + {}^{1}_{1}\mathrm{p} + 16.9\,\mathrm{MeV}$	16.9 MeV
${}^{1}_{1}\mathrm{p} + {}^{11}_{5}\mathrm{B}$	$\rightarrow$	$3\,{}^{4}_{2}\mathrm{He} + 8.7\,\mathrm{MeV}$	8.7 MeV

1.3 Plasma Confinement

In order to make nuclear fusion occur inside a fusion reactor, the fuel needs to be brought into the plasma state, a physical state where the neutral gas is ionized and achieves a quasi-neutral condition of positive ions and electrons [14]. In a fusion reactor, the fuel is fully ionized at very high temperatures. Therefore, it is necessary to confine the operating plasma to avoid damage in the reactor.

As mentioned in Section 1.2, the charged particles (ions and electrons), formed at high temperatures, are accelerated to very high speeds. An important implication is the loss of power by the emission of Bremsstrahlung radiation [15], which dominates when compared to energy loss by collisions or from synchrotron radiation. The Bremsstrahlung losses S_B are proportional to the $n_e^2\ T_e^{0.5}$, n_e being the electron density and T_e the electron temperature [15]. At the same time, the D–T nuclei are going to fuse, producing α–particles and neutrons. The α–particles are confined and release energy – S_{fus} – to the plasma.

Considering the total energy loss rate of the plasma through several mechanisms, S_{loss}, and the total available energy density of the plasma, U, the plasma confinement time can be determined by

$$\tau_E = \frac{U}{S_{loss}}. \tag{1.1}$$

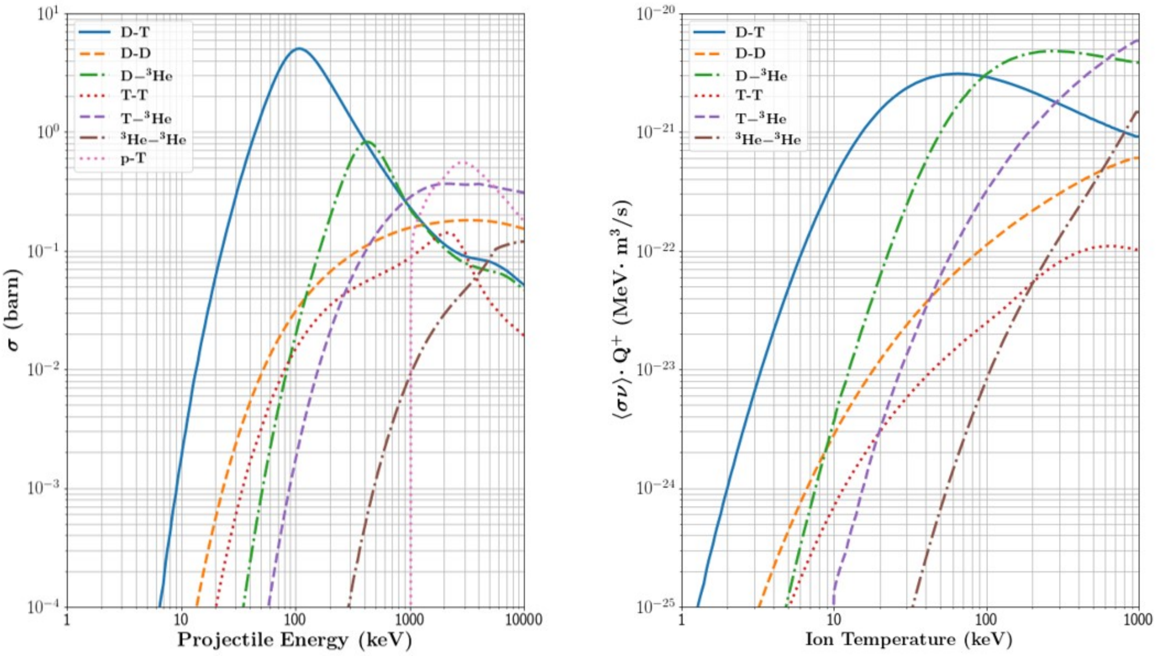

(a) (b)

Figure 1.5: (a) Cross sections of some nuclear fusion reactions as a function of the nucleus kinetic temperature (adapted from [12]); (b) Relative degree of reactivity in a hot plasma induced by the charged reaction products (adapted from [13]).

By applying the energy conservation law, the sum of the power density given to the plasma from the nuclear fusion reaction (S_{fus}) and from external heating (S_{ext}) should be equal to the power loss density,

$$S_{fus} + S_{ext} = S_B + S_{loss}. \tag{1.2}$$

Once the equilibrium and self-sustainability are attained, the external heating is expected to be turned off and the energy conservation law becomes

$$S_{fus} = S_B + S_{loss}. \tag{1.3}$$

To sustain the energy release, the energy released by the nuclear fusion reactions should be equal to or exceed the energy loss. By applying the Lawson criterion [16], optimal conditions for plasma confinement can be defined by the triple product of the ion density, ion temperature and confinement time, which should be given by

$$nT_i\tau_E = \frac{12\,k_B}{E}\frac{T^2}{\langle\sigma\nu\rangle} \tag{1.4}$$

where E is the energy of the particles and $E = E_\alpha = 3.52\,\text{MeV}$ for the D–T reaction. Six nuclear fusion triple products are presented in Figure 1.6. Again, the D–T reaction provides optimal conditions at the lowest temperature.

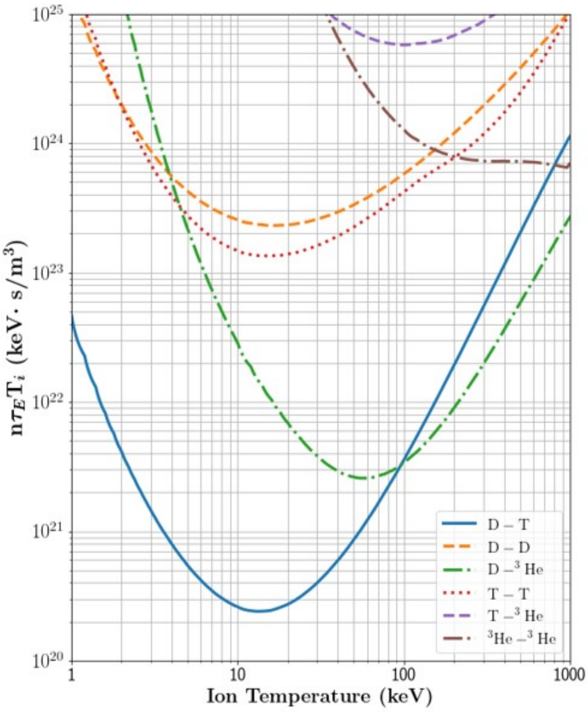

Figure 1.6: Triple product as a function of the ion temperature (calculated from [13]).

1.4 Fusion Reactors

1.4.1 International Thermonuclear Experimental Reactor (ITER)

The ITER project, currently under construction in southern of France (Cadarache), is one of the most ambitious projects in the world. It was originally initiated by the terms of a four-party agreement, signed in 1985, between the European Union Atomic Energy Community (28 member countries and 1 associated country), the Government of Japan, the Government of the United States, and the Government of the Russian Federation [17]. Nowadays, there is a total of 35 countries participating in the project [18]. The aims of ITER are to demonstrate the scientific and technological feasibility of fusion energy for commercial energy production and to test the technologies for the DEMOnstration power station (DEMO).

ITER is a magnetic confinement fusion reactor with toroidal shape, called tokamak, a concept developed by Andrei Sakharov and Igor Tamm in the 1960s [19] whose key components are shown in Figure 1.7. The concept is to confine the plasma inside the vacuum chamber using a magnetic field that allows the plasma to move in a torus shape and to have an infinite loop (ideally). The key parameter of the ITER tokamak is a 6.2 m major radius, confining 840 m^3 of plasma [20]. In order to confine such a plasma, a nominal magnetic field (B_0) of 5.3 T at the center of the chamber [21] results from a 11.8 T toroidal magnetic field (B_φ) and a 6.0 T poloidal magnetic field (B_ϑ) which can be achieved by conjugating superconducting magnets and coils. This confinement occurs inside the Vacuum Vessel (VV), sealed hermetically in order to provide primary high vacuum. These components will be enclosed by the cryostat to ensure low temperatures and secondary vacuum.

The goal of ITER is to produce 500 MW of thermal energy, which is around 10 times the heat injected into the plasma. To achieve this goal, ITER will be operating with the deuterium–tritium fusion reaction (D–T), shown in Table 1.1, which will produce α-particles carrying 20% of the total amount of energy

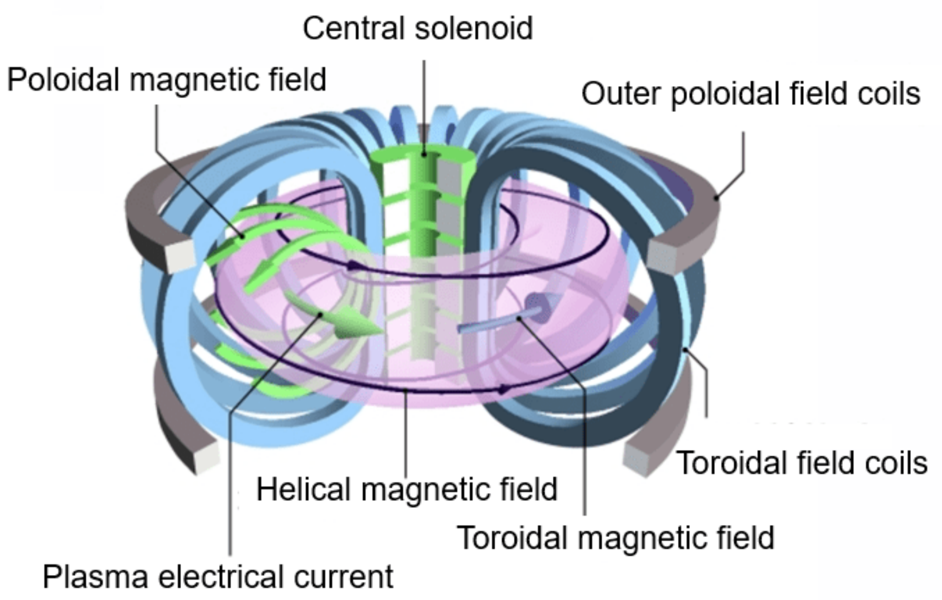

Figure 1.7: Key components of a tokamak [22].

produced in the fusion reaction. These α–particles are charged particles, confined with the plasma, and contribute to increase the temperature of the plasma through collisions with electrons, which in turn may increase the fusion rate [23]. This positive feedback will reduce the dependence on the external heating used to ignite the plasma. The other products of the D–T reaction, neutrons, are non-charged particles that carry 80% of the reaction energy. Neutrons are not magnetically confined and will interact with the walls of the vacuum chamber. The inner part of the ITER vacuum chamber will be covered by blanket modules, which will act as a barrier to moderate neutrons and absorb their kinetic energy [24]. At later stages, the blanket modules located in two dedicated Equatorial Port Plugs (EPPs) will be replaced by Test Blanket Modules (TBMs), which will be responsible to demonstrate Tritium production. These TBMs will contain ${}^{6}_{3}\mathrm{Li}$ and ${}^{7}_{3}\mathrm{Li}$, which can produce Tritium by interacting with neutrons through the reactions presented in Table 1.2. Tritium breeding is very important since Tritium is a Hydrogen isotope with a short half-life (12.3 years) [25], which is rarely found in nature. Therefore, tritium breeding is essential for future tokamaks powered by the D–T reaction.

Table 1.2: Tritium breeding example reactions [26].

Reaction	Released energy
${}^{2}_{1}\mathrm{D} + {}^{2}_{1}\mathrm{D} \rightarrow {}^{3}_{1}\mathrm{T} + {}^{1}_{1}\mathrm{p}$	4.03 MeV
${}^{6}_{3}\mathrm{Li} + {}^{1}_{0}\mathrm{n} \rightarrow {}^{3}_{1}\mathrm{T} + {}^{3}_{2}\mathrm{He}$	4.8 MeV
${}^{7}_{3}\mathrm{Li} + {}^{1}_{0}\mathrm{n} \rightarrow {}^{3}_{1}\mathrm{T} + {}^{3}_{2}\mathrm{He} + {}^{1}_{0}\mathrm{n}$	–2.5 MeV
${}^{7}_{3}\mathrm{Li} + {}^{1}_{0}\mathrm{n} \rightarrow 2\,{}^{3}_{1}\mathrm{T} + 2\,{}^{1}_{0}\mathrm{n}$	–10.3 MeV

The current timeline for the ITER Project [18] is:

2005	Decision to build ITER in France
2007	Formal creation of the ITER Organization (IO)
2007–2009	Land clearing and levelling
2010–2014	Ground support structure and seismic foundation for the tokamak
2012	Nuclear licensing: ITER becomes a Basic Nuclear Installation under French law
2014–2021	Construction of the tokamak Building
2010–2021	Construction of the ITER plant and auxiliary buildings for First Plasma
2008–2021	Manufacturing of the main First Plasma components
2015–2023	Largest components are transported along the ITER Itinerary
2020–2025	Main assembly phase I
Dec 2025	First Plasma
2026	Begin installation of in-vessel components
2035	Deuterium-Tritium Operation begins

ITER is an "experimental" reactor that hopefully will demonstrate the possibility to start and control the thermonuclear D–T reaction that will be used for energy production in future fusion power plants. To achieve this, one of the most important aspects of the project are the diagnostics systems that will monitor the ITER plasma. Some of these diagnostics will measure, monitor and/or control several physical quantities like temperature, velocity distributions of reaction products, densities, and plasma position in general. In parallel, other diagnostics will focus on detecting and analysing the instabilities and providing feedback to mitigate them by adjusting the plasma parameters. The knowledge and technology gained from ITER will be crucial for the development of DEMO, especially for the flawless control of the plasma.

1.4.2 DEMOnstration power station: the DEMO Project

The Demonstration Power Station (DEMO) Project is a proposed nuclear power station which aims at bridging the gap between ITER and the first commercial fusion power station [27–30], according to the EUROfusion roadmap (shown in Figure 1.8). One of the main differences between ITER and DEMO, shown in Table 1.3, is the tritium self-sufficiency. In order to achieve this while maintaining the reactor in GW power for sufficient operation time, tritium breeding is required, since tritium (one of the fuels) has low supplies in nature. Therefore, the DEMO reactor is planned to be built with full tritium breeding blanket wall. Furthermore, DEMO is expected to be much larger than ITER (see Table 1.4), with a plasma volume up to 3 times larger. This scale-up will hopefully be sufficient to produce 2000 MW of gross thermal output power, equivalent to 500 MW electrical output, with an input power of 80 MW. With these conditions, the breeding blanket wall is expected to experience very high thermal loads. Furthermore, long-term exposure to high neutron and γ fluxes (in the order of 1×10^{14} n/cm^2/s) might alter the mechanical properties of the materials, degrading their performance.

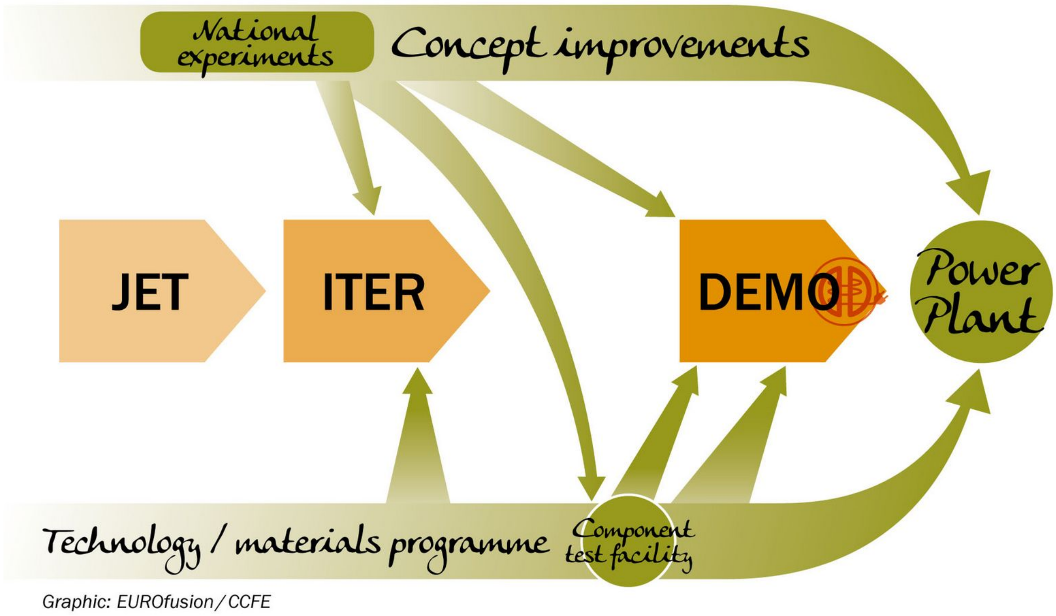

Figure 1.8: Path from ITER to DEMO and finally to a commercial power plant [31].

Table 1.3: Main differences between ITER and DEMO [32] [33].

ITER	DEMO
• Experimental device with physics and development missions. • 400 s pulses, long dwell time. • Experimental campaigns. Outages for maintenance, component replacements. • Large number of diagnostics. • Multiple HCD systems. • Large design margins, necessitated by uncertainties and lack of fully appropriate design codes. • Cooling system optimized for minimum stresses and sized for modest heat rejection. • Unique one-off design optimized for experimental goals. • No Tritium breeding requirement (except very small quantity in TBM). • Conventional 316 stainless steel structure for in-vessel components. • Very modest lifetime n-fluence, low dpa and He production. • Licensed as nuclear facility, but like a laboratory, not a reactor. • Licensing as experimental facility. • 'Progressive start-up' permits staged approach to licensing. • During design, licensing in any ITER party had to be possible.	• Nearer to a commercial power plant but with some development missions. • Long pulses (>2h) or steady state. • Maximize availability. Demonstrate effective and efficient maintenance and component replacement technologies. • Typically, only those diagnostics required for operation. However, there may be the need to have diagnostics for component testing and qualifications. • Optimized set of HCD systems. • With ITER (and other) experience, design should have smaller uncertainties. • Cooling system optimized for electricity generation efficiency (i.g., much higher temperature). • Move towards design choices suitable for series production. • Tritium breeding needed to achieve self-sufficiency. • Nuclear hardened, novel reduced activation materials as structure for breeding blanket. • High fluence, significant in-vessel material damage. • Licensing as nuclear reactor more likely. Potential for large Tritium inventory on-site. • Stricter approach may be necessary to avoid large design margins. • 'Progressive start-up' should also be possible (i.g., utilize a 'starter' blanket using moderate-performance materials and then switch to blankets with a more advanced-performance after a few MW yr/m^2). • Fewer constraints.

The current timeline for the DEMO project is [34]:

2014–2020	Pre-Concept design phase
2021–2027	Conceptual design phase
2029–2038	Engineering design phase
2040–2049	Procurement and construction phase
2050–2070	Comissioning and operation phase

1.5 Diagnostics for ITER and DEMO

Large tokamaks like ITER and DEMO require an extensive network of diagnostics able to measure plasma parameters for plasma control. Both reactors will feature diagnostics to measure, monitor and control the plasma in real-time. ITER is planned to have about 40 different systems, including Rogowski coils, Saddle loops, Radial Neutron Cameras (RNCs), Vertical Neutron Cameras (VNCs), Gamma-ray Spectrometers, Collective Thomson Scattering (CTS) systems, Bolometers, Charge eXchange Recombination Spectroscopy (CXRS) systems, Motional Stark Effects (MSEs) systems, Soft X-ray array systems, Electron Cyclotron Emission (ECE) systems, Main Plasma Reflectometer systems, Plasma Position Reflectometry (PPR) systems (descoped in 2019), Divertor Interferometer/Reflectometer, IR/Visible Cameras, Thermocouples, Pressure Gauges, Residual Gas Analysers, IR Thermography systems, and Langmuir Probes [35] [36].

A diverse set of diagnostics systems is also expected for DEMO [37]. Due to the higher radiation loads in the plasma facing components and the need for tritium self-sufficiency [38], the integration of these diagnostics systems in DEMO is subjected to constraints which go far beyond the ones currently faced in ITER. Therefore, some additional considerations for DEMO plasma diagnostics, listed in Table 1.5, need to be considered.

The expected effects of the harsh environment on diagnostics for several regions of the ITER reactor are shown in Figure 1.9. It is clear that whatever the type and wherever the diagnostics system is to be installed, the integration of the diagnostic under very high thermal loads and neutron irradiation is not an easy task [39].

1.6 Neutron irradiation impact on materials

Neutron irradiation might cause micro-structural defects in the materials, since neutrons collide with and transfer part of their kinetic energy to the atom nuclei, in some cases knocking the atoms out of their lattice position. If sufficient energy is transferred in the collisions, the recoil particles can cause further collisions and generate cascades of displaced atoms [40]. Although in metals most of these displaced atoms eventually recombine to vacate lattice positions, the remaining radiation defects and micro-structural re-arrangements change the material properties. The microscopic defects produced in materials due to irradiation (see Figure 1.10) are referred to as radiation damage, whereas the observable effects on the macroscopic properties of the materials are referred to as radiation effects [41]. Radiation effects include swelling, embrittlement, hardening, irradiation creep (fracture), transmutation and phase transitions. These radiation effects can also be seen from the material mechanical properties. The

Table 1.4: Overview of the main parameters of ITER and DEMO as compared to the best/highest achieved values in present devices (derived from [20]) [37].

Parameter	**Unit**	**ITER**	**DEMO steady-state**[1]	**Best achieved individual parameter**
Plasma volume	V (m^3)	840	900–2700	80 (JET)
Pulse length	(s)	400–3000	continuous wave	390 (Tore Supra)
Fusion Power	P_{fus} (MW)	$\sim$ 500	2500–5000	16 (JET)
Power multiplication	$Q=P_{fus}/P_{in}$	10	15–35	0.8 (JET)
Total number of neutrons	(n/s)	1.4×10^{21}	$(1.4–7) \times 10^{21}$	1.2×10^{19}
Neutron flux on first wall	(n/m^2s)	3×10^{18}	$(3–10) \times 10^{18}$	3×10^{17} (JET)
Neutron load on first wall	(MW/m^2)	$\sim$ 0.5	1–3	$\sim$ 0.05 (max) (JET)
Neutron fluence	(MW year/m^2)	0.3	5–15	Negligible
Neutron fluence	(n/m^2)	$\sim 3 \times 10^{25}$	$(50–150) \times 10^{25}$	$\sim 3 \times 10^{21}$
Displacement per atom in first wall	(dpa)	$\sim$ 3	50–150	0

[1] Since there is not yet a single steady-state DEMO design, ranges of values are given here, covering the various options.

radiation-induced swelling results in a volume increase that will affect the thermal conductivity, while embrittlement and radiation hardening lead to the increase of the Ductile to Brittle Transition Temperature (DBTT), yield strength, and ultimate tensile strength. These changes make the components more prone to the brittle failure, which should be avoided at all cost. The transmutation processes will have a direct impact on the thermomechanical properties of the material, namely, heat conductivity, heat capacity, and linear expansion coefficient [26].

Displacements per atom (dpa) are a measure of the effect of irradiation on materials, defined as the average number of times an atom is displaced from its normal lattice site by atomic collision processes [40]. As the materials of the future nuclear fusion reactors will be exposed to increasingly high doses of radiation, phenomena such as swelling, hardening and embrittlement need to be taken into account in the structural analyses [42–46]. The magnitude of the dpa effects also depends on the operating temperature of the materials [47]; furthermore, neutron-induced transmutations cause significant changes in the elemental composition of the materials, producing volatile elements such as hydrogen and helium which contribute to the development of cracks [47, 48].

Another important challenge for ITER and DEMO is the lack of irradiated material properties data available for the analysis and prototyping, considering the technology to procure the materials used for these reactors is very recent. Moreover, there are no present fusion reactors that can achieve the neutron fluence value to test the material properties under the expected nuclear environment [37].

1.7 Main objectives of this thesis

This thesis presents the work developed on two diagnostic systems developed by Instituto de Plasmas e Fusão Nuclear (IPFN/IST) for ITER and DEMO. The first is the PPR system developed for ITER in the

Table 1.5: Examples of requirements in the design of DEMO plasma diagnostics [42].

Type	Compatibility/requirement
Non-nuclear	• Avoidance of halogens (which can form acids in tritium plant) • Earthing and signal paths. • EMI screening (source or recipient) • Disruption and seismic acceleration forces • Vibration and other operational cyclic loads • Disruption-induced currents and voltages • ICRH and ECRH immunity • Vignetting of other systems (photon, particles) • UHV design principles • Fast particles impacts (i.e., erosion, heating) • Deposition of dust and coating on critical surfaces
Nuclear	• Real-time radiation-induced effects • Radiation damage (e.g., in mirrors and transparent optics) • Compatibility with rapid remote handling systems • Useful life between component replacements (if possible) • Neutron streaming (labyrinths, line of sight restrictions) • Tritium and active dust containment • Installation and operational clearances • Impact on neutron fluxes elsewhere • Thermal environment including self-nuclear heating • RAMI (reliability, availability, maintainability, inspectability)

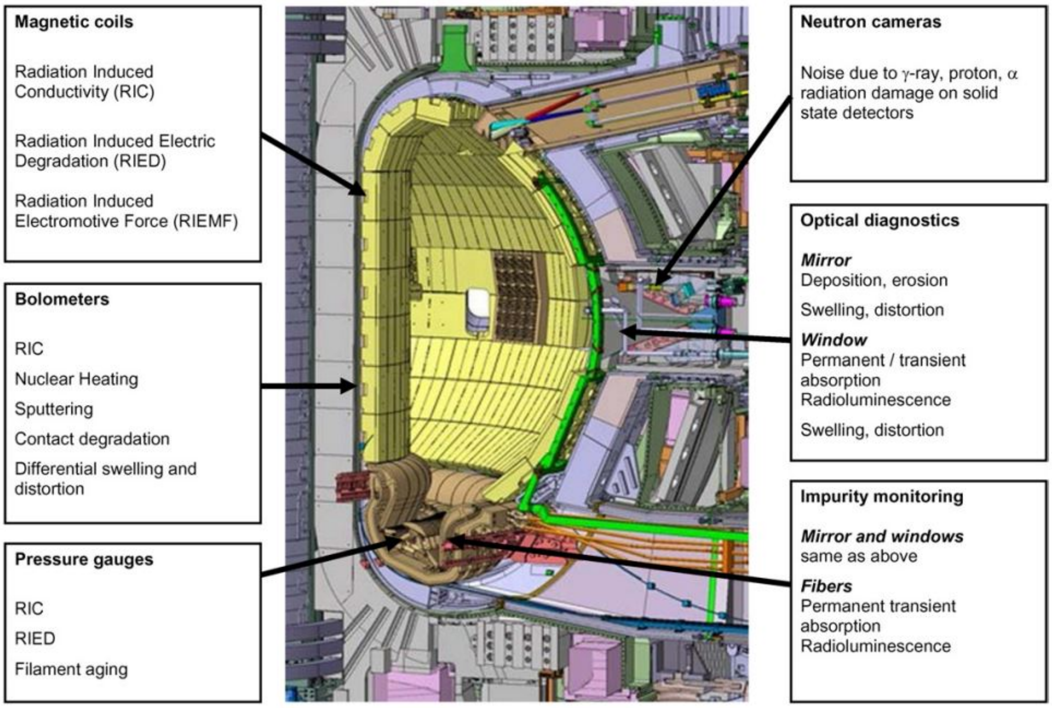

Figure 1.9: Environmental effects on diagnostic components located at close proximity to the ITER plasma [37].

frame of a partnership agreement between IPFN/IST and Fusion for Energy (F4E), which unfortunately was descoped by the ITER Organization (IO) during its development. Nevertheless, considerable knowledge was gathered during the development of this system, especially related to the simulation methodologies and expected outcomes. The second is the microwave (MW) multi-reflectometer system developed

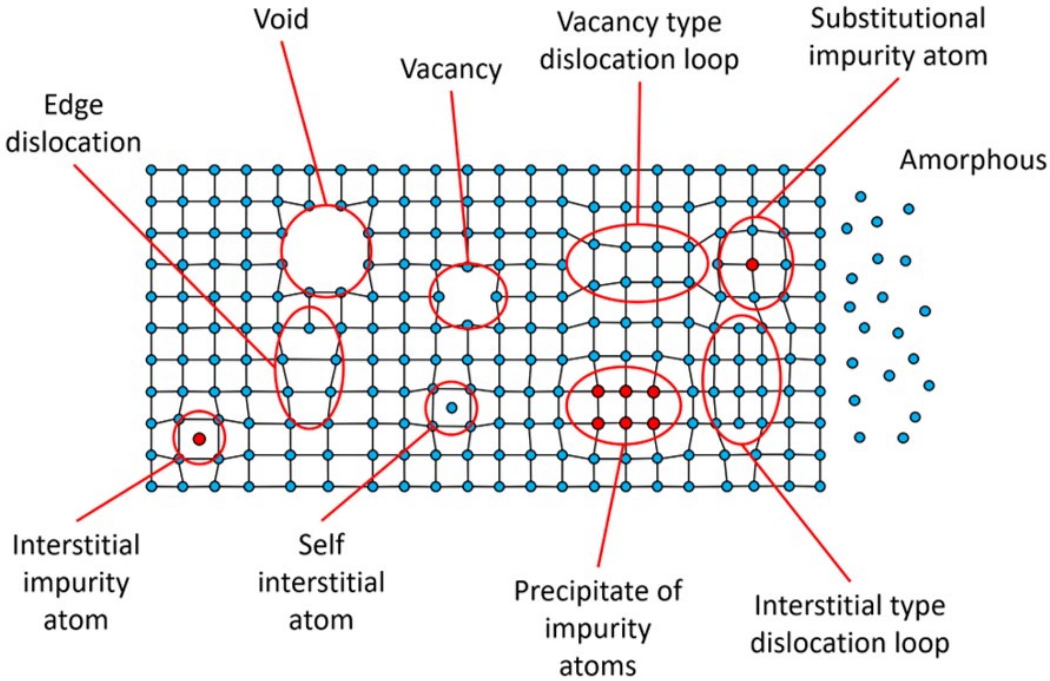

Figure 1.10: Defects on the lattice structure that can change the material properties [40].

by IPFN/IST for DEMO, in the frame of the EUROfusion Work Package Diagnostics & Control (WPDC).

Some components of these systems will be installed inside the vacuum vessel directly exposed to the plasma. Therefore, they will be subjected to high radiation doses from the plasma neutrons and the gamma photons generated in nuclear interactions with the surrounding materials. These radiation doses will contribute to the thermal loads in the systems and may cause irradiation-induced changes in the material properties, which can compromise the integrity of the components during the lifetime of the fusion reactors for which they are designed (ITER and/or DEMO).

The main objective of this thesis is to assess the integrity of the reflectometry diagnostics in ITER and DEMO. As ITER is at a much more advanced design stage when compared to DEMO, the methodologies employed in the thermal and structural analyses of its in-vessel components follow a strict standardized workflow, while in DEMO – which is currently in the conceptual design phase – there is more freedom in the choice of the tools to perform the analyses. Nevertheless, the methodologies learned in ITER are validated and can be applied to the design of in-vessel components for DEMO, despite the lack of experimental data related to some material properties at higher dpa.

The work presented in this thesis is focused on the requirement to ensure that both diagnostics perform their roles under neutron irradiation without significant damage, complying with the temperature limits for materials during operation. The first step to accomplish this is to perform neutronics simulations, neutronics being the study of the interactions between neutrons and matter. Besides the potential mechanical damage and transmutation, neutrons deposit their energy in the materials and contribute to increase their operation temperatures. Once the nuclear heat generation is evaluated, thermo-mechanical analyses are required to assess the impact of the thermal loads on the structural integrity of the system, in simulations which also take into account the gravity and electromagnetic loads. Furthermore, the thermo-mechanical analyses are used to evaluate the expected deformation of the waveguides, an important factor to assess the performance of reflectometry systems. In summary, this work covers several fields of knowledge: radiation-matter interaction, plasma physics, diagnostics engineering, heat transfer, Computational Fluid

Dynamic (CFD) and structural analyses.

Regarding the ITER PPR system, this thesis extends the work presented in [49] and [50], in which the neutronics simulations had already been performed. A thermal analysis of the PPR system is performed, following ITER's guidelines and using as input the nuclear loads calculated beforehand. This work was then used as reference for a detailed design study performed for the multi-reflectometer system of DEMO, which inlcuded CAD design, neutronics simulations and thermo-mechanical analyses.

Regarding the multi-reflectometer system of DEMO, this thesis extends the work initiated in [51, 52]. These two works adopted the integration concept presented in [53], the Diagnostics Slim Cassette (DSC), a "dummy poloidal section" fully dedicated to diagnostics [54, 55]. The results presented in [51] showed that the maximum temperature of the DSC First Wall (FW) in that previous design was more than 1000 °C, which is way above the maximum operation temperature allowed for EUROFER under neutron irradiation (550 °C). However, the work in [52] presented an alternative cooling system design which successfully brought down the maximum temperature of the DSC to 425 °C. The downside of this cooling system design is its complexity and difficulty to manufacture with the current available manufacturing technology. Therefore, this thesis aims to design a DSC with a cooling system able to keep its operation temperatures within the limit for EUROFER under neutron irradiation using cooling system configurations based on the technologies employed in the DEMO Breeding Blanket (BB) designs. Furthermore, the structural integrity of the DSC must be ensured, according to the guidelines for structural analyses for ITER and DEMO. The objective was then to assess the impact of the WG deformations due to thermo-mechanical loads on the MW measurements performed by the reflectometry system, and discuss the main issues related to the integration of the DSC in the DEMO tokamak.

This thesis is organized as follows: Chapter 2 introduces the background theory of reflectometry and surveys the reflectometry systems installed in existing tokamaks around the world. Chapter 3 presents the background theory and the tools used for obtaining the boundary conditions from the neutronics point of view, namely the volumetric heat deposition in the materials and the expected dpa values. Chapter 4 presents the background theory and the tools used for evaluating the integrity of diagnostic components. Chapter 5 contains the results of the ITER PPR thermal analyses. The details of the DEMO tokamak and its components related to this thesis are presented in Section 6.1, followed by the design studies and thermo-mechanical analyses for the cooling system of the DEMO DSC, presented in Chapter 7. The integration studies of the DSC in DEMO are covered in Chapter 8. Finally, the conclusions and suggestions for future work are reported in Chapter 9.

Chapter 2

Reflectometry Diagnostics

One of the main challenges in controlled fusion plasma reactors is the need to monitor and control the plasma shape and position in order to prevent the loss of confinement or plasma disruptions, which may cause damage to the inner wall and other components. Reflectometry is foreseen as a viable candidate to perform this role in future tokamaks, in addition to monitoring the plasma density at several positions.

Due to the plasma high temperature and the importance of maintaining that temperature to keep the ongoing fusion reactions, it is necessary to use non-perturbing probing diagnostics to measure important plasma parameters like the plasma electron density and associated fluctuations. MW reflectometry was first suggested for tokamak reactors in 1961 [56] as a way to measure the electron density. The method developed by Anisimov relies on the phase difference measurement between incident and reflected waves to recover the position of the reflecting plasma layer, which has a certain electron density.

Profile reflectometer systems have been developed and operated since the 1980s on several devices, such as ASDEX Upgrade (AUG) [57–62], DIII-D [63–65], Joint European Torus (JET) [66–68], and Tore Supra (TS) [69–71] . Over the past thirty years, these devices have successfully tested most of the key design features anticipated for profile reflectometry for ITER and DEMO.

The basic concept of reflectometry is based on the interaction between electromagnetic waves and plasmas. In particular, it is based on the idea that the propagating electromagnetic waves are reflected back when a critical density is reached (or when the local refractive index goes to zero). The reflected wave characteristics will allow the determination of the position of the critical layer and the reconstruction of the electron density profile, providing the necessary data for the roles the diagnostic is expected to perform. In the next section, the theoretical basis for this technique is described.

2.1 Physics of Reflectometry

Since millimetre wave reflectometry uses electromagnetic waves, the interactions between the probing waves and the plasmas can be described using Maxwell's equations. They provide the relations between the electric field **E**, the magnetic field **H**, the displacement field **D**, the magnetic flux density **B**, the charge density ρ and the current density **J** of the system in study. They can be written as follows [72]:

$$\nabla \cdot \mathbf{D} = \rho \tag{2.1}$$

$$\nabla \cdot \mathbf{B} = 0 \tag{2.2}$$

$$\nabla \times \mathbf{E} = -\frac{\partial \mathbf{B}}{\partial t} \tag{2.3}$$

$$\nabla \times \mathbf{H} = \mathbf{J} + \frac{\partial \mathbf{D}}{\partial t}. \tag{2.4}$$

with

$$\mathbf{J} = \sigma \mathbf{E} \tag{2.5}$$

where σ is the conductivity tensor.

Gauss' Law for electric fields, written in Equation (2.1), states that the electric flux through any closed surface is proportional to the total electric charge enclosed by this surface. Gauss' Law of magnetism (Equation (2.2)) suggests that the magnetic flux lines are closed and that there are no magnetic monopoles. Faraday's Law of induction, presented in Equation (2.3), mathematically describes the fact that a spatial variation of the electric field always accompanies a time variation of the magnetic field. Finally, Equation (2.4) is Ampère's Law, which explicitly describes that the sources of the magnetic field are the current density and the time variation of the displacement current field. These equations are coupled by the generic constitutive relations:

$$\mathbf{D}(\mathbf{r}, t) = \varepsilon(\mathbf{r}) \cdot \mathbf{E}(\mathbf{r}, t) \tag{2.6}$$

$$\mathbf{B}(\mathbf{r}, t) = \mu(\mathbf{r}) \cdot \mathbf{H}(\mathbf{r}, t) \tag{2.7}$$

where $\varepsilon(\mathbf{r})$ and $\mu(\mathbf{r})$ are the electric permittivity and magnetic permeability tensors, respectively, which take into account the character of the medium of propagation of the fields. In the case of an inhomogeneous and isotropic material as medium, i.e. where the permittivity and permeability are different for each position and are scalars, the wave propagation equation for the electric field is given by

$$\nabla^2 \mathbf{E}(\mathbf{r}, t) - \frac{\varepsilon(\mathbf{r})}{c^2} \frac{\partial^2 \mathbf{E}(\mathbf{r}, t)}{\partial t^2} = 0 \tag{2.8}$$

where c is the speed of light. Considering a plane wave with an electric field $\mathbf{E}(\mathbf{r}, t) = \mathbf{E}(\mathbf{r}) \exp[i\omega t]\, \mathbf{e_E}$, where ω is the frequency of the electric wave and $\mathbf{e_E}$ is its propagation direction vector. The solution of Equation (2.8) can be decoupled into components perpendicular to the propagation direction ($\mathbf{z}$ is assumed to be the propagation direction) as:

$$\frac{\partial^2 E_x}{\partial t^2} + \omega^2 \frac{\varepsilon_X(z)}{c^2} E_x = \frac{\partial^2 E_x}{\partial t^2} + k_0^2\, \varepsilon_X(z)\, E_x = 0 \tag{2.9}$$

$$\frac{\partial^2 E_y}{\partial t^2} + \omega^2 \frac{\varepsilon_O(z)}{c^2} E_y = \frac{\partial^2 E_y}{\partial t^2} + k_0^2\, \varepsilon_O(z)\, E_y = 0 \tag{2.10}$$

where $k_0 = \omega/c$ is the wave number of the propagating wave and $\varepsilon_{X,O} = n_{X,O}^2$ is the refraction index of the plasma for the extraordinary (X) and ordinary (O) modes, respectively. Both of these modes are the solutions for the decoupled wave equations on Equation (2.9) and Equation (2.10), which are perpendicular to the propagation direction; X-mode is where the electric field is perpendicular to the magnetic field and O-mode is where the electric field is parallel to the magnetic field. For reflectometry, the relevant case is when the waves with linear polarisation propagate in a direction perpendicular to the existing magnetic field ($\mathbf{k} \perp \mathbf{B}$), e.g. the toroidal magnetic field inside a tokamak.

Under the high-frequency approximation, in which the motion of the ions can be neglected and does not contribute to the polarisation of the medium, the Appleton-Hartree [73] relation of the refraction index becomes:

$$\varepsilon_{X,O} = n_{X,O}^2 = 1 - \frac{2\alpha(1-\alpha)}{2(1-\alpha) - \beta \mp \beta}, \tag{2.11}$$

where $\alpha = \omega_{pe}^2/\omega^2$, $\beta = \omega_{ce}^2/\omega^2$. The X-mode is represented by the minus sign on the denominator and the plus sign represents the O-mode. The ω_{pe} and ω_{ce} are the plasma and electron cyclotron frequencies defined by

$$\omega_{pe} = \sqrt{\frac{n_e e^2}{\varepsilon_0 m_e}} \tag{2.12}$$

$$\omega_{ce} = \frac{e\mathbf{B}}{m_e} \tag{2.13}$$

with n_e being the electron density, e the electron charge, m_e the electron mass and $\mathbf{B}$ the total magnetic field.

When the reflectometry antenna operates in O-mode, e.g. in the ITER PPR system, the refractive index can be expressed as:

$$n_O^2 = 1 - \frac{\omega_{pe}^2}{\omega^2} = 1 - \frac{n_e}{n_c} \tag{2.14}$$

with a cut-off frequency $\omega = \omega_{pe}$, and a cut-off density $n_c = \left(\frac{\omega}{e}\right)^2 \varepsilon_0 m_e$.

A complete and continuous wave equation solution which is described by the complex dielectric function written in Equation (2.11) is not yet found, but by splitting it case by case, the solution can be found. For a positive dielectric constant, $\varepsilon(z,\omega) > 0$ (in other words, $n(z,\omega)$ being a real number), the electric wave is propagating in the medium and the solution can be written as a linear combination of oscillating solutions:

$$E(z) = C_1 e^{ik_0\sqrt{\varepsilon(z,\omega)}z} + C_2 e^{-ik_0\sqrt{\varepsilon(z,\omega)}z} \quad , \quad C_1, C_2 \in \mathbb{R} \tag{2.15}$$

For a negative $\varepsilon(z,\omega)$ (the case in which $n(z,\omega)$ is an imaginary number), the valid solution is:

$$E(z) = C_1 e^{k_0\sqrt{|\varepsilon(z,\omega)|}z} \quad , \quad C_1 \in \mathbb{R} \tag{2.16}$$

which represents the wave that is damped along the propagation, also known as evanescent wave.

The most relevant case for microwave diagnostics is when $\varepsilon(z,\omega) = n(z,\omega)$, when the probing wave launched to the medium propagates until it finds a layer where the local plasma frequency equals the probing wave frequency $(\omega_{pe} = \omega)$, and the wave is reflected back by this layer [74]. The phase difference between the launched probing wave and the reflected wave is used to determine the position of the cut-off layer, since the wave phase changes according to the distance it travelled.

To summarize, the probing wave propagates in the region before the cut-off layer, $\varepsilon(z,\omega) > 0$, up to the cut-off layer, where $\varepsilon(z,\omega) = 0$; the reflected wave then propagates in the medium with $\varepsilon(z,\omega) > 0$ back to the receiver. The phase difference between the probing wave and the reflected wave can be derived and is given by [75]

$$\varphi = \frac{2\omega}{c}(z_A - z_e) + \frac{2\omega}{c}\int_{z_c}^{z_e} n(z,\omega)\,dz - \frac{\pi}{2} \tag{2.17}$$

where the first term represents the wave propagation in vacuum from the antenna located at z_A to the edge of the plasma located at z_e, the second term is related to the wave propagation in the plasma and the last term is related to the correction factor due to the phase change at the reflection layer (cut-off layer) [62] [76]. Using the assumption that the antenna is located at the edge of the plasma, there is no wave propagation in vacuum, and inserting the refraction index of Equation (2.14) in Equation (2.17), we get:

$$\varphi = \frac{2\omega}{c}\int_{z_c}^{z_e} \sqrt{1 - \frac{\omega_{pe}^2(z)}{\omega^2}}\,dz - \frac{\pi}{2} \tag{2.18}$$

The reflecting layer position $(z(\omega_c))$ can be found by applying the Abel inversion integral on Equation (2.18) [77,78]:

$$z(\omega_c) = z_e - 2c\int_0^{\omega_c} \frac{d\varphi}{d\omega}\frac{1}{\sqrt{\omega_c^2 - \Omega^2}}\,d\Omega \tag{2.19}$$

where $z(\omega_c)$ gives the position of each critical layer with the cut-off frequency $\omega_c = \omega_{pe}$, which can be used to trace back the electron density at that layer given by $\omega_c = \omega_{pe}\sqrt{n_e(z)\,e^2/\varepsilon_0 m_e}$. The group delay of the probing waves, from which the plasma relative position from the antenna is derived from, is directly measurable, and given by $\frac{d\varphi(\omega)}{d\omega}$. Knowing these relations, one can simply sweep the electromagnetic wave frequency to determine the electron density of the plasma at each layer, which can be done simultaneously using broadband reflectometry. On the other hand, the resonance frequency (the frequency that has the maximum energy transfer) for the O-mode is $\omega = \omega_{ce}$.

For the X-mode, the cut-off occurs for the cases that satisfy the condition $n_X^2(z,\omega) = 0$, which are:

$$\omega_{uc} = \sqrt{\omega_{pe}^2 + \frac{\omega_{ce}^2}{4}} + \frac{\omega_{ce}}{2} \tag{2.20}$$

and

$$\omega_{lc} = \sqrt{\omega_{pe}^2 + \frac{\omega_{ce}^2}{4}} - \frac{\omega_{ce}}{2} \tag{2.21}$$

where ω_{uc} and ω_{lc} are the upper and lower cut-offs. The frequency range between these two cut-offs is the range for the propagating wave. It is analytically impossible to extract the critical layer position due to the high complexity of its dispersion relation; therefore, numerical methods are used instead. However, this process is not straightforward, since the the index of refraction in this mode depends on the magnetic field, which is not always known. The resonance frequency for X-mode occurs at the upper hybrid frequency, $\omega = \omega_{uh} = \sqrt{\omega_{pe}^2 + \omega_{ce}^2}$.

2.2 Reflectometry diagnostics systems in existing tokamaks

In fusion experiments, MW reflectometry diagnostics are well known for their ability to measure the radial electron density profile independently of the magnetic reconstruction [58]. Reflectometry was successfully demonstrated as an alternative control technique in 2012 [58], increasing its range of potential applications in future tokamaks. Furthermore, its application to the study of Edge-Localized Mode

(ELM) events [79] shows its high temporal and spatial resolutions. Another important characteristic of reflectometry systems for future tokamaks is their radiation robustness and components life time, as their front-end components are metallic antennas and waveguides able to withstand high neutron and gamma fluxes for long operation periods. This section presents a summary of the characteristics of the reflectometry systems currently in operation in the four largest, most ITER–relevant tokamaks.

2.2.1 ASDEX Upgrade (AUG)

ASDEX Upgrade is an advanced tokamak reactor with a full tungsten (W) FW [80], as DEMO will be. It aims to prepare the physics base for ITER and DEMO focusing on essential plasma properties such as the plasma density, the plasma pressure and the wall load [81, 82]. Therefore, the equipment installed in ASDEX Upgrade has some of the characteristics required to face the challenges for ITER and DEMO.

The Frequency Modulation of a Continuous Wave (FM-CW) reflectometry system developed for ASDEX Upgrade is a very complex system with important measurement capabilities, installed close to the equatorial plane with 11 broadband channels (see Table 2.1): 7 channels located on the low-field side (LFS) and 4 channels located on the high-field side (HFS). Plasma density profiles are measured simultaneously in t $\geq$ 20 µs. It is expected to measure 3066 profiles for each side during one discharge.

Table 2.1: Broadband channels for profile measurements in AUG [61, 83].

Side	**Microwave bands**	**Probing frequencies** (GHz)	**Density coverage** (1×10^{19} m^{-3})
HFS	O-mode: K, Ka, Q, and V	18–70	0.45-6.5
LFS	O-mode: K, Ka, Q, V, W	18–110	0.45-14.5
	X-mode: Q and V	40–70	≥ 0

The unique features of reflectometry system installed in ASDEX Upgrade are [61]:

1. Good measurement accuracy using a linear model while measuring with O-mode only.
2. Automatic profiles measurement even in the presence of strong plasma turbulence.
3. The only existing reflectometry system that probes both LFS and HFS profiles.

ASDEX Upgrade was the first tokamak in which reflectometry was successfuly demonstrated as an alternative control technique [58]. This achievement becomes important to complement magnetic diagnostics for plasma control, especially for future long pulse tokamak devices, such as DEMO.

2.2.2 DIII-D

The DIII-D National Fusion Facility is a world-leading research facility that is pioneering the science and innovative techniques that will enable the development of nuclear fusion as an energy source for the next generation [84].

DIII-D developed the “doublet” shape, a configuration with an elongated hourglass-shaped plasma cross-section, which pioneered the D-shaped cross-section plasma adopted by many other tokamak such as JET, TCV, ASDEX-Upgrade, JT-60U, KSTAR, and EAST, which are preparing to address the challenges for ITER and beyond.

Table 2.2: Broadband channels for profile measurements in DIII-D [65,83,85].

Polarization	**Microwave bands**	**Probing frequencies** (GHz)	**Density coverage** (1×10^{19} m^{-3})
O-mode and X-mode	Q band	33–50	0–6.4
	V band	49–75	

The unique features of reflectometry system installed in DIII-D are:

1. Operates on dual polarization, both O-mode and X-mode simultaneously.
2. Monostatic corrugated circular antenna which acts as launcher and receiver.

2.2.3 Joint European Torus (JET)

The Joint European Torus or JET is the world's largest fusion reactor in operation [86], designed to study the nuclear fusion reaction in conditions close to the ones required for a nuclear fusion power plant. Therefore, since 1991, the experiment in JET is fueled by the deuterium-tritium fuel mix [87,88] that will be used for commercial power plant.

The reflectometry system in JET consists of six reflectometers and four correlation reflectometers integrated using a combining system that allows these ten instruments to share four waveguides (three for emission and one for reception). This combining system involves quasi-optical boxes to split the microwave beam using a polariser grid or a multi-mesh low-pass filter [89].

Table 2.3: The six JET reflectometers operating specifications [83,89].

Polarization	**Microwave bands**	**Probing frequencies** (GHz)	**Density coverage** (1×10^{19} m^{-3})
X-mode	Q band	33–51	0–14.9
	V band	49–76	
	W band	74–111	
	D band	109–150	
O-mode	V band	49–76	
	W band	74–111	

The unique features of the reflectometry system installed in JET are:

1. Operates using correlated reflectometers.
2. Splits the microwave beam using quasi-optical boxes.

2.2.4 Tore Supra (TS)

Tore Supra (recently upgraded and renamed to – WEST) is a tokamak designed to create long-duration plasmas using a superconducting toroidal magnet. Currently, TS holds the record of the longest plasma duration time of 390 s [90].

Table 2.4: Tore Supra reflectometers operating specifications [83, 91, 92].

Polarization	**Microwave bands**	**Probing frequencies** (GHz)	**Density coverage** (1×10^{19} m^{-3})
X-mode	V band	52–78	0–6.9
	W band	74–108	
	D band	105–150	
O-mode	Ka band	25–40	
	V band	40–75	
	W band	75–108	

The unique features of reflectometry system installed in TS are:

1. There is no need of a phase locking system since the modulation and demodulation is performed using the same quartz oscillator [93].
2. Square emitting and receiving antennas with the possibility of manual rotation to perform O-mode or X-mode measurements [92].
3. 5 µs measurement time [91].

2.3 Reflectometry diagnostics for ITER and DEMO

Since the success of AUG demonstrating reflectometry as an alternative control technique [58], and considering the performance of reflectometry systems in other existing tokamaks, the reflectometry systems of ITER and DEMO were/are designed with the aim to take advantange of some of the unique features mentioned in the previous section. These features include the frequency band swept, the polarization and the measurement time. Adaptation of these features can be done directly, since the cut-off layer – the density layer where the microwaves are reflected – is located at the edge of the plasma. Despite all of the similarities above, reflectometry diagnostics for ITER and DEMO have their own distinct challenges. These challenges include higher thermal and neutron fluxes, longer plasma pulses, Remote Maintenance (RM) compatibility and requirements of high availability [54]. More details about the reflectometry system of ITER can be found in Chapter 5, while the system proposed for DEMO is presented with more detail in Chapter 7.

Chapter 3

Neutron Physics and Modelling based on Monte Carlo Methods

3.1 Neutron Physics

Ever since the discovery of the neutron by James Chadwick in 1932 [94, 95], Neutron Physics has been an important research topic with many applications in several fields, including plasma physics. The classification of neutrons according to their energy is not standard across all fields. In Reactor Physics, the most general classification used as convention is [96][2]:

Thermal neutron	:	$\mathrm{E} \simeq 0.025\,\mathrm{eV}$
Epithermal neutron	:	$\mathrm{E} \sim 1\,\mathrm{eV}$
Slow neutron	:	$\mathrm{E} \sim 1\,\mathrm{keV}$
Fast neutron	:	$\mathrm{E} \geq 100\,\mathrm{keV}$

Since neutrons are particles without charge (neutral), they cannot be confined using electromagnetic fields and they are not constrained by Coulomb forces when they interact with matter. As such, they are in general more difficult to shield than protons or electrons. The main types of interactions between neutrons and matter are summarized in Figure 3.1. These nuclear reactions can be divided into 2 categories, according to whether the incoming neutron is scattered or absorbed.

There are two main types of interactions between neutrons and matter according to their energy:

1. Scattering is the main interaction between neutrons and matter when the neutron is energetic. This interaction can be divided into:

    - Elastic scattering. When the neutron is scattered after colliding with the nucleus and leave the nucleus with the same number of protons and neutrons as it had before the reaction [97]. The total kinetic energy is the same before and after the collision.
    - Inelastic scattering. When the total kinetic energy before and after the neutron collision with the nucleus is not conserved. The scattered neutron is not necessarily the same neutron that hit the nucleus initially.

[2] In fusion neutronics, fast neutrons are usually associated with energies above 1 MeV.

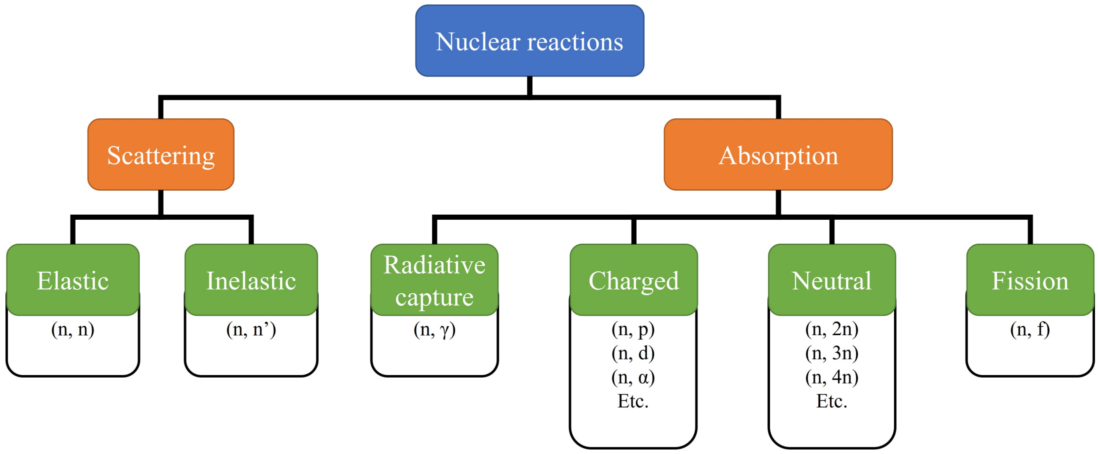

Figure 3.1: Various categories of neutron interactions. The letters separated by commas in the parentheses show the incoming and outgoing particles [97].

2. Absorption is the interaction where the neutron is absorbed by the target nucleus to form a compound nucleus, releasing additional radiation to stabilize. There are several different kinds of absorption reactions, according to the type of radiation that is released:

   - Electromagnetic radiation. The absorbed neutron carries enough energy to take the compound nucleus to an excited state and release an electromagnetic wave in the form of a γ particle. This process is also known as radiative capture.
   - Charged particle. By releasing one or more charged particles, the element of the target nucleus before and after the reaction is transmuted into a different element.
   - Neutral particle. In this process, the element of target nucleus is maintained but there is a change in the mass number (it becomes a new isotope).
   - Fission. The absorption of the neutron produces a compound nucleus that gains the kinetic energy and the binding energy of the neutron. If its energy exceeds the "critical energy" of fission, the nucleus will split. The fission reaction is not deterministic; similar reactions might result in different products. As an example, the ^{235}U fission product yield illustrated in Figure 3.2 shows that several different nuclei can be produced as an outcome of a fission reaction, each split according to some probability.

3.1.1 Neutron cross-section

From the previous section, it is clear that the interactions between neutrons and matter are not deterministic but probabilistic in nature. It is a crucial part of neutron physics to understand how probable a reaction between a neutron and a nucleus is or how this probability varies with the energy of the incident neutron. When a neutron beam hits a target material, the reaction rate (R) may be written as

$$R = \sigma N I, \tag{3.1}$$

where I is the flux of the neutron beam (neutrons/cm^2 s^{-1}), N is the the number of target atoms per unit area (atoms/cm^2) and σ, known as microscopic cross-section, is a proportionality constant that represents the probability that a reaction will take place when a neutron hits one atom of the target. The cross-section

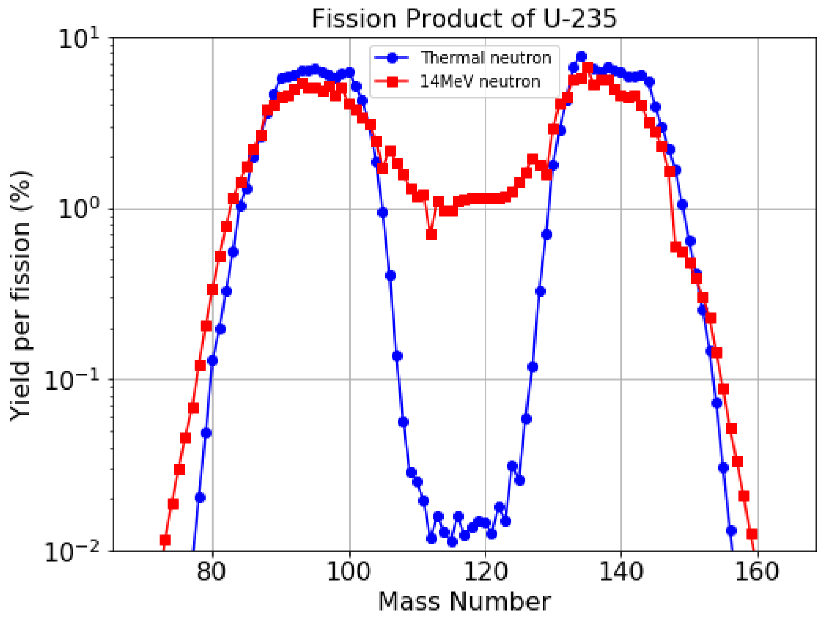

Figure 3.2: Product yield curves for thermal neutron fission of ^{235}U [98].

σ is then given by

$$\sigma = \frac{R}{NI}, \tag{3.2}$$

and has units of area. Different cross-sections describe the different interaction processes; the total cross-section is the sum of the different reaction cross-sections. Following the logic of Figure 3.1,

$$\sigma_t = \sigma_s + \sigma_a, \tag{3.3}$$

where σ_s is the scattering cross-section, which includes the elastic and inelastic scattering cross-section, and σ_a is the absorption cross-section, which includes radiative capture, fission and the remaining processes in which the incident neutron is absorbed.

Microscopic cross-sections are usually presented in barns (1 b = 1×10^{-24} cm^2). The total cross-section of a nuclei (an example is presented in Figure 3.3) can be divided into three regions. In the low energy region, the cross-section is inversely proportional to the velocity of the incident neutron ν; therefore, this region is also known as the $\frac{1}{\nu}$ region. Following the low-energy region is the resonance region, where several peaks appear. The first peak of this resonance region is usually separated and can be theoretically described by the Breit-Wigner Formula [99]. Lastly, the high energy region is the unresolved resonance region.

Another important quantity is the macroscopic cross-section, which is defined by

$$\Sigma_t = \Sigma_s + \Sigma_a = n\sigma_t \tag{3.4}$$

where n is the atomic density (atoms/cm^3) of the material. This macroscopic cross-section is necessary to define the neutron mean free path (λ), which is the average distance travelled by a neutron inside a material before it interacts with a nucleus. This mean free path can be formulated as the inverse of the total macroscopic cross-section:

$$\lambda = \frac{1}{\Sigma_t} \tag{3.5}$$

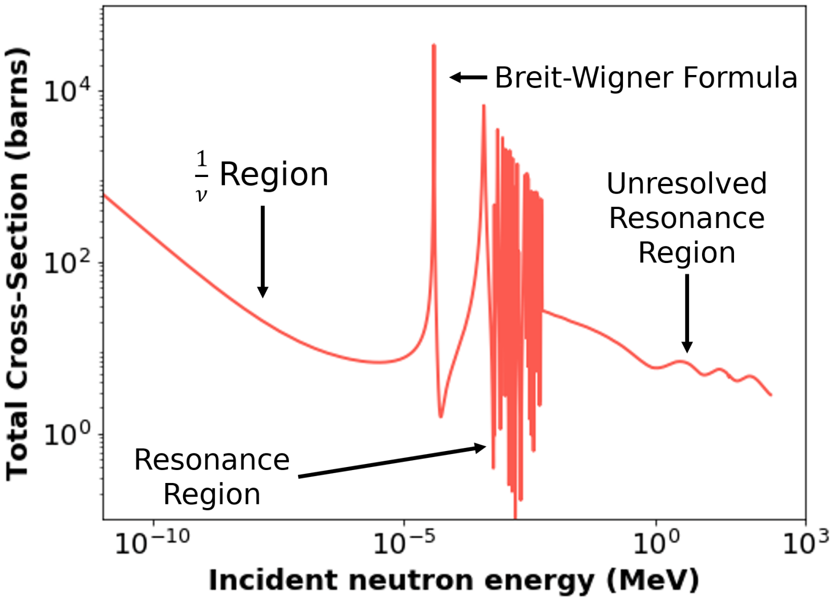

Figure 3.3: Total Cross-Section of ^{188}W [100].

3.1.2 Neutron shielding

As neutrons have high penetration ability and cannot be confined by electromagnetic fields, it is important to understand the mechanisms involved in neutron moderation and absorption, the processes through which neutrons transfer their kinetic energy to the environment (in general, the total cross-section increases as the neutron loses energy). The average energy transferred to the atom per elastic scattering reaction can be written as

$$\overline{\Delta E} = \frac{1}{2}\left[1 - \left(\frac{A-1}{A+1}\right)^2\right] E_{n0} \tag{3.6}$$

$$\frac{\overline{\Delta E}}{E_{n0}} = \frac{1}{2}\left[1 - \left(\frac{A-1}{A+1}\right)^2\right] \tag{3.7}$$

where E_{n0} is the incidental neutron energy [101] and A is the atomic weight number. From these equations it can be seen that neutrons lose more energy when they collide with lighter nuclei. On average, half of the neutron energy will be transferred in an elastic collision with an Hydrogen nucleus (in a head-on collision, it can lose all of its energy in a single collision). In collisions with heavier nuclei, a lower fraction of the energy is transferred. As such, it can be anticipated that lighter materials make better moderators than heavier nuclei.

Though moderation by inelastic scattering is less important as elastic scattering in light nuclei, it becomes the principal mechanism for neutron moderation in heavier elements [102]. The common practice in reactor calculations is to define a new variable called "lethargy", which is defined as the logarithmic energy reduction

$$u = \ln(E_{n0}/E), \tag{3.8}$$

and the lethargy difference

$$\xi = \overline{\Delta u} = 1 - \frac{(A-1)^2}{2A} \ln\left(\frac{A-1}{A+1}\right), \tag{3.9}$$

which is important for defining the number of collisions needed to slow down a neutron with energy E_{n0} to any desired energy E, given by [103]

$$n = \frac{1}{\xi} \ln\left(\frac{E_{n0}}{E}\right). \tag{3.10}$$

The average number of collisions needed to thermalise 14 MeV neutrons in the most common elements in fusion environments is presented in Table 3.1.

Table 3.1: Average number of collisions needed to thermalise 14 MeV neutrons in the most common elements in fusion environments.

Element	**Mass number**	**Number of collisions**
H	1	20
D	2	28
T	3	37
Li	7	77
Be	9	97
C	12	128
O	16	168
Fe	56	571
W	183	1850
Pb	207	2092

It can be seen easily from Table 3.1 that lower atomic number elements slow down neutrons more effectively. While the number of collisions needed to thermalise neutrons is inversely proportional to the neutron shielding effectiveness, it does not follow necessarily that the best neutron shielding materials are the best neutron moderators. This is because the main purpose of neutron moderation is to reduce the neutron energies, not to absorb them (this distinction is important in fission reactors). Therefore, light water, which is one of the best neutron shielding materials, is a worse moderator when compared to heavy water or graphite, due to the higher absorption cross section.

Another important aspect is that although heavier elements might require more collisions to moderate neutrons, if the mean free path of the element is smaller (due to a higher density, for example), it might also be effective for neutron shielding, since the number of interactions between neutrons and the nuclei will compensate for the lower atomic weight.

In summary, the most effective neutron shielding materials are the elements with a mass comparable to the neutron (i.e., low atomic number elements), high neutron capture cross-section (e.g., boron, cadmium, and gadolinium), and high atomic density (e.g., iron, tungsten, and lead). There is no single element that can fulfil all these criteria, but mixing the materials is often a solution to take advantage of each criterion.

3.2 The Monte Carlo Method

The Monte Carlo method is an artificial stochastic (probabilistic) technique, which with its large number law and asymptotic theorems [104] relies on the generation of random numbers to study physical problems which are too complex to solve using deterministic methods [105, 106]. Before Monte Carlo methods were invented, statistical sampling was used to determine the uncertainties of simulation results and not for the solution itself. This shift is what makes the Monte Carlo method so special, since it can solve problems with either stochastic or deterministic nature.

In general, the main components of a Monte Carlo algorithm are [107]:

- Probability distribution functions (pdfs) – the physical (or mathematical) system must be described by a set of pdfs;
- Random number generator – a source of random numbers uniformly distributed on the unit interval must be available;
- Sampling rule – a prescription for sampling from the specified pdf, assuming the availability of random numbers on the unit interval;
- Scoring (or tallying) – the outcomes must be accumulated into overall tallies or scores for the quantities of interest;
- Error estimation – an estimate of the statistical error (variance) as a function of the number of trials and other quantities must be determined.
- Variance reduction techniques – methods for reducing the variance in the estimated solution to reduce the computational time of Monte Carlo simulations.
- Parallelization and vectorization – efficient use of advanced computer architectures.

The Monte Carlo method was developed during World War II and used as first step for the production of Hydrogen bombs in the late 50s. Nowadays, the applications of Monte Carlo simulations cross several fields of knowledge. They have been used for industrial engineering and operations research (where Monte Carlo methods offer new approaches to solve classical optimization problems) [108], in chemistry (study of the chemical kinetics), in computational biology (allowing the monitorization of the chemical behaviour of specific molecules with considerable precision) or in the development of new materials and structures (such as organic light emitting diodes (LEDs)) [109, 110]. In Physics, Monte Carlo is heavily used to model the interaction of ionizing radiation with matter, thus becoming relevant for this work.

3.2.1 Pseudo-random number generation

As mentioned in Section 3.2, one of the main components of Monte Carlo algorithms is the random number generator to perform the simulations. Though the original idea requires truly random numbers, it would be impossible in practice to reproduce. Therefore, as long as there is some method to produce numbers with enough degree of randomness from the initial state of the generator, also known as Pseudo–random numbers, the Monte Carlo method can work with it.

It is important to verify that a set of pseudo-random numbers constitutes a uniform distribution of numbers which then can be changed to any particular non-uniform probability distribution needed for any particular problem. The commonly used method for this transformation is the *Inverse Function Method*. For any probability distribution $f(x)$ defined in a certain interval $[a, b]$, the sum of all individual probabilities after normalization in the interval sums up to unity,

$$\Pr(a < x < b) = \int_a^b f\left(x'\right) dx' = 1, \tag{3.11}$$

where $f\left(x'\right) dx'$ is the probability that value x is falling between x' and $x' + dx'$ with $f\left(x'\right)$ as its pdf. Considering this, any random number u in the interval $[0, 1]$ can be written as

$$u = F(x) = \int_a^x f(t)\, dt, \tag{3.12}$$

with $F(x)$ as its cumulative distribution function (cdf). From this, a new pdf of random number between 0 and 1 can be easily obtained by inverting Equation (3.12), known as percent point function (ppf) or the quantile function

$$x = F^{-1}(u). \tag{3.13}$$

An example of this method applied to the normal distribution can be seen in Figure 3.4.

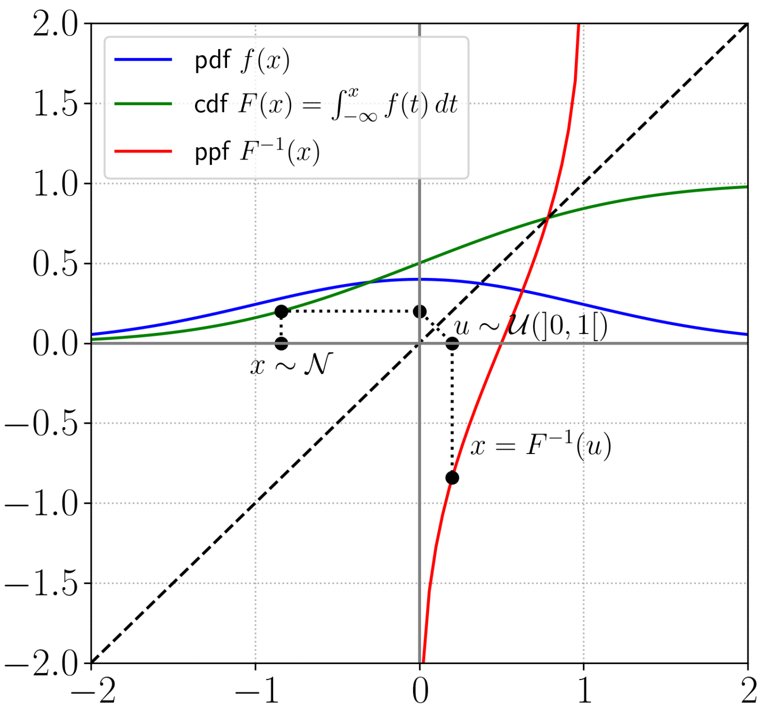

Figure 3.4: Inverse transform method applied to normal distribution.

In nuclear physics, the probability of the neutron to travel the distance x before being absorbed by a nucleus is a decaying exponential in space, $\Pr(x) = C_1 e^{-xC_2}$, C_2 being the inverse of the mean free path defined in Equation (3.5). This function is then interpreted as a random number in the Monte Carlo simulation or a decision process during the simulation.

3.3 Monte Carlo N-Particle Code

The Monte Carlo N-Particle Code (MCNP) is a particle transport code based on the Fortran language developed at the Los Alamos National Laboratory [111]. This code is used for solving complex problems that are too difficult to solve using deterministic methods. The code is particularly important for neutron and photon transport simulations and it can work in several modes: neutron only, photon only, neutron and photon, neutrons and other particles, etc. MCNP can model these particles' transport and interactions using available cross-section data.

In its normal mode, MCNP is an analogue Monte Carlo code which will simulate and follow each particle from its birth until it is absorbed. By doing this, the code will measure and record many histories and average their behaviour. All of the particle histories are a result of the random numbers being selected at each point of each particle path, where reactions need to be "selected" according to their probabilities. Therefore, when the number of source particles is set to 10^9, MCNP will simulate 10^9 histories [112], using the Monte Carlo method. By simulating such a large number of particles, it is expected to have enough statistics to model the average behavior of the particles with low relative uncertainties. Quantities that can be estimated using tallies in MCNP include particle flux, energy deposition, particle current, etc.

Every simulation using MCNP starts with the preparation of an input file. The input file of MCNP consists of three blocks:

- The first block is dedicated to the geometric description of the cells that make up the system – it contains references to the boundary surfaces of each cell.
- The second block contains the definition of each of the surfaces used in the first block.
- The third block defines the material composition, the source particle specifications and the tallies (detectors) defined by the user.

The geometry used in MCNP is defined using Constructive Solid Geometry (CGS), a method to build a geometry out of physical primitives [113] by doing Boolean operations such as union, subtraction, and intersection between surfaces to create the full geometric models [114]. The geometries can also be obtained automatically using other codes that convert Computer Aided Design (CAD) models into the MCNP format, as will be explained in Section 3.5. Since the physics of the interactions between radiation and matter is stored in the cross-section data, the material definition in the third block must include the isotopic composition of the materials and the cross-section evaluations to be used in the cells (linked to the library where MCNP imports the cross-section data for each isotope). The tally section is where MCNP gets the information about the quantities the user is aiming to calculate – the detectors – and their location.

3.3.1 Tallies for Particle Flux and Energy Deposition Estimations

As mentioned before, it is important to accumulate the quantities of interest from the Monte Carlo simulation. The most common quantities of interest asked from the MCNP simulation are the particle fluxes and the energy deposited by the particles in the cells.

Particle fluxes can be measured through a surface or an entire cell, and each of these two variants is a different tally in MCNP. As an example, the averaged particle flux through a surface, with units of particle/cm^2, can be measured using F2 tallies, which is the result of

$$\mathrm{F2} \equiv \overline{\varphi}_S = \frac{1}{A}\int_{E_i} dE \int_{t_j} dt \int dA\varphi\left(\vec{r}, E, t\right), \tag{3.14}$$

where A is the area of the surface of interest, E_i represents the several energy bins over which the integration is performed, t_j are the time intervals and $\varphi\left(\vec{r}, E, t\right)$ is a scalar flux defined by

$$\varphi\left(\vec{r}, E, t\right) = \int d\Omega\, \Psi\left(\vec{r}, \hat{\Omega}, E, t\right), \tag{3.15}$$

where $d\Omega$ is the solid angle and $\Psi\left(\vec{r}, \hat{\Omega}, E, t\right) = \nu n\left(\vec{r}, \hat{\Omega}, E, t\right)$, ν being the velocity and n the particle density in the direction of $\hat{\Omega}$ [111].

Whenever particles interact with matter, they transfer some of their energy to the cells they cross. To measure the amount of energy, in MeV/g, deposited as heat in a cell, F6 tallies are used. The deposited energy calculated by F6 tallies is given by

$$\mathrm{F6} \equiv H_t = \frac{\rho_a}{m}\int_{E_i} dE \int_{t_j} dt \int dV \int d\Omega\sigma_t\left(E\right) H\left(E\right) \Psi\left(\vec{r}, \hat{\Omega}, E, t\right), \tag{3.16}$$

where ρ_a and m are, respectively, the atomic density and mass of the cell. It is important to note that F6 tallies are dependent on the energy-dependent function $\sigma_t\left(E\right) H\left(E\right)$ which differs according to the type of particle, where $\sigma_t\left(E\right)$ is the microscopic total cross-section in barns and $H\left(E\right)$ is the heating number in MeV/collision. The heating number is different for neutrons and photons. For neutrons, the expression is given by

$$H_n\left(E\right) = E - \sum_i p_i\left(E\right)\left[\overline{E}_{i,out}\left(E\right) - Q_i + \overline{E}_{i,\gamma}\left(E\right)\right], \tag{3.17}$$

where $p_i\left(E\right) = \sigma_i\left(E\right)/\sigma_t\left(E\right)$ is the probability of reaction i at neutron incident energy E, $\overline{E}_{i,out}\left(E\right)$ is the average exiting neutron energy for reaction i at neutron incident energy E, Q_i is the Q-value of reaction i and $\bar{E}_{i,\gamma}$ is the average exiting gamma energy for reaction i at neutron incident energy E [111]. For photons (or gammas), the heating number is given by

$$H_p\left(E\right) = E - \sum_{i=1}^{3} p_i\left(E\right)\left[\overline{E}_{i,\gamma}\left(E\right)\right], \tag{3.18}$$

where $i = 1, 2, 3$ represents incoherent (Compton) scattering, pair production, and photoelectric absorption reaction, respectively.

These two variables can also be estimated by covering the region of interest with a mesh in a 3D grid, in Cartesian or cylindrical coordinates, defined by the user. The mesh is implemented by defining the limits of the mesh and the number of divisions in each direction for the selected coordinates. By applying a mesh to estimate the quantities, the results of each bin are the averaged values of the tally for several components that fall inside each bin.

3.3.2 Tallies for Displacement per Atom Estimations

The dpa mentioned in Section 1.5 is an important quantity that measures the impact of the radiation on the mechanical properties of solids. During material irradiation, the interaction between radiation and matter can lead to atoms being taken out of their equilibrium position in the material lattices [115]. In MCNP, the dpa is calculated as

$$\mathrm{dpa} = \left(\int \sigma_{\mathrm{DPA}}\,(\mathrm{E})\,\varphi\,(\mathrm{E})\,\mathrm{dE} \right) \times \mathrm{t}, \tag{3.19}$$

where σ_{DPA} is the displacement cross-section for an incident particle with energy E, $\varphi(\mathrm{E})$ is the incident particle flux and t is the irradiation time. This quantity can be measured using F2 or F4 tallies in MCNP, given that sets of cross-sections for dpa are provided. In this case, with suitable cross-section libraries, the dpa can be calculated using the same tallies that usually measure the particle flux $\varphi(\mathrm{E})$, if the irradiation times are provided as a normalization factor to the tally. Similar estimations can be obtained using mesh tallies.

3.3.3 Relative Error Estimation

All tally estimations are accompanied by a relative error of the measurement. This error is given by

$$\mathrm{R} = \frac{\mathrm{S}_{\overline{\mathrm{x}}}}{\overline{\mathrm{x}}}, \tag{3.20}$$

where $\overline{\mathrm{x}}$ is the mean value of the quantity x being measured and $\mathrm{S}_{\overline{\mathrm{x}}}$ is the estimated variance of $\overline{\mathrm{x}}$. Both $\overline{\mathrm{x}}$ and $\mathrm{S}_{\overline{\mathrm{x}}}$ are calculated for a total of N simulated particles, can be written as follows [116]:

$$\overline{\mathrm{x}} = \frac{1}{\mathrm{N}} \sum_{\mathrm{i}=1}^{\mathrm{N}} \mathrm{x}_{\mathrm{i}}, \tag{3.21}$$

$$\mathrm{S}_{\overline{\mathrm{x}}} = \frac{1}{\sqrt{\mathrm{N}}} \sqrt{\frac{1}{\mathrm{N}-1} \sum_{\mathrm{i}=1}^{\mathrm{N}} (\mathrm{x}_{\mathrm{i}} - \overline{\mathrm{x}})^2} \approx \frac{1}{\sqrt{\mathrm{N}}} \sqrt{\overline{\mathrm{x}^2} - \overline{\mathrm{x}}^2}. \tag{3.22}$$

From Equation (3.20) and Equation (3.22), to bring down the relative error (R) one can increase the number of histories or reduce the scope of the simulations. The first method, related to the first term of Equation (3.22), is a direct drawback of the Monte Carlo method, since to bring down $\mathrm{S}_{\overline{\mathrm{x}}}$ by half of its initial value, the number of histories need to be increased by a factor of 4. The second method, related to the second term of Equation (3.22), is to use advanced variation reduction techniques in MCNP, to increase statistical sampling in the regions of interest while also reducing the wasted effort in unimportant regions [117].

3.4 Nuclear Data Libraries

For projects that are heavily dependent on particle interaction simulations, like ITER and DEMO, the experimental data that make possible to create libraries with complete cross sections for all kinds of nuclear interactions are crucial. The reference cross section library for neutron interactions in these projects is the Fusion Evaluated Nuclear Data Library (FENDL) [118]. For DEMO, the Joint Evaluated Fission and Fusion File (JEFF) [119] libraries are also recommended, together with FENDL [120].

FENDL is a single high-quality library combined from nuclear cross section libraries from many laboratories and research groups. Though most of the data available is from the Evaluated Nuclear Data File (ENDF), created and updated frequently by the Cross Section Evaluation Working Group (CSEWG) [12] [121], some isotope data need to be complemented with data from other libraries such as JEFF, developed by Nuclear Energy Agency (NEA) [100] [122], the Japanese Evaluated Nuclear Data Library (JENDL), developed by the Japan Atomic Energy Agency (JAEA) [123], the Biblioteka Rekomendovannykh Ocenennykh Nejtronnykh Dannykh (BROND) libraries developed by Centr po Jadernym Dannym (CJD) or the Nuclear Data Center from the Russia Federation [124].

The neutronics simulations in this work were performed using FENDL/MC-2.1 or FENDL2.1 and FENDL3.1, which contain pointwise continuous-energy cross section data [125].

3.4.1 Benchmark and evaluation of nuclear data

For nuclear fusion applications, nuclear libraries need to be benchmarked with experiments. Benchmarking activities have been carried out by several groups worldwide. One of them is the ENEA neutronics group in Frascati, which uses the Frascati Neutron Generator (FNG) to produce 14 MeV neutrons [126]. In the experiment detailed in [127], neutron and gamma fluxes were measured in several positions inside the experimental bulk shielding. The bulk shielding mock-up consisted of series of intercalated Copper and Stainless Steel (SS-316) blocks. The geometry of this mock-up experiment is illustrated in Figure 3.5. A comparison was made between the experimental results and several Monte Carlo simulations using previously benchmarked and validated data libraries. As a general conclusion, the FENDL–2.1 data library proved adequate for fusion design calculations, with deviations between experimental and simulation results in Stainless Steel within $\pm$ 30% at 1 m of depth in the shielding.

Other benchmark experiments have been done for neutron interactions with tungsten [129] and other breeding blanket materials [130–132], in which the neutron and gamma flux results obtained with MCNP simulations and several nuclear data libraries were compared to experimental data. The benchmarks showed that the MCNP simulation results using FENDL2.1 and JEFF3.1 were within the expected uncertainties when compared to the experimental values. These results were also presented in the NEA Data Bank Monitoring in 2006, where it was concluded that the FENDL2.1 libraries were suitable for fusion applications. They have been recommended for ITER neutronics simulations since then.

As DEMO is the next step after ITER, the extension of the nuclear data libraries for expected energy range related to DEMO operating conditions is paramount. This fact became the motivation for laboratories worldwide to perform the experiments to extend the FENDL2.1 library [118]. In 2012, the International Atomic Energy Agency (IAEA) released FENDL3.1, which is an extension of FENDL3.0 and FENDL2.1 [133]. This extension includes the addition of several isotopes, covering more materials used for fusion applications [133]. Moreover, the energy range for neutron induced reactions was extended from a maximum of 20 MeV to 150 MeV [134]. This extension was also benchmarked by experimental results. A shielding material benchmark was conducted in the TIARA experiment in Japan [135], while a benchmark for tungsten was conducted using the FNG [136]. The results show very good agreement between experimental data and the results obtained with MCNP simulations [137].

The data library for photon-induced reactions was already included in the distribution of MCNP. It

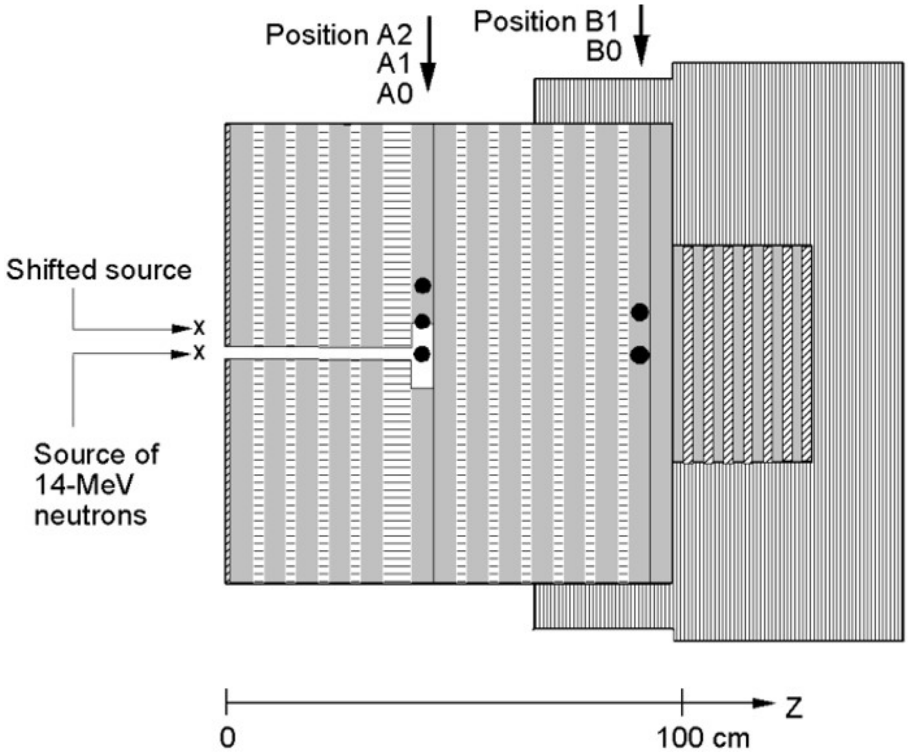

Figure 3.5: Layout of the Streaming Experiment (the Bulk Shield Experiment used the same block without channel and cavity) (obtained from [128]).

was first released in 1982 [138]. Like the libraries for neutron-induced reactions, the data in MCPLIB was obtained from different sources around the world and provide all the cross-sections for energies ranging from 1 keV to 100 MeV for elements with atomic number below 94 and 1 keV to 15 MeV for heavier elements [138]. In 2002, this data library was extended to cover incident photon energies from 1 keV to 100 GeV [139]. Another update to correct a bug in Doppler broadening for some elements has been released in 2012 with the name of MCPLIB84 [140, 141]. The benchmark of several photon libraries was done for the 2012 Reference Model of DEMO, and showed that the MCPLIB84 libraries describe the reference scenario better than the remaining libraries when the Doppler broadening is corrected [142].

The recommendation by F4E and by EUROFusion to use FENDL2.1 libraries for ITER neutronics simulations and both FENDL3.0 and 3.1 for DEMO is based on the successful reproduction of experimental results by the Monte Carlo simulations while using these libraries. For gammas, the MCPLIB84 library is the one recommended for ITER and DEMO.

3.5 Software for Geometry Conversion to MCNP

The Multi-Physics Coupling Analysis Modelling (MCAM) software, developed by the Chinese Academy of Sciences (CAS) [143] [144] [145], is used to convert CAD geometries to the CGS format used by Monte Carlo radiation transport codes like MCNP, TRIPOLI [146], GEometry ANd Tracking (Geant4) [147], FLUktuierende KAskade (FLUKA) [148], etc. MCAM is part of a package developed by the same team which also includes the radiation transport code SuperMC [149].

Another software that can perform automatic conversion of CAD models into the Monte Carlo input format is McCad [150], developed by Karlsruhe Institute of Technology (KIT) [151]. This software is available as a module of the Salome_7.4.0 platform [152], which is the platform used by code_aster [153] and code_saturne [154], software codes developed by Electricité de France (EDF) for thermo-mechanical and CFD analysis. Both MCAM and McCad were used in this work to convert CAD models to the MCNP input format.

3.6 Summary

This chapter presents the background theory of Monte Carlo simulation and the benchmarks for the nuclear data libraries used for the simulations. The neutronics simulations described in this chapter are an essential part of the engineering analyses performed in the design of nuclear reactors, and in particular for future fusion reactors like ITER and DEMO, where intense neutron and gamma fluxes will interact with the reactor materials. The nuclear heat loads and dpa calculated in these simulations are post-processed and used as input in multiphysics analyses which involve thermo-mechanical, structural and fluid dynamics simulations. More details on these multiphysics analyses are presented in the next chapter.

Chapter 4

Stress analysis and modelling

4.1 Stress classification and linearization

4.1.1 Design and manufacturing rules

The guidelines of design and manufacturing followed by ITER are provided in the AFCEN RCC-MR 2007 code [155], which was developed for Sodium Fast Reactors (SFRs) and Research Reactors (RRs). The scope of these guidelines is limited to the mechanical components considered to be important in terms of nuclear safety and operability.

In order to ensure the stipulated safety margins relative to the mechanical damage that may result from operation loads, RCC-MR 2007 classifies the possible types of damage according to their effects, and provides a complete framework to assess the integrity of the designed equipment.

RCC-MR proposes two routes – P-type and S-type damage – for assessing the structure against excessive deformation, plastic instability/collapse, progressive deformation, and fatigue. The P-type damage route, defined as a failure resulting from the application of permanent loads, is devoted to ensure that the different parts of the component are properly dimensioned to withstand the design mechanical loads. The S-type damage route, defined as a failure resulting from the application of repeated loads, is focused on guaranteeing protection against localized failures. The work presented in this thesis is based on the P-type damage route, while the fatigue analysis, which corresponds to the S-type damage, is left for future work.

In order to take into account failures in various operating conditions, the RCC-MR classifies the reactor operating conditions into 4 categories in terms of occurrence probability and damage intensity. The 1st and 2nd categories are the normal operating conditions, including normal operating incidents (i.e. upset conditions), start-up, and shutdown. The 3rd category corresponds to the emergency situations that might imply reactor shut down and appropriate inspection of the equipment. Finally, the 4th category refers to situations which are highly improbable but which consequences on components are studied for safety reasons.

The RCC-MR code also defines three service limits for the assessment of the different load combinations. Service level A criteria ensure margins regarding all damages along the life duration of the component, while service level C criteria ensure less safety margins than level A, by considering no cyclic damages on the component. The last service level criteria is level D, which ensures less margins than level C and cannot guarantee the restart of the reactor. The complete loading categories and the service level requirements to be met are listed in Table 4.1.

Table 4.1: Loading categories and service levels [156].

Loading Category	Category Conditions (Damage Limits)	Service Level
I. Operational Loading	Normal	A
II. Likely Loading	Upset	A
III. Unlikely Loading	Emergency	C
IV. Extremely Unlikely Loading	Faulted	D

4.1.2 Stress breakdown

To ensure the safety of a reactor, a standard or reference method and limit is required. For structural analysis of nuclear components, there are two most common references: the ASME code [157–159] and the RCC-MR code [160, 161]. Although both references use the same method to define the stress, they have different criteria definitions. The method used in both of these references to define the stress is known as *stress linearization*. It consists of performing line integration through the thickness of the structure and resolve the stresses into membrane, bending, and peak components. The line paths, also known as supporting line segments, are straight lines running from the inside to the outside of the section under study. Away from discontinuities, the line segment path is a line perpendicular to the mid-surface of the structure, and the length (h), as shown in Figure 4.1, is equal to the thickness of the wall, presented by direction 3. In the discontinuity zones, the line segment path is the shortest line joining the two surfaces of the wall. The breakdown of the stress component is shown in Figure 4.2, where the abscissa of a point of the supporting line is denoted by x_3. The total stress can be composed of membrane stress, bending stress (which varies linearly along the supporting line segment), and non-linear stress.

The total stress tensor, σ_{ij}, is the stress value obtained at the given point under the effect of all the loadings to which the apparatus is subjected.

Membrane Stress

The membrane stress tensor, $(\sigma_{ij})_m$, is defined as the averaged value of the stresses across the thickness of the shell, and can be calculated using

$$\left(\sigma_{ij}\right)_m = (1/h) \int_{-h/2}^{+h/2} \sigma_{ij}\, dx, \tag{4.1}$$

where h is the thickness of the shell and x is the direction along the line support segment.

Bending Stress

The bending stress tensor, $(\sigma_{ij})_b$, is the normal stress an object encounters when it is subjected to a large load at a particular point that causes the object to bend. It can be calculated as

$$\left(\sigma_{ij}\right)_b = \left(\frac{12x}{h^3}\right) \int_{-h/2}^{+h/2} \sigma_{ij}\, x\, dx. \tag{4.2}$$

Linearly Distributed Stress

The linearly distributed tensor, $(\sigma_{ij})_l$, is the portion of the total stress tensor which varies linearly along the supporting line segment [47]. It is the sum of the membrane and bending stress tensor, and its

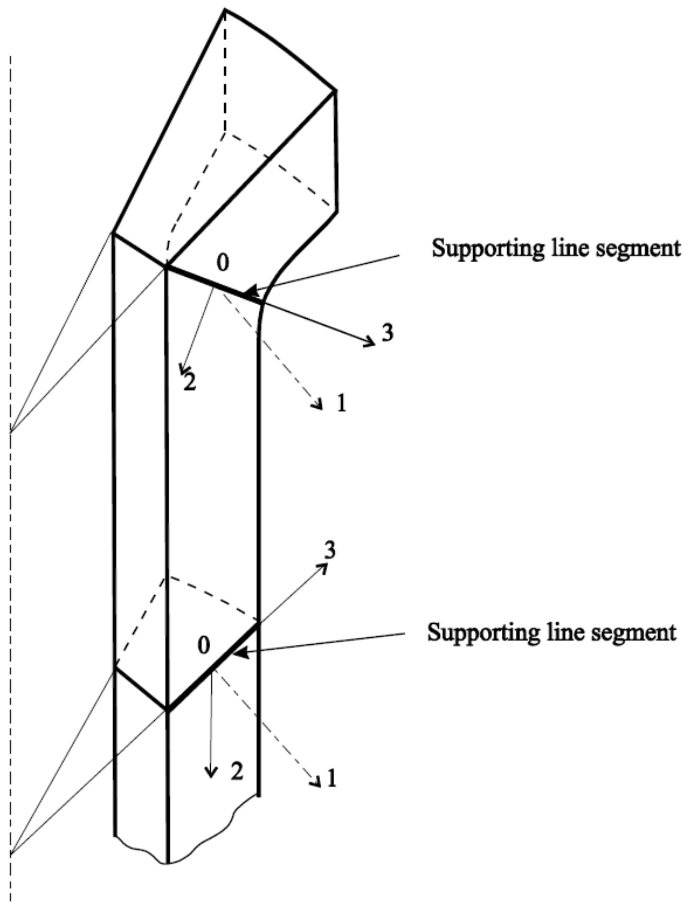

Figure 4.1: Supporting line segment [47].

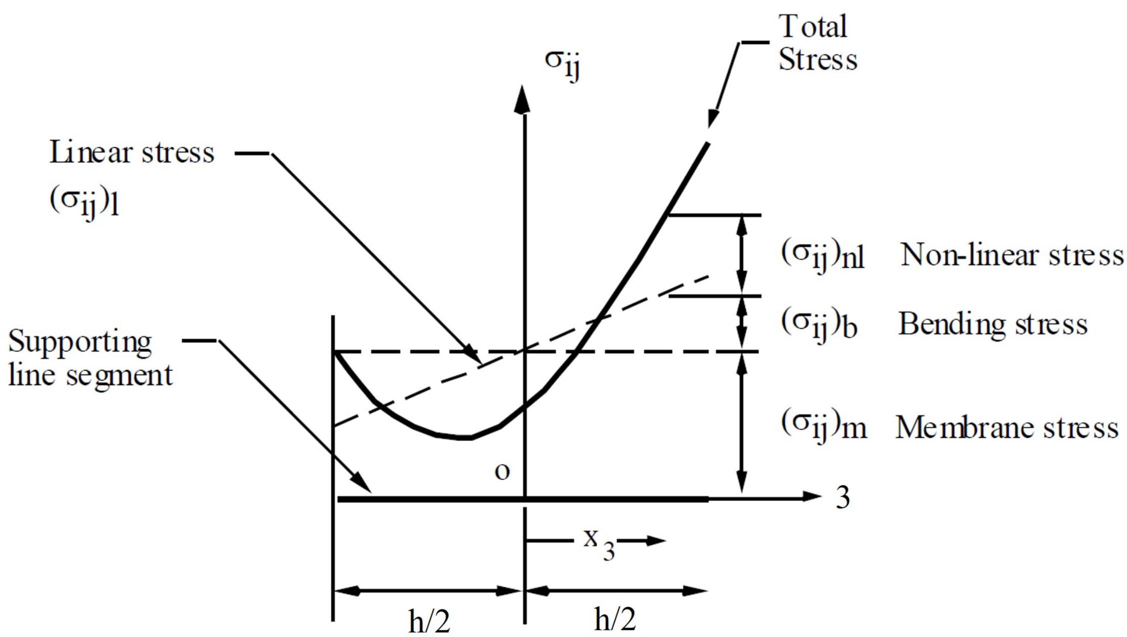

Figure 4.2: Stress component breakdown [47].

component values are given by

$$\left(\sigma_{ij}\right)_l = \left(\sigma_{ij}\right)_m + \left(\sigma_{ij}\right)_b . \tag{4.3}$$

Note that the membrane stress value is a constant and the bending stress value is a function of x.

Non-linearly Distributed Stress

The non-linearly distributed stress is the difference between the total stress σ_{ij} and the linearly distributed stress $(\sigma_{ij})_l$. Its components, $(\sigma_{ij})_n l$, are given (as a function of x) by the following equation:

$$\left(\sigma_{ij}\right)_{nl} = \sigma_{ij} - \left(\sigma_{ij}\right)_l = \sigma_{ij} - \left[\left(\sigma_{ij}\right)_m + \left(\sigma_{ij}\right)_b\right] . \tag{4.4}$$

4.1.3 Stress Classification and categorization

The stress classification is done to identify, basically, the "Primary" (P) and the "Secondary" (Q) stresses. The former are directly related with the equilibrium equations while the later are related with the compatibility equations. So, in general, they come respectively from mechanical and thermal loads. But in a structural discontinuity there is an additional stress related to the need of compatibility between the connected parts, also known as *local membrane stress*. Thus, even for mechanical loads there are secondary stresses in a given discontinuity [162]. The stress classification is presented in Table 4.2, with $\sigma = P_m + P_b + F + Q$, if $L_m = 0$, or $\sigma = P_L + P_b + F + Q$, with $P_L = P_m + L_m$.

Table 4.2: Stress classification [47].

Total stress σ				
Primary stress		**Non-primary stress**		
Primary membrane stress	Primary bending stress	Peak stress	Secondary stress	Additional Local membrane stress
P_m	P_b	F	Q	L_m

The exact value of the primary stress can be determined by the smallest stress field which balances all the forces and loads, which leads to the lowest value of the maximum intensity in the stress field. This value is often difficult to determine, therefore an upper bound of the primary stress is often used for the analysis. This upper bound is determined by any stress field that balances the volumetric forces and loads applied on the surfaces within the structure of interest [47].

While the primary membrane stress, P_m, and the primary bending stress, P_b, can be obtained from Equation (4.1) and Equation (4.2), the additional local primary membrane stress, L_m, is caused by mechanical loads applied to the gross structural discontinuity. This additional local membrane stress can be caused by a mechanical load applied to a nozzle or the presence of a stiff support boss that creates a local stress concentration [47].

The peak stress itself is the increment of stress added to the primary-plus-secondary stresses because of local discontinuities or local thermal stresses. This additional stress cannot cause an overall deformation of the structure since it is generally very localized and redistributed by plasticity. Nevertheless, this stress is important in the fatigue analysis since it can point out the most probable crack sources.

This stress classification and categorization is summarized in Table 4.3. The combination of these stresses then need to be assessed following the RCC-MR or ASME guide as mentioned in Section 4.1.2.

Table 4.3: Stress classification [156].

			Origin of stresses				
Part of vessel	**Area concerned**	**Type of stress**	**Internal pressure**	**Loads of a mechanical origin**	**Loads resulting from displacements**	**Axial thermal gradient**	**Thermal gradient through thickness**
Any shell	Area far from all discontinuity	$(\sigma_{ij})_m$	P_m	P_m	Q	Q	Q
		$(\sigma_{ij})_b$	P_b	P_b	Q	Q	Q
		$(\sigma_{ij})_{nl}$	← – – – – – – Not applicable – – – – – – →				F
Formed heads, flat heads, conical heads	Central zone and knuckle zone	$(\sigma_{ij})_m$	P_m	P_m	Q	Q	Q
		$(\sigma_{ij})_b$	P_b	P_b	Q	Q	Q
		$(\sigma_{ij})_{nl}$	← – – – – – – Not applicable – – – – – – →				F
	Fittings : crown torus, knuckle cylindrical	$(\sigma_{ij})_m$	P_L	P_L	Q	Q	Q
		$(\sigma_{ij})_b$	Q	Q	Q	Q	Q
		$(\sigma_{ij})_{nl}$	← – – – – – – Not applicable – – – – – – →				F
Head or flange junction with vessel shell	Crotch region	$(\sigma_{ij})_m$	P_L	P_L	P_L	Q	Q
		$(\sigma_{ij})_b$	Q	Q	Q	Q	Q
		$(\sigma_{ij})_{nl}$	F	F	F	F	F
Perforated head or shell	Ligament in an uniform pattern	$(\sigma_{ij})_m$	P_m	P_m	P_m	Q	Q
		$(\sigma_{ij})_b$	P_b	P_b	Q	Q	Q
		$(\sigma_{ij})_{nl}$	F	F	F	F	F

4.1.4 Stress Limits

There are two modes of failure directly related to the primary stress intensity in the material, which are Immediate Plastic Collapse (IPC) and Immediate Plastic Instability (IPI), and one mode related to the primary and secondary stresses, called Immediate Plastic Flow Localization (IPFL) [161]. These first two modes are to prevent global fracture and the last mode is to prevent cracking on the structure. In order to avoid these two failure modes, the stresses experienced by a structure need to be assessed. In order to assess the stresses according to RCC-MR or ASME rules, it is necessary to define the stress limits, which depend on the material, temperature (T), and the neutron fluence (Φt) on the components. These limits are then multiplied by a certain factor, depending on the service level, and then compared to the results from the structural analysis.

Nominal and minimum yield strength (R_{p02}, $R_{p02,min}$)

The yield strength is the engineering stress at which, by convention, it is considered that plastic deformation of the material has commenced. For materials whose yield point cannot easily be defined, the specified offset yield strength, (usually 0.2%) is used. This specified offset yield strength corresponds to the point where permanent deformation will start to occur. To obtain these quantities, a line with slope equal to the material modulus of elasticity is translated to the 0.2% strain in the stress-strain curve plot. The stress value of the intersection point between this line and the stress-strain curve is the specified yield strength [163].

Nominal and minimum ultimate tensile strength (R_m, $R_{m,min}$)

The ultimate tensile strength is the calculated stress at the point of maximum load in an uniaxial tension test at a given temperature and at a given strain rate [47].

Allowable primary membrane stress intensity (S_m)

S_m is a temperature (T) and neutron fluence (Φt) dependent allowable stress intensity defined as the lesser of the quantities in Table 4.4 for all metallic materials except bolts.

Table 4.4: Coefficients used for obtaining S_m.

Annealed Austenitic stainless steels	**Materials other than annealed Austenitic stainless steels**
1/3 $R_{m,min}$ (20 °C,0)	1/3 $R_{m,min}$ (20 °C,0)
1/3 $R_{m,min}$ (T,0)	1/2.7 $R_{m,min}$ (T,0)
1/3 $R_{m,min}$ (T,Φt)	1/2.7 $R_{m,min}$ (T,Φt)
2/3 $R_{p02,min}$ (20 °C,0)	2/3 $R_{p02,min}$ (20 °C,0)
0.90 $R_{p02,min}$ (T,0)	2/3 $R_{p02,min}$ (T,0)
0.90 $R_{p02,min}$ (T,Φt)	2/3 $R_{p02,min}$ (T,Φt)

For EUROFER, the allowable primary membrane stress intensity for level A criteria can be calculated as [163]:

$$S_m^A = \min\left[\frac{2}{3}\,R_{p02,min}\,(20\,°C)\,,\,\frac{2}{3}\,R_{p02,min}\,(T)\,,\,\frac{1}{3}\,R_{m,min}\,(20\,°C)\,,\,\frac{1}{2.7}\,R_{m,min}\,(T)\right] \tag{4.5}$$

and knowing that the stress limit depends on the criteria level from [156], which implies that the safety margin will also be affected. The allowable stress limit for level D criteria can be calculated as:

$$S_m^D = \min\left[2.4\,S_m^A, 0.7\,R_{m,min}\,(T)\right] \tag{4.6}$$

The quantities related to the failure modes and their limits according to the service levels of RCC-MR are tabulated in Table 4.5.

Damage	**Quantity**	**Limit**	
		Level A	**Level D**
IPC	$\overline{P_m}$	S_m^A	S_m^D
IPI	$\overline{P_L + P_B}$	1.5 S_m^A	1.5 S_m^D
IPFL	$\overline{P_L + Q_L}$	3 S_m^A	no limit

Table 4.5: P-type damage structural criteria summary [164].

In case the material hardens due to the irradiation, the value of S_m is controlled by the unirradiated value if the time of loading is not specified. On the other hand, if it softens due to irradiation, the value of S_m is controlled by the irradiated value. In the case of EUROFER97, based on the limited data available in [163], though the yield strength increases with the irradiation fluence, the hardening nearly vanishes at temperatures of 400 °C and above. Furthermore, it has been shown that thermal aging at 400, 500 and 600 °C for 10 000 h does not cause degradation of the tensile properties. Thus, for this thesis, the stress limit used for analysis will be based on the unirradiated value of the yield strength and ultimate tensile strength data of EUROFER97.

4.2 Basic Finite Element Method theory for mechanical analysis

When a solid body is subjected to external forces, it tends to move (to be displaced) from its original position. The main goal of a structural analysis is to find or calculate the displacement, the difference between the initial and the final position of the body [165]. In a 3-D geometry, the displacement vector, $\{u\}$, can be projected into the general coordinate directions x, y, z, and can be represented in matrix form as

$$\{u\} = \begin{Bmatrix} u_x \\ u_y \\ u_z \end{Bmatrix} \tag{4.7}$$

where $\{u\}$ is the displacement vector in matrix form and u_x, u_y and u_z are the displacement vector components in the x, y and z directions, respectively. The non-dimensional quantity of displacement, known as *strain* tensor, $[\varepsilon]$, has six different components and can be written as

$$[\varepsilon] = \begin{bmatrix} \varepsilon_x & \gamma_{xy} & \gamma_{zx} \\ \gamma_{xy} & \varepsilon_y & \gamma_{yz} \\ \gamma_{zx} & \gamma_{yz} & \varepsilon_z \end{bmatrix} \tag{4.8}$$

where ε_x, ε_y, and ε_z are the components of the *normal strain*, which is perpendicular to the surface components, and γ_{xy}, γ_{yz}, and γ_{zx} are the components of the *shear strain*, which is parallel to the surface of the body. The relation between strain vector and displacement vector can be written as

$$[\varepsilon] = [D]\,\{u\} \tag{4.9}$$

where [D] is the differentiation operator matrix:

$$[D] = \begin{bmatrix} \frac{\partial}{\partial x} & 0 & 0 \\ 0 & \frac{\partial}{\partial y} & 0 \\ 0 & 0 & \frac{\partial}{\partial z} \\ \frac{\partial}{\partial y} & \frac{\partial}{\partial x} & 0 \\ 0 & \frac{\partial}{\partial z} & \frac{\partial}{\partial y} \\ \frac{\partial}{\partial z} & 0 & \frac{\partial}{\partial x} \end{bmatrix} \tag{4.10}$$

Another important quantity in the structural analysis is the *stress*, which is defined as the magnitude or intensity of the force per unit area on the surface on which they act [165]. Like the strain tensor, the stress tensor $\{\sigma\}$ consists of six components and can be written as

$$[\sigma] = \begin{bmatrix} \sigma_x & \tau_{xy} & \tau_{zx} \\ \tau_{xy} & \sigma_y & \tau_{yz} \\ \tau_{zx} & \tau_{yz} & \sigma_z \end{bmatrix} \tag{4.11}$$

The relation between *stress* and *strain* in the elastic regime follows *Hook's law* [166],

$$[\sigma] = [E] \left[\varepsilon^{el}\right] \tag{4.12}$$

where $\{\varepsilon^{el}\}$ is the elastic strain vector, which in the presence of a temperature field is defined as

$$\left[\varepsilon^{el}\right] = [\varepsilon] - \left[\varepsilon^{t}\right] \tag{4.13}$$

with

$$\left[\varepsilon^{t}\right] = \begin{bmatrix} \frac{\partial(\alpha T)}{\partial x} & 0 & 0 \\ 0 & \frac{\partial(\alpha T)}{\partial y} & 0 \\ 0 & 0 & \frac{\partial(\alpha T)}{\partial z} \end{bmatrix}, \tag{4.14}$$

where α is the coefficient of thermal expansion and T is the temperature. The elasticity matrix [E] is defined as

$$[E] = \begin{bmatrix} \lambda + 2\mu & \lambda & \lambda & 0 & 0 & 0 \\ \lambda & \lambda + 2\mu & \lambda & 0 & 0 & 0 \\ \lambda & \lambda & \lambda + 2\mu & 0 & 0 & 0 \\ 0 & 0 & 0 & \mu & 0 & 0 \\ 0 & 0 & 0 & 0 & \mu & 0 \\ 0 & 0 & 0 & 0 & 0 & \mu \end{bmatrix} \tag{4.15}$$

where

$$\lambda = \frac{\nu E}{(1+\nu)(1-2\nu)} \tag{4.16}$$

and

$$\mu = \frac{E}{2(1+\nu)}, \tag{4.17}$$

E being the elasticity modulus, known as *Young's modulus*, and ν being *Poisson's ratio*.

The main equation to solve a problem in equilibrium is

$$[D]^T [\sigma] - \{F_b\} = 0 \tag{4.18}$$

where $\{F_b\} = \{F_x, F_y, F_z\}$ is the force vector acting on the body in the x, y, and z directions and the superscript T means the current temperature at the point in question. In the presence of a thermal load, Equation (4.18) will change into:

$$[D]^T [E] \left([D]\{u\} - \left[\varepsilon^t\right]\right) - \{F_b\} = 0. \tag{4.19}$$

This shows that the thermal load contribution can be applied as another body force. Therefore, Equation (4.19) can be rewritten as

$$[D]^T [E] [D] \{u\} - \{F_{th}\} - \{F_b\} = 0. \tag{4.20}$$

To solve these sets of equations, there is a need of boundary conditions in the form of a specified displacement, in this case

$$\{u\} = \{u\}_{boundary} \text{ on } S_u \tag{4.21}$$

where S_u is the location of the boundary surface. Another way to set the boundary condition is by specifying a superficial force $T_s = \{P_x, P_y, P_z\}$ which can be converted to local stresses as

$$\{T_s\} = \begin{bmatrix} n_x & 0 & 0 \\ 0 & n_y & 0 \\ 0 & 0 & n_z \\ n_y & n_x & 0 \\ 0 & n_z & n_y \\ n_z & 0 & n_x \end{bmatrix} [\sigma] \text{ on } S_T, \tag{4.22}$$

where $\{n\} = \{n_x, n_y, n_z\}$ is the unit normal vector going outward from S_T and S_T is the location of the applied force.

In engineering, where multi-axial loads are common occurrences, the equivalent stress (von Mises stress) is used to express the stress value and compare it with the value of the yield stress [166]:

$$\sigma_v = \sqrt{\frac{\left(\sigma_x - \sigma_y\right)^2 + \left(\sigma_y - \sigma_z\right)^2 + (\sigma_z - \sigma_x)^2 + 6\left(\tau_{yz}^2 + \tau_{zx}^2 + +\tau_{xy}^2\right)}{2}}. \tag{4.23}$$

The equivalent strain is calculated by dividing the von Mises stress by Young's modulus:

$$\varepsilon_v = \frac{\sigma_v}{E}. \tag{4.24}$$

4.3 Heat transfer fundamentals

Heat transfer can be simply defined as thermal energy in transit due to a spatial temperature difference [167]. Thus, whenever there exists a temperature difference in a medium or between media, heat transfer will occur. In 1-phase heat transfer phenomena, there are 3 mechanisms of heat transfer: conduction, convection, and radiation. In multi-phase heat transfer, phenomena like melting and evaporation have to be taken into account in the modelling. In this work, only 1-phase heat transfer was considered, since melting must be avoided inside a tokamak reactor, to prevent disruptions.

4.3.1 Conduction

Conduction is a mode of heat transfer which occurs through a solid or a stationary fluid (gas or liquid) due to the random motion of its constituent atoms, molecules and/or electrons [167]. This phenomenon was first formulated by Joseph Fourier in his book *Théorie Analytique de la Chaleur* in 1882 [168] [169]. It stated that the heat flux (q'') by conduction is proportional to the magnitude of the temperature gradient and opposite to it in sign. If the constant of proportionality is labelled as k, the relation between heat flux and temperature gradient can be written as

$$q'' = -k\frac{dT}{dx}. \tag{4.25}$$

The constant of proportionality, k, is called *thermal conductivity*. Equation (4.25) is called the 1-dimensional *Fourier Law*. Furthermore, Equation (4.25) can be rewritten in a form of heat transfer rate (q) as

$$q = -\frac{kA\Delta T}{L} = \frac{\|\Delta T\|}{R_{cond}}, \tag{4.26}$$

where *L* is the length of the material geometry, *A* is the cross-sectional area of the material geometry and R_{cond} is the thermal resistance of conduction, given by

$$R_{cond} = \frac{L}{kA}. \tag{4.27}$$

4.3.2 Convection

Convection is a heat transfer mode that uses an intermediate medium (liquid or gas) to transfer the heat. This mode comprised of two mechanisms. In addition to energy transfer due to *random molecular motion* (diffusion), energy is also transferred by the *bulk* (or *macroscopic*) *motion* of the fluid, also known as *advection* [167].

The first formulation of convective heat transfer was when Isaac Newton did an experiment with his linseed oil thermometer and found that the rate of cooling of any warm body at any moment is proportional to the temperature difference between the body and its surrounding medium [170]. This can be written as

$$\frac{dT_s}{dt} \propto T_s - T_\infty, \tag{4.28}$$

where T_∞ is the bulk temperature of the fluid and T_s is the temperature of the body surface. This equation implies that the heat transfer rate (*heat flow*) is also proportional to the temperature difference and can be rephrased in terms of $q'' = q/A$ as

$$q'' = \bar{h}\,(T_s - T_\infty) = \frac{(T_s - T_\infty)}{R_{conv}}, \tag{4.29}$$

where $\bar{h}$ is the *film coefficient* or *heat transfer coefficient* and $R_{conv} = \frac{1}{\bar{h}}$ is the thermal resistance of convection. Equation (4.11) is also known as the steady-state form of Newton's law of cooling. The region where the temperature gradient exists inside the fluid is called *thermal boundary layer* and is shown in Figure 4.3.

4.3.3 Radiation

Thermal radiation is the energy emitted by matter at non-zero temperature regardless of the form of matter [167]. While the heat transfer by conduction or convection requires a medium to transfer energy, that is not the case of radiation since in this mode, the energy transfer occurs in the form of electromagnetic waves. Therefore, in vacuum conditions, radiation heat transfer is the most efficient mode of heat transfer for an isolated body.

The model for the perfect thermal radiator is known as *black body*. This body absorbs (or emits) all energy that reaches it and reflects nothing. No other body emits more energy (for a given temperature), and it emits radiation in all directions (isotropic). The intensity, which is the energy per unit area, of the radiative heat transfer can be modelled as illustrated in Figure 4.4. For each arbitrary elemental surface

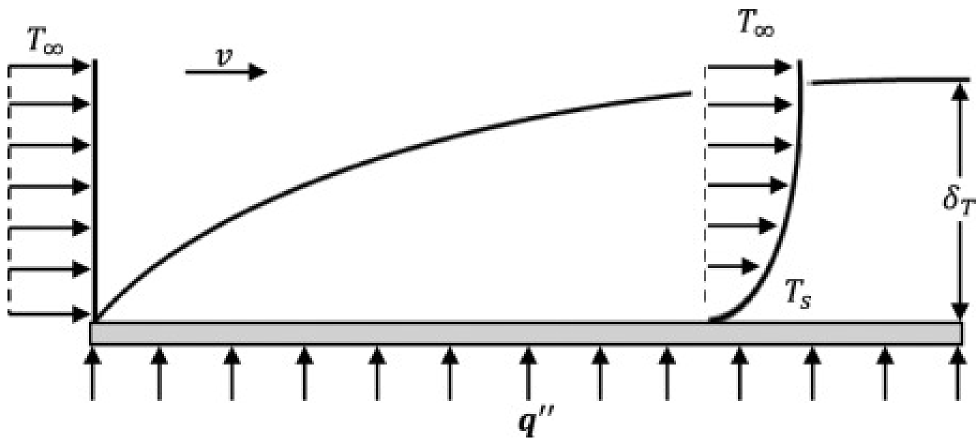

Figure 4.3: Thermal boundary layer [171].

A_a, the radiation spectral intensity can be written as

$$I_{\lambda,e}(\lambda,\vartheta,\varphi) \equiv \frac{dq}{dA_a \cos\vartheta\ \sin\vartheta\, d\vartheta\, d\varphi\, d\lambda} = \frac{dq}{dA_a \cos\vartheta\, d\omega\, d\lambda}, \tag{4.30}$$

where $(dq/d\lambda) \equiv dq_\lambda$ is the rate at which radiation of wavelength λ leaves dA and passes through dA_a, and

$$d\omega = \frac{dA_a}{r^2} \tag{4.31}$$

is the differential solid angle defined as the region between the rays of a sphere and is measured by the area ratio of dA_a on the sphere and the sphere's radius squared. After rearrangement, Equation (4.30) can be written as

$$dq_\lambda = I_{\lambda,e}(\lambda,\vartheta,\varphi)\, dA_a \cos\vartheta\ \sin\vartheta\, d\vartheta\, d\varphi\, d\lambda. \tag{4.32}$$

The spectral radiation flux associated with dA_a is

$$dq''_\lambda = I_{\lambda,e}(\lambda,\vartheta,\varphi)\ \cos\vartheta\ \sin\vartheta\, d\vartheta\, d\varphi, \tag{4.33}$$

where the spectral heat flux emitted into a hypothetical hemisphere above dA, as shown in Figure 4.4, can be written as

$$E_\lambda = q''_\lambda(\lambda) = \int_0^{2\pi}\int_0^{\frac{\pi}{2}} I_{\lambda,e}(\lambda,\vartheta,\varphi) \cos\vartheta \sin\vartheta\, d\vartheta\, d\varphi. \tag{4.34}$$

For a blackbody, the *total, hemispherical emissive power* can be calculated with

$$E_b = q''_b(\lambda) = \int_0^{\infty} E_\lambda(\lambda) d\lambda = \int_0^{\infty}\int_0^{2\pi}\int_0^{\frac{\pi}{2}} I_{\lambda,e}(\lambda,\vartheta,\varphi) \cos\vartheta \sin\vartheta\, d\vartheta\, d\varphi\, d\lambda. \tag{4.35}$$

By defining the blackbody spectral intensity, first determined by Planck [172] and known as *Planck Distribution*, as

$$I_{\lambda,b}(\lambda,T) = \frac{2hc_o^2}{\lambda^5\left[\exp(hc_o/\lambda k_B T) - 1\right]} \tag{4.36}$$

and putting it into Equation (4.35), it may be shown, by integration, that

$$E_b = \sigma T^4, \tag{4.37}$$

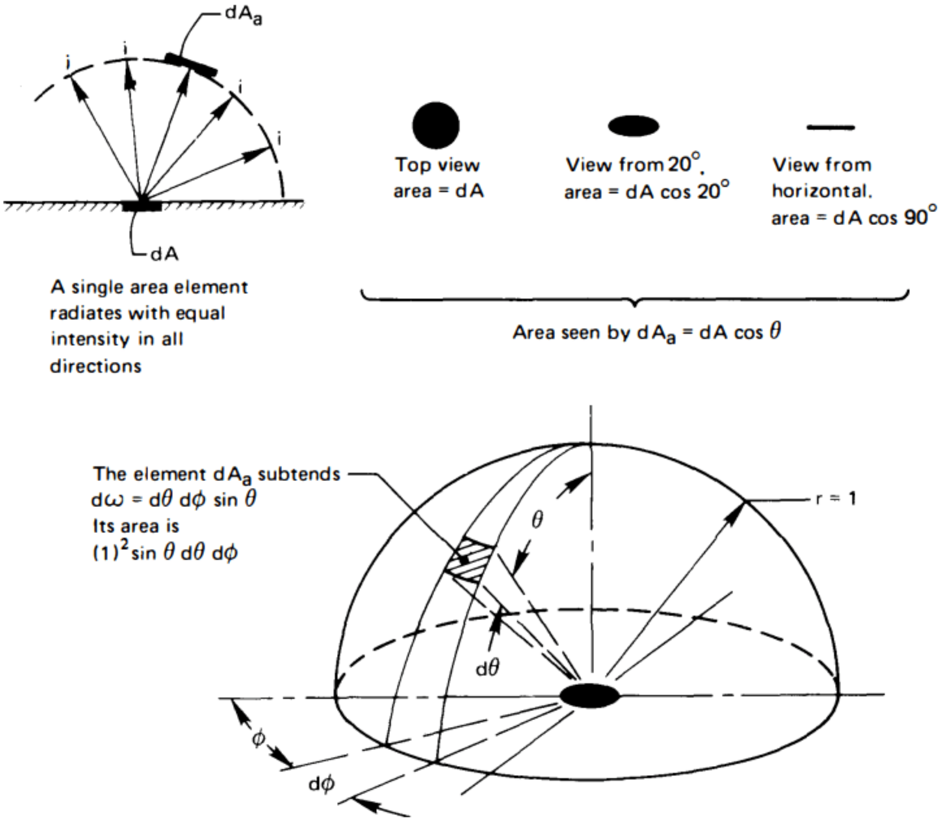

Figure 4.4: Radiation intensity through a unit sphere [169].

where σ is the *Stefan-Boltzmann* constant.

No material exists with the perfect properties of a *blackbody*. Therefore, it is important to introduce the concept of *gray-body*, an imperfect black body which partially absorbs the incident radiation energy. The ratio between the total emitted energy of a gray-body surface and a blackbody surface at the same temperature is known as the total *hemispherical* emissivity, $\varepsilon(\mathrm{T})$:

$$\varepsilon(\mathrm{T}) = \frac{\mathrm{E_e(T)}}{\mathrm{E_b(T)}} \tag{4.38}$$

with $0 < \varepsilon < 1$. For simplicity, Equation (4.38) can also be written as

$$\mathrm{E_e} = \varepsilon(\mathrm{T})\sigma\mathrm{T}^4. \tag{4.39}$$

In the case of real surfaces, the incident energy distribution is shown in Figure 4.5. A fraction, α, of the total energy (at a specific wavelength λ and temperature T), called *absorptance*, is absorbed in the body; another fraction, ρ, called *reflectance*, is reflected from it; and another fraction, τ, called *transmittance*, passes through. The relation of these coefficients can be rewritten as

$$\alpha\,(\lambda, \mathrm{T}) + \rho\,(\lambda, \mathrm{T}) + \tau\,(\lambda, \mathrm{T}) = 1. \tag{4.40}$$

It must be noted that these coefficients are functions of the geometry of the bodies, the temperature of the surface and the wavelength of the incident radiation. For an *opaque* body, there is no transmission of the energy, and by applying *Kirchhoff's law*, which states that a body in thermodynamic equilibrium emits as much energy as it absorbs in each direction and at each wavelength, Equation (4.40) simply becomes

$$\rho(\lambda, T) = 1 - \alpha(\lambda, T) = 1 - \varepsilon(\lambda, T)\,. \tag{4.41}$$

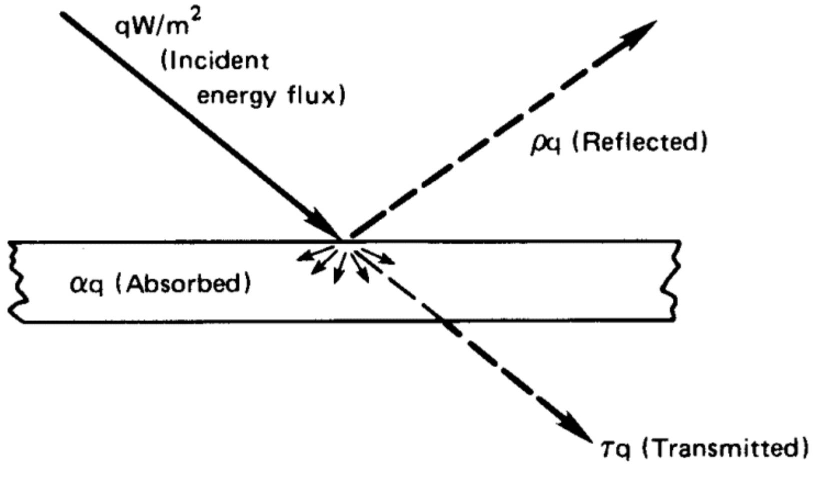

Figure 4.5: The distribution of incident energy on a translucent slab [169].

Another important concept for radiation is the *total radiosity*, defined as the total rate at which all the radiant energy leaves the surface. The radiosity takes into account the reflected portion of the radiation as well as the direct emission of the surface. With a similar formulation as that of Equation (4.34), the total radiosity can be written as

$$J = \int_0^\infty J_\lambda(\lambda)d\lambda = \int_0^\infty \int_0^{2\pi} \int_0^{\frac{\pi}{2}} I_{\lambda,e+r}(\lambda, \vartheta, \varphi)\cos\vartheta \sin\vartheta \, d\vartheta \, d\varphi \, d\lambda = \varepsilon E_+(1-\varepsilon)G, \tag{4.42}$$

where

$$G = \int_0^\infty G_\lambda(\lambda)d\lambda = \int_0^\infty \int_0^{2\pi} \int_0^{\frac{\pi}{2}} I_{\lambda,r}(\lambda, \vartheta, \varphi)\cos\vartheta \sin\vartheta \, d\vartheta \, d\varphi \, d\lambda \tag{4.43}$$

is defined as the rate at which radiation is incident per unit area from all directions and at all wavelengths.

When there are two finite surfaces with different temperature states, the radiation heat transfer works both ways. Therefore, the concept of a *view factor* (also called *shape factor*) must be introduced. The view factor F_{ij} is defined as the fraction of the radiation leaving surface A_i that is intercepted by surface A_j. For two arbitrarily oriented surfaces A_i and A_j, illustrated in Figure 4.6, the elemental areas of each surface, dA_i and dA_j, are connected by a line of length R and form the polar angles ϑ_i and ϑ_j with the surface normals $\mathbf{n}_i$ and $\mathbf{n}_j$.

In this case, Equation (4.32), which based on the spherical coordinates, could be rewritten as a function of the elemental surfaces dA_i and dA_j as

$$dq_{i\to j} = I_{e+r,i} \cos\vartheta_i \, dA_i \, d\omega_{j\to i} = J_i \frac{\cos\vartheta_i \cos\vartheta_j}{R^2} dA_i dA_j. \tag{4.44}$$

The total rate at which radiation leaves surface i and is intercepted by j may be obtained by integrating

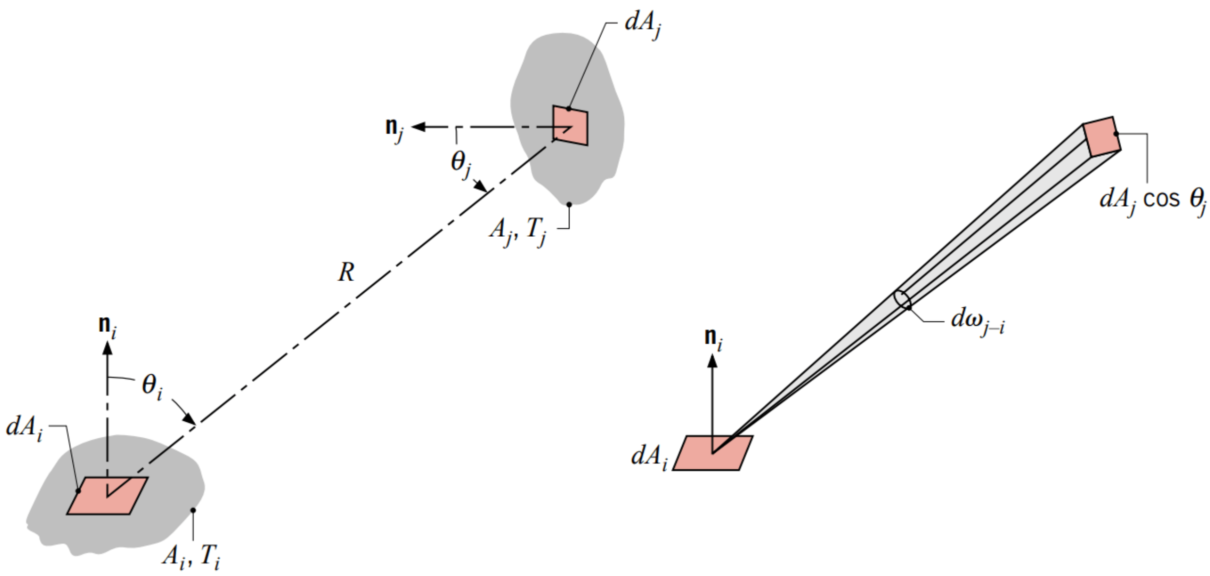

Figure 4.6: View factor associated with radiation exchange between elemental surfaces of area dA_i and dA_j [167].

over the two surfaces:

$$q_{i\to j} = J_i \int_{A_i}\int_{A_j} \frac{\cos\vartheta_i \cos\vartheta_j}{\pi R^2} dA_i dA_j, \tag{4.45}$$

where the radiosity J_i is uniform across the surface A_i. The view factor of the radiation leaving surface A_i intercepted by A_j is

$$F_{ij} = \frac{q_{i\to j}}{A_i J_i} = \frac{1}{A_i}\int_{A_i}\int_{A_j} \frac{\cos\vartheta_i \cos\vartheta_j}{\pi R^2} dA_i dA_j. \tag{4.46}$$

Therefore, the important relation between the view factors of two interacting surfaces can be formulated as

$$A_i F_{ij} = A_j F_{ji}, \tag{4.47}$$

which is known as the *reciprocity relation*. Another important relation is the *summation rule*, formulated as

$$\sum_{j=1}^{N} F_{ij} = 1. \tag{4.48}$$

It is important to note that Nusselt's analogy shows that any surface which covers the same area on the hemisphere has the same view factor. Therefore, any intermediate surface geometry can be used without changing the values of the view factors. The *Hemicube method* calculates view factors by projecting the radiating surface into an imaginary cube [173].

From Equation (4.35), Equation (4.42), and Equation (4.43), the net radiative flux from a surface i can be written as

$$q_i'' = \frac{q}{A} = J_i - G_i \tag{4.49}$$

and the net radiative heat transfer may be expressed as

$$q_i = A_i \left(J_i - \frac{J_i - \varepsilon_i E_{bi}}{1 - \varepsilon_i} \right) = \frac{E_{bi} - J_i}{(1-\varepsilon_i)/\varepsilon_i A_i} \tag{4.50}$$

or

$$q_i = \sum_{j=1}^{N} \frac{J_i - J_j}{(A_i F_{ij})^{-1}}. \tag{4.51}$$

Thus, the thermal resistance of radiation heat transfer can be calculated as

$$R_{rad} = \frac{1 - \varepsilon_i}{\varepsilon_i A_i} \tag{4.52}$$

if one of the interacting surfaces is a blackbody ($\varepsilon = 1$), or as

$$R_{rad} = \frac{1}{A_i F_{ij}} \tag{4.53}$$

if both surfaces are not blackbodies ($0 < \varepsilon < 1$).

4.3.4 Multimode Heat Transfer

In reality, a heat transfer phenomenon with one mode only happens rarely. Therefore, a concept to combine the calculation of several modes of heat transfer, each with a different formulation, is mandatory. For this purpose, it is useful to use an analogy with Ohm's law, as illustrated in Figure 4.7. Ohm's law, in electrical systems, states that the current through a device is always directly proportional to the potential difference applied to the device [174]. The coefficient of proportionality in this case is known as *resistance*. In a thermal system, the electrical potential difference is analogous to the heat energy (thermal potential difference), the electric current is analogous to the heat flow, and the coefficient of proportionality is called the thermal resistance. Therefore, Ohm's law can be written for a thermal system as

$$R_{th} = \frac{\Delta E}{q_{i,ext}}, \tag{4.54}$$

where the total incoming heat flow, $q_{i,ext}$, can be written as

$$q_{i,ext} = q_{i,rad} + q_{i,cond} + q_{i,conv}. \tag{4.55}$$

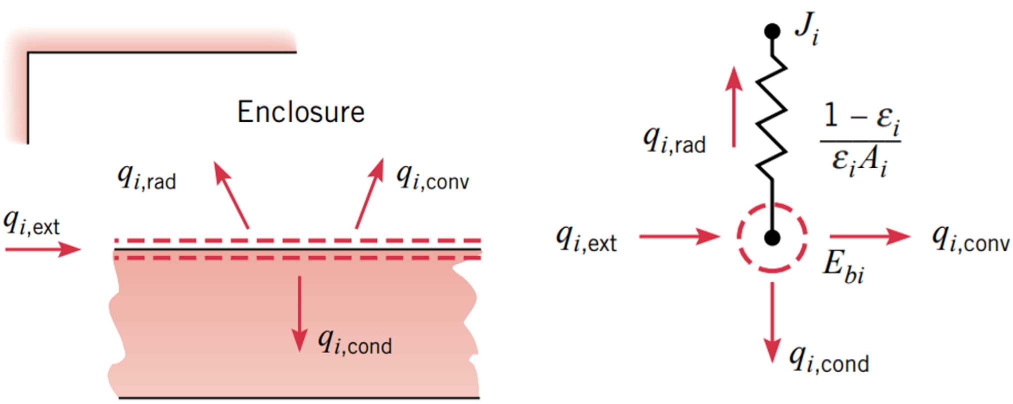

(a) surface energy balance (b) electrical circuit analogy

Figure 4.7: Multimode heat transfer from a surface in an enclosure [167].

4.4 Finite Element Method (FEM)

The Finite Element Method (FEM) is a numerical technique used to approximate the solution of boundary and initial-value problems characterized by Partial Differential Equations (PDEs) [175] that can be formulated as functional minimization [176]. The idea of this method is to discretize the domain of interest into several subdomains, and then find a solution which respects the continuity of the problem (see Figure 4.8). These subdomains are called *finite elements* or *mesh* and are connected through points called *nodes*. Depending on the problem, several finite element types can be used. Calculations using FEM provide results on each node and the spatial resolution of the problem is obtained by interpolation of the nodal solution.

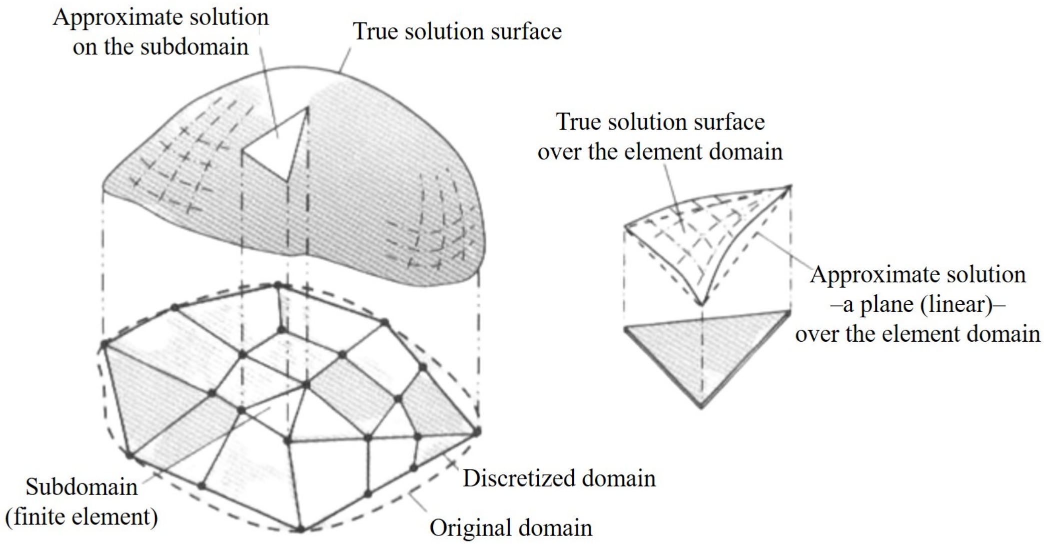

Figure 4.8: Example of FEM discretization over a 2D domain taken from [177].

The FEM is famous for its robustness to solve any field problem (e.g. heat transfer, electromagnetism, etc.). This method also allows the use of many shapes, boundary conditions and initial conditions without any restrictions. These advantages are also supported by the *mesh* assembly which resembles the actual domain of interest. In order to achieve a better approximation, in most cases grading the *mesh* and/or building one with shapes that comply with the regions where the field gradients are high is the solution [178].

In order to develop a Finite Element (FE) model, the physical model and its differential equations that describe the problem, also known as *strong formulation*, must be built along with the boundary conditions. This strong formulation is then converted into weighted integral statements of the set of equations (*weak formulation*), allowing the dependent variables to be transferred into the weight function. This step is important since it includes the natural boundary conditions in the integral statement [177]. This set of equations is then represented in the form of a matrix, which then needs to be solved.

The solution of the FE model can be achieved by two methods: the direct method and the iterative method. The first gives the exact solution of the equation involving the inverse matrix to get the quantities of interest. For example, to solve Equation (4.18) for the unknown quantity σ, the mathematical equation for the direct approach becomes

$$\sigma = \left([\mathrm{D}]^{\mathrm{T}}\right)^{-1} \{\mathrm{F_b}\}. \tag{4.56}$$

While this method gives the exact solution for the problem of interest, it usually require very extensive computational resources. The reason for this is that the number of nodes, which also represents the number of equations, is usually very large.

The iterative method, on the other hand, starts with an initial guess and iterates until it reaches a solution that satisfies stopping criterion. Usually, a tolerance value (residual) is obtained. For the same example case (calculate the displacement vector from Equation (4.18)), the iterative method starts with an initial guess $\{u_0\}$ and calculates the solution for step 1 ($\{u_1\}$) by solving the equation

$$[A]\{u_1\} = [A]\{u_0\} + \{F_b\} - [D]^T, \{u_0\} \tag{4.57}$$

where the matrix $[A]$=diag$[D]^T$. This process is repeated up to step n, which can be written as

$$[A]\{u_n\} = [A]\{u_{n-1}\} + \{F_b\} - [D]^T, \{u_{n-1}\} \tag{4.58}$$

where the matrix solution $\{u_n\}$ which satisfies the original equation is found by minimizing the residual, the difference between the guessed solution and the original function, written as

$$R = |[A]\{u_n\} - [A]\{u_{n-1}\}| = \left|\{F_b\} - [D]^T\{u_{n-1}\}\right|. \tag{4.59}$$

This method is usually preferred when the number of Degrees of Freedom (D.O.Fs) is very large, since it consumes less CPU memory. Thus, for the same computational resources, the iterative method can solve larger problems.

4.4.1 Finite Element Equation for Heat Transfer

The FEM can handle a complex problem with multimode heat transfer by solving a general equation for one FE, which can be expressed as

$$([k] + [h_{conv}] + [h_{rad}])[T] = \left[Q^{conv}\right] + \left[Q^{rad}\right] + \left[Q^{g}\right], \tag{4.60}$$

where k is the material heat conductivity, h_{conv} is the film coefficient, $Q^g$is the internal heat generation, Q_{rad} is the total heat flux received by the boundary surface element, Q_{conv} is the element convection surface heat flow vector, and h_{rad} is defined as

$$h_{rad} = \psi\sigma\left(T^2_{source} + T^2_{target}\right)\left(T_{source} + T_{target}\right), \tag{4.61}$$

where ψ includes the surface areas, emissivities and view factors.

It is important to notice that the FEM is built for the solid domain. This means that the convective and radiative heat transfer modes are generally modelled as boundary conditions. Therefore, separate calculations are usually required to obtain them.

Regarding the conductive heat transfer mode, the FEM can easily simulate the heat conduction using the 3-D equation

$$-\frac{\partial q''}{\partial x} - \frac{\partial q''}{\partial y} - \frac{\partial q''}{\partial z} + Q^g = \rho c\frac{\partial T}{\partial t} \tag{4.62}$$

where Q^g is the internal heat generation, ρ is the material density and c is the heat capacity of the material.

By applying Fourier's law, Equation (4.62) becomes

$$\frac{\partial}{\partial x}\left(k\frac{\partial T}{\partial x}\right)+\frac{\partial}{\partial y}\left(k\frac{\partial T}{\partial y}\right)+\frac{\partial}{\partial z}\left(k\frac{\partial T}{\partial z}\right)+Q^{g}=\rho c\frac{\partial T}{\partial t}. \tag{4.63}$$

The method adopted by ITER to simulate the plasma thermal radiation of the plasma is done in two steps: 1) calculate the thermal radiation and 2) apply it to the boundary surfaces as a heat flux boundary condition. This method simplifies the calculation of radiation heat transfer, making it dependent only on the shapes of the interacting surfaces.

4.5 Computational Fluid Dynamics (CFD)

In order to model the convective heat transfer in a complex geometry, a numerical tool known as Computational Fluid Dynamics (CFD) is required. CFD itself is a branch of fluid mechanics which uses numerical analysis to perform calculations of the interactions of a flowing fluid, usually with the Finite Volume Method (FVM), which conserves a general flow variable φ within a finite control volume as a balance between the various processes tending to increase or decrease it [179]. In other words:

$$\begin{bmatrix}\text{Rate of change of}\\ \varphi\text{ in the control volume}\\ \text{with respect to time}\end{bmatrix}=\begin{bmatrix}\text{Net rate of increase of}\\ \varphi\text{ due to}\\ \text{convection into}\\ \text{the control}\\ \text{volume}\end{bmatrix}+\begin{bmatrix}\text{Net rate of increase of}\\ \varphi\text{ due to}\\ \text{diffusion into}\\ \text{the control}\\ \text{volume}\end{bmatrix}+\begin{bmatrix}\text{Net rate of}\\ \text{creation of}\\ \varphi\text{ inside}\\ \text{the control}\\ \text{volume}\end{bmatrix}$$

The governing equations of fluid flow are the Navier-Stokes equations, which involve the conservation laws of physics, namely, the consevation of mass, Newton's second law of motion and the first law of thermodynamics. The conservation of mass is presented in the continuity equation, which can be written as

$$\frac{\partial\rho}{\partial t}+\boldsymbol{\nabla}\cdot\left(\rho\mathbf{U}\right)=0, \tag{4.64}$$

where ρ is the fluid density, t is time, and $\mathbf{U}$ is the fluid flow velocity vector in 3-dimensions that can be decomposed into its directional components $\mathbf{U_i}$ with $i = 1, 2, 3$. Newton's second law of motion states that the acceleration of an object is dependent on the net forces acting on the object and the object mass, and by applying *Cauchy's momentum equation*, the momentum equations of the fluid control volume can be expressed as

$$\frac{\partial}{\partial t}\left(\rho\mathbf{U}\right)+\boldsymbol{\nabla}\cdot\left(\rho\mathbf{U}\times\mathbf{U}\right)=-\nabla p+\boldsymbol{\nabla}\cdot\tau+\mathbf{S_M}, \tag{4.65}$$

where

$$\tau=\mu\left(\nabla\mathbf{U}+(\nabla\mathbf{U})^{T}-\frac{2}{3}\delta\boldsymbol{\nabla}\cdot\mathbf{U}\right) \tag{4.66}$$

and ∇p is the volumetric pressure gradient, τ is the viscous stress tensor, μ is the fluid dynamic viscosity and $\mathbf{S_M}$ is the momentum source or the sum of the body forces.

The last conservation law of physics in the set is the first law of thermodynamics, which states that energy cannot be created or destroyed; it can only be converted from one form to another. In mathematical terms, it can be written as

$$\frac{\partial}{\partial t}\left(\rho h_{tot}\right) + \frac{\partial p}{\partial t} + \boldsymbol{\nabla} \cdot \left(\rho h_{tot}\mathbf{U}\right) = \boldsymbol{\nabla} \cdot k\nabla T + \boldsymbol{\nabla} \cdot (\mathbf{U} \cdot \tau) + \mathbf{U} \cdot \mathbf{S_M} + \mathbf{S_E}, \tag{4.67}$$

where h_{tot} is the total enthalpy, related to the static enthalpy $h(T, p)$ by

$$h_{tot} = h + \frac{1}{2}\mathbf{U}^2. \tag{4.68}$$

The term $\boldsymbol{\nabla} \cdot (\mathbf{U} \cdot \tau)$ represents the work due to viscous stresses, the term $\mathbf{U} \cdot \mathbf{S_M}$ represents the work due to external momentum sources, and $\mathbf{S_E}$ is the energy source.

From Equations (4.64), (4.65) and (4.67), it can be seen that there are 5 equations (1 continuity equation, 3 momentum equations, and 1 energy equation) with 6 unknowns, namely the temperature, pressure, density, and the velocity in 3 directions (x, y, and z). Therefore, the Navier-Stokes equations are known to have a closure problem, which means that assumptions must be made to allow approximate solutions of the equations for practical applications. The closure assumptions will differentiate the type of fluid flow modelling, and divide CFD into three categories, namely, Direct Numerical Simulation (DNS), Large Eddy Simulation (LES), and Reynolds-averaged Navier Stokes equation (RANS) simulation [180]. These three numerical methods vary in computational cost and number of D.O.Fs. As a result, they also affect the geometrical complexity and the modelling importance. The most used turbulence model for practical applications is RANS, which allows very complex geometries to be simulated, due to the lower number of D.O.Fs.

It is widely known that in the RANS method the quantities are decomposed into the time-averaged (mean) component and the time-varying (fluctuating) component. This decomposition is known as Reynolds decomposition. The fluid flow velocity ($\mathbf{U}$) is decomposed into mean component, $\overline{U}$, and fluctuating component, u, with the relation

$$\mathbf{U_i} = \overline{U_i} + u_i = \frac{1}{\Delta t}\int_t^{t+\Delta t} \mathbf{U_i}\, dt + u_i, \tag{4.69}$$

where Δt is a time scale that is large relative to turbulent fluctuations, but small relative to the time scale to which the equations are solved [181]. With this decomposition, the Navier-Stokes equation can be rewritten in terms of these time-averaged quantities and their fluctuations as

$$\frac{\partial \rho}{\partial t} + \frac{\partial}{\partial x_j}\left(\rho \overline{U_j}\right) = 0 \tag{4.70}$$

$$\frac{\partial \left(\rho \overline{U_i}\right)}{\partial t} + \frac{\partial}{\partial x_j}\left(\rho \overline{U_i U_j}\right) = -\frac{\partial p}{\partial x_i} + \frac{\partial}{\partial x_j}\left(\tau_{ij} - \rho \overline{u_i u_j}\right) + \mathbf{S_M} \tag{4.71}$$

and

$$\frac{\partial \left(\rho h_{tot}\right)}{\partial t} - \frac{\partial p}{\partial t} + \frac{\partial}{\partial x_j}\left(\rho \overline{U_j} h_{tot}\right) = \frac{\partial}{\partial x_j}\left(\lambda \frac{\partial T}{\partial x_j} - \rho \overline{u_j h}\right) + \frac{\partial}{\partial x_j}\left[\overline{U_i}\left(\tau_{ij} - \rho \overline{u_i u_j}\right)\right] + \mathbf{S_E}. \tag{4.72}$$

These equations contain the second order turbulence flux term, $\rho \overline{u_j h}$, and the viscous work term, $\frac{\partial}{\partial x_j}\left[\overline{U_j}\left(\tau_{ij} - \rho \overline{u_i u_j}\right)\right]$.

The total enthalphy, h_{tot} is given by

$$h_{tot} = h + \frac{1}{2}\overline{U_i U_j} + k, \tag{4.73}$$

where k is the turbulent kinetic energy, given by

$$k = \frac{1}{2}\overline{u_i^2}. \tag{4.74}$$

The two most used RANS turbulence models in industrial applications, namely the k–ε turbulence model and the k–ω turbulence model, are presented in the next section. The k–ε model allows to simulate flows with high Reynolds numbers, but requires a wall function to overcome inaccuracies in the near-wall region. The k–ω model has better performance when the flow is in the near-wall region; however, it is very sensitive to free stream conditions.

4.5.1 The standard $k - \varepsilon$ turbulence model

The two-equation $k - \varepsilon$ turbulence model is the most popular RANS, which performs well for most cases, especially when the case itself is in the high Reynolds number range, $Re = \frac{\rho UL}{\mu}$, where ρ is the density of the fluid, U is the fluid flow velocity, L is the characteristic linear dimension, and μ is the dynamic viscosity of the fluid. This turbulence model has the advantage that no geometry-related parameters are included in modelling the turbulence transport equation, but it also has the disadvantage of a very stiff coupling between the conservation equations with the overall system of equations and the inaccuracy in the near-wall region. In order to overcome the disadvantages of this model, there are several near wall treatments developed for the $k - \varepsilon$ model, such as the standard wall function, the non-equilibrium wall function [181], and the enhanced wall treatment. Each of these wall functions has a different requirement for the dimensionless wall distance y^+, which is defined as

$$y^+ = \frac{y u_\tau}{\nu}, \tag{4.75}$$

where y is the absolute distance from the wall and u_τ is the so called friction velocity, expressed by

$$u_\tau = \sqrt{\frac{\tau_w}{\rho}}, \tag{4.76}$$

with the wall shear-stress, τ_w, as

$$\tau_w = \mu \left(\frac{d\overline{U_i}}{dy}\right)_{y=0}. \tag{4.77}$$

The standard wall function and the non-equilibrium wall function require the value of y^+ at the closest cell from the wall to be between 30 and 300 $(30 < y^+ < 300)$, while the enhanced wall treatment requires this value to be less than 1. For complex geometries, however, it can go up to 5 $(y^+ < 5)$.

In the $k - \varepsilon$ turbulence model, the momentum equation (Equation (4.71)) becomes

$$\frac{\partial}{\partial t}\left(\rho\overline{U_i}\right) + \frac{\partial}{\partial x_j}\left(\rho\overline{U_i U_j}\right) = -\frac{\partial p'}{\partial x_i} + \frac{\partial}{\partial x_j}\left[\mu_{eff}\left(\frac{\partial\overline{U_i}}{\partial x_j} + \frac{\partial\overline{U_j}}{\partial x_i}\right)\right] + \mathbf{S_M}, \tag{4.78}$$

where μ_{eff} is the effective viscosity defined by

$$\mu_{eff} = \mu + \mu_t = \mu + C_\mu \rho \frac{k^2}{\varepsilon}, \tag{4.79}$$

C_μ is a constant and p' is a modified pressure, defined by

$$p' = p + \frac{2}{3}\rho k + \frac{2}{3}\mu_{eff}\frac{\partial \overline{U_k}}{\partial x_k}. \tag{4.80}$$

The Reynolds averaged energy equations become

$$\frac{\partial (\rho h_{tot})}{\partial t} - \frac{\partial p}{\partial t} + \frac{\partial}{\partial x_j}\left(\rho \overline{U_j} h_{tot}\right) = \frac{\partial}{\partial x_j}\left(\lambda \frac{\partial T}{\partial x_j} + \frac{\mu_t}{Pr_t}\frac{\partial h}{\partial x_j}\right) + \frac{\partial}{\partial x_j}\left[\overline{U_i}\left(\tau_{ij} - \rho \overline{u_i u_j}\right)\right] + \mathbf{S_E}. \tag{4.81}$$

In addition, there is also the transport equation for the turbulence kinetic energy (k) and the turbulence dissipation rate (ε), defined as

$$\frac{\partial}{\partial t}(\rho k) + \frac{\partial}{\partial x_j}\left(\rho \overline{U_j} k\right) = \frac{\partial}{\partial x_j}\left[\left(\mu + \frac{\mu_t}{\sigma_k}\right)\frac{\partial k}{\partial x_j}\right] + P_k - \rho\varepsilon + P_{kb} \tag{4.82}$$

and

$$\frac{\partial}{\partial t}(\rho \varepsilon) + \frac{\partial}{\partial x_j}\left(\rho \overline{U_j}\varepsilon\right) = \frac{\partial}{\partial x_j}\left[\left(\mu + \frac{\mu_t}{\sigma_\varepsilon}\right)\frac{\partial \varepsilon}{\partial x_j}\right] + \frac{\varepsilon}{k}\left(C_{\varepsilon 1}P_k - C_{\varepsilon 2}\rho\varepsilon + C_{\varepsilon 1}P_{\varepsilon b}\right), \tag{4.83}$$

where $C_{\varepsilon 1}$, $C_{\varepsilon 2}$, $C_{\varepsilon 2}$, σ_k, and σ_ε are constants. P_k is the turbulence production due to viscous forces, modeled using

$$P_k = -\rho \overline{u_i u_j}\frac{\partial \overline{U_j}}{\partial x_i} = \mu_t\left(\frac{\partial \overline{U_i}}{\partial x_j} + \frac{\partial \overline{U_j}}{\partial x_i}\right)\frac{\partial \overline{U_i}}{\partial x_j} - \frac{2}{3}\frac{\partial \overline{U_k}}{\partial x_k}\left(3\mu_t \frac{\partial \overline{U_k}}{\partial x_k} + \rho k\right). \tag{4.84}$$

P_{kb} and $P_{\varepsilon b}$ represent the influence of the buoyancy forces, with the buoyancy production term P_{kb} modeled as

$$P_{kb} = \begin{cases} -\dfrac{\mu_t}{\rho\sigma_\rho} g_i \dfrac{\partial \rho}{\partial x_i} & \text{if full buoyancy model} \\ \\ \dfrac{\mu_t}{\rho\sigma_\rho}\rho\beta g_i \dfrac{\partial T}{\partial x_i} & \text{if Boussinesq buoyancy model,} \end{cases} \tag{4.85}$$

where $P_{\varepsilon b}$ is assumed to be proportional to P_{kb}, with the relation

$$P_{\varepsilon b} = C_3 \cdot \max(0, P_{kb}), \tag{4.86}$$

where the dissipation coefficient (C_3) and the Turbulent Schmidt number σ_ρ are constants.

4.5.1.1 The RNG $k - \varepsilon$ turbulence model

The difference between the RNG $k - \varepsilon$ and the standard $k - \varepsilon$ turbulence model in the previous section is the expansion of the Reynolds stress and the production of dissipation terms. The RNG $k - \varepsilon$ has an additional term in its turbulent dissipation equation that significantly improves the accuracy for rapidly strained flows.

The transport equations of the RNG $k-\varepsilon$ model are similar to the standard $k-\varepsilon$ turbulence model. The difference is in the turbulence dissipation's transport equation, which becomes

$$\frac{\partial(\rho\varepsilon)}{\partial t}+\frac{\partial}{\partial x_j}\left(\rho\overline{U_j}\varepsilon\right)=\frac{\partial}{\partial x_j}\left[\left(\mu+\frac{\mu_t}{\sigma_{\varepsilon RNG}}\right)\frac{\partial\varepsilon}{\partial x_j}\right]+\frac{\varepsilon}{k}\left(C_{\varepsilon 1RNG}P_k-C_{\varepsilon 2RNG}\rho\varepsilon+C_{\varepsilon 1RNG}P_{\varepsilon b}\right), \quad (4.87)$$

where $C_{\varepsilon 2RNG}$ is a constant and

$$C_{\varepsilon 1RNG}=1.42-f_\eta \quad (4.88)$$

with

$$f_\eta=\frac{\eta\left(1-\frac{\eta}{4.38}\right)}{1+\beta_{RNG}\eta^3} \quad (4.89)$$

and

$$\eta=\sqrt{\frac{P_k}{\rho C_{\mu RNG}\varepsilon}}. \quad (4.90)$$

The $k-\varepsilon$ turbulence model performs particularly well in confined flows, including a wide range of flows with industrial engineering applications. However, the near wall resolution calculations are bounded by the size of the grid close to the wall, which can increase the computational cost exponentially if the geometry under investigation is very complex.

4.5.2 The $k-\omega$ turbulence model

The other popular two-equation turbulence model is the $k-\omega$ model, which instead of using the transport of the turbulence dissipation rate (ε), uses the transport of the turbulence frequency (ω), which can be written as

$$\omega=\frac{\varepsilon}{\beta' k}, \quad (4.91)$$

where β' is a constant and k is the turbulence kinetic energy.

The standard $k-\omega$, also known as Wilcox $k-\omega$, model assumes the relation between the turbulence kinetic energy and the turbulent frequency as turbulence viscosity, written as

$$\mu_t=\rho\frac{k}{\omega} \quad (4.92)$$

The transport equation for the turbulence kinetic energy (k) can be written as

$$\frac{\partial}{\partial t}(\rho k)+\frac{\partial}{\partial x_j}\left(\rho\overline{U_j}k\right)=\frac{\partial}{\partial x_j}\left[\left(\mu+\frac{\mu_t}{\sigma_k}\right)\frac{\partial k}{\partial x_j}\right]+P_k-\beta'\rho k\omega+P_{kb}, \quad (4.93)$$

while the turbulence frequency (ω) transport equation can be written as

$$\frac{\partial}{\partial t}(\rho\omega)+\frac{\partial}{\partial x_j}\left(\rho\overline{U_j}\omega\right)=\frac{\partial}{\partial x_j}\left[\left(\mu+\frac{\mu_t}{\sigma_\omega}\right)\frac{\partial\omega}{\partial x_j}\right]+\alpha\frac{\omega}{k}P_k-\beta\rho\omega^2+P_{\omega b}, \quad (4.94)$$

where α, β, σ_k, and σ_ω are constants.

P_k is calculated in the same way as in the $k-\varepsilon$ turbulence model, with the Reynolds stress tensor,

$\rho\overline{u_i u_j}$, calculated from

$$-\rho\overline{u_i u_j} = \mu_t \left(\frac{\partial \overline{U_i}}{\partial x_j} + \frac{\partial \overline{U_j}}{\partial x_i} \right) - \frac{2}{3}\delta_{ij} \left(\rho k + \mu_t \frac{\partial \overline{U_k}}{\partial x_k} \right) \tag{4.95}$$

and $P_{\omega b}$ calculated as

$$P_{\omega b} = \frac{\omega}{k} \left((\alpha + 1) C_3 \max \left(P_{kb}, 0 \right) - P_{kb} \right). \tag{4.96}$$

4.5.2.1 The Baseline (BSL) $k - \omega$ turbulence model

The $k-\omega$ turbulence model is substantially more robust than the $k-\varepsilon$ turbulence model in the near-wall layers [182]. However, the values of ω outside the boundary layer are very sensitive, and in the regions far from the wall the standard-scale equation is dominated by the turbulence dissipation rate. Therefore, a variant of the $k-\omega$ turbulence model, the Baseline (BSL) $k-\omega$ model, tries to solve this undesirable feature of the Wilcox $k-\omega$ model, which is significantly dependent to the ω value specified at the inlet. This problem is solved by transforming the $k-\varepsilon$ model into the $k-\omega$ formulation with a subsequent addition of the corresponding equations [181]. In other words, the turbulence transport equations consist of the equations from the Wilcox $k-\omega$ model multiplied by a blending function F_1 and then added by the $k-\varepsilon$ model turbulence transport equation multiplied by (1-F_1). The blending function F_1 depends on the position of the nodes. When the cell is close to the wall the value of F_1 approaches 1; it decreases at larger distances from the wall, and once it is outside the boundary layer, the value of F_1 becomes 0.

Without buoyancy forces activated, the transport equation of the Wilcox $k-\omega$ model becomes

$$\frac{\partial}{\partial t}\left(\rho k\right) + \frac{\partial}{\partial x_j}\left(\rho \overline{U_j} k\right) = \frac{\partial}{\partial x_j}\left[\left(\mu + \frac{\mu_t}{\sigma_{k1}} \right) \frac{\partial k}{\partial x_j} \right] + P_k - \beta' \rho k \omega \tag{4.97}$$

$$\frac{\partial}{\partial t}\left(\rho \omega\right) + \frac{\partial}{\partial x_j}\left(\rho \overline{U_j} \omega\right) = \frac{\partial}{\partial x_j}\left[\left(\mu + \frac{\mu_t}{\sigma_{\omega 1}} \right) \frac{\partial \omega}{\partial x_j} \right] + \alpha \frac{\omega}{k} P_k - \beta \rho \omega^2 \tag{4.98}$$

and the transformed $k-\varepsilon$ turbulence transport model can be written as

$$\frac{\partial}{\partial t}\left(\rho k\right) + \frac{\partial}{\partial x_j}\left(\rho \overline{U_j} k\right) = \frac{\partial}{\partial x_j}\left[\left(\mu + \frac{\mu_t}{\sigma_{k2}} \right) \frac{\partial k}{\partial x_j} \right] + P_k - \beta' \rho k \omega. \tag{4.99}$$

$$\frac{\partial}{\partial t}\left(\rho \omega\right) + \frac{\partial}{\partial x_j}\left(\rho \overline{U_j} \omega\right) = \frac{\partial}{\partial x_j}\left[\left(\mu + \frac{\mu_t}{\sigma_{\omega 2}} \right) \frac{\partial \omega}{\partial x_j} \right] + 2\rho \frac{1}{\sigma_{\omega 2} \omega} \frac{\partial k}{\partial x_j} \frac{\partial \omega}{\partial x_j} + \alpha_2 \frac{\omega}{k} P_k - \beta_2 \rho \omega^2 \tag{4.100}$$

By multiplying the equations from the Wilcox $k-\omega$ model by F_1 and the transformed $k-\varepsilon$ equations by 1-F_1, and adding both corresponding equations also including the buoyancy effects, the transport equations for BSL can be written as

$$\frac{\partial}{\partial t}\left(\rho k\right) + \frac{\partial}{\partial x_j}\left(\rho \overline{U_j} k\right) = \frac{\partial}{\partial x_j}\left[\left(\mu + \frac{\mu_t}{\sigma_{k3}} \right) \frac{\partial k}{\partial x_j} \right] + P_k - \beta' \rho k \omega + P_{kb} \tag{4.101}$$

$$\frac{\partial}{\partial t}\left(\rho \omega\right) + \frac{\partial}{\partial x_j}\left(\rho \overline{U_j} \omega\right) = \frac{\partial}{\partial x_j}\left[\left(\mu + \frac{\mu_t}{\sigma_{\omega 3}} \right) \frac{\partial \omega}{\partial x_j} \right] + \left(1 - F_1\right) 2\rho \frac{1}{\sigma_{\omega 2} \omega} \frac{\partial k}{\partial x_j} \frac{\partial \omega}{\partial x_j} + \alpha_3 \frac{\omega}{k} P_k - \beta_3 \rho \omega^2 + P_{\omega b}, \tag{4.102}$$

where β', α_1, β_1, σ_{k1}, $\sigma_{\omega 1}$, α_2, β_2, σ_{k2}, and $\sigma_{\omega 2}$ are constants.

The blending function F_1 can be calculated as

$$F_1 = \tanh\left(\arg_1^4\right) \tag{4.103}$$

with

$$\arg_1 = \min\left(\max\left(\frac{\sqrt{k}}{\beta'\omega y}, \frac{500\nu}{y^2\omega}\right), \frac{4\rho k}{CD_{k\omega}\sigma_{\omega 2}y^2}\right), \tag{4.104}$$

where y is the distance to the nearest wall, $\nu = \frac{\mu_t}{\rho}$ is the kinematic viscosity and

$$CD_{k\omega} = \max\left(2\rho\frac{1}{\sigma_{\omega 2}\omega}\frac{\partial k}{\partial x_j}\frac{\partial \omega}{\partial x_j}, 1.0 \times 10^{-10}\right). \tag{4.105}$$

4.5.2.2 The Shear Stress Transport (SST) turbulence model

Though the BSL model combines the advantages of the Wilcox $k-\omega$ and the $k-\varepsilon$ turbulence model, it still fails to properly predict the onset and amount of flow separation from smooth surfaces. The main reason is that these models do not account for the turbulent shear stress transport. Because of this, the turbulence eddy-viscosity is overpredicted. The $k-\omega$ SST model overcomes this problem by adding a limiter to the eddy-viscosity formulation:

$$\nu_t = \frac{\mu_t}{\rho} = \frac{a_1 k}{\max\left(a_1\omega, SF_2\right)}, \tag{4.106}$$

where

$$S = \sqrt{2S_{ij}S_{ij}} = \frac{1}{2}\left(\frac{\partial \overline{U_i}}{\partial x_j} + \frac{\partial \overline{U_j}}{\partial x_i}\right) \tag{4.107}$$

and

$$F_2 = \tanh\left(\arg_2^2\right) \tag{4.108}$$

with

$$\arg_2 = \max\left(\frac{2\sqrt{k}}{\beta'\omega y}, \frac{500\nu}{y^2\omega}\right). \tag{4.109}$$

Another production limiter is also used in the SST model to prevent the build-up of turbulence in the stagnation region [182], which can be written as

$$P_k = \mu_t\frac{\partial \overline{U_i}}{\partial x_j}\left(\frac{\partial \overline{U_j}}{\partial x_i}\right) \rightarrow \widetilde{P_k} = \min\left(P_k, 10 \cdot \beta'\rho k\omega\right) \tag{4.110}$$

Therefore, the complete transport equation of the SST model can be written as:

$$\frac{\partial}{\partial t}\left(\rho k\right) + \frac{\partial}{\partial x_j}\left(\rho\overline{U_j}k\right) = \frac{\partial}{\partial x_j}\left[\left(\mu + \frac{\mu_t}{\sigma_{k3}}\right)\frac{\partial k}{\partial x_j}\right] + \widetilde{P_k} - \beta'\rho k\omega + P_{kb} \tag{4.111}$$

and

$$\frac{\partial}{\partial t}\left(\rho\omega\right) + \frac{\partial}{\partial x_j}\left(\rho\overline{U}_j\omega\right) = \frac{\partial}{\partial x_j}\left[\left(\mu + \frac{\mu_t}{\sigma_{\omega 3}}\right)\frac{\partial \omega}{\partial x_j}\right] + 2\left(1 - F_1\right)\rho\frac{1}{\sigma_{\omega 2}\omega}\frac{\partial k}{\partial x_j}\frac{\partial \omega}{\partial x_j} + \alpha_3\frac{\omega}{k}\widetilde{P_k} - \beta_3\rho\omega^2 + P_{\omega b}. \tag{4.112}$$

The essential feature of this turbulence model is an accurate and robust near wall treatment, which affects multiple parameters, especially the heat transfer coefficient. Furthermore, the $k - \omega$ SST model allows the use of coarser grids with the computed wall shear-stress (see Equation (4.77)), which affects tremendously the turbulence transport and subsequently the heat transfer coefficient; the wall shear-stress varies slightly and all solutions follow the logarithmic profile on the far from the wall region [182]. Thus this turbulence model was chosen to be used on this thesis.

4.6 ANSYS Workbench

ANSYS Workbench is a commercial code platform which includes tools to perform thermal analyses, structural analyses, electromagnetic analyses, computational fluid dynamics, and design optimization (see Figure 4.9). This software suite has the tools to couple analysis modules, which can be used separately to model the different phenomena that impact a system and share its boundary conditions.

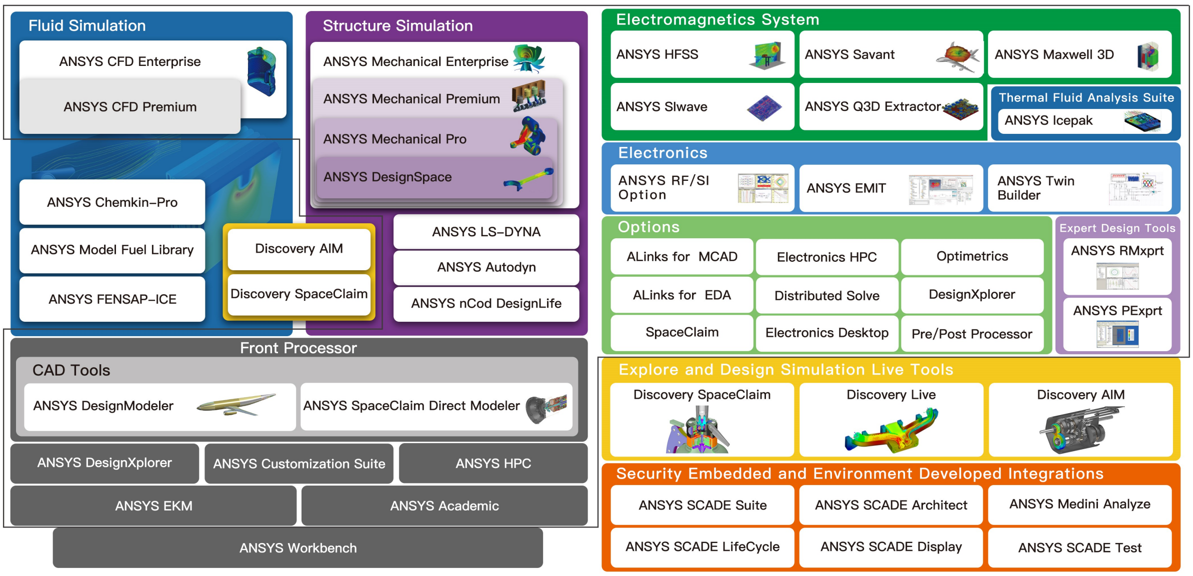

Figure 4.9: ANSYS modules.

The relevant modules of ANSYS used in this thesis are ANSYS SpaceClaim for geometry design, ANSYS Mechanical for the thermal and structural analyses, and ANSYS CFX for the CFD analyses. ANSYS Mechanical uses the formulation presented in Equation (4.60) to calculate the temperature distribution inside the domain of interest and the concept presented in Section 4.2 to perform structural analyses. As mentioned before, the CFD analyses presented this thesis were performed using the SST turbulence model presented in Section 4.5.2.2.

Following the guidelines of ITER mentioned in Section 4.4.1, a separate calculation is needed for thermal radiation in order to get a boundary condition that is only dependent on the geometry. In ANSYS, this calculation can be done with the radiosity solver, which can be found in ANSYS Mechanical APDL and ANSYS CFD (CFX or FLUENT). This radiosity solver calculates the view factors of interacting surfaces using Equation (4.44) for each element surface, and solves Equations (4.45)–(4.48) for the total interaction between surfaces. The view factor calculations presented in this thesis were calculated using Mechanical APDL for ITER PPR and ANSYS CFX for DEMO, briefly described in the following sections.

4.6.1 Radiation heat transfer calculation using APDL

In the ANSYS Mechanical user interface, although the thermal radiation heat transfer can be modelled, the function to calculate the view factors is not featured explicitly. Therefore, in order to obtain the view factors separately, they need to be defined and calculated through a script in ANSYS Mechanical ANSYS Parametric Design Language (APDL). The macro script for the APDL calculation consists of several parts, namely the constant definition, pre-processing, solution calculation, output command and saving.

In the constant definition part, the user can define the constants or parameters required for the use case, such as the multiplication scale that is only specified for each specific case. In the pre-processing part, the user defines the geometrical model, the selected components, the emissivities and the radiation direction from each components. The solution part consist of commands to calculate the view factors using the hemicube method (presented in Section 4.3.3), the resolution of the hemicube, and the space temperature for the enclosure of interest. Finally, in the last part the user defines the commands to specify the output parameters of interest and the format of the output file. The macro used for the view factor calculations used in this thesis can be found in Appendix B.

4.6.2 Radiation heat transfer calculation using ANSYS CFX

Thermal radiation in ANSYS CFX is modelled based on the Discrete Transfer Model (DTM) developed by Lockwood and Shah [183], which is based on ray-tracing and solves one dimensional equations along a multitude of individual rays [184]. These equations can be written as

$$\frac{\mathrm{dI}}{\mathrm{ds}} = \mathrm{k_a}\left(\mathrm{I_b} - \mathrm{I}\right), \tag{4.113}$$

where I is the ray intensity, $\mathrm{k_a}$ is the absorption coefficient of the medium, and $\mathrm{I_b}$ is the blackbody intensity.

In this model, the rays are started only on the boundary surfaces and are solved only along the paths between two boundary walls rather than being partially reflected at the walls and traced into extinction [183]. The equation to calculate the intensity results from the integration of the radiation transfer equation along the distance in the direction of the ray, and can be written as

$$\mathrm{I_{n+1}} = \mathrm{I_n} e^{-\mathrm{k_a}\Delta \mathrm{s}} + \mathrm{I_b}\left(1 - e^{-\mathrm{k_a}\Delta \mathrm{s}}\right). \tag{4.114}$$

The intensity balance per cell and ray is given by

$$\mathrm{I_{net}} = \mathrm{I_n} - \mathrm{I_{n+1}} = \mathrm{I_n}\left(1 - e^{-\mathrm{k_a}\Delta \mathrm{s}}\right) + \mathrm{I_b}\left(1 - e^{-\mathrm{k_a}\Delta \mathrm{s}}\right), \tag{4.115}$$

where $\mathrm{I_n}$ and $\mathrm{I_{n+1}}$ is the intensity at the cell n and n + 1 along the ray direction, and Δs is the finite difference distance between cell n and n + 1 along the ray.

The source-term of the radiation equation is the sum of all intensity changes caused by all rays passing through a cell,

$$S_{rad} = \sum_{rays}(I_{net}\Delta\Omega F), \tag{4.116}$$

where $\Delta\Omega$ is the finite difference solid angle and F is the surface area.

The initial intensity for all rays starting at the walls of the computational domain is defined as

$$I_0 = (1-\varepsilon)\sum_{rays}\left(I_{n\cdot s<0}\frac{\Delta\Omega}{\pi}\right) + \varepsilon\frac{\sigma}{\pi}T^4. \tag{4.117}$$

4.7 Mesh system

4.7.1 Mesh element type

The choice of the mesh element types in ANSYS Workbench depends on the geometry of the system (2-D or 3-D) and on the element shape function (linear or quadratic). Considering these factors, there are a total of 12 mesh element types: 4 types of 2-D mesh elements and 8 types of 3-D mesh elements (see Figure 4.10).

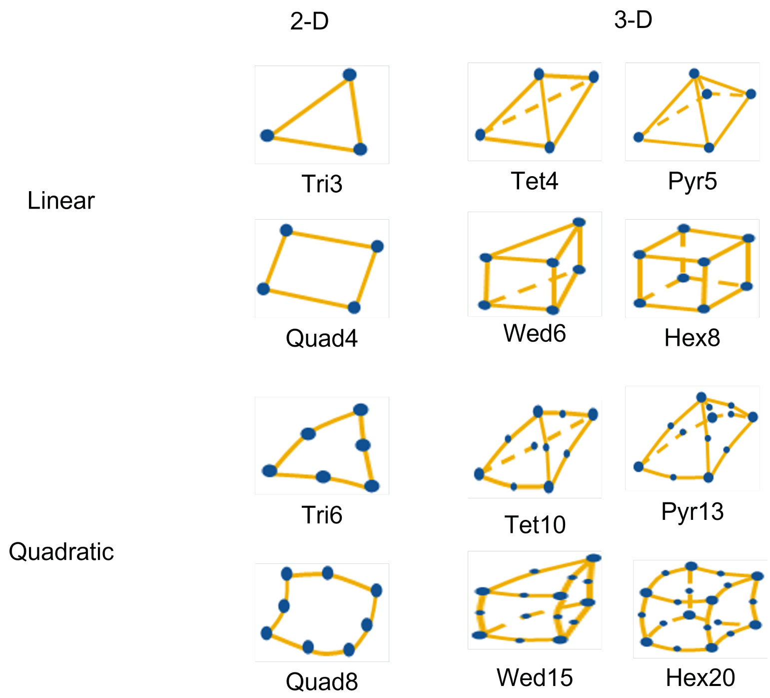

Figure 4.10: ANSYS mesh element types (adapted from [185]).

4.7.2 Mesh quality metric

According to [186], there are eight mesh quality metrics which can be used to check the quality of the applied mesh system. Among others, the most commonly used as reference are the element quality and the skewness metrics.

4.7.2.1 Element quality

The element quality metric is the ratio of the volume to the edge length of a given element, expressed by

$$\text{Quality} = \begin{cases} C\left(\text{area}/\sum(\text{EdgeLength})^2\right) & \text{for 2-D mesh elements} \\ C\left(\text{volume}/\sqrt{\left[\sum(\text{EdgeLength})^2\right]^3}\right) & \text{for 3-D mesh elements} \end{cases}, \tag{4.118}$$

where C is a constant dependent on the shape of the mesh element, presented in Table 4.6. The value of the element quality ranges between 0 and 1, where 1 indicates a perfect cube or square element and 0 indicates that the element has a zero or negative volume, which means that the bounding faces are intersecting or wrongly oriented. Low values are often caused by very sharp corners, very distorted surfaces or invalid mesh methods.

Table 4.6: Values of C for mesh quality [186].

Element	**Value of C**
Triangle	6.92820323
Quadrangle	4.00000000
Tetrahedron	124.70765802
Hexagon	41.56921938
Wedge	62.35382905
Pyramid	96.00000000

4.7.2.2 Skewness

Skewness is one of the primary quality measures for a mesh, which determines how close a face or cell is to the ideal (i.e., equilateral or equiangular) and converts this assessment into a value between 0 and 1. This value can be calculated as Equation (4.119)

$$\text{skewness} = \begin{cases} \dfrac{\text{Optimal Cell Size} - \text{Cell Size}}{\text{Optimal Cell Size}} & \text{for triangles and tetrahedra} \\ \max\left[\dfrac{\vartheta_{\mathrm{max}} - \vartheta_{\mathrm{e}}}{180 - \vartheta_{\mathrm{e}}}, \dfrac{\vartheta_{\mathrm{e}} - \vartheta_{\mathrm{min}}}{\vartheta_{\mathrm{e}}}\right] & \text{for all cell and face shapes} \end{cases} \tag{4.119}$$

where the optimal cell size is the size of an equilateral cell with the same circumradius, while ϑ_{max} and ϑ_{min} are the largest and the smallest angle in the face or cell and ϑ_{e} is the angle for an equiangular face/cell (e.g., 60 for a triangle and 90 for a square). The skewness value is then compared to the values presented in Table 4.7 to assess the quality of the mesh.

In 2D, a good mesh system should consist of good or better cells, since the presence of fair or worse cells indicates poor boundary node placement. In 3D, most cells should be good or better, but a small percentage of fair or worse cells may coexist with these [186].

Table 4.7: Mesh quality based on the skewness value [186].

Skewness value	**Cell Quality**
1	degenerate
0.9 – <1	bad (sliver)
0.75 – 0.9	poor
0.5 – 0.75	fair
0.25 – 0.5	good
>0 – 0.25	excellent
0	equilateral

4.8 Fluid-Solid Interaction (Fluid-Solid Interaction (FSI))

In geometries with active cooling systems, coupled FEM-CFD analysis with a Fluid-Solid Interface (FSI) is the optimal way to simulate all the phenomena involved, since this method can make use of the advantages of FEM and CFD and then couple the quantities at the interfaces. The disadvantage of this method is the computational time, which will be longer when compared to the FEM-only analysis or the CFD-only analysis. Therefore, high-performance computers (HPCs) may be required to perform these simulations.

There are several CFD code modules in ANSYS Workbench, among which are ANSYS CFX and ANSYS FLUENT. The differences between ANSYS CFX and ANSYS FLUENT can be seen in Table 4.8. While ANSYS FLUENT has the option to use GPU acceleration, its formulation uses the cell-centered FVM, which means that there will be another approximation when the quantities are coupled with the solid counterpart in ANSYS Mechanical. ANSYS CFX, on the other hand, can easily couple the quantities with ANSYS Mechanical, as long as the mesh at the interface share the same nodes. As such, ANSYS CFX was used in this work to perform simulations for DEMO, in which the reflectometry system is cooled by an active cooling system.

Table 4.8: Differences between ANSYS CFX and ANSYS FLUENT.

Aspect	ANSYS CFX	ANSYS FLUENT
Pure 2-D solver	not available	available
Formulation	node-based FVM	cell-centered FVM
Polyhedral and cut-cell mesh	not-possible	possible
Solver type	Coupled	Segregated
	Pressure-based	Pressure-based or Density-based
Numerical method	Fully Implicit	Explicit and Implicit option
Shape function	evaluate gradients	staggered grid
Flux balance	accounted	not accounted
Programming language	FORTRAN	C
Modification	almost locked	open to modify using User-defined function (UDF)
GPU acceleration	not available	available

Part II

ITER Plasma Position Reflectometry (PPR)

Chapter 5

Thermal analysis of the ITER PPR system [3]

5.1 Design of the Reflectometry system for ITER

The ITER reflectometry diagnostic, also known as PPR system, was designed as a real-time supplement to the magnetic diagnostics, which are vulnerable to errors due to drifts, especially during very long (>1000 s) pulse operation. The PPR system aimed to measure the position of a specified cutoff layer using the ordinary mode (O-mode) with FM-CW (see Section 2.1), operating in the frequency range 15 GHz–90 GHz, which corresponds to the density range $0.03 \times 10^{20}\,\mathrm{m}^{-3}$–$1.01 \times 10^{20}\,\mathrm{m}^{-3}$ [83].

5.1.1 System description

The Plasma Position Reflectometry (PPR) system consisted of four reflectometers that would be used in ITER to measure the plasma edge density profile at four locations [187], known as gaps 3, 4, 5, and 6, shown in Figure 5.1. These reflectometers were distributed poloidally and toroidally in the vacuum vessel, [49,50,188] between blanket modules, and would have antennas and part of the transmission lines directly exposed to the plasma in gaps 4 and 6, illustrated in Figure 5.2. These components would be subjected to significant nuclear [49, 50, 188, 189], inertial, electromagnetic, pressure, thermal-hydraulic and pretension loads [190] which could compromise their integrity during the lifetime of ITER.

The system of gap 4 would have the antennas installed in the LFS of sector 9 between the blanket modules (BMs) of rows #11 and #12 and attached to a 90° bend support. The support itself would be bolted to the standard VV attachments, the so-called "bosses", which are welded to the vessel wall [191]. Straight and curved sections of rectangular WG would be used to route the microwaves between the 90° bends and one of the bottom feed-outs of upper port 1.

The system of gap 6 would have its antennas installed in the HFS of sector 7 between the BMs of rows #3 and #4. As in gap 4, the antennas of gap 6 would be attached to the support of the 90° bends, which in turn would be attached to the VV. The WGs of gap 6 would routed from the antennas to one of the upper feed-outs of upper port 14. These WGs were planned to be located behind the BMs and to pass through the intersection between the BMs of rows #4 and #5, as shown in Figure 5.4. Previous studies [50] had determined that these were the locations where the WGs would be subjected to the highest nuclear loads.

[3] After the work presented in this chapter was performed, ITER decided to descope the PPR system. Nevertheless, lessons learned on the design activities of the PPR system will be applied to the DEMO multi-reflectometer system design.

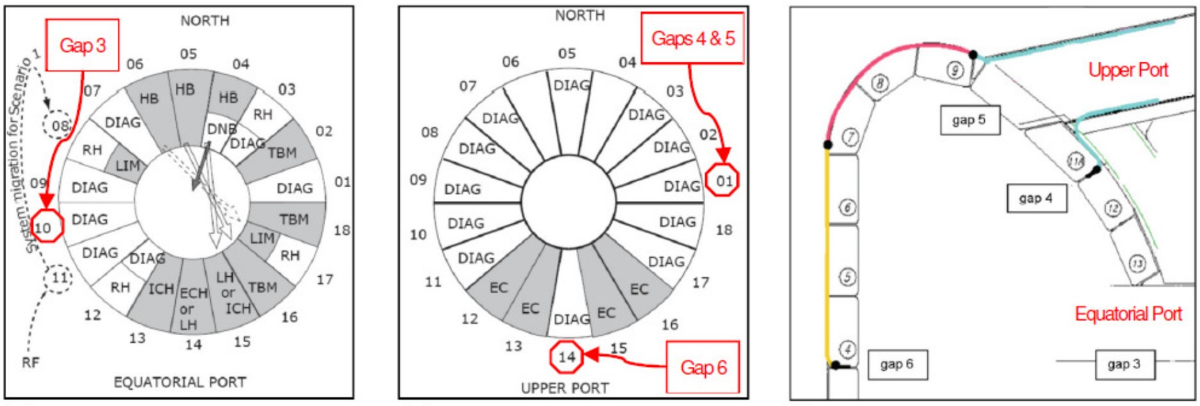

(a) (b) (c)

Figure 5.1: Location of gaps 3 – 6.(a) Equatorial port. (b) Upper ports. (c) Waveguide routing in the vacuum vessel, presented in different line colours for each WG path (obtained from [83]).

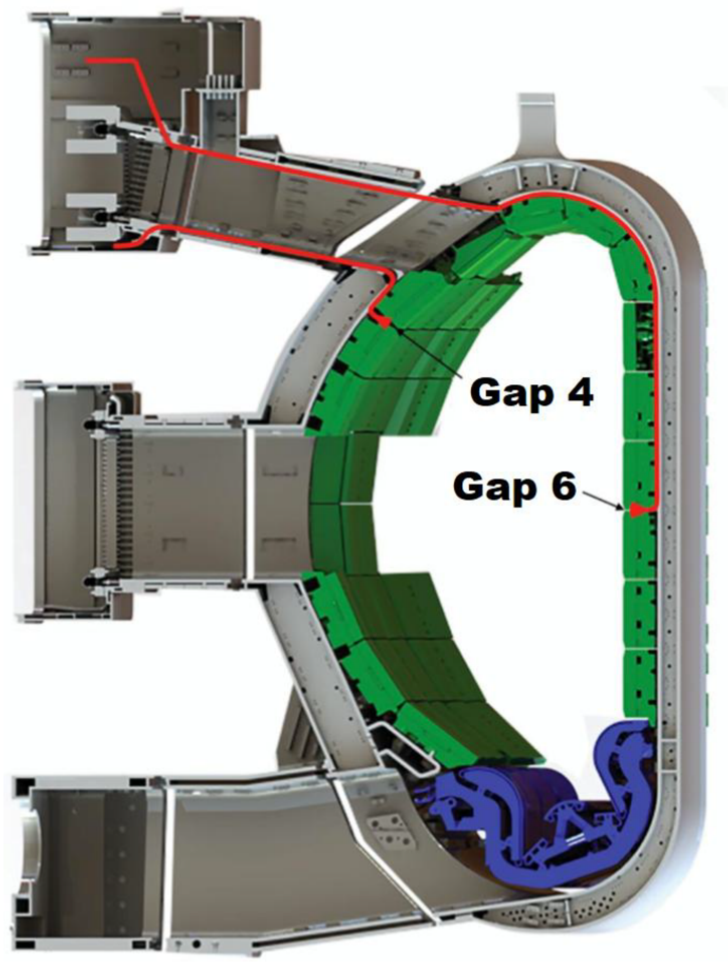

Figure 5.2: Location of the PPR in-vessel components of gaps 4 and 6.

In the developed design, all the PPR components that would be installed in-vessel were made of ITER-grade stainless steel (SS) 316L(N)-IG, which has the maximum allowable operating temperature of 450 °C under neutron irradiation [192]. The temperature-dependent thermal and mechanical properties of this material were extracted from [192] (pages 65–98). In order to reduce ohmic losses, the WG components had their inner surfaces coated with a very thin (15 µm–25 µm) layer of copper which was not modelled in the thermal analysis, since it has negligible impact on the calculated temperatures, due to its thickness[4].

The antennas as well as the 90° bends and corresponding supports were Quality Class 1 (QC1) non-SIC (Safety Important Class) components.

5.1.2 Approach description

In the following part, thermal analyses of the ITER PPR system in-vessel components are performed, with the objective of understanding how the system would perform under the expected ITER operating conditions, in order to optimize the design of the system to comply with the temperature limits. The PPR system design heavily depended on the existence of apertures between the BMs of the ITER reactor, which uses multiple BMs to shield the VV. In these gaps, the PPR components would be subjected to high radiation doses, which would contribute to increase the thermal loads in the system and might cause irradiation-induced changes in the material properties, as well as excessive temperatures in some of the components, compromising their structural integrity [191]. Thermal analyses were thus required to identify possible risks requiring mitigation actions during the subsequent engineering design phases, and to evaluate the need for specific prototyping and testing of these in-vessel components. As the PPR system was planned to operate without active cooling, the study presented in this chapter was a fundamental step in the development of the system.

5.2 Workflow for thermal analysis

The thermal analyses described for the ITER PPR system were carried out using the commercial engineering analysis software ANSYS (Workbench, APDL, and SpaceClaim) and following the workflow presented in Figure 5.3, which includes the following activities [191, 193]:

- Extract from the ITER ENOVIA database [194, 195] the most up-to-date CAD models of the PPR in-vessel components, using CATIA V5 [196].
- Perform geometrical simplifications of the PPR in-vessel components using ANSYS SpaceClaim [197]–these consist of eliminating screws and small faces, of splitting edges and of removing interferences.
- Perform geometrical simplifications of the surrounding blanket modules and transform them into surfaces that follow the topology of the modules.
- Model the plasma as a surface with the shape of the gap between the blanket modules.
- Using ANSYS Mechanical APDL [197], compute the view factors from the plasma and use them to estimate the heat flux hitting the PPR front-end components.
- Using ANSYS Mechanical [197], perform the steady-state and transient thermal analyses, taking into account the heat loads applicable to the components.

[4] The temperature gradient of the copper layer surfaces is negligible, i.e., the temperature of the top surface of the copper layer is identical to that of the bottom surface and to that of the stainless steel. Hence, not considering the copper-coating layer will have a negligible impact on the results of the thermal analysis.

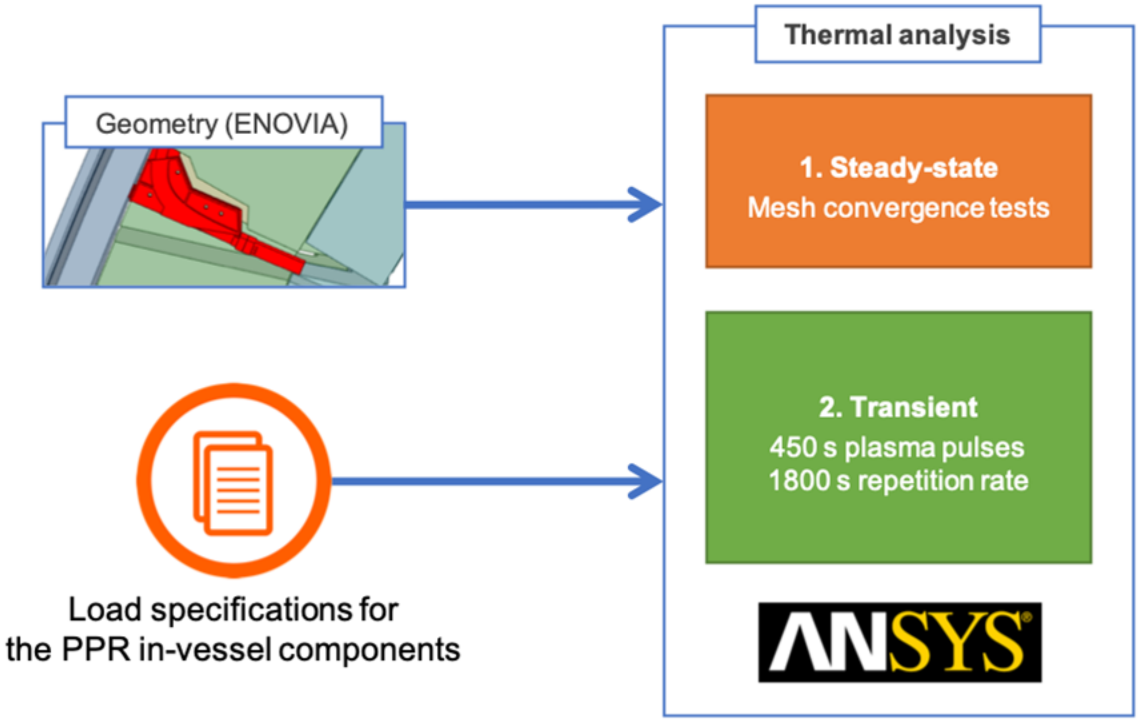

Figure 5.3: Workflow for the thermal analysis.

5.3 PPR Waveguide section

It had been shown in a previous study [50] that the WGs would be subjected to higher nuclear loads at several locations. One of these locations was at the intersection between the BMs of rows #4 and #5, as illustrated in Figure 5.4.

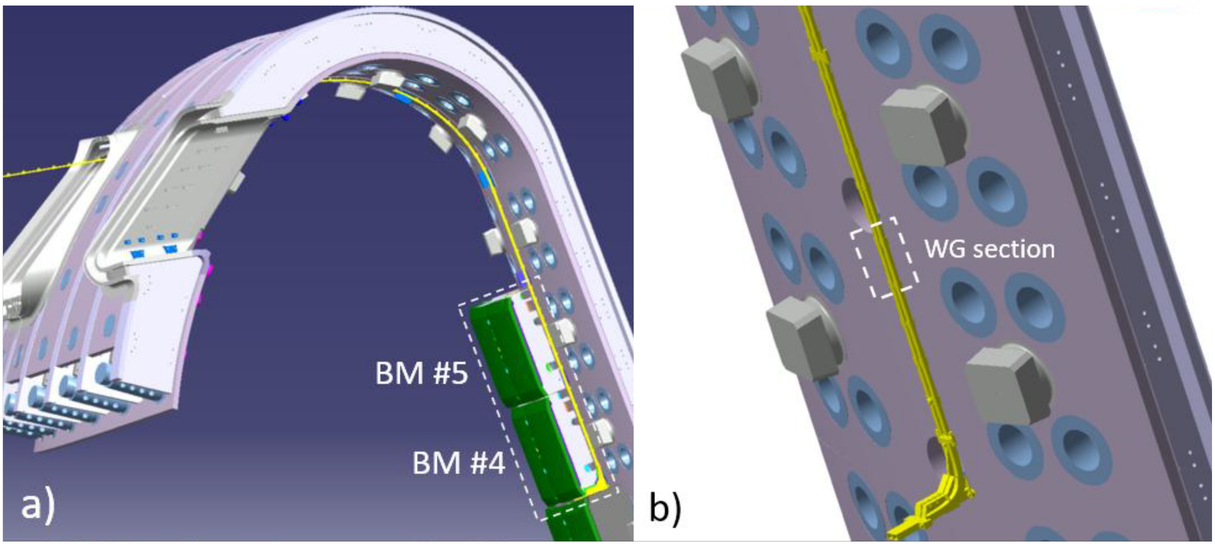

Figure 5.4: a) CAD model of the PPR system (highlighted in yellow) and neighboring structures. b) Detail of the WG section of interest (the BMs are omitted for clarity).

5.3.1 Geometry

In order to focus on the geometry of interest, a system-specific model containing the geometry of interest and the surrounding parts was prepared. This system-specific model, shown in Figure 5.5, consists of a section of VV and the WG section with its support and connection to the VV, the so called *bosses*.

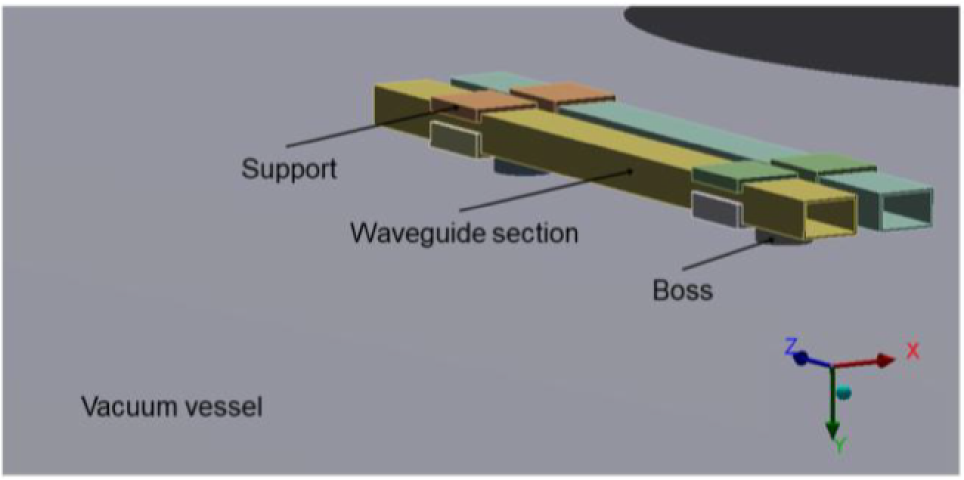

Figure 5.5: Finite element model of a section of the PPR waveguides.

5.3.2 Plasma thermal radiation

The plasma thermal radiation was calculated using the method specified in Section 4.6.1, according to [190], which resulted in a view factor map that was then multiplied by the constant surface heat flux of 350 kW/m^2. The results of this calculation were then imported as heat flux to ANSYS Mechanical, as shown in Figure 5.6. As expected, the highest heat flux values were obtained at the intersection between the BMs, dropping to zero in the parts of the WG section not exposed to the plasma.

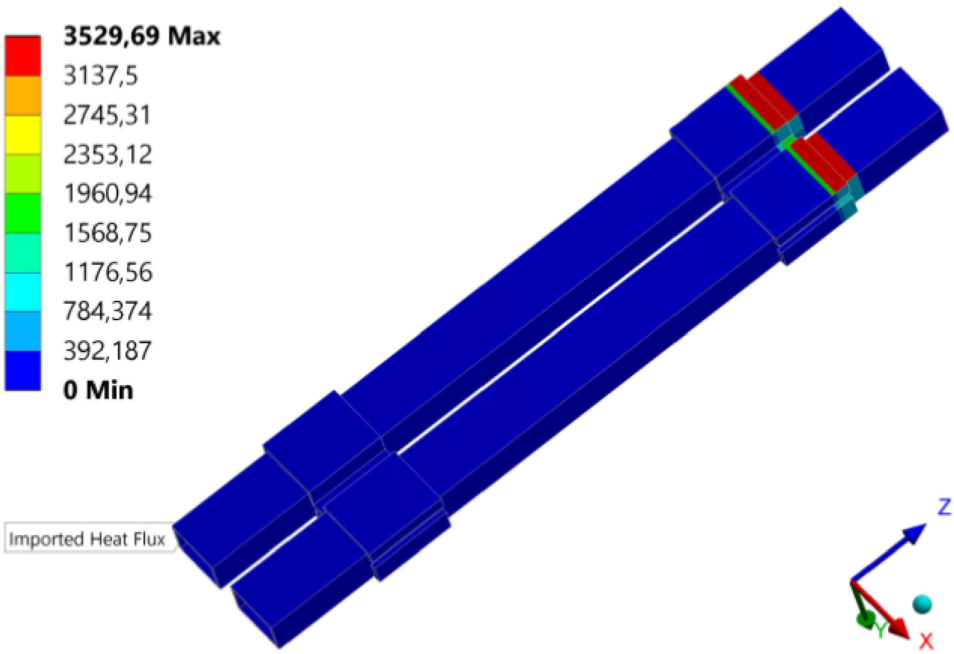

Figure 5.6: Calculated plasma thermal radiation contribution on the waveguide section (W/m^2).

5.3.3 Nuclear heat deposition

As mentioned before, the nuclear heat deposition for the waveguide section had already been calculated in a previous work [50] performed with the Monte Carlo simulation program MCNP6 [198], using a standard ITER neutronics model -–Reference Model C-Model v2.1— with the most up-to-date design information of the ITER machine. The model of the PPR components was created from the CAD design of the system, with some simplifications to avoid conversion errors, such as the removal of spline surfaces, fillets and screws. This model was then converted to the MCNP format using MCAM [144] and implemented in the ITER Reference Model.

The nuclear heat loads obtained in each cell of the waveguides are presented in Figure 5.7, which also shows the segmentation of the geometry assumed in the MCNP model. Longer cells, located behind the blanket modules, alternate with shorter cells that lie at the gaps between blanket modules, since the latter would be directly exposed to the plasma and are therefore the best candidates for "hot spots" in the waveguide structure.

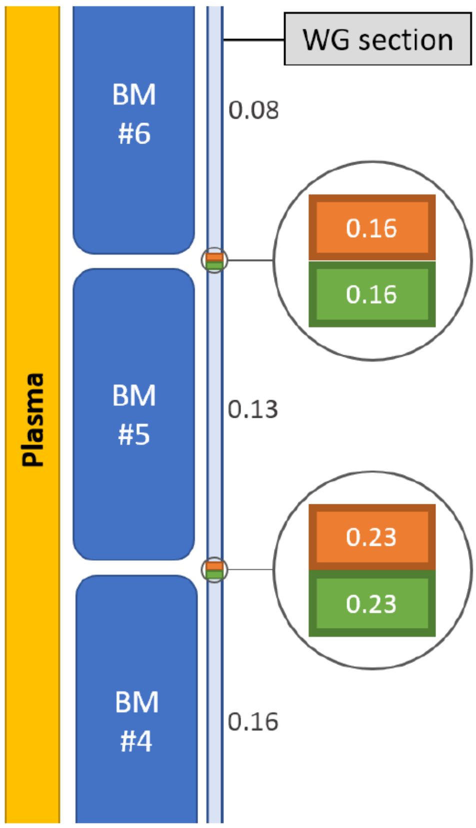

Figure 5.7: Nuclear heat loads (W/cm^3) in the PPR waveguide section [50].

Maximum nuclear heat load values of 0.23 W/cm^3 were obtained in the gap between the blanket modules (BM) of rows #4 and #5, while behind the blanket modules this value decreases to 0.16 W/cm^3 (behind the blanket module of row #4) and 0.13 W/cm^3 (behind the blanket module of row #5). The most conservative value (0.23 W/cm^3) was chosen for the thermal analysis.

5.3.4 Other boundary conditions

An initial temperature of 100 °C was applied to all simulated components assuming that temperature equilibrium between the VV and the components has been reached before operation. A constant temperature boundary condition of 300 °C was applied to the first wall surfaces and a constant temperature boundary condition of 110 °C was applied to the blanket shielding module surfaces. A transient thermal map provided by IO for sector #1 was rotated by 240° and applied to the VV inner shell of sector #7, as shown in Figure 5.8. A surface-to-surface radiation model was applied to all components with constant emissivity value of 0.5, to simulate a gray-body radiation of the material.

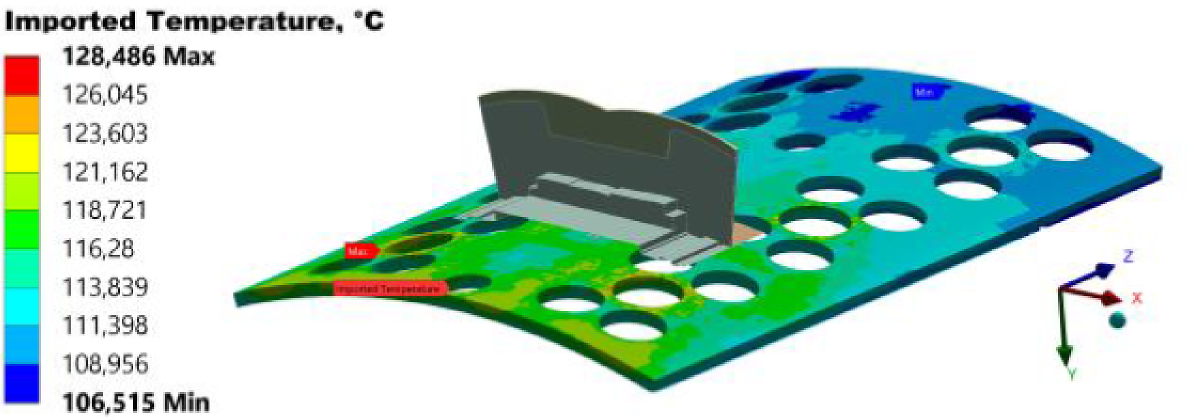

Figure 5.8: Transient temperature map applied to the VV inner shell.

5.3.5 Mesh convergence test

In order to determine the element size of the mesh, a convergence analysis was performed for the waveguide section. This was done using the model previously described and the Hex Dominant method [186]. The results are presented in Figure 5.9 and details of the mesh system selected to apply it can be found in Table 5.1.

Table 5.1: Mesh system description.

Part	**Meshing method**	**Body size** (mm)
Plasma	Multizone	10
Blanket shielding modules	Quadrilateral Dominant	10
First Walls	Quadrilateral Dominant	5
Waveguide section	Hex Dominant	1
Supports	Hex Dominant	2
Bosses	Multizone	1
Vacuum Vessel	Hex Dominant	10
Pockets	Multizone	10

From Figure 5.9, it is possible to verify that the results of the maximum temperature are sensitive to the mesh size and start to converge for element sizes smaller than 8 mm. Since the difference between the maximum temperature values obtained with an element size of 2 and 1 mm is small, it was decided to use an element size of 2 mm throughout the analysis. Details of this mesh system are presented in Figure 5.10.

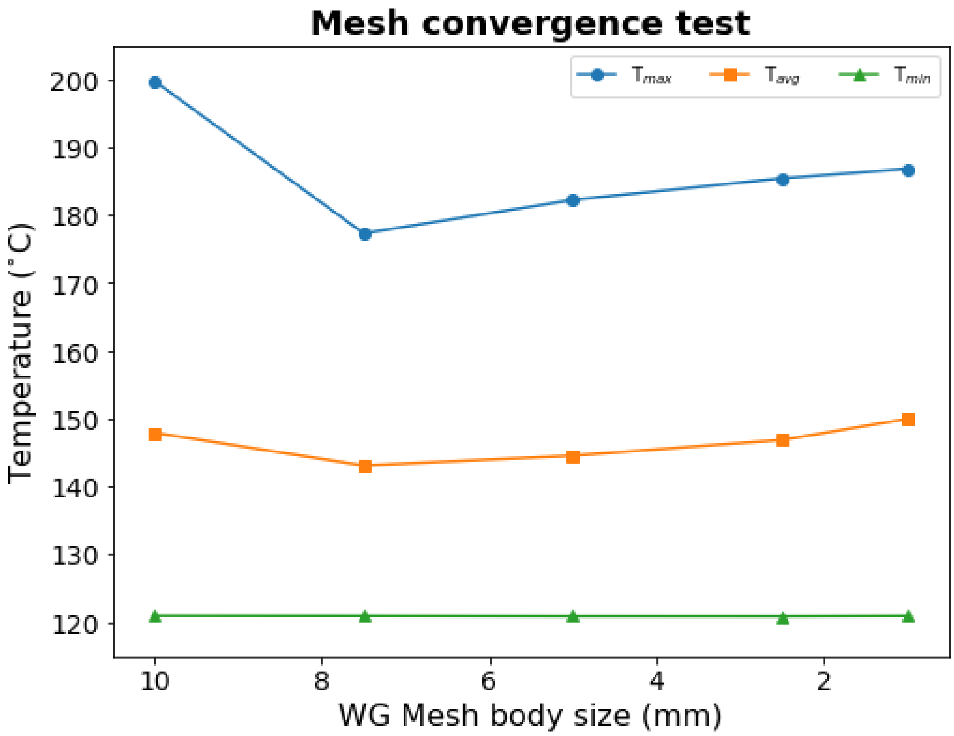

Figure 5.9: Mesh convergence test results for the PPR waveguide section.

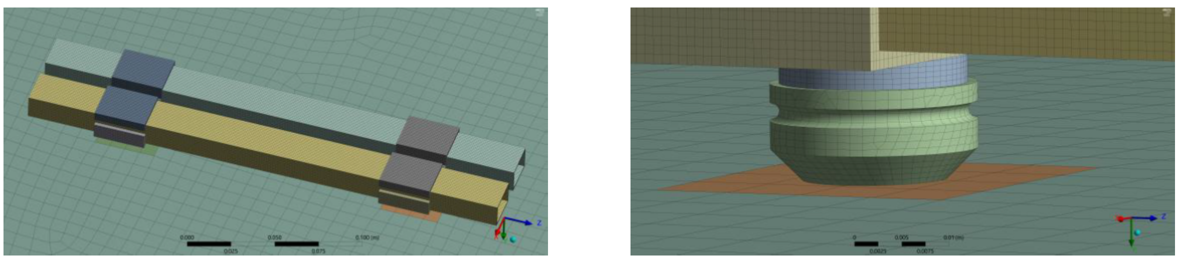

(a) (b)

Figure 5.10: Mesh details of the (a) waveguides and supports; (b) simplified model of the bosses.

5.3.6 Steady-state thermal analysis

Considering the absence of active cooling system dedicated to the WGs of the PPR system and the vacuum condition inside the ITER tokamak, only conduction and radiation heat transfer were considered for this work.

The results presented in Figure 5.11 reveal that the maximum temperature in the waveguides and supports is 187 °C, which is well below the maximum allowable temperature for stainless steel 316L(N)-IG under neutron irradiation. The minimum temperature is 120 °C, located at the bottom surfaces of the boss, which are well protected from the plasma and have a direct connection with the VV. This temperature is limited by the VV, which acts as the ultimate heat sink of this case.

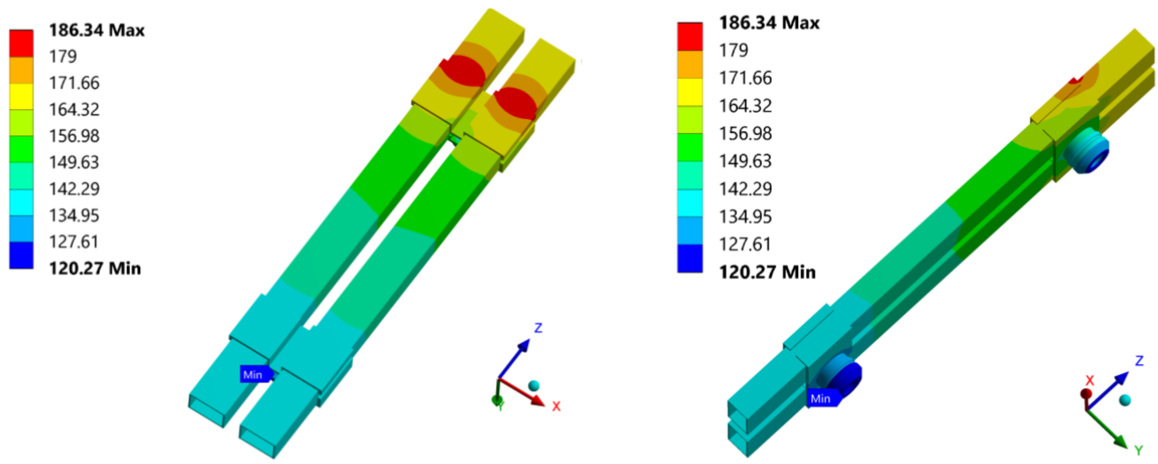

Figure 5.11: Temperature distribution (°C) in the PPR waveguide section.

5.4 PPR Front-end components

5.4.1 Reference Models

The CAD models of the PPR front-ends of gaps 4 and 6 used in the analyses are based on the reference models extracted from the ITER ENOVIA database – the ENOVIA trees of the PPR in-vessel components of gaps 4 and 6 are shown in Figure 5.12.

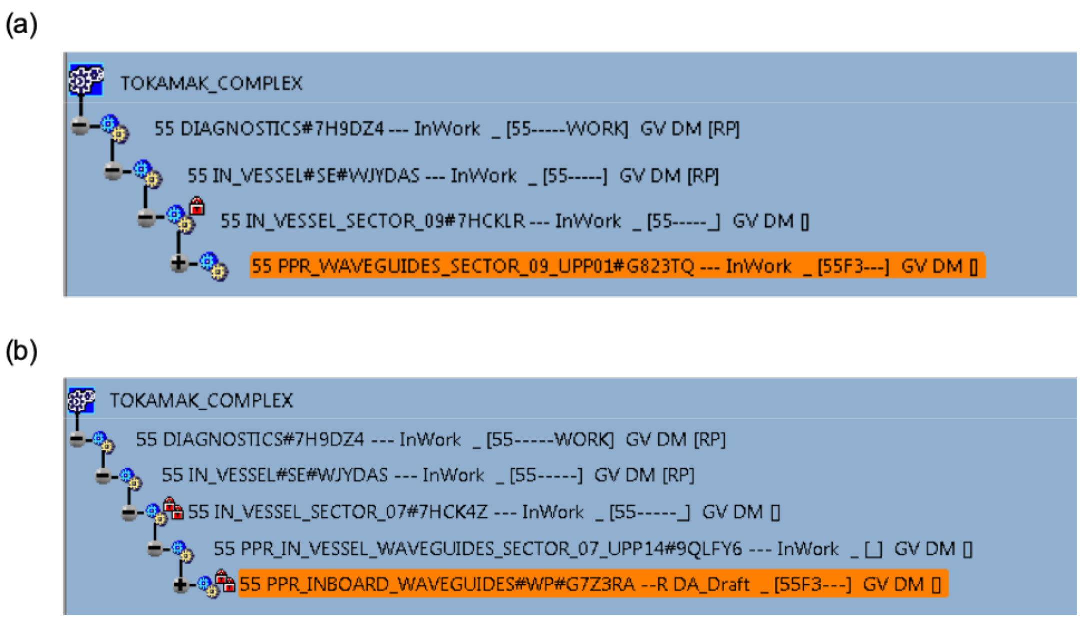

Figure 5.12: ENOVIA trees of the in-vessel components of (a) gap 4 and (b) gap 6.

As mentioned in Section 5.2, the extracted CAD models were simplified through the removal of screws and holes, making them more suitable for the thermal FEM and Finite Element Analysis (FEA) and increasing their efficiency. The simplified models were imported in ANSYS to create the FEM and imported into the thermal FEA to estimate the thermal quantities in the components. Figure 5.13 illustrates this workflow.

Figure 5.13: Conversion steps from the ENOVIA CAD models to the ANSYS thermal FEA.

5.4.2 Nuclear Heat Loads

The nuclear heat loads for the PPR antennas and 90° bend supports in gaps 4 and 6 are specified in [190] and reproduced here for convenience (see Figure 5.14). These loads where applied by dividing the models into separate cells[5], as shown in Figure 5.14 in the case of the front-end components of gap 6.

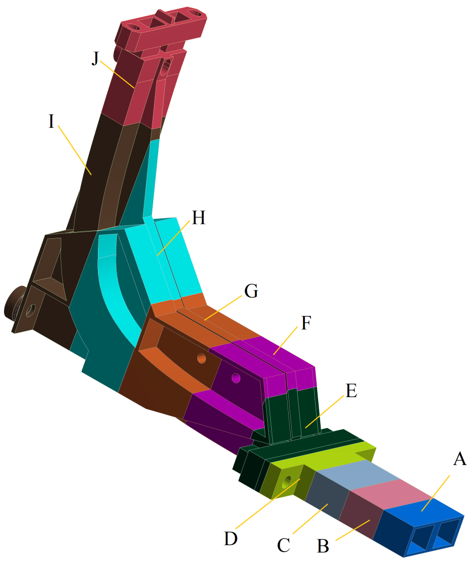

Section	Nuclear Heat Load (W/cm^3)	
	Gap 4 [49]	Gap 6 [50]
A	3.7	2.9
B	3.1	2.3
C	2.4	2.0
D	2.0	1.7
E	2.6	1.5
F	0.9	1.2
G	0.5	0.9
G	0.3	0.6
I	0.2	0.4
J	0.1	0.2

Figure 5.14: Nuclear loads specified for gaps 4 and 6 and their application to the front–end of gap 6.

5.4.3 Plasma Thermal Radiation

According to [190], in the regions of the first-wall apertures of the PPR gaps, between BMs #11 and #2 for gap 4 and between BMs #3 and #4 for gap 6, the plasma radiation results in a constant surface heat flux of 350 kW/m^2.

[5] Although there are some differences between the current design of the antennas and 90° bend supports of gaps 4 and 6 and the designs used for the nuclear analyses, these differences are not enough to impair the applicability of the estimated nuclear heat loads.

The specified heat flux needs to be scaled by the view factors from the plasma. These view factors and corresponding heat fluxes in the PPR front-end components were estimated following eq. (4.46), using the ANSYS Mechanical APDL macro shown in Appendix B.

The obtained heat fluxes are presented in Figure 5.15. As expected, the maximum values are obtained at the tip of the antennas: 64 kW/m^2 for gap 4 and 39 kW/m^2 for gap 6. The lowest values are obtained behind the blanket modules and in the inner parts of the support, i.e. in the surfaces that are shielded from the plasma. The thermal fluxes experienced by the antennas are larger on the sides when compared to the top, due to the shape of the gaps (the BMs shields the top surfaces as shown in top left corner of Figure 5.3).

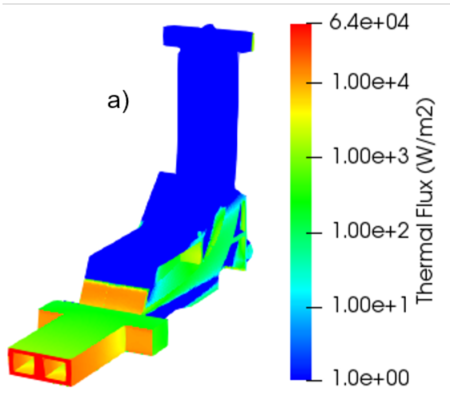

Figure 5.15: Plasma heat flux in the PPR antennas and support: a) gap 4 system. b) gap 6 system.

5.4.4 Temperature Distribution in the Vacuum Vessel

The operation temperature of the VV was obtained from a transient thermal map of the inner wall of sector #1 provided by the IO. This map was applied directly in the thermal analyses of the system of gap 4, which is located in the same sector. For gap 6 (sector #7), the map was rotated by 240° in the toroidal direction [191]. The temperature distribution map in the region of the PPR front-end of gap 6 can be seen in Figure 5.16-—the locations of the three attachments (bosses) between the 90° bend support and the VV are also shown.

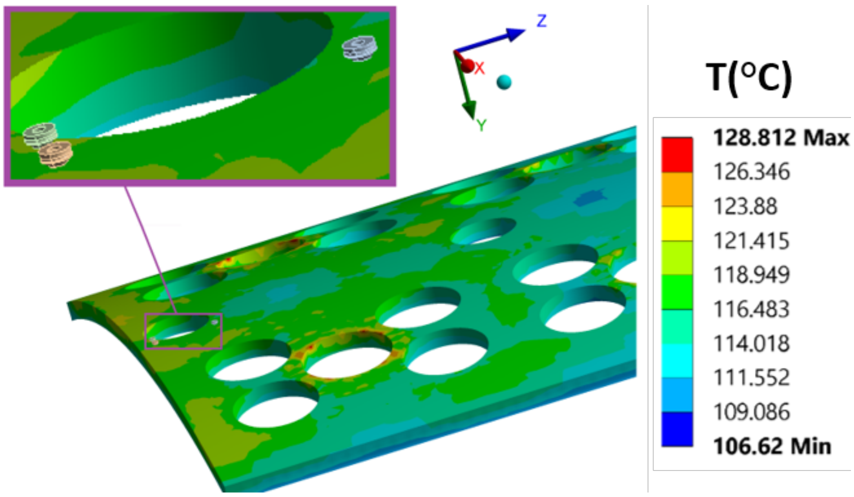

Figure 5.16: Temperature distribution in the VV and position of the attachment bosses in gap 6.

5.4.5 Mesh Quality assessment

The shared topology function was applied in order to have the exact same nodes in the interface between separate cells. This must be done to accommodate the mesh connections (similar to patch-conforming method in tetrahedral mesh). The details of the mesh system, applied to both systems, are shown in Table 5.2.

Table 5.2: Mesh configuration.

Part	**Meshing method**	**Body size** (mm)
Plasma	Multizone	20
Blanket shielding modules	Quadrilateral Dominant	10
First Walls	Quadrilateral Dominant	10
Antenna and Supports	Hex Dominant	4
Bosses	Multizone	1
Vacuum Vessel	Hex Dominant	20

The first step before running the whole set of analyses was to identify a suitable mesh. This was done using the model of the PPR in-vessel antennas described in Section 5.2 and controlling the element size of the antenna and support bodies. The Hex Dominant [186] method was used for meshing. The average skewness of the mesh systems was 0.39 for the system of gap 4 and 0.42 for the system of gap 6.

The results of the mesh convergence tests are listed in Table 5.3, where it can be observed that the obtained temperatures are consistent for different mesh sizes.

Table 5.3: Mesh convergence result.

Body size (mm)		**8.6**	**5.0**	**4.5**	**3.5**	**2.8**
$\mathbf{T_{max}}$(°C)	**gap 4**	739.56	739.49	739.40	739.60	739.59
	gap 6	672.40	672.71	672.74	672.86	672.95

Although larger element sizes might have been chosen, a general element size of 5 mm was used throughout the analysis. This choice makes it easier to export the results for the structural analyses or even for prototype testing.

Figure 5.17 and Figure 5.18 show the element quality of the FEM of gaps 4 and 6 for a mesh with an element size of 5 mm-—as can be observed, the majority of the elements are of the Hex20 type, described in Section 4.7.1.

The simplified CAD model and mesh of gap 6 is shown in Figure 5.19. A model with similar simplifications was used for gap 4.

5.4.6 Steady-state Thermal Analysis

The steady-state thermal analysis of the PPR front-end components in gap 4 yielded a very high operation temperature (739 °C), well above the temperature limit of 450 °C for SS 316L(N)-IG under neutron irradiation, as shown in Figure 5.20. Furthermore, the aperture in front of the antenna of gap 4 is toroidally

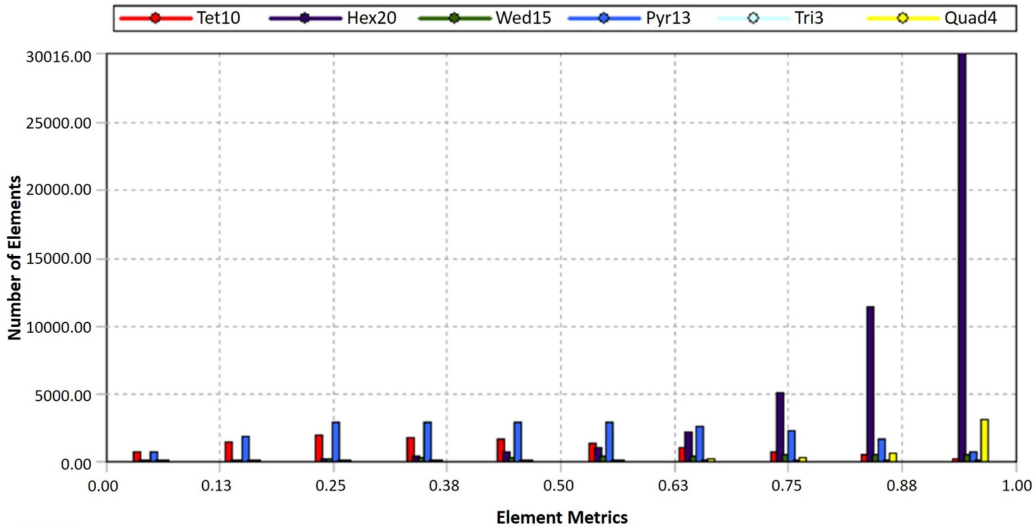

Figure 5.17: Element quality of gap 4.

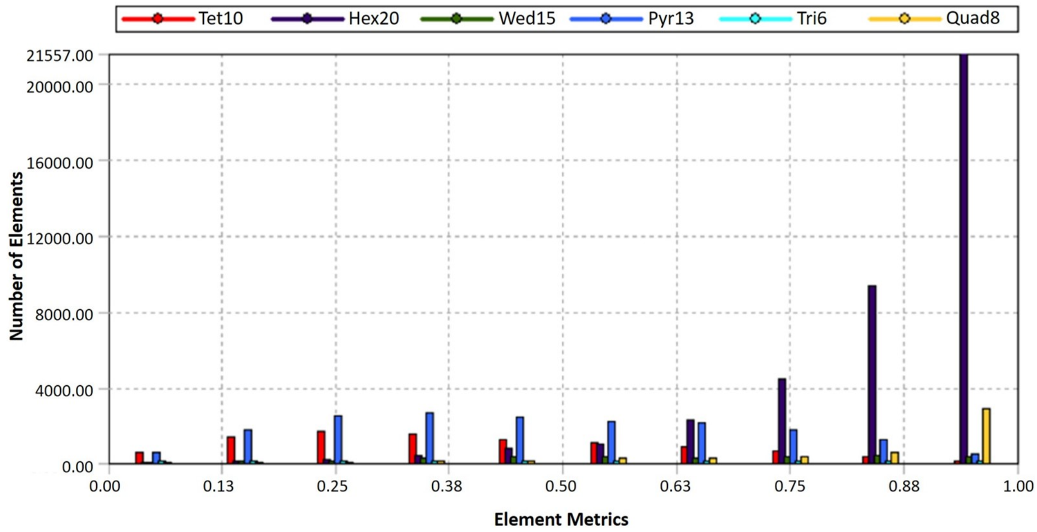

Figure 5.18: Element quality of gap 6.

asymmetric, which makes the temperature distribution of the PPR system also asymmetric in this direction. The minimum temperature was obtained not in the contact with the VV, which acts as the heat sink, but in the flange of the waveguide, which is protected by the shield block of the upper blanket.

Concerning gap 6, the results of the steady-state thermal analysis presented in Figure 5.21 show that the operating temperatures of the PPR front-end components are also well above the allowable temperature limit of 450 °C, not only in the antenna, which reaches a peak temperature of 673 °C, but also in part of the support. Since the aperture of gap 6 is smaller than that of gap 4, the obtained temperatures are also smaller (∼66 °C), as expected.

5.4.7 Transient Thermal Analysis

Since ITER will operate in a pulsed regime, the operating temperatures obtained from the steady-state thermal analyses can be regarded as very conservative. Therefore, a transient thermal analysis was conducted for both gaps in order to get a more realistic estimation of the operation temperatures.

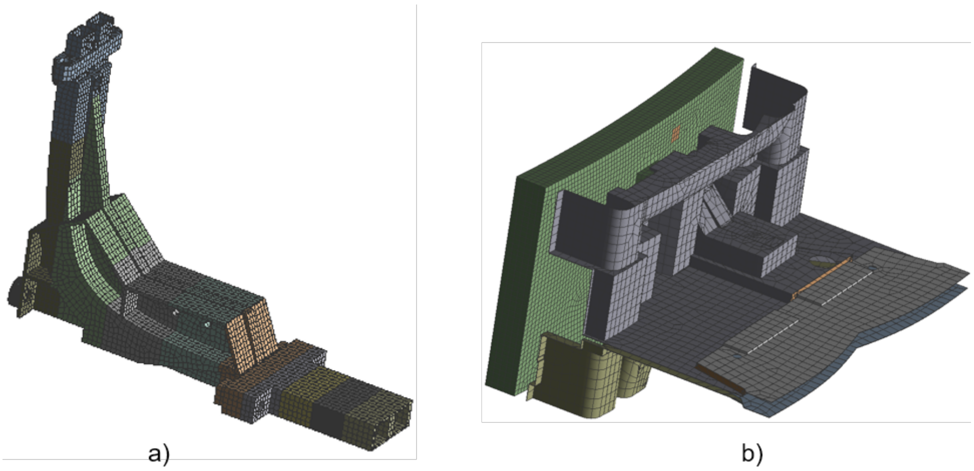

Figure 5.19: Simplified CAD model and mesh for the PPR front-end of gap 6: a) antenna and 90° bend support and b) surrounding blanket modules and VV.

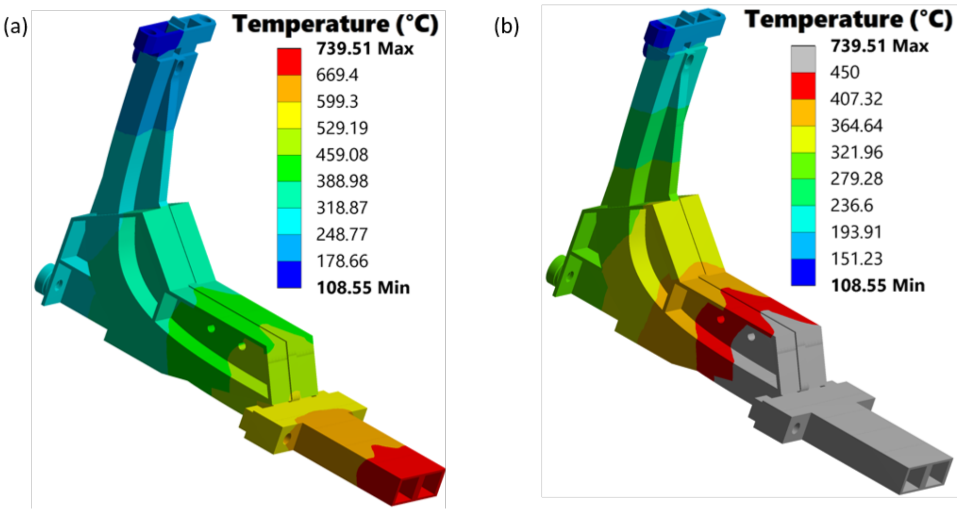

Figure 5.20: Temperature distribution in the PPR front-end components of gap 4 from the steady-state thermal analysis: (a) normal scale and (b) scale with temperature limit of 450 °C.

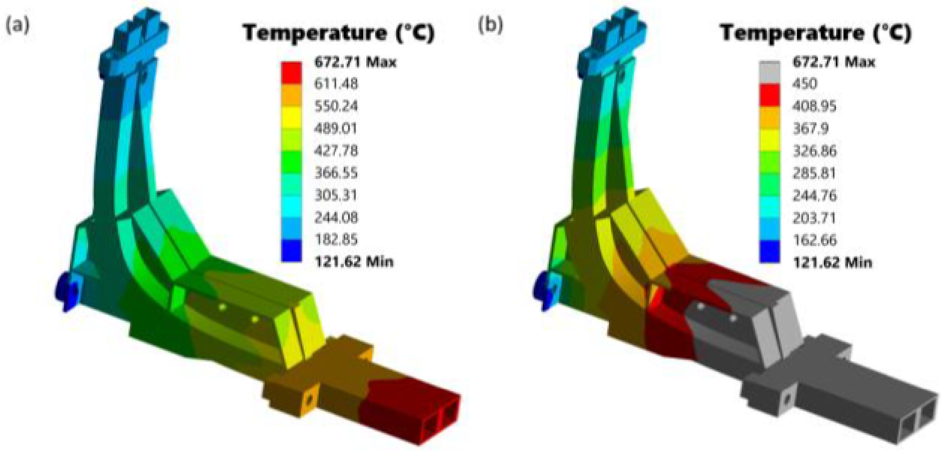

Figure 5.21: Temperature distribution in the PPR front-end components of gap 6 from the steady-state thermal analysis: (a) normal scale and (b) scale with temperature limit of 450 °C.

Figure 5.22 depicts the operation temperatures from the transient thermal analysis reached by the PPR front-end components of gap 4 after 5 ITER pulses. Though the operation temperature of the antenna is reduced by applying pulsed Heat Fluxes (HF) and Nuclear Heat loads (NH), it still reaches a maximum of 675 °C, much higher than the material limit of 450 °C. The support, on the other hand, is completely below 450 °C with the exception of the flange.

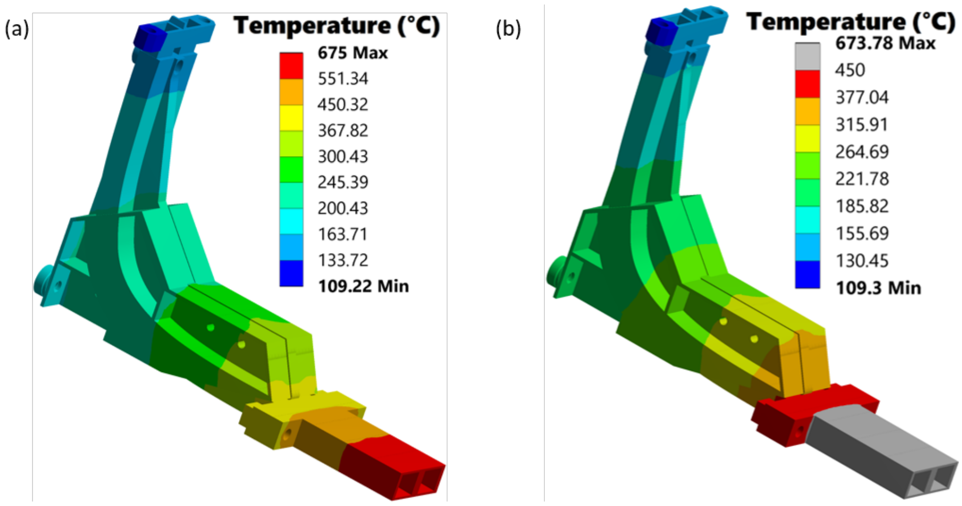

Figure 5.22: Temperature distribution in the PPR front-end components of gap 4 from the transient thermal analysis: (a) normal scale and (b) scale with temperature limit of 450 °C.

The evolution of the maximum temperature in the PPR front-end components of gap 4 during the 5 pulses is shown in Figure 5.23 and Figure 5.24, where it can be observed that it converges after 3 pulses, meaning that the selected number of pulses (5) is adequate to capture the maximum temperature of the front-end components. The results presented in Figure 5.23 also show that the contribution of the thermal flux is comparable to the contribution of the nuclear heat loads at the tip of the antenna, whereas in the support the nuclear loads are dominant (Figure 5.24).

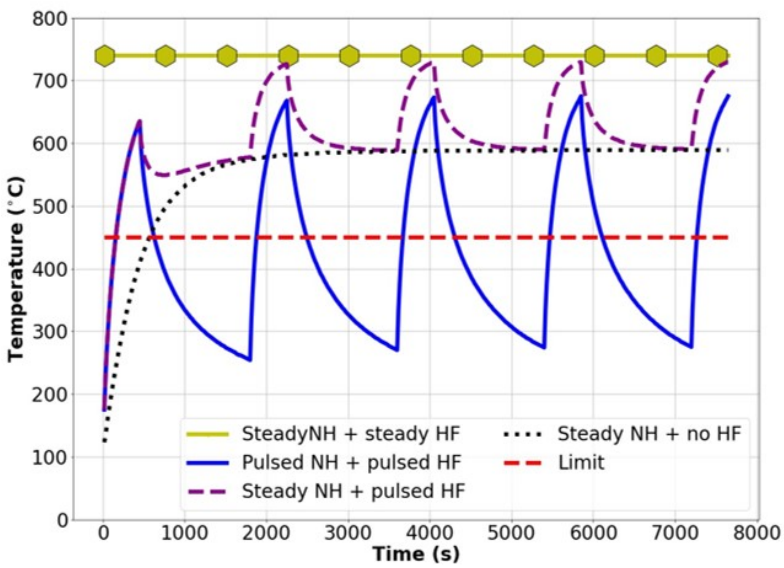

Figure 5.23: Evolution of the maximum temperature reached in the antennas of gap 4 during 5 ITER pulses.

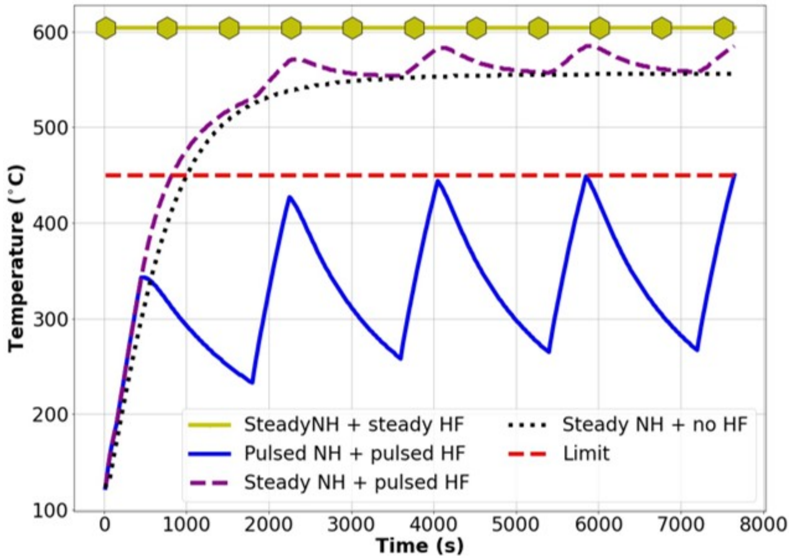

Figure 5.24: Evolution of the maximum temperature reached in the supports of gap 4 during 5 ITER pulses.

Concerning gap 6, the operation temperatures of the antenna are also reduced by applying pulsed thermal fluxes and nuclear heat loads, as shown in Figure 5.25. However, as well as in gap 4, the temperatures in the antenna are still well above the material limit. Though the operation temperature of the antenna is above the temperature limit, the maximum temperature of the support is below 450 °C.

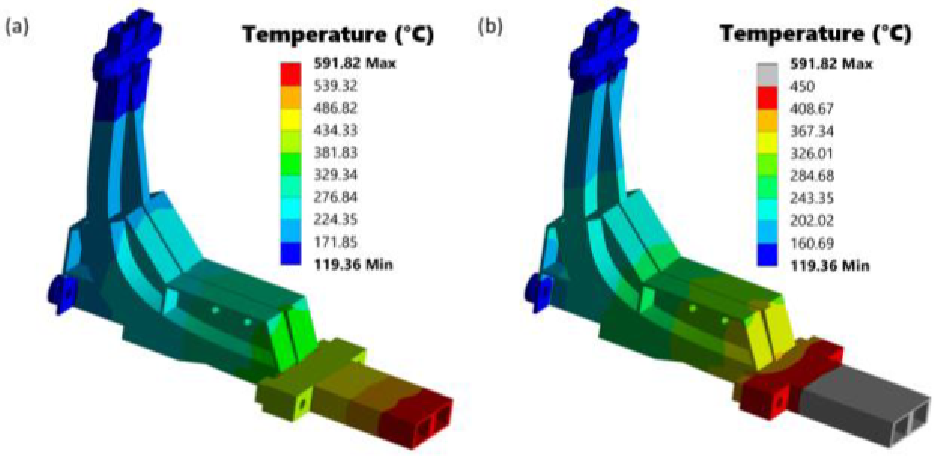

Figure 5.25: Temperature distribution in the PPR front-end components of gap 6 from the transient thermal analysis: (a) normal scale and (b) scale with temperature limit of 450 °C.

Figure 5.26 and Figure 5.27 illustrate the evolution of the maximum temperature during the 5 pulses in the antennas and supports of gap 6, respectively. As in gap 4, the peak temperature converges to 592 °C after 3 pulses. Moreover, the contribution of the nuclear heat loads can be observed to dominate the whole process, whereas the contribution of the thermal fluxes from the plasma becomes less important for components closer to the VV.

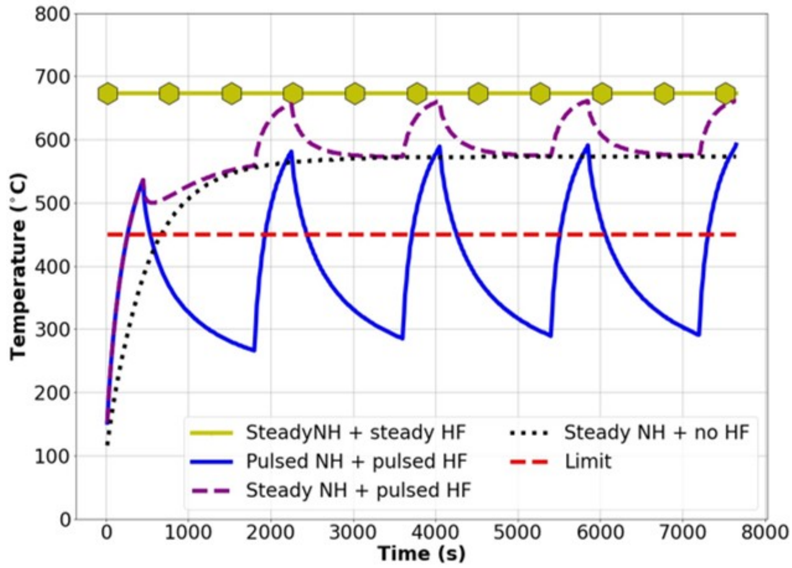

Figure 5.26: Evolution of the maximum temperature reached in the antennas of gap 6 during 5 ITER pulses.

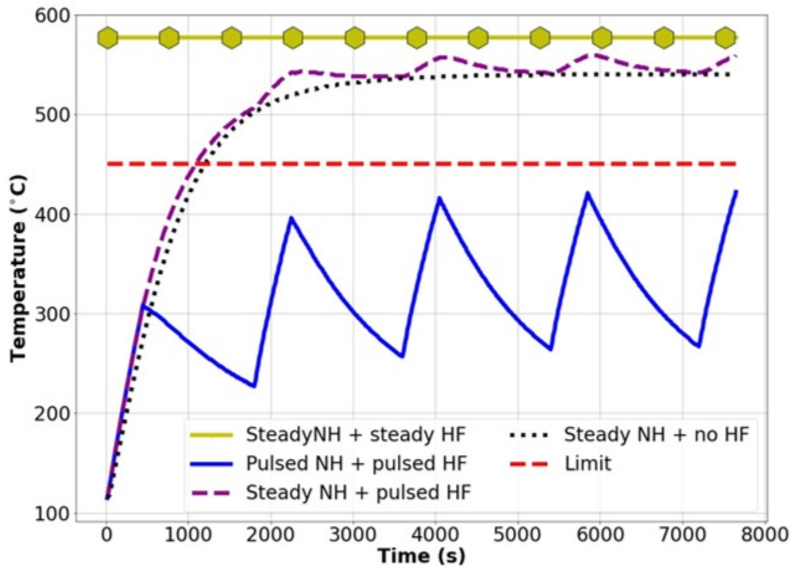

Figure 5.27: Evolution of the maximum temperature reached in the supports of gap 6 during 5 ITER pulses.

5.4.8 Contact Surface Sensitivity Analysis

In face of the high operation temperatures reached by the front-end components of gaps 4 and 6, an additional study was carried out to check if these temperatures could be reduced by increasing the contact surface between the 90° bend support and the VV. This study was carried out for the system of gap 6 and consisted of (i) changing the size of the attachments (bosses) to the VV and (ii) adding volume to the back of the support to increase the contact surface with the VV.

The bosses are standard ITER catalogue parts used to attach components to the VV. The current size of the bosses used to attach the 90° bend support of gap 6 to the VV has already been maximized, taking into account the allowable clearance distances to other surrounding structural components in the VV. Therefore, the sensitivity analysis was carried out by reducing the size of the bosses by 5 mm, instead of increasing it. As shown in Figure 5.28, this modification had a negligible impact on the operation temperatures, which increased by only 5 °C (to 596 °C).

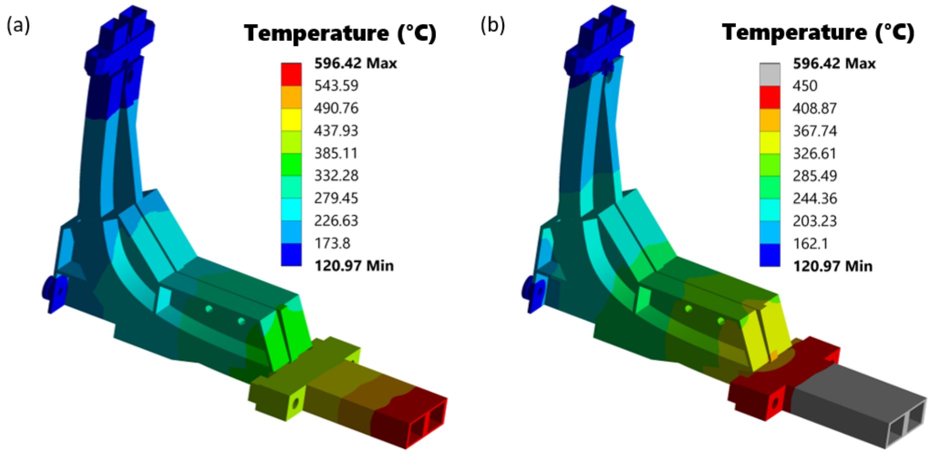

Figure 5.28: PPR temperature distribution (20 mm diameter bosses): (a) standard scale and (b) scale with temperature limit of 450 °C.

The other possibility to increase the contact surface to the VV is by changing the design of the 90° bend support. Two modifications were assessed: (i) extending the body of the support above the attachments, until it touches the VV wall, as shown in Figure 5.29 (a); and (ii) extending the body of the support around the bosses, as shown in Figure 5.29 (b). Although the extended contact provided by these modifications is not perfect, since it would be achieved by compression once the support is bolted to the bosses, both changes would increase the heat flow capacity to the surface to the VV.

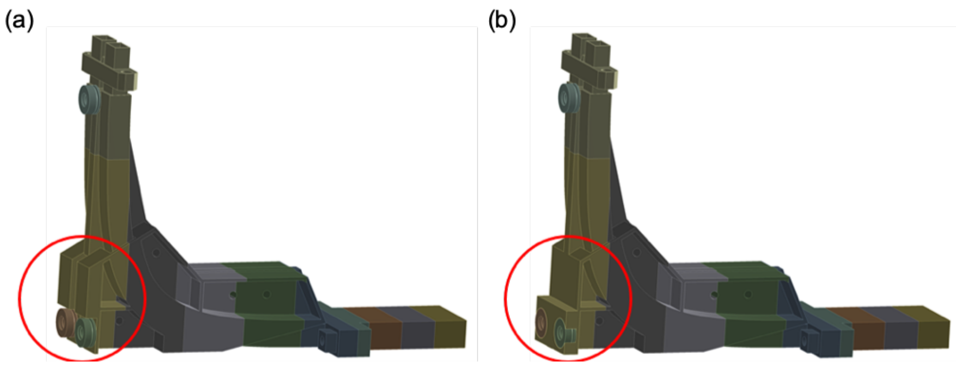

Figure 5.29: Design modifications on the 90° bend support: (a) support extension above the lower bosses and (b) support extension around the lower bosses.

The results of the thermal analyses corresponding to these changes are shown in Figure 5.30. As can be observed, the modifications done to the support have no impact on the operation temperature of the antennas. These results were somehow expected since the contact surface was increased in the back of the support, but the cross-sectional area of the waveguides and support, which forms the heat flow bottle neck, was kept unchanged. Therefore, the impact on the overall capacity of the structure to remove heat from the tips of the antennas was negligible.

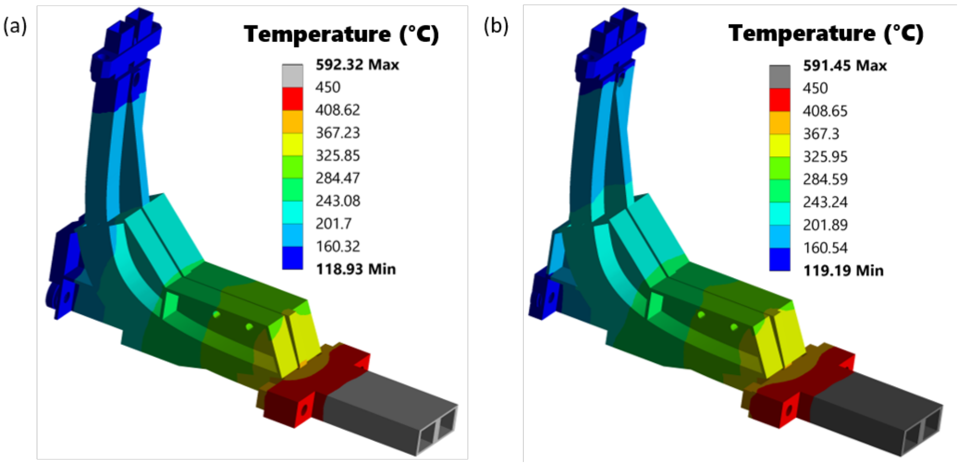

Figure 5.30: Temperature distribution in the modified PPR antenna and support: (a) volume extended in the poloidal direction and (b) volume extended in the toroidal direction.

5.5 Summary and discussion

Like many other in-vessel components, the integrity of the waveguide section and the front-end components of the PPR system depends on the temperature distribution and the displacement per atom experienced by the components, since both of these variables can modify the mechanical properties of the material. The dpa in ITER is expected to be low enough not to impact the material properties. For safety reasons, the maximum allowable operation temperature for stainless steel 316L(N)-IG under neutron irradiation is 450 °C, which is the driving limit for the thermal analyses of the PPR in-vessel components. This value is related to the thermal stresses that may compromise the structural integrity of these components.

Considering an initial temperature of 100 °C and the VV environment (only radiation and conduction heat transfer must be considered), a steady-state thermal analysis was carried out to obtain the temperature distribution in a PPR WG section. The analysis revealed a maximum temperature of 187 °C in the waveguides (see Figure 5.11), well below the maximum allowable temperature for stainless steel 316L(N)-IG under neutron irradiation (450 °C).

The temperature distribution in the analyzed PPR section varies from 120 °C at the bottom surfaces of the boss to 187 °C in the part of the waveguide section directly exposed to the plasma, near the support.

This chapter also presented the results of the thermal analyses performed for the front-end components (antennas and 90° bend supports) of the PPR systems in gaps 4 and 6. The temperature distributions in the components were estimated with steady-state and transient thermal analyses performed with ANSYS Mechanical, using the heat loads and the thermal map of the vacuum vessel specified by the IO.

The results indicate that the operation temperatures of the PPR antennas in both gaps would be well above the limit of 450 °C for the selected material (SS 316L(N)-IG) under neutron irradiation. The front-end of gap 4 reaches a maximum temperature of 675 °C at the tip of the antennas, with the antennas and part of the support above 450 °C. In gap 6, the maximum temperature of 592 °C was obtained also at the tip of the antennas, with the temperatures in the support below (but very close to) 450 °C.

An additional study was conducted aiming to assess the impact on the operation temperatures of both gaps if the contact surface between the 90° bend support and the VV is increased. The corresponding results show that increasing the contact surface – within the limits stipulated by the available space in the apertures and by the possible dimensions of the attachments – has a negligible impact on the operation temperatures at the tips of the antennas.

In face of these results, the integrity of the antennas of the PPR systems of gaps 4 and 6 would surely be compromised. In order to avoid this, different materials should be considered for the front-ends of gaps 4 and 6. A nickel-based superalloy, for example Inconel 718, would be an option, as it is a structural material suitable for high temperature applications, with a maximum working temperature under neutron irradiation above 700 °C [199].

Part III

Multi-reflectometer system for DEMO

Chapter 6

Reflectometry system for DEMO

6.1 The DEMO Tokamak

Compared to ITER, DEMO will have a reduced set of diagnostics focused on plasma control [200]. Accordingly, those diagnostics are essential for the operation of DEMO. Therefore, their maintenance is of key importance. Moreover, with the temperatures and radiation levels expected inside the vacuum vessel [201], Remote Maintenance (RM) is essential. Due to these conditions, all diagnostics and, in particular, their in-vessel components are designed with Remote Handling (RH) compatibility in mind. In order to fulfill these requirements, the adopted strategy has been that all in-vessel diagnostic components should be hosted either in a port plug, or in a DSC to facilitate a expedite exchange by RM.

The DSC was a concept developed in the first place for the integration of reflectometry in DEMO, which is foreseen as the main backup solution for the magnetics diagnostic [202], the latter being the main tool for plasma behavior real-time monitoring. As failure of both magnetics and MW reflectometry would put equilibrium control of the DEMO plasma at risk, one of the considerations while designing the DSC is its integration with the blanket in such a way that it can be replaced in case of failure. In recent years, the DSC has also been considered to host other diagnostics, such as magnetics sensors [203] and the ECE [204], which increases the value of these integration studies.

The aim of the work presented in the following chapters is to provide design solutions that can be adapted to the existing as well as to future BB and Upper Port (UP) designs. Therefore, it is important to identify the main integration constraints for the DSC and adapt the solutions accordingly. The main constraints are:

1. The BB segmentation i.e., the way in which the BB is divided into separate segments (in the current DEMO design there are 5 BB segments per sector).
2. The "chimneys" protruding from the top of each BB segment into the UP opening (through which the pipes carrying the BB cooling and breeding fluids are connected to the BB segments; these "chimneys" are also the interface used to remove/install the BB segments themselves).
3. The BB pipe modules (groups of breeding and cooling fluid pipes between each BB segment and the ex-vessel, along with their support structure).
4. The space available in the UPs.
5. The UP neutron shield plug, the Upper Limiters (ULs) or other diagnostics systems housed in the UPs.
6. The locations of the Equatorial Ports (EPs), which are envisioned to accommodate the Outboard

Midplane Limiter (OML), the Electron Cyclotron (EC) launcher for the Heating and Current Drive (HCD) system, as well as port-based diagnostics for Diagnostics and Control (DC).

To explain these constraints with more detail, the following section provides a more extensive description of the DEMO tokamak, including illustrations of the VV and its maintenance ports, the blanket segmentation, the pipework for breeding and cooling fluids, the limiters and the UP neutron shield plug, as these components will provide the boundary conditions that will shape the design and integration of the DSC. The description of DEMO presented in this chapter, as well as the integration studies presented in Sections 8.1.1–8.1.4, are part of a team effort, published in [205]. More details about the DEMO tokamak can be found in that study.

6.1.1 Vacuum vessel and blankets

In current DEMO design, the VV is segmented into a total of 16 22.5° sectors, with two Toroidal Field Coils (TFCs) as limits in the toroidal direction. Each sector of the VV is a main support for the BB, the divertor, the port plug limiters and the port-based diagnostics. An illustration of a 22.5° sector is presented in Figure 6.1. There are three different ports through which access to the inside of the DEMO VV is provided, depicted in Figure 6.1: 1) the UP, which allows entry from the upper part of the tokamak; 2) the Lower Port (LP), which offers access from below, in particular to the divertor; and 3) the EP, which provides radial access. The UPs are mainly required for the maintenance of the BB segments, besides enabling the connection of pipes that carry cooling and breeding fluids to the BB–indicated as Helium-Cooled Pebble Blanket (HCPB) piping in Figure 6.1, as used for the HCPB blanket concept [206] (one of various blanket concepts studied for DEMO)–, while the EPs are expected to accommodate the OMLs as port plug components, besides the EC launcher for the HCD system and port-based diagnostics for DC. Therefore the main port involved in this thesis is the UP, although the location of the EP also has an impact on the design and integration of the DSC.

A 22.5° sector of VV in DEMO is planned to host and give support to 5 BB segments (shown in fig. 6.2), two in the Inboard Blanket (IB) and three in the Outboard Blanket (OB): a Left InBoard Segment (LIBS), a Right InBoard Segment (RIBS), a Left OutBoard Segment (LOBS), Centre OutBoard Segment (COBS), and a Right OutBoard Segment (ROBS). Each BB segment has a surface which faces the plasma, the so called FW, and two lateral sides (which originally extended radially), dubbed Side Walls (SWs), besides a Back Plate (BP), which closes the rear of the segments, and the bottom and top caps.

The UP through which the BB maintenance will be carried out is constrained not only by the number and the toroidal width of the TFCs (in the toroidal direction), but also by two upper Poloidal Field Coils (PFCs), which limit its span in the radial direction. With these constraints, the UP aperture is restricted to a narrow shape, bounded by red lines, that is seen through the VV (shown in Figures 6.1 and 6.2).

The BB segmentation of the latest design of the DEMO tokamak is presented in Figure 6.2. This segmentation adopts parallelization of the SWs of the COBS and the corresponding adjacent walls of the LOBS and ROBS. This parallelization aims to avoid clashes between the OB BB segments. Furthermore, this segmentation also adopts a straight interface between the IB and OB BB segments across each port.

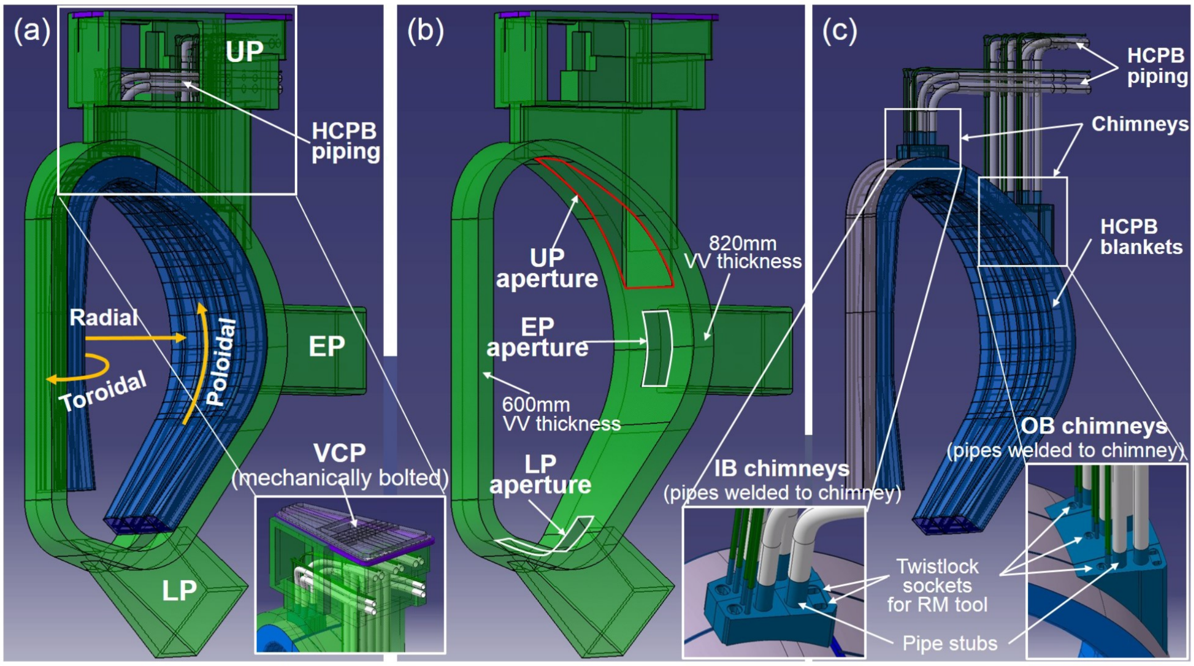

Figure 6.1: One sector of DEMO VV, with the HCPB BB concept. The insets offer different perspectives of: (a) the UP; (c) the "chimneys" with the RM tools socket (taken from [205]).

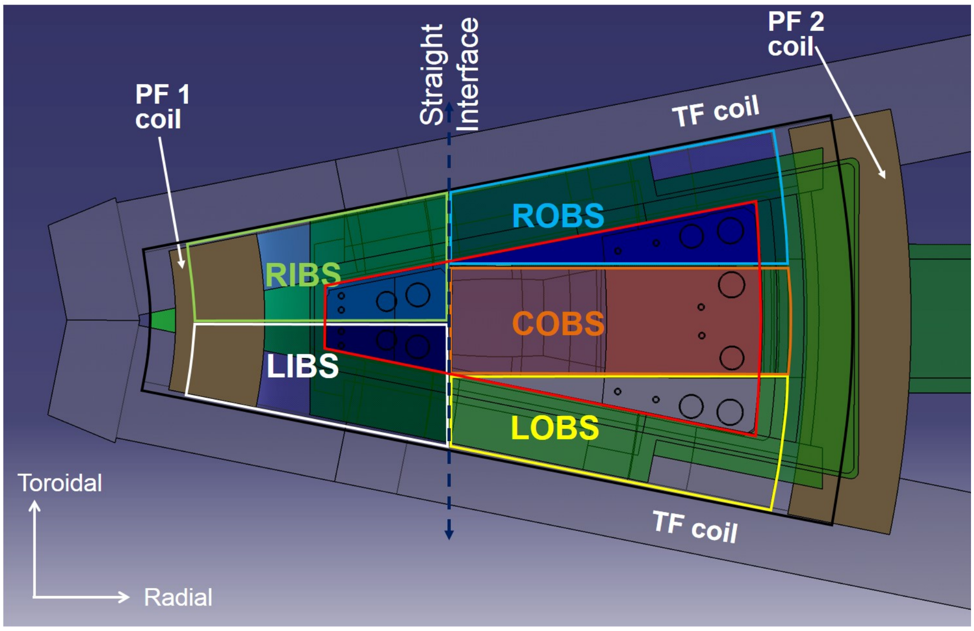

Figure 6.2: BB segments in DEMO and the UP opening on the VV (CAD model taken from [207]).

6.1.2 DEMO WCLL blanket concept

Various BB concepts for DEMO have been proposed and studied over the years [206, 208]. The BB concept considered in this thesis is the Water-Cooled Lithium Lead (WCLL), which uses EUROFER as structural material and relies on liquid Lithium Lead (LiPb) as tritium breeder (through its Li component), neutron multiplier (by virtue of its Pb component), and as tritium carrier [38, 209–211].

6.1.2.1 SMS architecture

The current architecture reference for the DEMO BB is the Single Module Segment (SMS), which consists of a stack of 100 Breeding Units (BUs), as shown in Figure 6.3. In this approach, each BB segment is composed by the FW, the SW, the bottom and top caps, and the BP, supported by a Back Supporting Structure (BSS). This BSS attaches the BB to the VV (using the keys shown in Figure 6.4 and corresponding housings in the VV). In the SMS the profile of the FW follows the last closed magnetic surface without sharp edges and discontinuities. The poloidal length of the Inboard Blanket Segment (IBS) is ∼13 m, while for the Outboard Blanket Segment (OBS) it is ∼14 m; the toroidal length of the FW for the IBS is ∼1.12 m, for the COBS it is ∼1.48 m, whilst for the LOBS and ROBS it is ∼1.24 m [212]. The radial thickness of the IBS is in the range from 770 mm–1200 mm, and that for the OBS is 1000 mm [211].

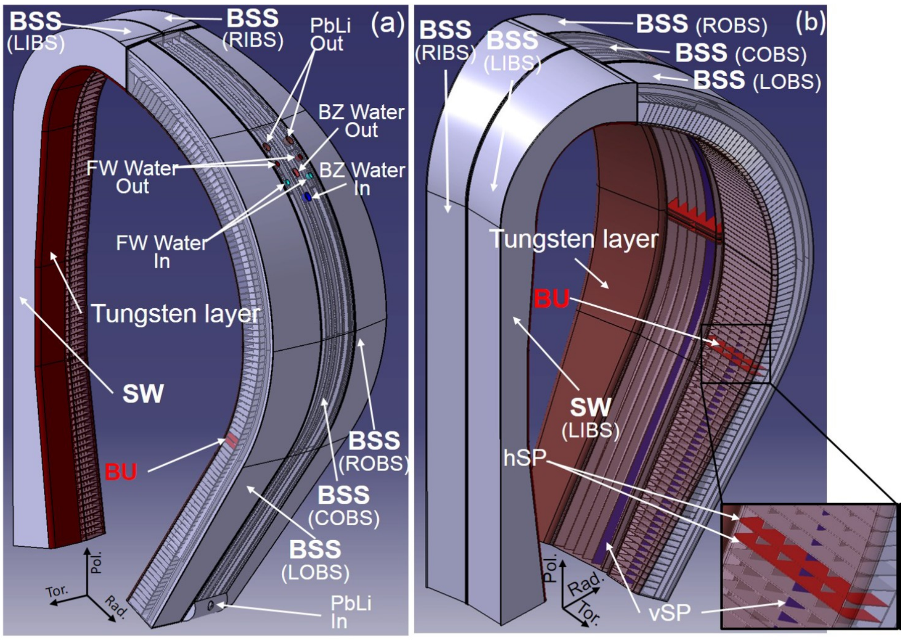

Figure 6.3: The WCLL blanket design with SMS architecture (CAD model by CREATE-ENEA [213]).

6.1.2.2 Breeding units

Each of the BUs comprises the FW-SW, the Breeding Zone (BZ) (the corresponding part of the LiPb), water manifolds, and the BSS. A stack of 2 BUs with a height of 270 mm in the equatorial slice of the COBS is highlighted in red in Figure 6.3 and presented in detail in Figure 6.5.

The FW-SW is a U-shaped 25 mm thick plate, cooled by water circulated in channels connected to the water manifold on the BSS. The BZ is reinforced by Stiffening Plates (SPs), horizontally and vertically, and baffle plates to give more stability to the structure. BPs are used to separate the BZ from the PbLi and the water manifold. The PbLi manifold (see Figure 6.5) is a coaxial rectangular structure through which the BZ is filled with the breeding material. This breeding material is cooled by water flowing inside Double-Walled Tubess (DWTs), delivered and collected through the corresponding water manifold (see Figure 6.5).

Each BB segment is sustained by a continuous steel plate (with maximum radial thickness of 100 mm)

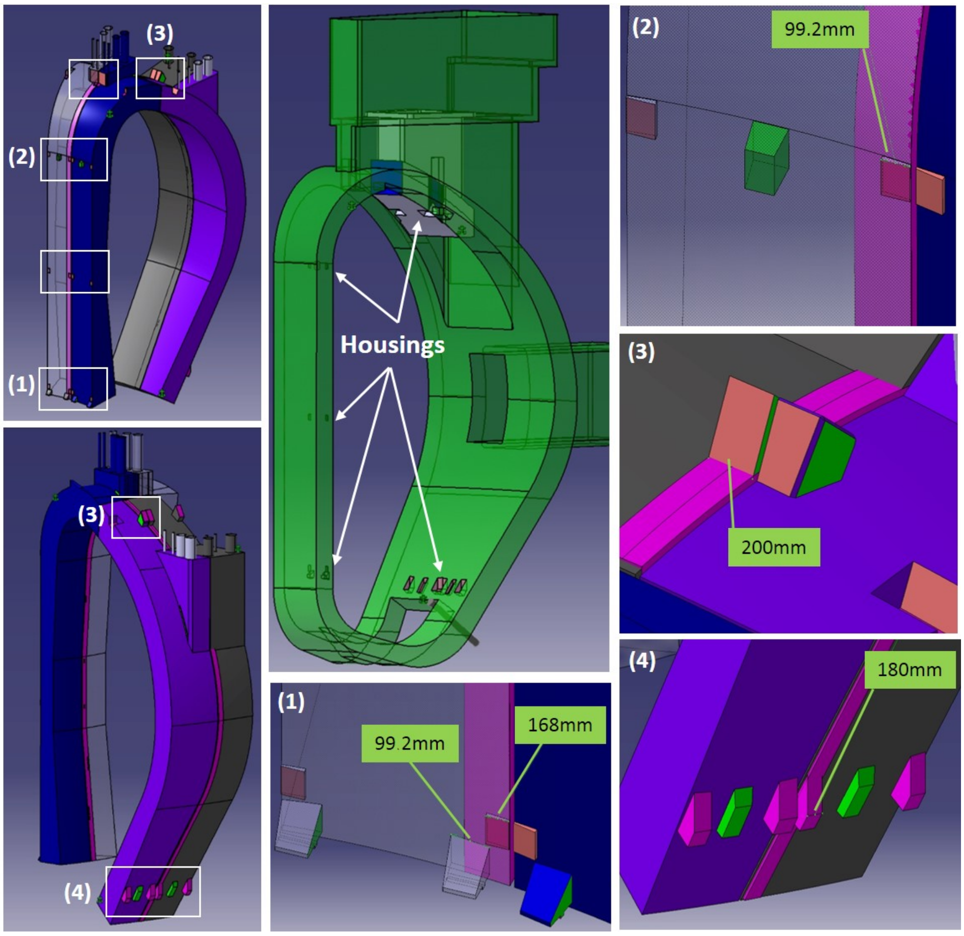

Figure 6.4: The key and housing concept of the BB support structure concept in comparison with the (200 mm wide) DSC in pink (CAD model taken from [214]).

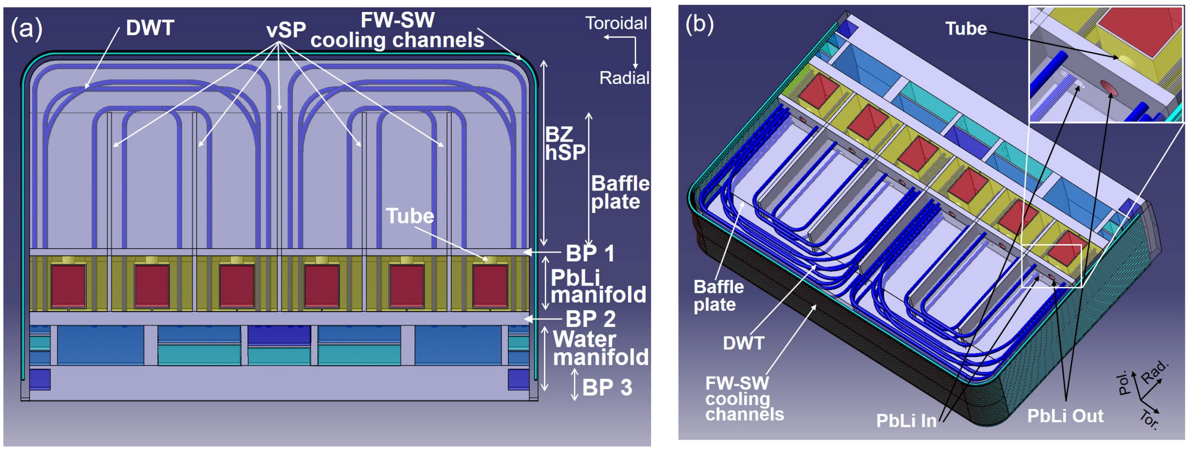

Figure 6.5: A breeding unit of COBS highlighted in Figure 6.3: (a) cross sectional (top) view; (b) perspective view (CAD model by CREATE-ENEA [213]).

on its back which is known as BSS (see Figures 6.3 and 6.5). This BSS or BP3 closes the rear of the BB segments and becomes the backbone of the BB segments. The functions of this BSS are: (1) supporting structural loads of the BZ and providing stiffness to the whole structure; (2) housing the FW-SW water coolant manifold; (3) shielding the VV and the Toroidal Field (TF) coils from plasma radiation; and (4) housing the BB attachment system to the VV.

6.1.2.3 The WCLL pipes

In the current design of WCLL BB concept, the feeding pipes are routed through the UP and lower port (see Figure 6.6). It is expected to have ten pipes arranged in five rows of two pipes routed through the UP. The lower port is expected to have five input pipes of PbLi, two input pipes are connected to the IB BB and the other three are connected to the OB BB. Important to note that when this work was done, the "chimneys" for WCLL concept were not yet designed, therefore the HCPB "chimneys" are used to delimit the region. Moreover, the PbLi inlet pipes for LOBS and ROBS in the lower port are not yet included in this model.

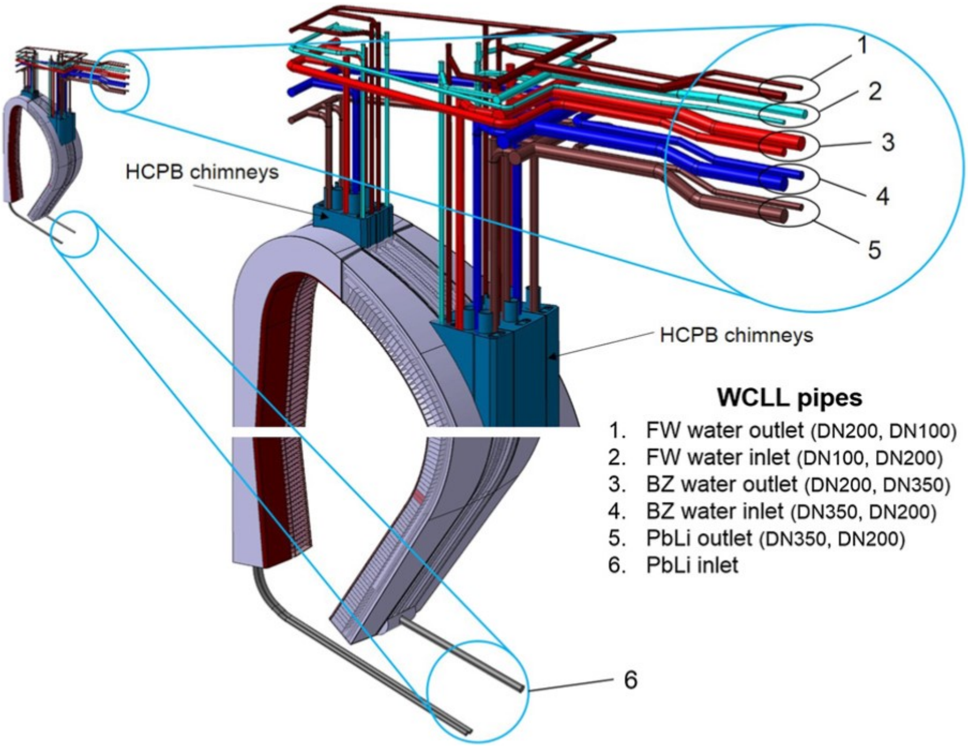

Figure 6.6: Feeding pipes for the WCLL BB concept using, for illustrative purposes, the "chimneys" of the HCPB concept (CAD Models: WCLL from [213]; HCPB "chimneys" from [215]).

6.1.3 Pipe "chimneys", pipe modules and space availability in the UP

The "chimneys" (see Figure 6.7) contain the interfaces to remove/install the BB segments with recourse to a set of 3 twistlock pins–rotating connectors as used in shipping containers–in the RM tool (the Hybrid Kinematic Mechanism (HKM) [216, 217]) and the corresponding twistlock sockets in the "chimneys", into which the twistlock pins are inserted and rotated to secure the connection. The same "chimneys" also provide connections between the Primary Heat Transfer System (PHTS) pipes and the pipe stub which is expected to be weld or cut during the installation or removal of the BB. In addition, it is worth noting that space in these "chimneys", through which the connections from the UP to the inside of BB are required to pass, is very limited.

Regarding the pipe modules, which group the cooling and breeding pipework for each BB segment, the structure will be a space-frame arrangement (with a rigid structure body) [218] to minimize the weight while keeping the rigidity of the support structure. These pipe modules will be removed and replaced through the UP whenever BB maintenance is carried out–prior to the BB removal–, with recourse to the same RM tool (HKM) used to manipulate the BB. Therefore, the pipe modules are provided on the the top with an interface similar to that of the BB “chimneys”. In face of the limited space in the UP, it is expected that all the interfaces between the BB and the ex-vessel are grouped inside these pipe modules, especially from the IB.

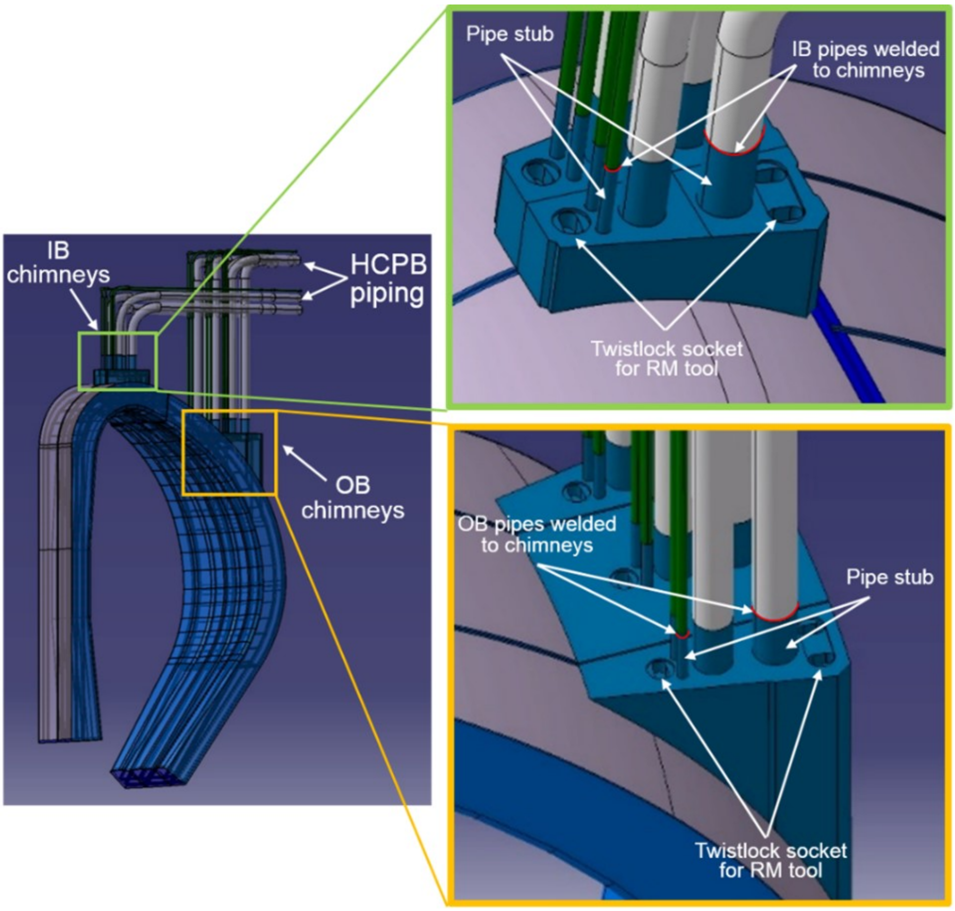

Figure 6.7: The “chimneys” and the piping (welded to the “chimneys”) through which fluids enter and exit the BB segments in the HCPB concept [215] (taken from [219]).

6.1.4 Limiters

Although the FW in DEMO is to be actively cooled and protected by a plasma-facing tungsten armour (2 mm–3 mm thick), it is anticipated that plasma transient events may bring extreme energy and power densities far exceeding the FW heat flux limit. The protection of the BB FW from these events involves the installation in certain regions of the machine of dedicated discrete limiters with appropriate design and cooling such that they can withstand the transient heat loads while providing protection to the BB FW [220–223].

Given that the thermal loads can be so large that their plasma facing tungsten armour can be damaged, a key feature of these limiters is that they will be sacrificial components, requiring replacement more frequently than the BBs–or the neutron shield–themselves. So as to reduce the time required for their remote replacement, the limiters (except for the IB limiters) will be installed in dedicated ports, integrated as port plug components, such that their removal does not require prior removal of other In-Vessel Components

(IVCs). A consequence of such an integration in DEMO is that they will have an impact on the integration of the DSC as well.

In the current concept it is envisaged to install limiters in or through the UP and the EP: 8 ULs, 4 OMLs, as illustrated in Figure 6.8, besides 4 Outboard Lower Limiters (OLLs), and 4 Inboard Midplane Limiters (IMLs) [220, 221, 223]. The limiters that have direct contribution to the design of the DSC are the ULs and the OMLs.

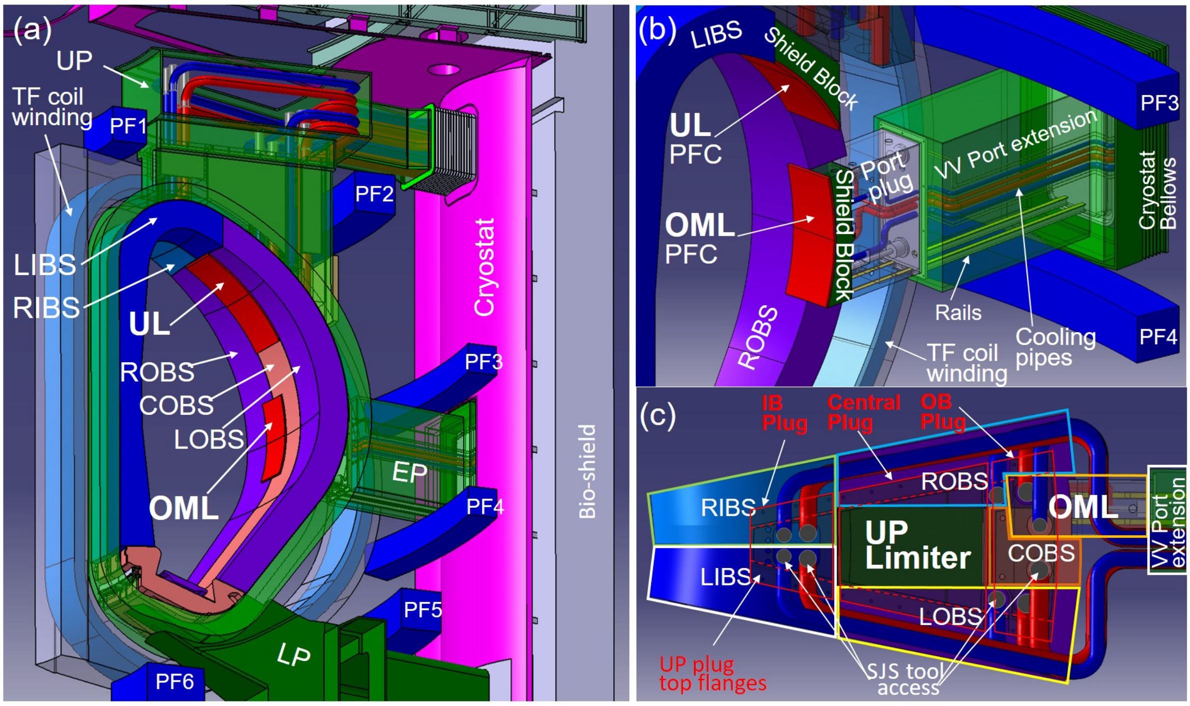

Figure 6.8: Limiters proposed for the UP and EP illustrated with the HCPB piping. Figure (c) depicts an upper view of the sector (CAD model from [224]).

The ULs limiters will be installed at 8 out of 16 UPs, whereas the DSC for MW reflectometry is to be implemented in two sectors or eventually four sectors if the DSC is also chosen to host the magnetic sensors. Each UL, with overall area of 1.5 m × 3.4 m, will replace the top section of the COBS. These ULs are planned to be installed or removed vertically so that the removal kinematics does not interfere or clash with other hardware in the port [218]. Therefore it is reasonable to presume that there will be no DSC wherever the UL is present, given the space restrictions prevailing in the UP [218].

Regarding the OML, it is foreseen that 4 OMLs will be placed, separated by 90° periods [225]. The corresponding limiter, with an overall surface area of 1.1 m × 2.8 m, is attached to an EP plug. This port plug reaches all the way through the blanket to the plasma and so the port itself must be toroidally offset from the sector centreline in order to avoid splitting the blanket segments vertically, as depicted in Figure 6.8. This offsetting requires cut-outs in adjacent BB segments of only ∼0.6 m (approximately 1/3 of their nominal toroidal width), so as to maintain their vertical integrity/stability [222]–but having an impact on the integration of the DSC.

6.1.5 UP neutron shield plug

The neutron shield plug in DEMO is a component of the UP that resulted from the division of the COBS into a reduced size COBS segment and a small plug (at its upper end) [226]. A consequence of this division is that the UP plug needs its own active cooling (most likely the same coolant used for PHTS), coolant pipes (possibly grouped into its own pipe module), and pipe connections. This component is expected to act as a neutron shield to the components behind it (the magnetic field coils) [227]. A previous version of the UP plug is illustrated in Figure 6.9. It should be noted that the neutron shield plug also acts as a "keystone", which helps to hold the five BB segments in position during operation. Therefore, this component is expected to be removed through the UP before the removal of the blanket modules [218].

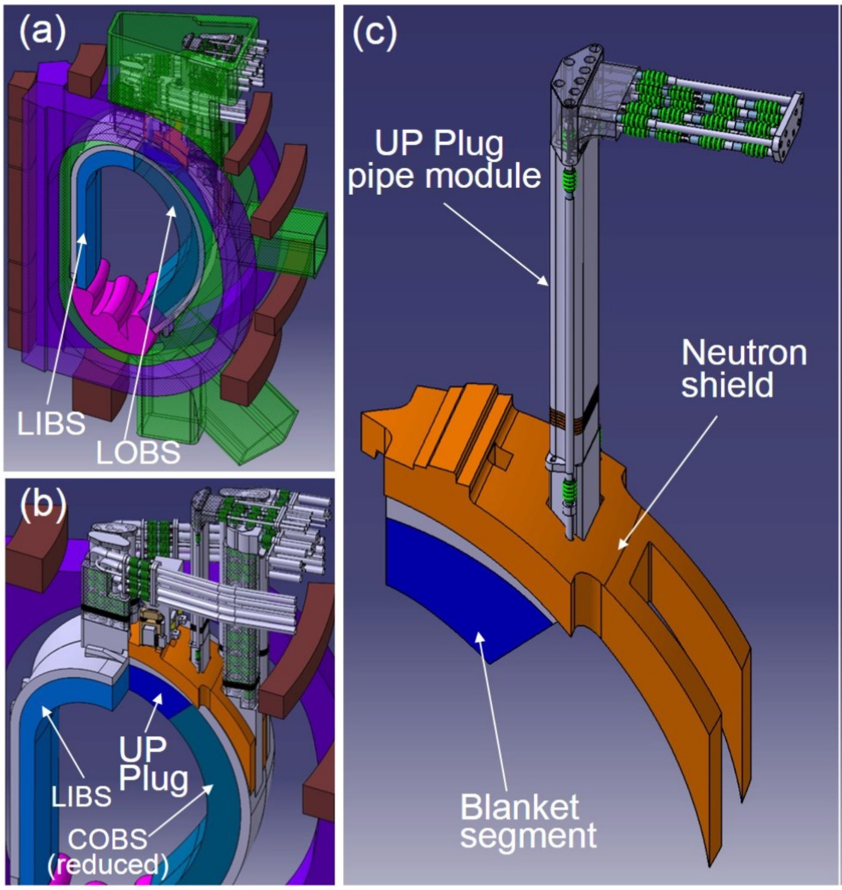

Figure 6.9: The upper port plug or "keystone" concept, with the neutron shield and corresponding pipe module attached in (c) (CAD model from [228], taken from [205]).

6.2 The DEMO reflectometry diagnostic

Since the aim of the DEMO reactor is to generate electricity, the plan is to implement a minimum set of diagnostics, focused only on the diagnostics that are needed for controlling the tokamak plasma. Those diagnostics must be repairable or replaceable if needed [54] [205]. Therefore, the space and the RH compatibility are major challenges of designing the in-vessel components of DEMO reactor diagnostics system.

Microwave reflectometry measurements have been recently proposed for the next-generation fusion reactor, DEMO, as a suitable backup for magnetics sensors, the main tool for plasma behavior real-time monitoring [54]. The role of the reflectometry diagnostic in DEMO is twofold: i) to provide the radial edge density profile at several poloidal angles and ii) to provide data for the feedback control for plasma position and shape. The implementation of reflectometry requires that the antennas be placed in front of the plasma. As such, they are foreseen to be made of EUROFER, with the possible addition of tungsten coating, taken from the experience of the breeding blanket project for the use of materials for in-vessel components [38].

In order to fulfill the control system requirement of the DEMO reactor [202], the reflectometry system shall be able to measure the plasma electron density in the pedestal region, where the high-density gradient occurs, with a temporal resolution of 1 ms, maximum precision of 5%, maximum noise level of 2%, and maximum latency of 0.01. The planned functions and bands projected for the reflectometry system taken from [229] are shown in Table 6.1

Table 6.1: Projected functions and bands for the reflectometry system of DEMO.

Function	**Position**	**IEEE Frequency Band**	**Frequency** (GHz)	$\mathbf{n_e}$ ($\times 1 \times 10^{19}$ m^{-3})
Plasma position and shape control	14 poloidal positions not in the equatorial plane	K, Ka, U, E (O-mode)	18-26.5, 26.5-40, 40-60, 60-90	0.3 to 10
Plasma position and shape control + Density profile edge to core	Equatorial LFS and HFS	K, Ka, U, E (O-mode) + D, G (X-mode)	18-26.5, 26.5-40, 40-60, 50-75, 75-110 + 110-170, 170-260	0.3 to 14.9

Ray-tracing and 2D Finite-Difference Time-Domain (FDTD) simulations (see Figure 6.10) have shown that at the equatorial level the "single pair" approach for emitting and receiving antennas will be able to provide good spatial resolution[6] [230]. Near the lower and upper ports, however, the curvature of the plasma will cause significant problems for the operation and accuracy of reflectometry measurements. At these locations, a cluster of 4–6 antennas (3–5 per emitting antenna) may be required to ensure that the reflected beam is captured, even under conditions of larger plasma-wall distance. Therefore, to fulfill the reflectometry requirements, it is anticipated that up to 100 antennas will be required, distributed in 16 different poloidal locations [230]. The dimensions of these antennas and waveguide, shown in Figure 6.11,is driven by the lowest frequency intended to be used, which is 15 GHz, which corresponds to the $n_e = 0.3 \times 10^{19}$ m^{-3}.

[6]These simulations were conducted by A. Silva, F. Silva and E. Ricardo at IPFN/IST

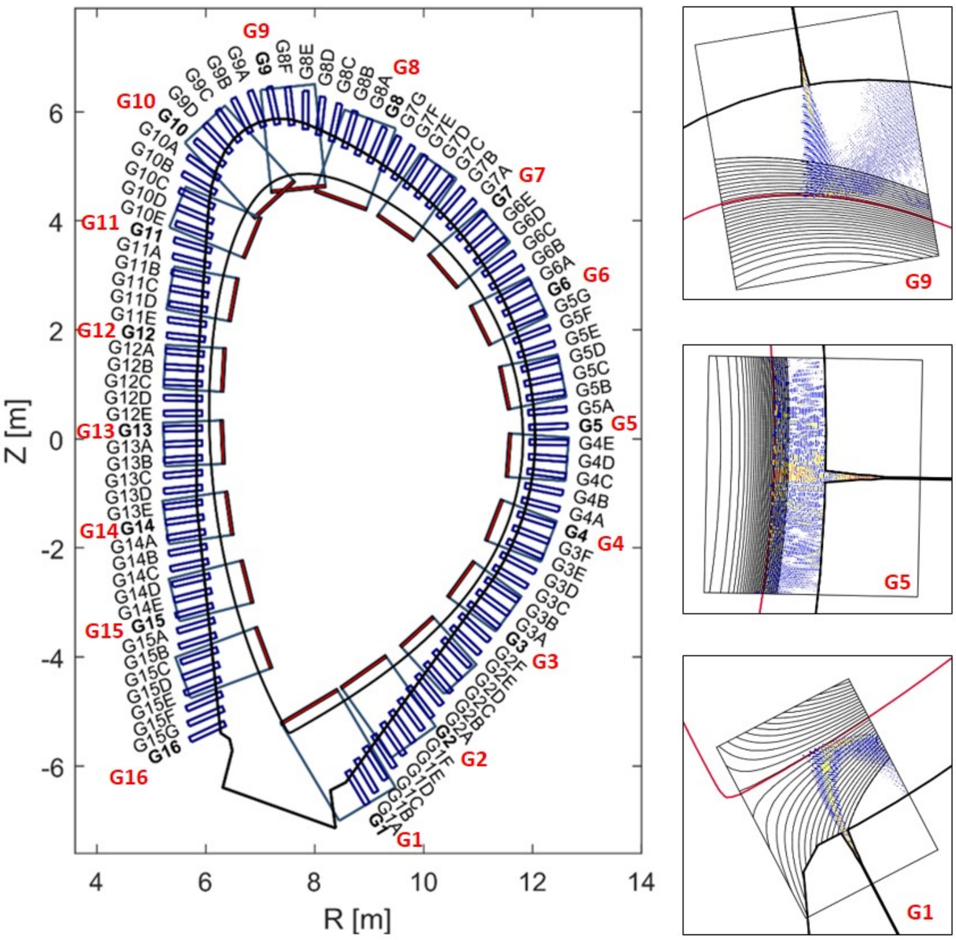

Figure 6.10: Poloidal distribution of the antennas and their performance at several locations.

6.2.1 The Diagnostics Slim Cassette concept

Given that all these components will be in-vessel, and they may experience nuclear and thermal loads 10 to 50 times larger than on ITER, it is important to design the reflectometry system in such a way that it can be replaced in case of failure. Thus, the primary integration approach for reflectometry in DEMO has been based on the DSC concept [53], a "dummy poloidal section" fully dedicated to diagnostics to be integrated with the BB, illustrated in Figure 6.12 [53]. The DSC is considered to have a thickness of 20 cm–25 cm in the toroidal direction, containing all the antennas and corresponding WGs, which are routed to the ex-vessel through the UP.

Along with the development of the DEMO BB segmentation, various DSC concepts were designed and studied. These initial designs, based on the DEMO BB 2015 baseline configuration (which adopted the Multi-Module Segment (MMS) concept [206]) were presented in [51, 53] and studied further in [52], in a work that included an improvement to the DSC cooling system performance and kept the maximum operation temperatures within the temperature limit of EUROFER. However, the cooling system proposed in that study was very complex and involved a stack of alternating cooling channel plates. In order to manufacture this cooling system concept, a special technique, Hot Isostatic Pressing (HIP), is required to avoid compromising the mechanical properties of the material. The HIP technique, employed in the manufacturing of the ITER divertor [232, 233], would allow complex cooling labyrinths to be integrated into near-solid stainless steel. However, it should be remarked that the DSC segment will be much larger

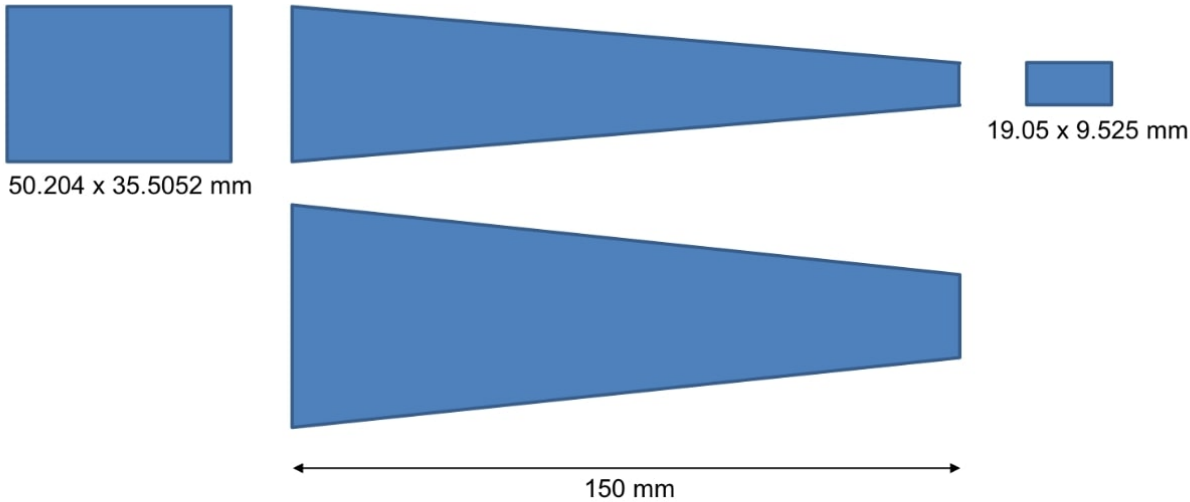

Figure 6.11: The antenna and WG inner dimensions.

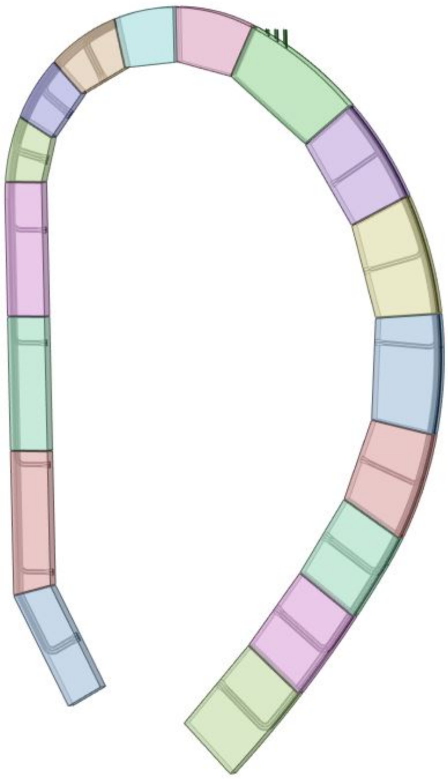

Figure 6.12: CAD representation of the DSC with the integrated antenna and WGs based on the DEMO BB 2015 baseline [231].

than the ITER divertor cassette (>12 m of height), and as such it would not be possible to manufacture the DSC using the HIP method in existing facilities [234]. Furthermore, these previous works were performed considering the Helium Cooled Lithium Lead (HCLL) [235] blanket configuration as reference. Since 2017, the DEMO BB design has adopted the SMS architecture [205], and the diagnostics have been designed with the WCLL BB in mind. Therefore, one of the objectives of the work presented in this thesis was to design a DSC with a cooling system that ensures operation temperatures below the temperature limit of EUROFER (550 °C) [236–239], adapted to the current BB concept and possible to manufacture with current technology.

Chapter 7

Thermo-mechanical analysis of a multireflectometry system for DEMO

7.1 Workflow and simulation tools

Figure 7.1 illustrates the steps followed to perform the simulations for optimizing the cooling channel design for the DSC. The CAD software CATIA V5 [196] is used to develop the CAD models, which then must be imported to ANSYS SpaceClaim [197] for simplifications—removal of fillets, screws, and other unnecessary complications—before they can be used in the nuclear and thermal analyses. For the nuclear analysis, the model is then decomposed as basic geometry, exported as STEP file and imported into the CAD-based modelling program McCad [240] [151] for conversion to the MCNP input format. The neutronics simulations are performed in the Monte Carlo simulation program MCNP6 [111], after implementation of the converted model in a DEMO neutronics reference model, and the nuclear heat loads in the components of the DSC are then used as input in ANSYS Workbench v19.1 [197] for the coupled thermal analysis (ANSYS Mechanical and CFD). The CAD models prepared in ANSYS SpaceClaim are used directly in the thermal analysses.

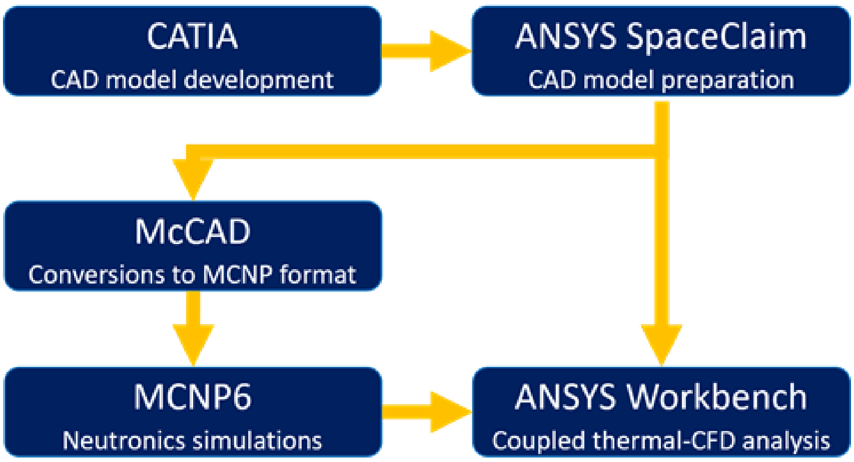

Figure 7.1: Workflow for the nuclear and thermal analyses.

7.2 Input and assumptions

7.2.1 WG routing

As up to 100 antennas will be needed to fulfill the reflectometry requirements, one of the most important integration studies is to design the routing of the WGs inside the DSC for the new DEMO design introduced in 2017. For this purpose, input was taken from a previous work on the performance of reflectometry at 16 poloidal locations in the blanket, presented in [230].

A 20 cm wide (toroidal direction) DSC was designed, with the exact shape of the blankets, and clusters of pyramidal antennas were introduced in the first wall at the 16 locations. As more receiving antennas will be required to collect the reflected beams in gaps located further away from the equatorial plane, more antennas were introduced at these locations. In an iterative process, that aimed at using as much available space as possible, rectangular WGs were attached to the antennas and routed to the upper port. The main constraint, besides space, was the minimum radius of curvature required from reflectometry: 50 mm.

The DSC design is presented in Figure 7.2, which shows all the WGs on the left side and the WGs in different planes on the right side. The maximum number of antennas and WGs that could be introduced in the 20 cm wide DSC was 73. Their implementation was a major design effort that allowed to perform most of the integration studies presented in this thesis, along with neutronics simulations to evaluate the neutron streaming through the DSC WGs, as well as and the possible effects on the integrity of the VV [234].

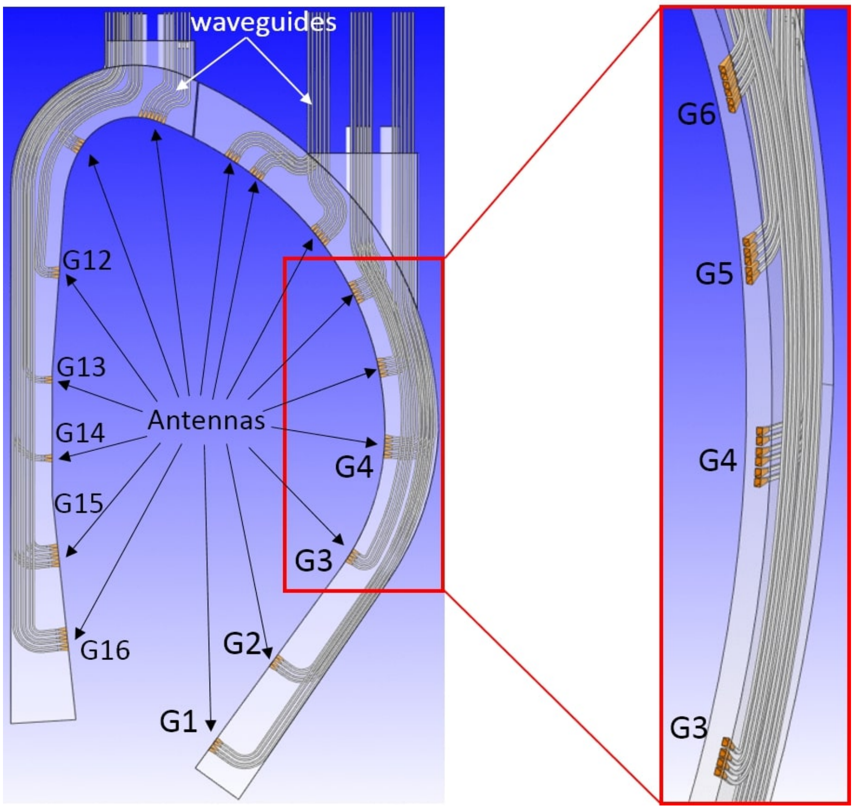

Figure 7.2: The DSC concept applied to the 2017 DEMO reference model, including the routing of WGs to/from the antennas in 16 different clusters (G1 to G16) [200]

7.2.2 CAD design of a DSC segment

As the performance of reflectometry at the 16 poloidal locations is currently under study, the nuclear and thermal analyses presented here were carried out for a location that will have the antennas directed perpendicularly to the plasma, at the equatorial plane in the inboard side (see Figure 7.3). To have the antennas recessed from the plasma, a 10 cm cube was carved at the front of this module. Although in the current design this module has only one pair of antennas, the other 10 WGs that run through it were included in the design. The module is composed by the following components:

- A 2 mm tungsten layer on the outside (facing the plasma), with a dedicated cooling system.
- EUROFER components including the fill block (neutron shield / structural material), antennas and WGs.
- Water cooling system inside the fill block (water enters the system at 295 °C, 15.5 MPa).

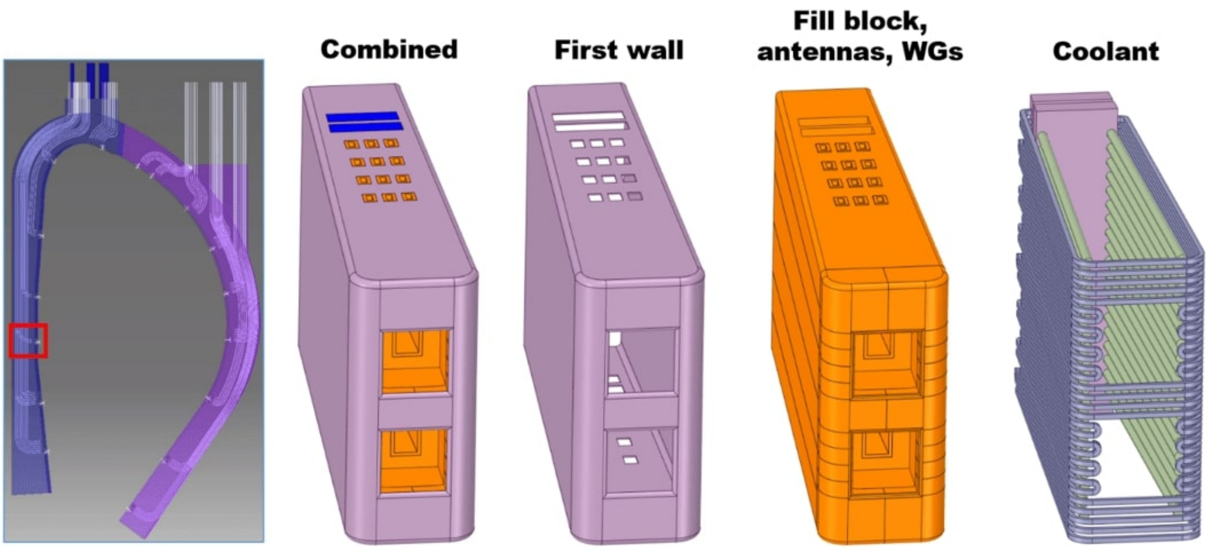

Figure 7.3: CAD model of a DSC segment at the equatorial plane (inboard).

The water cooling channels inside the DSC module consist of the FW cooling channels, which were kept mostly unchanged compared to the BB FW cooling channels, and the cooling channels for the antennas and shielding block (designed with some features of the HCPB BB). The cooling channels for the antennas and shielding blocks are concentric cylinders in which water circulates from the outer cylinder to the inner one, as illustrated in Figure 7.4. This design makes the cooling system more effective and easier to manipulate in later design iterations. It also makes the DSC easier to manufacture, since the EUROFER shielding block can be split into vertical components surrounding the antennas, the WGs and the cooling channels [219, 229].

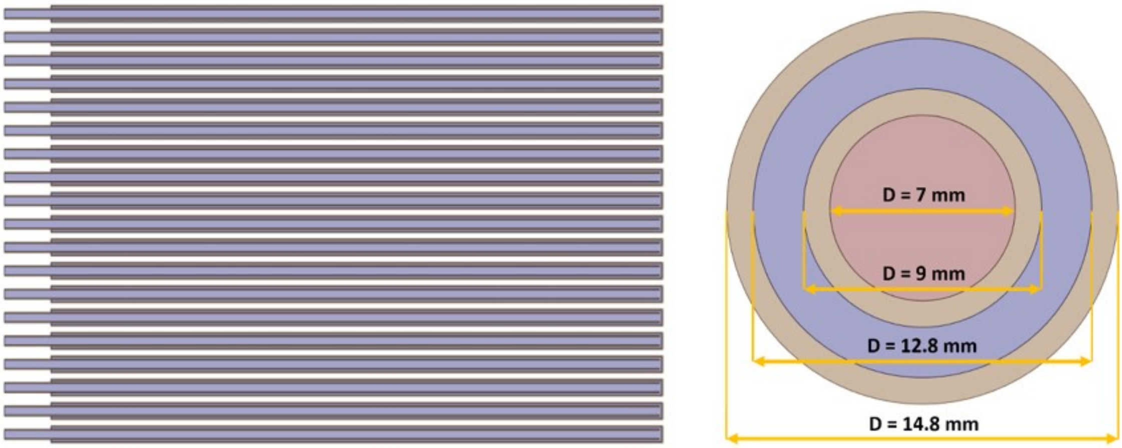

Figure 7.4: Shielding blocks cooling channels. Left: toroidal point of view. Right: detail of the cross-section of each channel.

7.2.3 Nuclear analysis

For the nuclear analysis, the CAD model was decomposed and then converted to the MCNP input format using the CAD-based modelling program McCad. The result is presented in Figure 7.5 and Figure 7.6. This very complex model, which captures all the details and the curvatures of the two cooling systems, was then implemented in the 22.5-degree 2017 Generic DEMO MCNP model [241], as shown in Figure 7.7. Using this model, neutronics simulations were performed to assess the nuclear loads in the system.

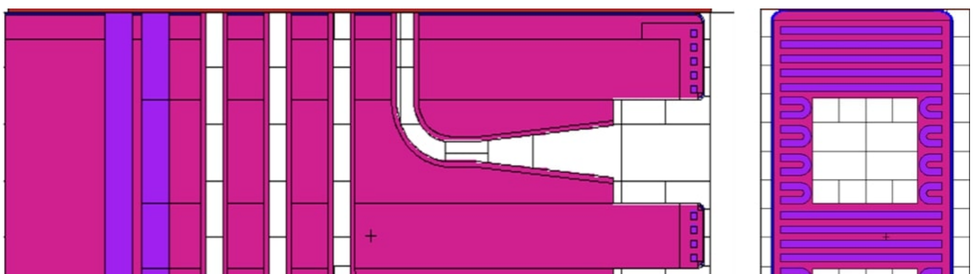

Figure 7.5: Poloidal (left) and front (right) planes of the MCNP model of the DSC.

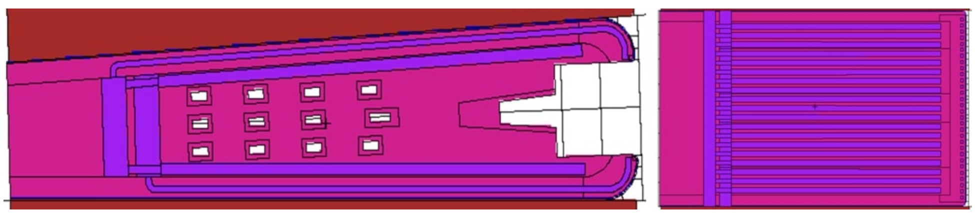

Figure 7.6: Toroidal (left) and poloidal (right) planes of the MCNP model of the DSC.

The MCNP simulations were run with mode N P to simulate the transport of neutrons and photons, using FENDL 3.1 cross sections [118]. The results were normalized to a fusion power of 2037 MW, corresponding to 7.232E20 n/s [120]. To keep the statistical errors below 10% and to ensure that all tallies pass the 10 statistical tests of MCNP, 2E9 source particles were simulated. A very fine mesh with 750000 bins (7.8 mm x 2.8 mm x 4.4 mm) was defined to calculate the nuclear heat loads in the DSC module, to be used as input in the thermal analysis.

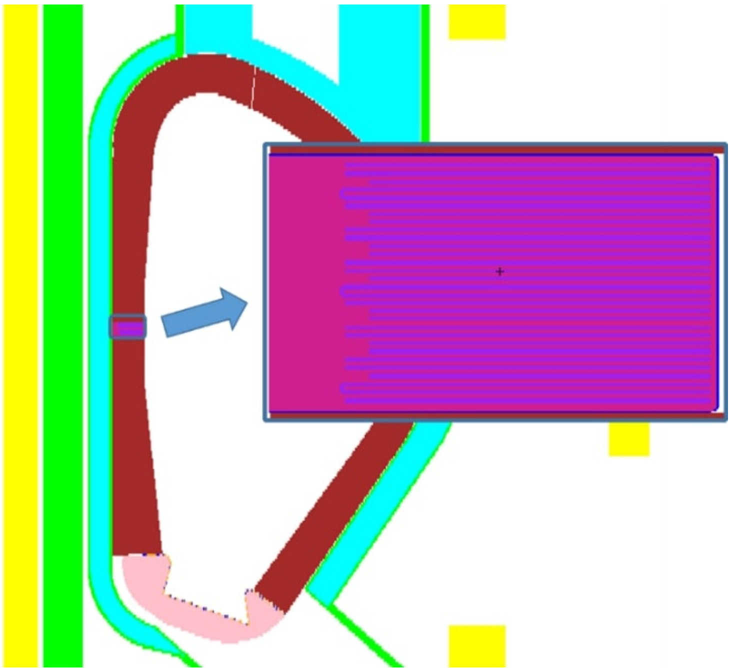

Figure 7.7: Poloidal view of the DSC integration in the MCNP reference model.

7.2.4 Coupled thermal analysis

7.2.4.1 Thermal radiation from the plasma

The thermal radiation from the plasma can be calculated using ANSYS CFX, by modelling the vacuum region between the plasma surface and the DSC as a fluid domain (Figure 7.8). The fluid domain is modelled using the properties of ideal gas for air at a pressure of 1E-10 Torr (minimum value to simulate vacuum). The other boundary conditions for this calculation were:

- Power density of 500 kW/m^2 at the plasma surface.
- Surface-to-surface Discrete Transfer Model (Shah model [183]) for the radiation phenomena, to take into account the direction of the radiation receiving surfaces.
- Emissivity of the plasma surface and the DSC surfaces set to 1 (Black-body radiation).
- The rest of the fluid domain surfaces was assumed to be adiabatic (the only heat transfer mechanism is by radiation).

7.2.4.2 Steady-state thermal analysis setup for the solid elements

To reduce the computational time of each simulation, the thermal analysis of the solid elements was performed using the steady-state thermal analysis module of ANSYS Mechanical, since ANSYS Mechanical can make use of the GPU accelerator and CFX does not support this feature. The geometry used for

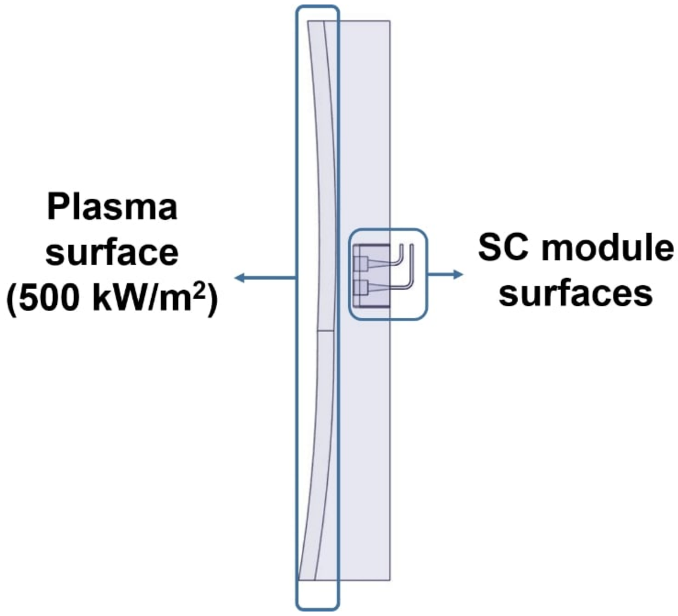

Figure 7.8: Modelling the thermal radiation from the plasma.

this analysis consisted of the solid parts of the geometry shown in Figure 7.3 (tungsten cover, fill blocks, antennas, and waveguides). The temperature-dependent thermo-physical properties of the materials (EUROFER and tungsten) were taken from the WCLL blanket design [242].

The nuclear heat loads (input from the nuclear analysis described in previous section) were imported as internal heat generation in all the solid elements, and the plasma thermal radiation was defined as heat flux to the plasma-facing surfaces.

The other boundary conditions were:

- FSI definition for all solid surfaces interacting with the coolant.
- Constant temperature of 400 °C in both sides of the module (assuming contact with the WCLL BB).
- Thermal radiation with emissivity of 0.5 in the front surfaces of the system.
- Adiabatic boundary condition for all the remaining surfaces.

7.2.4.3 Steady-state CFD analysis setup for the water coolant

Since the fluid domain does not interact directly with the plasma, the thermal load for the fluid domain is just the nuclear heat load, imported as internal heat generation, and the heat on the walls of the cooling channels, modelled with system coupling between ANSYS Mechanical and ANSYS CFX. The operation pressure and the static temperature of the water coolant are set to Pressurised Water Reactor (PWR) conditions (295 °C, 15.5 MPa for the inlet). The corresponding temperature-dependent thermo-physical properties of water, taken from the WCLL blanket design [242], were imported and applied as a function of the operation temperature using profile data tools.

The other boundary conditions were:

- Adiabatic condition applied to the walls.
- Inlet mass flow rate and outlet static pressure at flow domain inlet and outlet sections.
- No-slip condition at the interface between coolant and the EUROFER cooling channels.
- Reynold Averaged Navier-Stokes (RANS) equations, two-equation k – ω SST model employed to simulate the turbulence effects.

- Buoyancy effect modelled by setting the gravity on the z-direction as –9.8 m/s^2.

7.2.4.4 System coupling setup

The system coupling module of ANSYS Workbench was used to couple the thermal analysis of the solid elements and the CFD analysis through the fluid-solid interface. With this module, the total forces and heat fluxes are conservative across the FSI interface and information is sent both ways until the solution converges for both the solid steady-state thermal and the steady-state CFD analysis. The information sent from the solid steady-state thermal analysis is the cooling channel wall temperature, while the film heat transfer coefficient and the coolant temperature are sent from the CFD simulation to the solid steady-state thermal analysis as feedback.

7.3 Results

7.3.1 Nuclear analysis

Figure 7.9 and Figure 7.10 show the neutron and photon fluxes in the DSC module, while the nuclear heat loads are presented in the same poloidal plane in Figure 7.11 and at the first wall circuit in Figure 7.12. As mentioned before, in these results the statistical errors are below 10% everywhere. As expected, the nuclear heat loads by neutrons are much higher in the water than in EUROFER, while the heat loads by photons are higher in EUROFER and lower in water. When both are summed, there is not a sizable difference between the total heat loads in EUROFER and water. These nuclear heat loads were used as input in the thermal analysis.

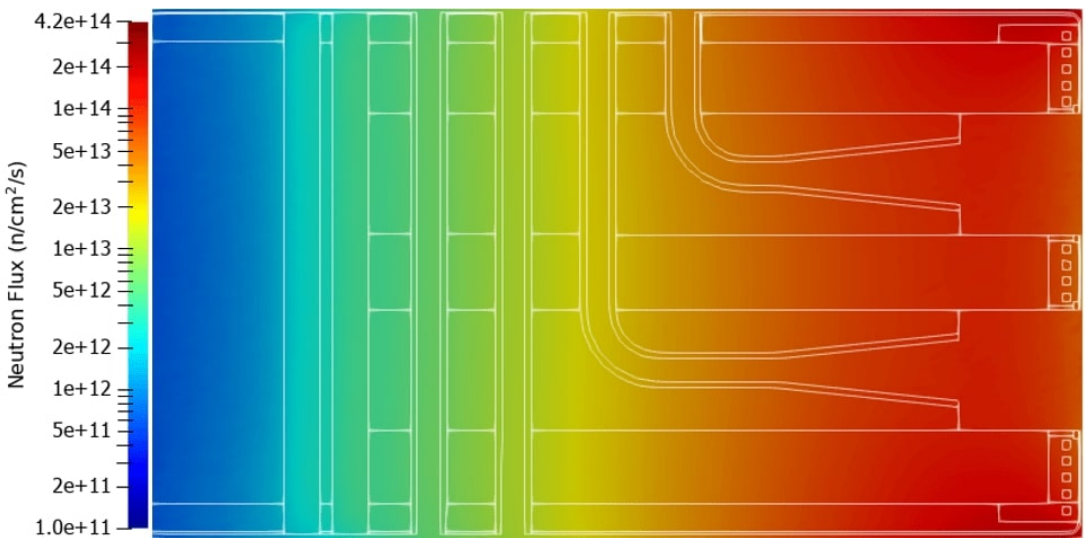

Figure 7.9: Neutron fluxes (n/cm^2/s) in the DSC module.

7.3.2 Plasma thermal radiation

From this calculation, a maximum heat flux of 316 kW/m^2 was obtained, as presented in Figure 7.13. To improve the clarity, a narrower scale is provided on the right, which shows the effectiveness of the 10 cm cube carved in the first wall to reduce the thermal loads on the antennas.

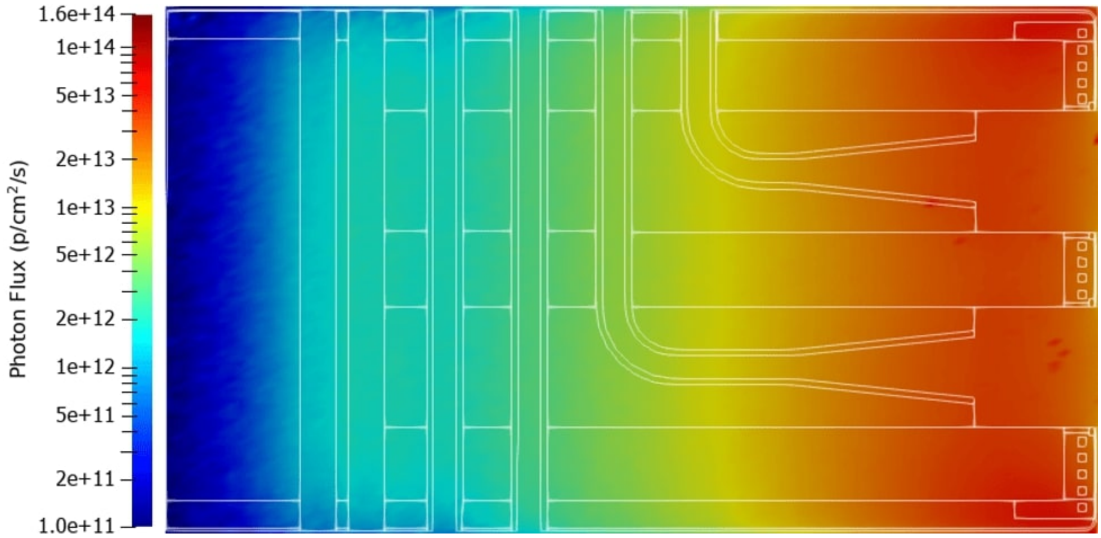

Figure 7.10: Photon fluxes (n/cm^2/s) in the DSC module.

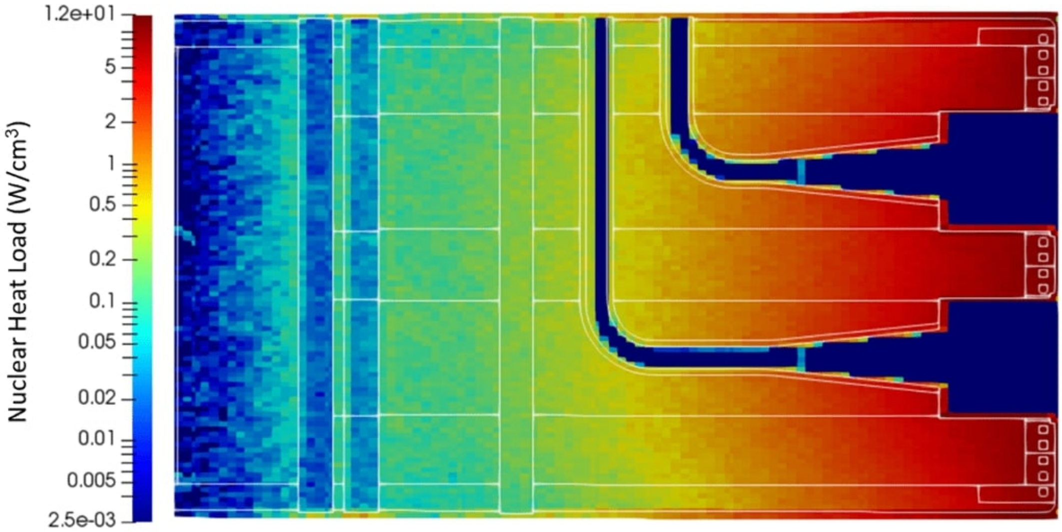

Figure 7.11: Nuclear heat loads (W/cm^3) in the DSC module.

7.3.3 Mesh convergence test

In order to determine the element size of the mesh, a convergence analysis was performed for the WG section. This was done using the model previously described and the Multizone method [186]. The mesh system of the DSC solid components is presented in Table 7.2 and details of the mesh system can be found in Table 7.1.

In order to save time, the convective heat transfer of the mesh convergence study was modelled using a constant value for the film coefficient (13 019 W/m^2°C) assuming a constant bulk temperature of the water coolant (304.11 °C). These values were obtained from an initial coupled thermal simulation with arbitrary mesh size.

From Table 7.2, it is possible to verify that the results of the maximum temperature are sensitive to the mesh size and start to converge for element sizes smaller than 5 mm. Since the difference between the maximum temperature values obtained with an element size of 5 and 4.75 mm is small, it was decided to use an element size of 5 mm throughout the analysis. The mesh system details are illustrated in Figure 7.14

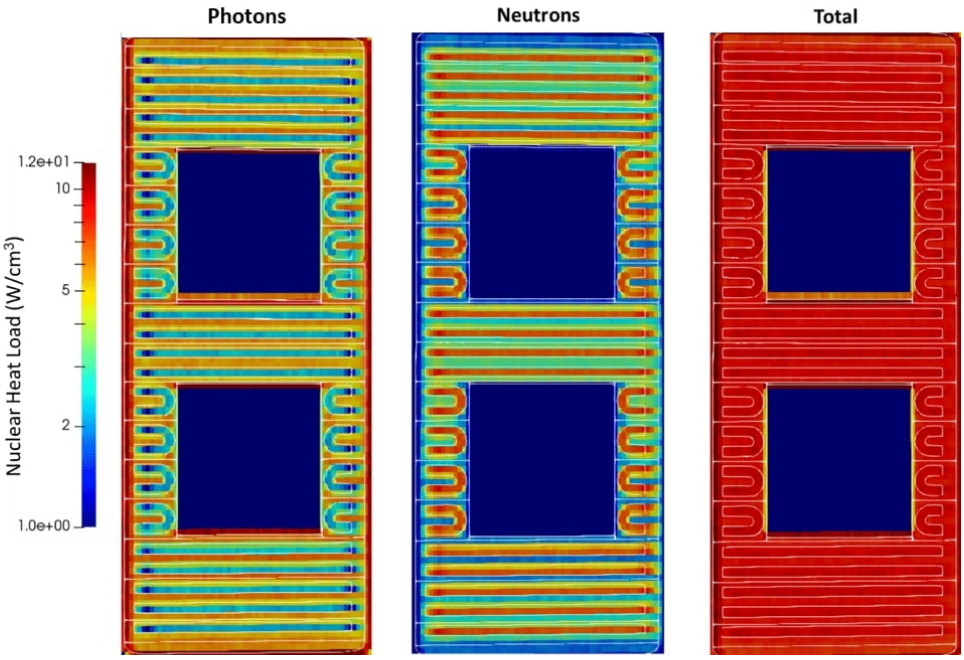

Figure 7.12: Nuclear heat loads (W/cm^3) in the front of the DSC module.

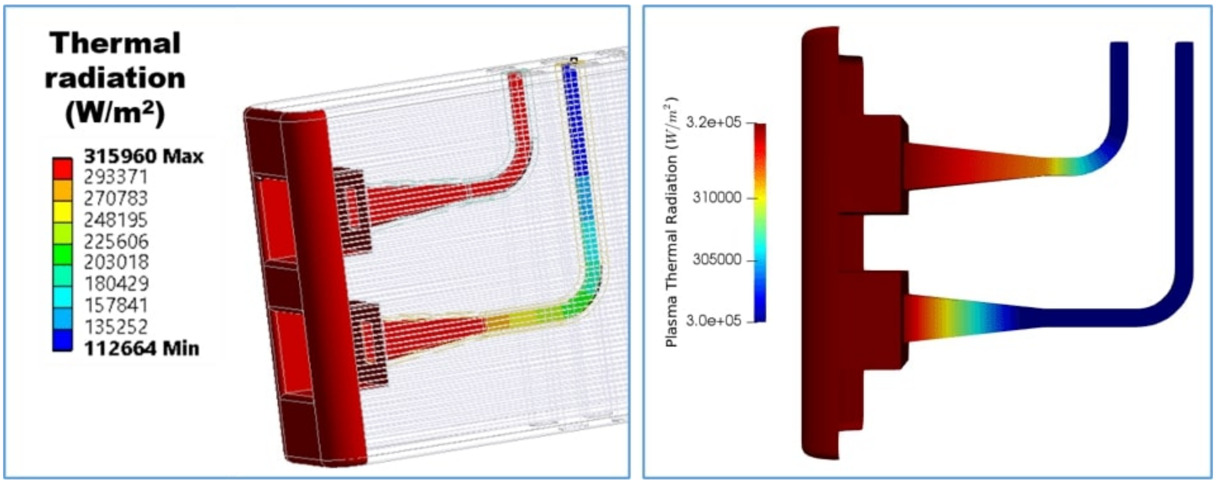

Figure 7.13: Thermal radiation from the plasma to the DSC surfaces. Left: ANSYS output. Right: same results plotted with a narrower scale using Paraview [243] [244].

Table 7.1: Mesh system description.

Part	**Meshing method**	**Body size** (mm)
Antennas	Multizone	2.5
Waveguides	Multizone	2.5
Tungsten armour	Multizone	2.5
DSC	Multizone	5

Figure 7.15 shows the element quality (see Section 4.7.2) of the FEM of the DSC for a mesh with an element size of 5 mm, along with the one from the CFD model of the water coolant. As can be observed,

Table 7.2: Mesh convergence test results for the DSC module.

Body size (mm)	**14**	**12**	**8**	**7.5**	**5**	**4.75**
$\mathbf{T_{max}}$(°C)	591.93	607.55	607.79	608.39	613.71	615.96

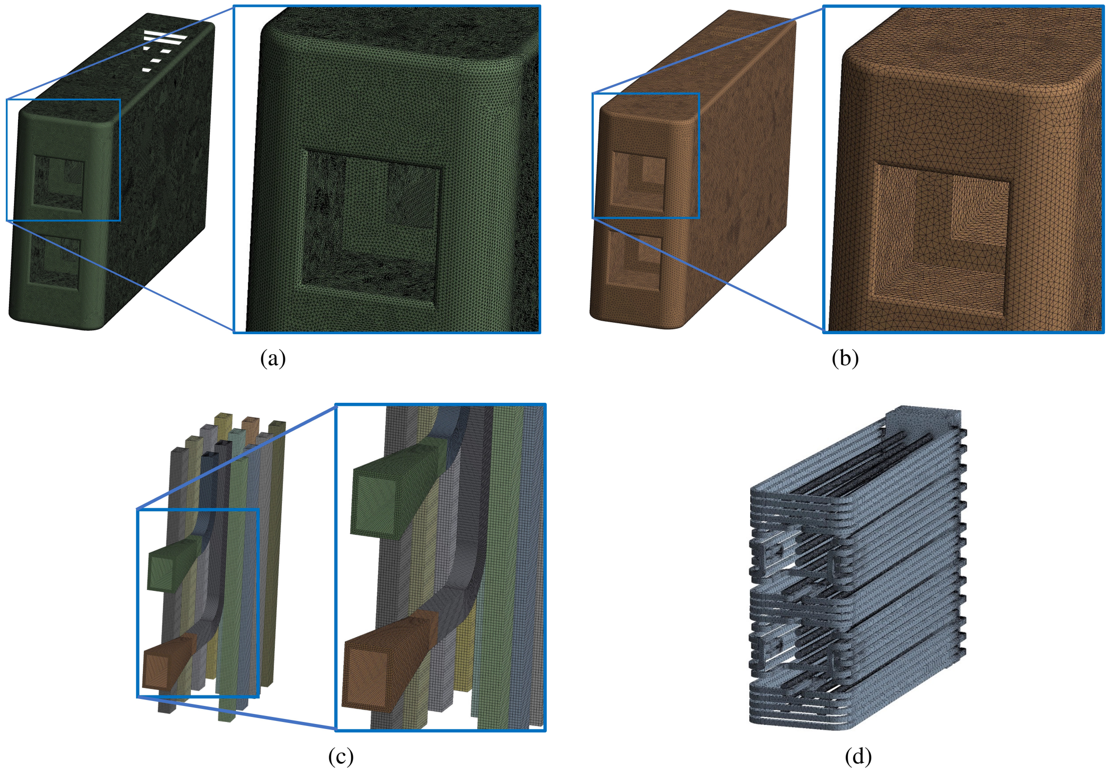

Figure 7.14: Mesh details of the (a) Tungsten armour; (b) Shielding block; (c) Antennas and waveguides; (d) Water coolant.

the majority of the elements are Tet10, described in Section 4.7.1. This is due to the complexity of the DSC geometry, which requires tetrahedral elements. Since the majority of the elements are Tet10, it is wise to check the average skewness value of the mesh system. The average skewness value of the solid part of the DSC is 0.30, while the one of the water coolant is 0.22. This corresponds to good and excellent quality, respectively (see Table 4.7).

7.3.4 Coupled thermal-CFD analysis

The operation temperatures obtained with the current design of DSC module are presented in Figure 7.16. The maximum temperature is 996 °C, obtained at the tips of the reflectometry antennas and on the walls that surround them. This is because the edges of the antennas are sharp and located too far away from the shielding block cooling channels. The temperatures in the first wall, on the other hand, are much lower, below 500 °C in most of the module except for the hotspots at the top and bottom parts, which nevertheless have temperatures more than 300 °C lower than the antennas. In these simulations, the water flow rate was optimized to ensure that its maximum temperature does not reach the boiling point of water at 15.5 MPa (344.79 °C). Figure 7.17 shows that the maximum temperature in water, obtained for the first wall cooling circuit, is below 342.4 °C. This is achieved with a total mass flow rate of 4.59 kg/s in the

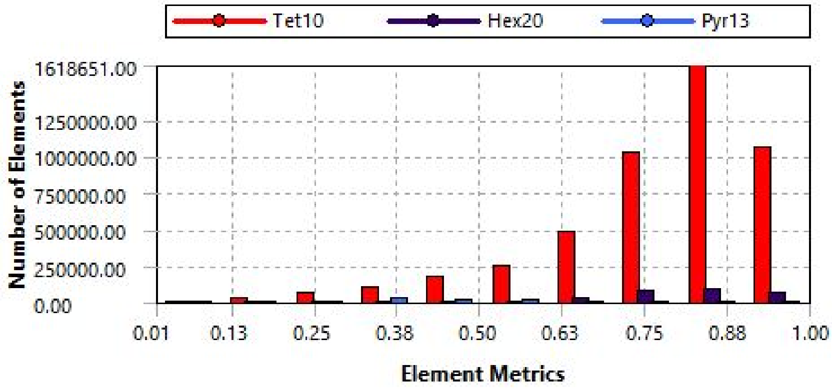

(a)

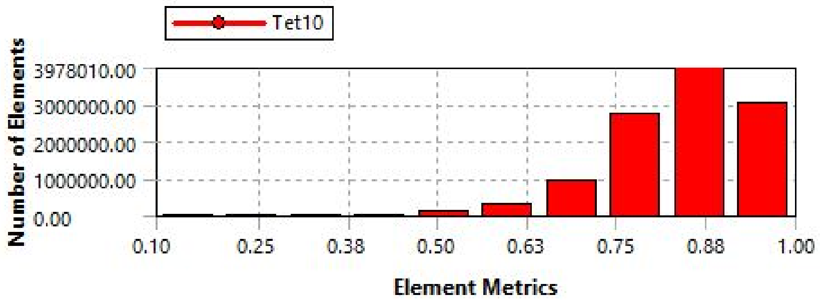

(b)

Figure 7.15: Element quality metric of the DSC: a) DSC solid; b) Water coolant.

DSC inlet. In the fill blocks cooling system, the water temperature is always below 320 °C.

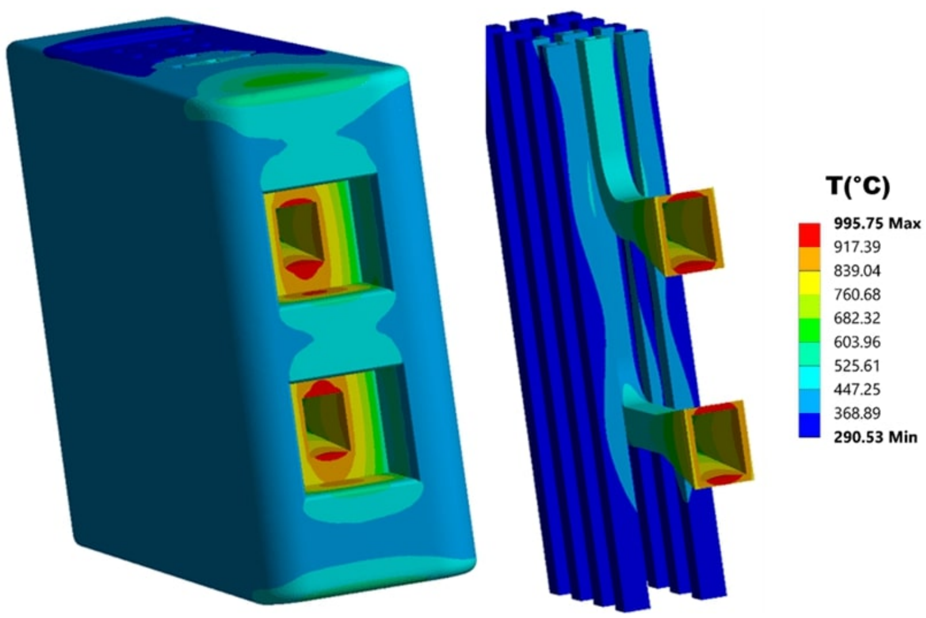

Figure 7.16: Temperature distribution (°C) in the DSC module.

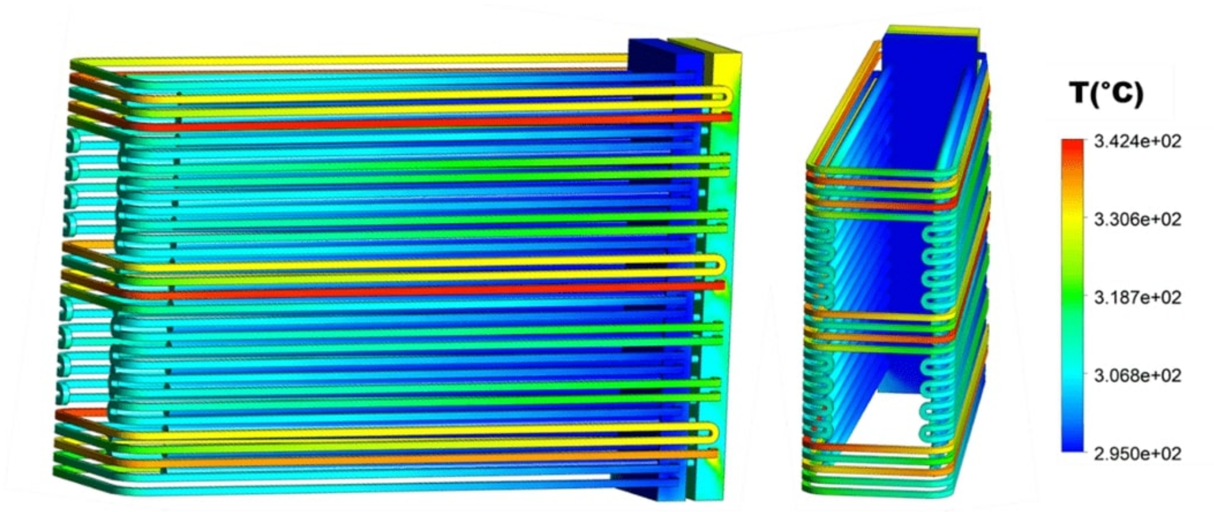

Figure 7.17: Temperature distribution (°C) in the water coolant.

7.3.5 Updated fill block cooling channels design

The results show that the operation temperature of the current DSC design is way above the maximum allowable temperature for EUROFER under neutron irradiation. Therefore, a new design of the cooling system is required, with the aim to remove the hotspots presented in Figure 7.16. This can be achieved by moving the fill block cooling channels closer to the hotspots while adjusting the length of each cooling channel to follow the DSC first wall topology. To do this, the position of the cooling channels was changed in the toroidal direction, so that in the new design the cooling channels are inserted between the waveguide rows, as shown in Figure 7.18 and Figure 7.19.

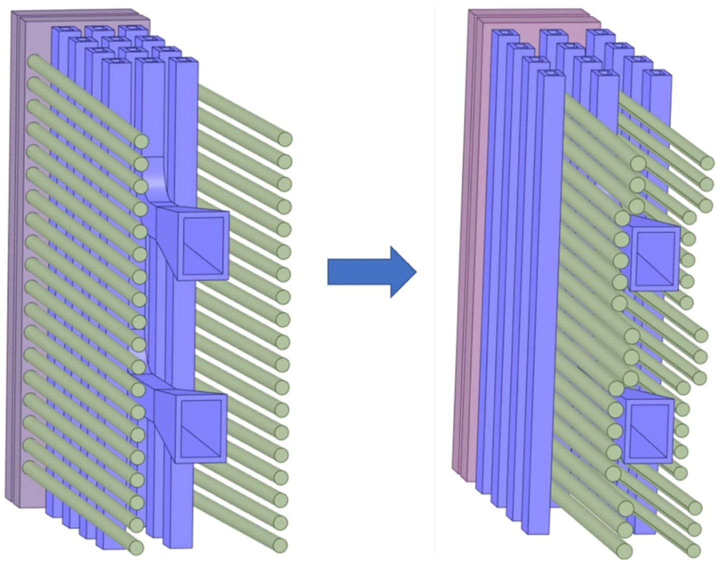
Figure 7.18: Updated design for the fill blocks cooling system.

After the change in the fill block cooling system design, a new MCNP model was created and the nuclear heat loads were recalculated, as shown in Figure 7.20. The thermal radiation from the plasma and the remaining boundary conditions, including the coolant inlet total mass flow rate, were kept unchanged, as they are not affected by the new design. In the updated thermal analysis, the maximum temperature

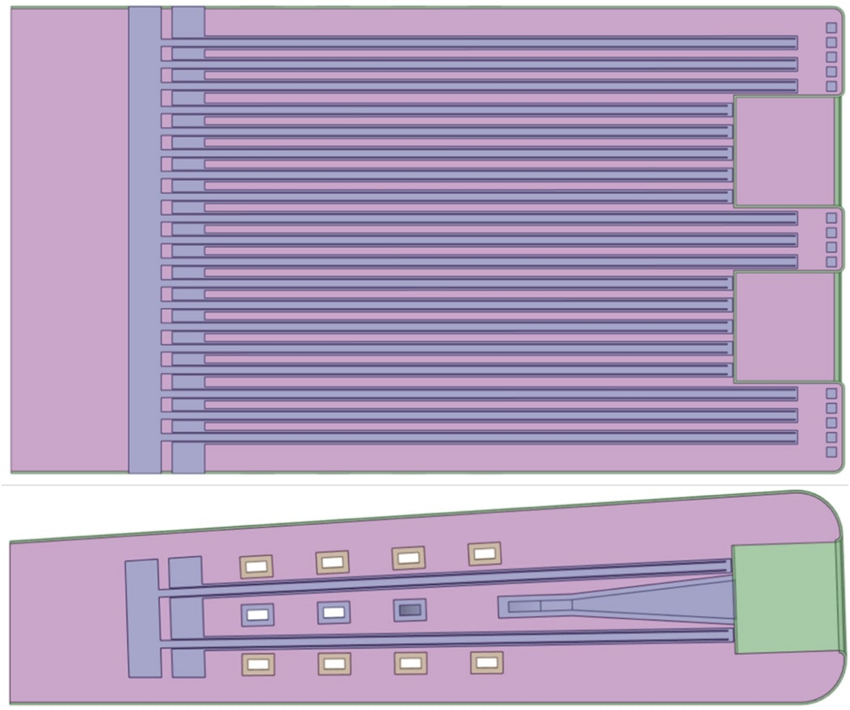

Figure 7.19: Detail of the updated design for the shielding blocks cooling system.

obtained in the DSC module was 656 °C (at the tip of the antennas), as illustrated in Figure 7.21 and Figure 7.22. Figure 7.23 shows that the temperature of water in the cooling channels remains below the boiling point.

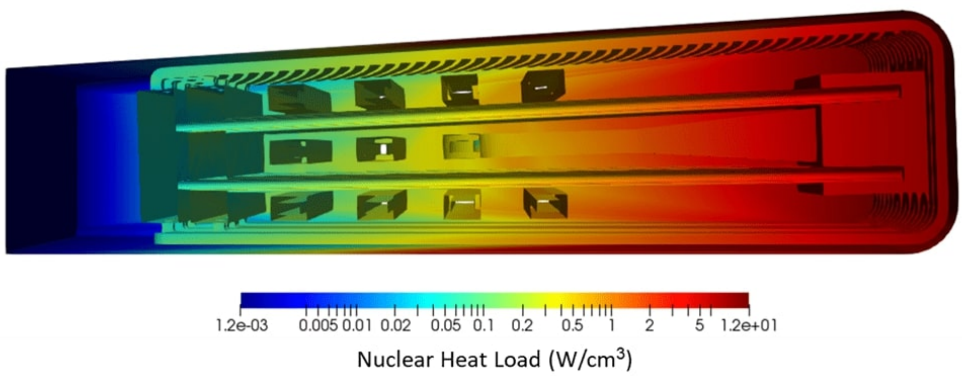

Figure 7.20: Total nuclear heat loads (W/cm^3) in the updated design of DSC module.

The maximum temperature obtained with the new configuration is more than 300 °C lower than in the previous case, which shows the effectiveness of the updated design to lower the operation temperatures close to the antennas. Furthermore, it is only $\sim$ 30 °C higher than the maximum temperature obtained in EUROFER in the thermal analyses of the HCPB BB ([245], page 27). It is also important to notice that steady-state thermal and CFD analyses like the one presented here lead to conservative estimations, when compared to the more realistic transient ones.

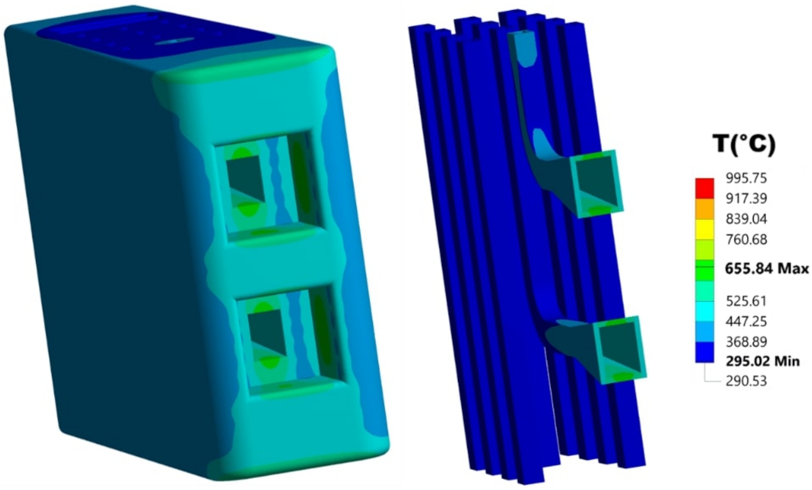

Figure 7.21: Temperature distribution (°C) in the DSC module: plasma-facing surface(left) and antennas and WGs (right).

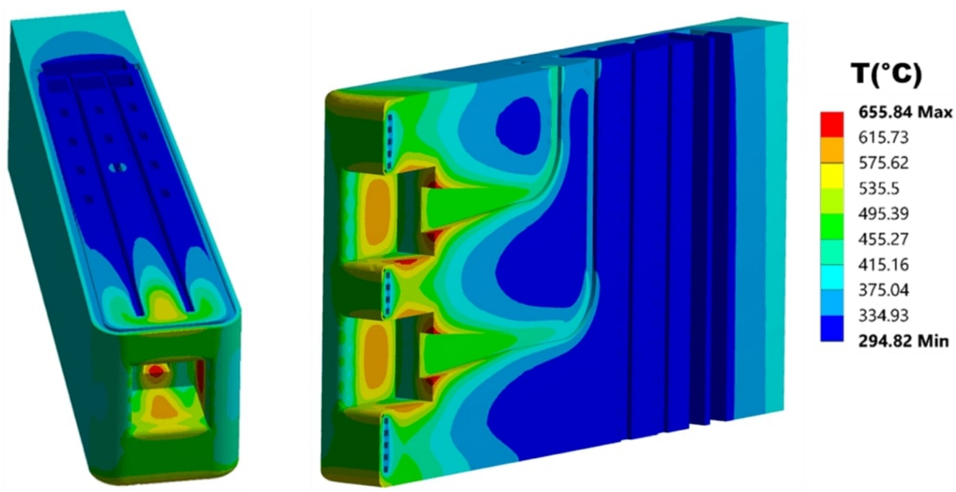

Figure 7.22: Temperature distribution (°C) in the DSC module: toroidal (left) and poloidal (right) cuts.

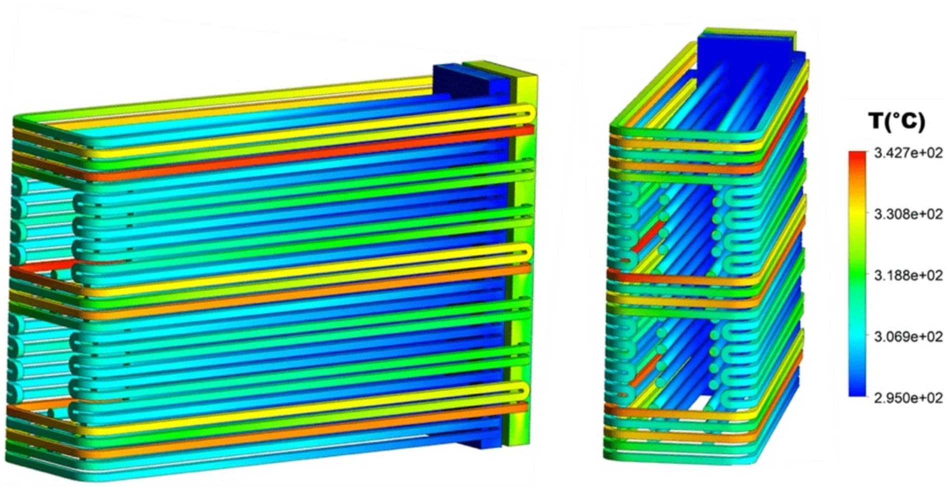

Figure 7.23: Temperature distribution (°C) in the updated cooling system.

7.3.6 Updated first wall cooling channels design

In the results presented in the Section 7.3.5 there are hotspots (see Figure 7.24) with temperatures more than 100 °C above the maximum operation temperature of EUROFER (550 °C), located at the tips of the antennas and surrounding surfaces. Optimizing the fill block cooling channels did not remove these hotspots since they are difficult to reach by the fill block cooling without compromising the structural integrity of the DSC. Thus, a new design of the FW cooling system is required, with the aim to bring the temperatures in these hotspots below the limit for EUROFER under irradiation. As Figure 7.24 shows, the FW cooling pipes need to be rerouted to cover the surfaces of the cube carved between the antennas and the FW.

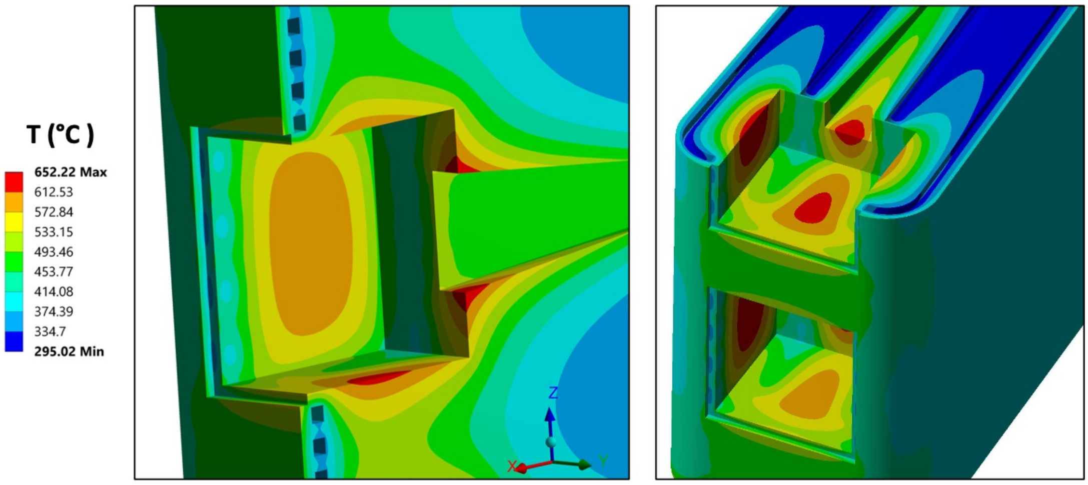

Figure 7.24: Hotspots in EUROFER around the antenna.

Several iterations on the cooling system design were simulated in ANSYS [197]. The most relevant ones are presented in Figure 7.25. The first one reroutes two of the cooling pipes in each antenna opening, such that they pass below and above the antenna, and fold the cooling channels on the side of the cavity to reach the hotspots in the middle of the cavity side surfaces. This reduced the temperatures close to the antenna but not enough to comply with the limit, while the hotspots on the top and bottom surfaces of the cavity still remained. In addition to that, folding the cooling channels responsible to cool the side walls of the cavity lead to new hotspots in the FW. In the remaining two configurations there are several changes, mostly to bring some of the pipes to the five surfaces of the cube cavity. The one on the right is shown in more detail in Figure 7.26, in comparison with the previous configuration. With this configuration the hotspots were removed everywhere except in the antennas, where it was not possible to bring the temperatures below 550 °C. As with the remaining plasma-facing components, this shows that the antennas need to be made of tungsten instead of EUROFER. This is not only because tungsten has a higher temperature limit (1300 °C), but also because it acts as a thermal shield for the EUROFER components behind it, which would also have temperatures above 550 °C if the antennas were not made of tungsten.

Using the updated cooling system design, the DSC module segment located at the equatorial plane IB (G14) will have a maximum temperature of 656 °C in the tungsten FW layer, as shown in Figure 7.27. The maximum is obtained in the surface surrounding the antenna; everywhere else, the temperatures are below 550 °C. The antennas reach 581 °C.

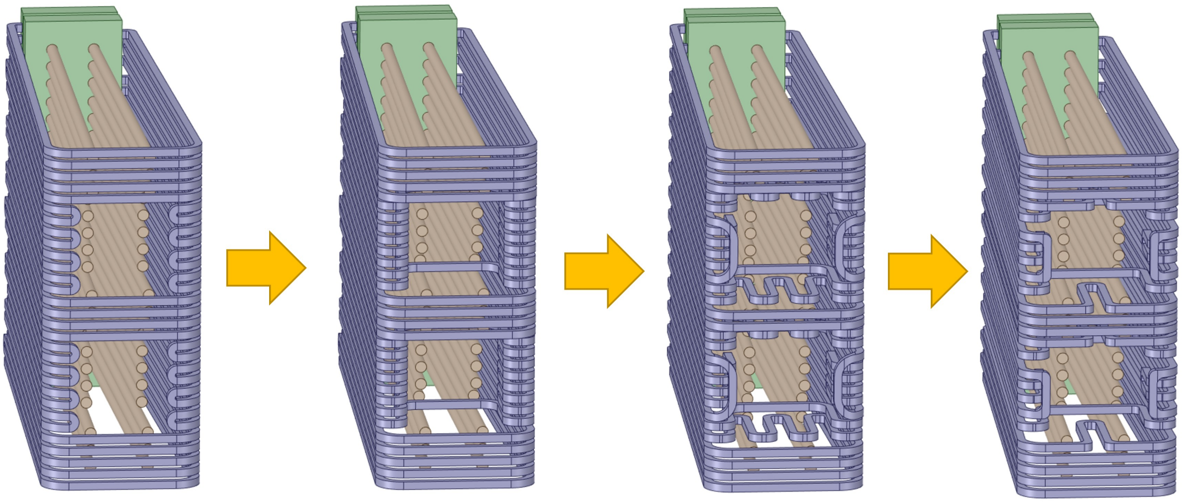

Figure 7.25: DSC cooling channel optimization iteration.

The maximum operation temperatures in EUROFER, shown in Figure 7.28 and Figure 7.29, are below 550 °C everywhere in the DSC module and comply with the limit. There are still hotspots at the edges of the FW opening, but with temperatures below 541 °C. The updated cooling system brings the EUROFER operation temperatures down by more than 100 °C.

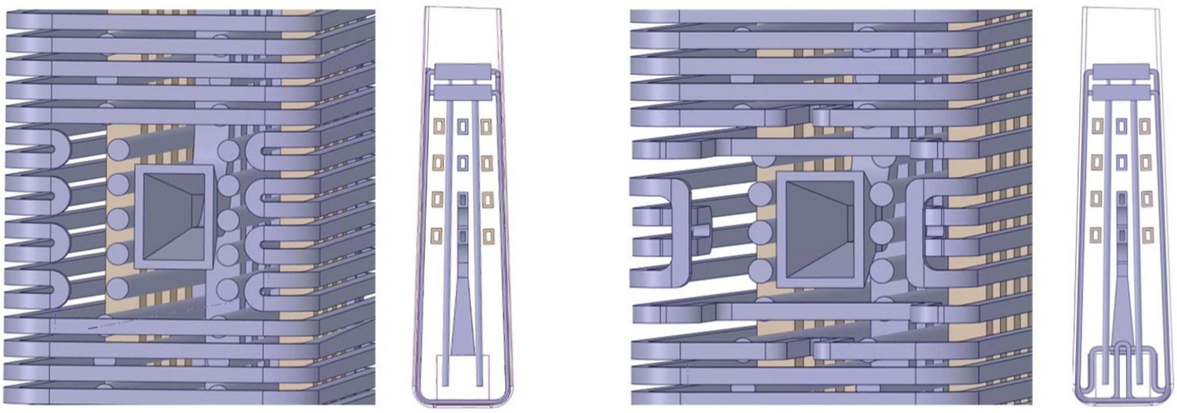

Figure 7.26: Comparison between cooling pipe configurations.

The maximum temperature reached by the water coolant is 326.4 °C (see Figure 7.30), which is very close to the 328 °C outlet temperature foreseen for the WCLL blanket, whose thermodynamic cycle is based on PWR conditions, with the water coolant entering at 295 °C and exiting at 328 °C, at 15.5 MPa [242]. This means that with this design the coolant will be close to the ideal outlet temperature for which the energy conversion system is optimized for [246]. Another important result is the maximum velocity of the water coolant inside the cooling channels, also shown in Figure 7.30. It is expected to be 3.81 m/s, much lower than the limit of 7 m/s [247] established to prevent erosion.

From the previous results for the equatorial plane IB module, the maximum temperatures at the different gaps can be approximated using the neutron wall load ratios calculated in [247] (page 221). These ratios were used to scale the nuclear heat load map of gap G14, presented in Figure 7.20. New simulations were run for the boundary conditions of each gap. The maximum temperatures obtained in these simulations are presented in Table 7.3. In summary, the maximum temperature in EUROFER is always

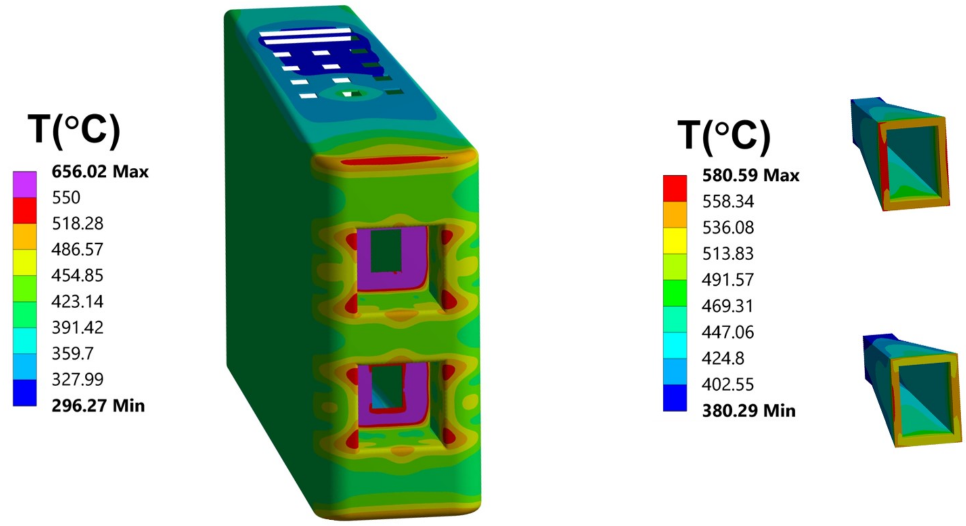

Figure 7.27: Operation temperatures (°C) in tungsten, in FW layer.

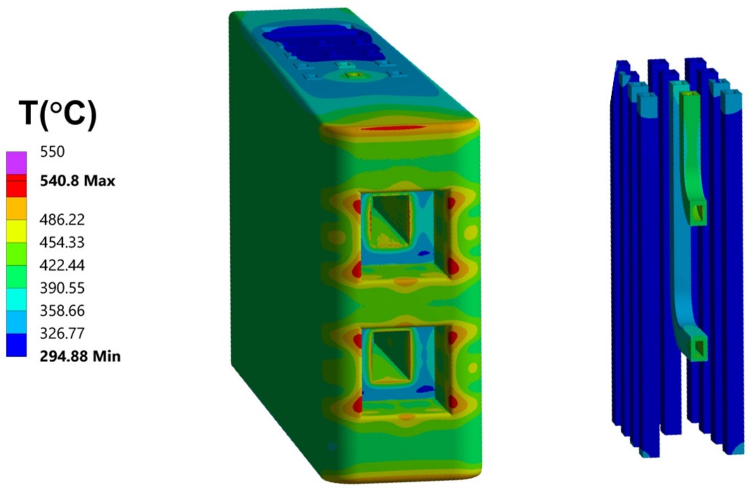

Figure 7.28: Operation temperature (°C) in the DSC module. Left: EUROFER shielding. Right: WGs.

below the limit for EUROFER under irradiation. These results show that with relatively simple changes to the cooling system design it is possible to comply with temperature limits for all the materials in the DSC.

7.4 Structural analysis of the DSC module

In order to evaluate the thermo-mechanical behaviour of the DSC module, a simplified geometry was prepared by removing the tungsten layer, simplifying fillets and corners, using symmetry boundary conditions in several locations [245, 247] and reducing the size of the geometry to only a quarter of the DSC module (see Figure 7.31).

The boundary conditions applied to the geometry are 1) symmetry in the poloidal direction on the top and bottom surfaces, to model the SMS structure of the DSC, and 2) symmetry in the toroidal direction, to model the other half of the DSC structure, as shown in Figure 7.32 and following the boundary conditions

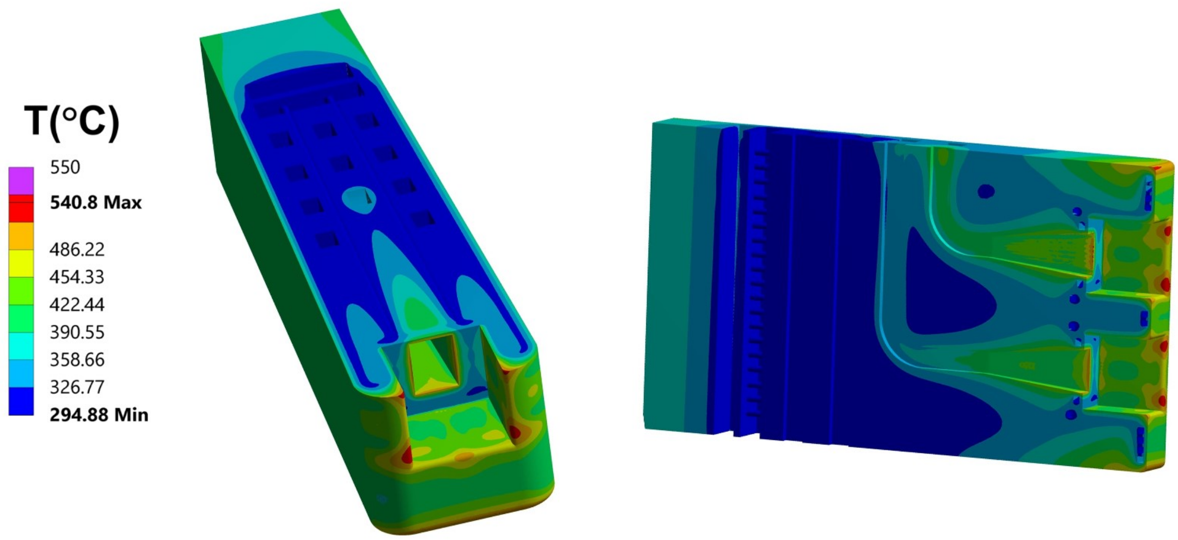

Figure 7.29: Temperature distribution (°C) in the DSC module: toroidal (left) and poloidal (right) cuts.

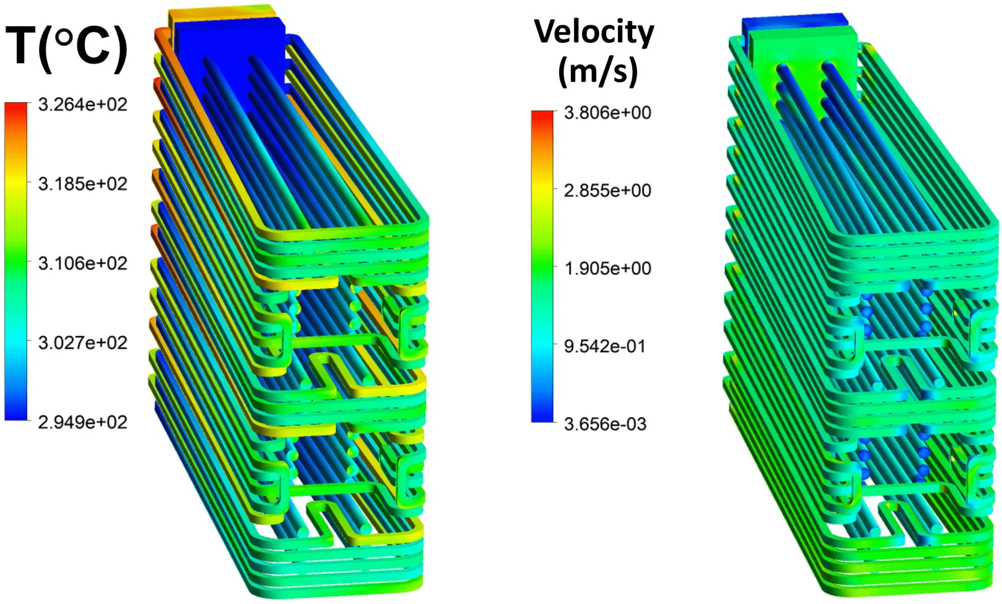

(a) (b)

Figure 7.30: Cooling system of the DSC: (a) Temperature distribution (°C); and (b) Velocity distribution (m/s).

applied in [245, 248]. A fixed support constraint was applied on the single middle edge located on the toroidal symmetry surfaces (see Figure 7.33). This constraint models the unity of this geometry and its symmetry counterpart. This boundary constraint also means that the deformation result will be relative to this edge position, as shown in the results of [245], where the maximum deformation of the model is in the order of 1.4 mm instead of 16.5 mm as reported in [249]. A frictionless support was applied to the back surface of the geometry, to provide some degree of freedom on the poloidal direction, following [245] (see Figure 7.33).

In order to calculate the primary and thermal stresses (secondary stresses) in the DSC, multiple loads were applied to the DSC following the operation case of [250], which means that only thermo-mechanical

Table 7.3: Estimated maximum temperatures at the 16 gap positions foreseen for reflectometry. The neutron wall load ratios were obtained from [247].

Location	**Ratio**	T_{max}(°C)			
		W layer	**W antennas**	**EUROFER**	**WGs**
Gap 01	0.682	641.50	570.49	532.80	476.24
Gap 02	1.073	658.07	582.53	542.65	480.95
Gap 03	1.205	661.77	586.03	547.97	482.78
Gap 04	1.209	661.92	586.18	549.20	482.85
Gap 05	1.164	660.62	584.95	546.28	482.21
Gap 06	1.164	660.62	584.95	546.28	482.21
Gap 07	1.055	657.55	582.05	542.18	480.69
Gap 08	0.886	652.76	577.49	537.83	478.28
Gap 09	0.886	652.76	577.49	537.83	478.28
Gap 10	0.700	641.99	570.97	533.27	476.50
Gap 11	0.500	635.94	564.97	527.39	473.18
Gap 12	0.705	642.12	571.09	533.39	476.56
Gap 13	0.977	655.38	579.99	540.22	479.61
Gap 14	1.000	656.02	580.59	540.80	479.93
Gap 15	0.764	643.74	572.65	534.90	477.39
Gap 16	0.409	633.44	562.57	525.06	471.90

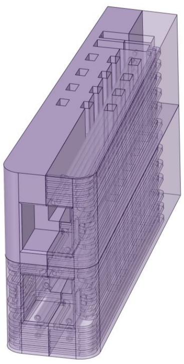

(a)

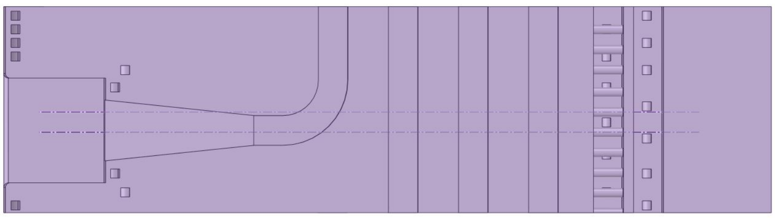

(b)

Figure 7.31: The reduced geometry: (a) placed together with the original geometry (in transparency); (b) side view of the reduced geometry and its discontinuous region.

loads, coolant pressure and gravity were considered. The gravity load was modelled by applying a standard earth gravity of 9.8066 m/s^2. The coolant design pressure of 15.5 MPa was multiplied by a safety factor of 1.15, resulting in a total of 17.825 MPa applied to the wetted surfaces of the cooling channels inside the DSC module (see Figure 7.34), following [251]. Finally, the temperature map from the thermal

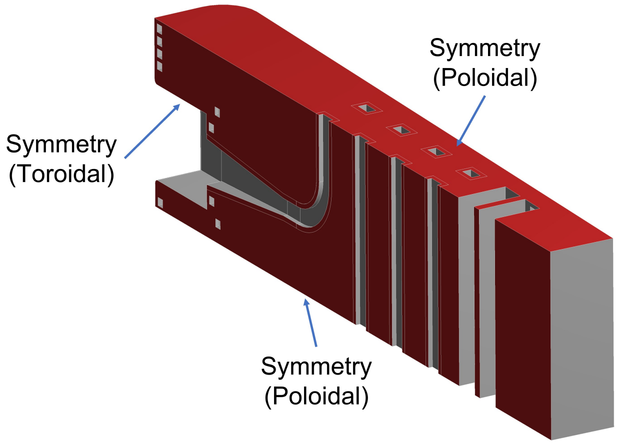

Figure 7.32: Symmetry boundary conditions of the DSC module based on a sliced unit.

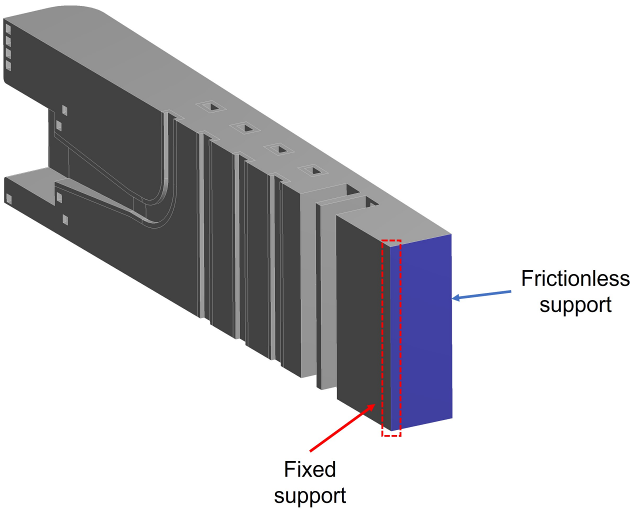

Figure 7.33: Support boundary conditions of DSC module based on a sliced unit.

analysis (see Figure 7.28) was imported as a thermal load.

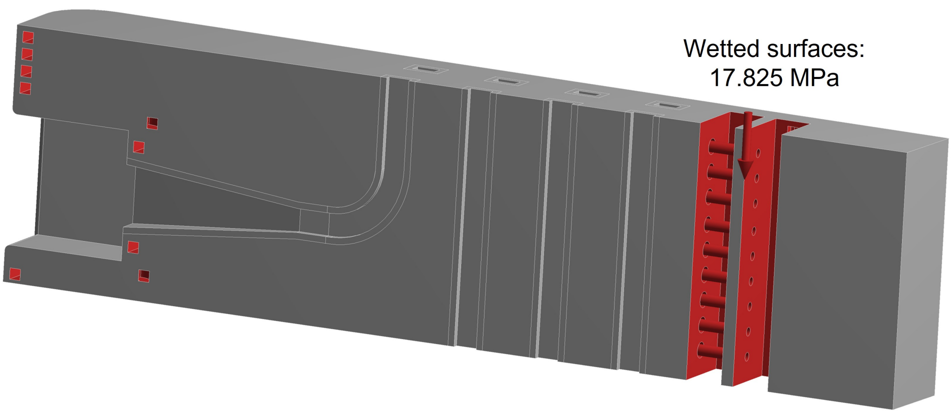

Figure 7.34: Pressure load on the DSC module based on a sliced unit.

The calculated equivalent Von Mises stress distribution of the P+Q stresses (see Section 4.1.3) is presented in Figure 7.35. Direct observation reveals that the stress distribution is mostly concentrated in the antenna apertures, due to the thermal stresses. The other factor affecting these results is the temperature gradients between surfaces of the DSC module: a temperature difference between close surfaces will result in a steeper gradient (and therefore higher stresses) than a similar temperature difference between surfaces which are further apart. This is the reason why the locations of the maximum stresses are not exactly the same as the locations of the maximum temperatures.

Following the procedure of [252] to assess the thermo-mechanical loads based on the Stress Linearization (SL) of the stress tensor on a path defined along the thickness of a region where the Von Mises stresses are higher. Therefore, the critical areas in the DSC module geometry were identified by looking closely to the Von Mises stress field presented in Figure 7.35. As expected, the region close to the plasma-facing component has the highest stresses and becomes the critical area. The paths chosen for the analysis are according to the supporting line segment definition presented in Section 4.1.2.

The paths for stress assessment on the simplified geometry of the DSC module are presented in Figure 7.36. To calculate the stress on these paths, line integration and stress breakdown were done inside ANSYS, following Equations (4.1)–(4.4). In order to prevent Immediate Plastic Collapse (IPC) and Immediate Plastic Instability (IPI), the criteria in Table 4.5 were used. The results of these calculations were then compared to the stress limit presented in Table 4.5. These stress assessments with regard to the RCC-MR level A criteria are presented in Table 7.4.

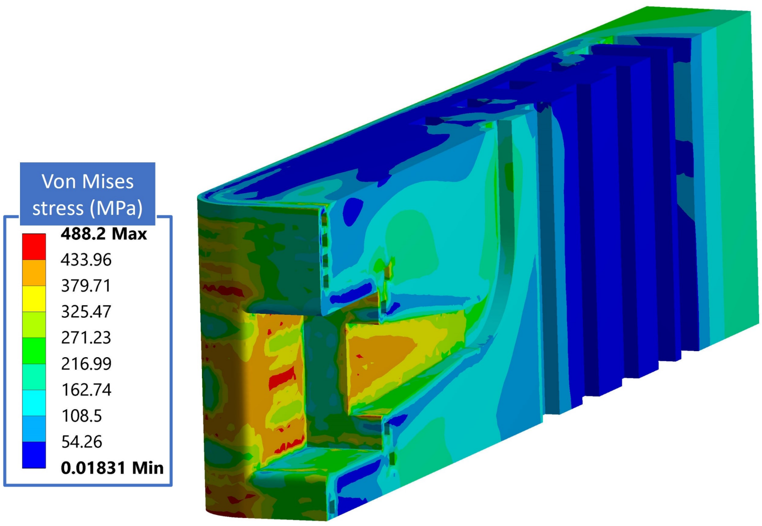

Figure 7.35: Equivalent von Mises stress (MPa) of the sliced unit of the DSC module.

The results of the stress linearization for Immediate Plastic Collapse and Immediate Plastic Instability are in line with the results of the cases presented in [247] for the WCLL BB. This is expected, since the dimensions of the FW cooling channels were adopted from the WCLL design. Regarding the Immediate Plastic Flow Localization test, the results show that the current design is expected to withstand the primary and secondary loads without compromising the structural integrity of the DSC. Furthermore, since the results presented in Table 7.4 comply with the RCC-MR level A criteria, the safety of the components for the specified operation throughout the DSC lifetime is ensured.

Regarding the Fill Block (FB) cooling channels, though they are inspired by the design of the HCPB BB, there are a few differences. In the HCPB BB, the FB channels are used to breed tritium and consist of metallic (solid and liquid) and ceramic materials. These compositions create additional stress because of the differential thermal expansion between materials. In the DSC, however, the FB channels are used only

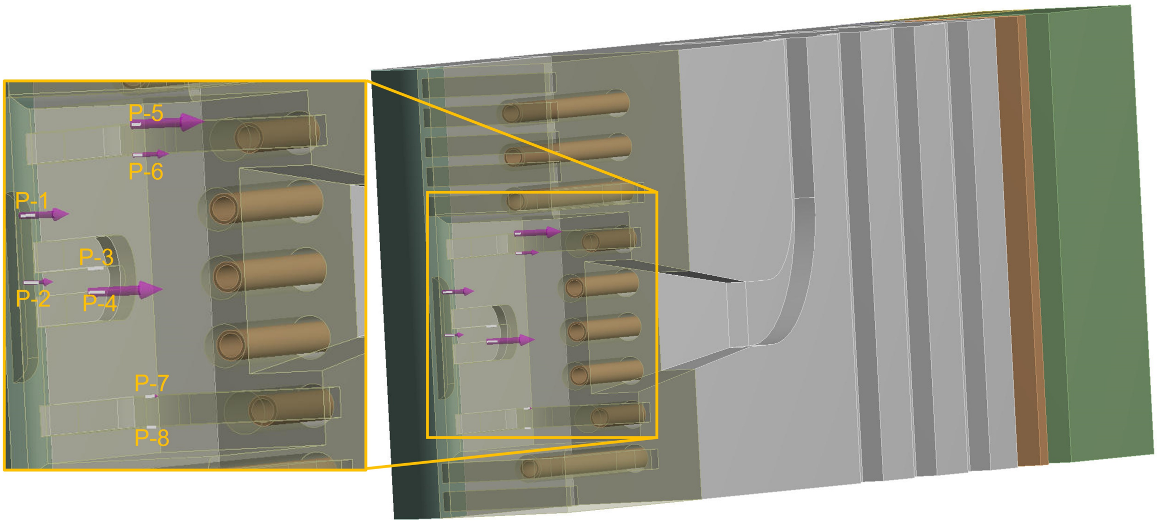

Figure 7.36: Layout of the stress linearization.

Table 7.4: Results of stress linearization of critical region compared with RCC-MR level A.

Path	**T$_{avg}$** (°C)	**Immediate Plastic Collapse**			**Immediate Plastic Instability**			**Immediate Plastic Flow Localization**		
		Value (MPa)	**Limit** (MPa)	**Ratio**	**Value** (MPa)	**Limit** (MPa)	**Ratio**	**Value** (MPa)	**Limit** (MPa)	**Ratio**
P-1	451.5	20.4	157.0	0.13	37.5	235.4	0.16	411.3	470.9	0.87
P-2	429.5	22.7	163.2	0.14	37.0	244.8	0.15	401.6	489.6	0.82
P-3	381.4	19.1	175.4	0.11	31.4	263.1	0.12	430.4	526.2	0.82
P-4	382.6	20.2	175.1	0.12	34.6	262.6	0.13	434.2	525.3	0.83
P-5	377.9	26.4	176.2	0.15	41.6	264.3	0.16	402.4	528.6	0.76
P-6	395.4	31.0	172.0	0.18	45.3	258.1	0.18	389.9	516.1	0.76
P-7	397.0	30.3	171.7	0.18	44.2	257.5	0.17	371.5	515.0	0.72
P-8	380.2	30.5	175.7	0.17	47.6	263.5	0.18	374.0	527.0	0.71

for cooling purposes and the material is EUROFER. Therefore, the thermal expansion is more uniform in the DSC. The thermal stress distribution in the FB region of the DSC module is thus lower than the one expected for the HCPB BB. This is the reason why the current HCPB design does not satisfy the level A criteria of RCC-MR.

7.5 Impact of dpa on the DSC module structural integrity

The dpa (radial profile) in gap G14 of the DSC, calculated in a previous work[7] [253] for two irradiation phases, is presented in Figure 7.37. Phase 1 corresponds to the 1st DEMO operation phase (continuous operation over 5.2 calendar years (CYs) at 30% of the nominal fusion power (2000 MW of output power), leading to 1.57 full power years (FPY), while phase 2 corresponds to the 2nd DEMO operational phase

[7] These simulations were conducted by A. Lopes and R. Luís at IPFN.

(continuous operation over 14.8 CYs at 30% of nominal fusion power), leading to a total of 4.43 FPYs. This means that the DSC FW in gap G14 will experience 20 dpa after the 1st DEMO operational phase and 50 dpa after the 2nd DEMO operational phase. As mentioned in Section 1.5, these dpa values may compromise the integrity of the diagnostic system by causing swelling, hardening and embrittlement of the materials. Thus, a structural assessment taking this parameter into account is paramount.

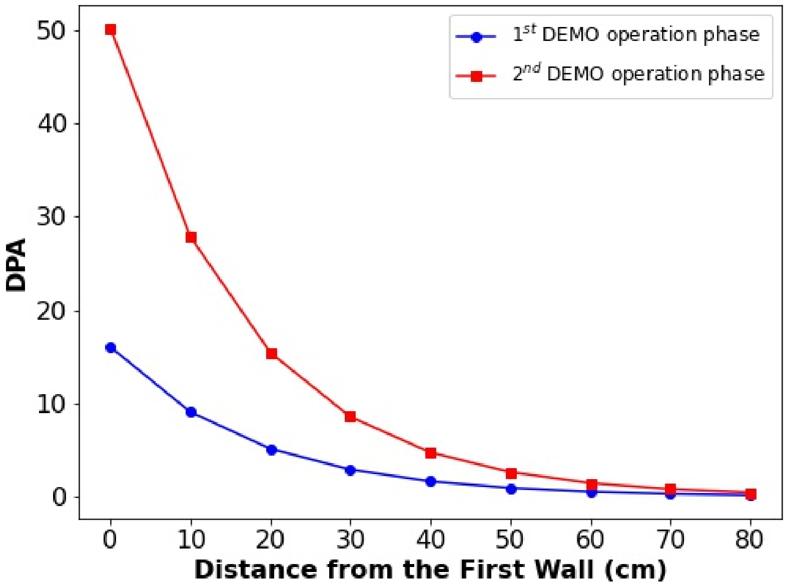

Figure 7.37: dpa in the DSC (poloidal plane view) [253].

Currently, the data for the swelling and embrittlement of EUROFER are limited and cannot be included in the current work. However, the data related to dpa-dependent material hardenning of EUROFER, though limited to low irradiation temperatures, can be extrapolated to get some insight on the effects for the operation temperatures foreseen for the DSC, with some assumptions. The first assumption is that the polynomial function used to calculate the yield strength and the ultimate tensile strength (see Table A.14 and Table A.15) for temperatures lower than 350 °C can be extended to the range of interest. The second assumption is that, in case the dpa value of interest is not in the DEMO material database, it can still be approximated by linear summation of the following functions and coefficients

$$\mathrm{F_c} = (\mathrm{C_1 F_1}) + (\mathrm{C_2 F_2})\,, \tag{7.1}$$

where $\mathrm{F_1}$ and $\mathrm{F_2}$ are polynomial functions available in the database and $\mathrm{F_c}$ is the yield strength or tensile strength in the case of interest. Coefficients $\mathrm{C_1}$ and $\mathrm{C_2}$ can be rewritten as:

$$\mathrm{C_1} = 1 - \left| \frac{\mathrm{d_c} - \mathrm{d_{lim1}}}{\mathrm{d_{lim1}} - \mathrm{d_{lim2}}} \right| \tag{7.2}$$

and

$$\mathrm{C_2} = 1 - \left| \frac{\mathrm{d_c} - \mathrm{d_{lim2}}}{\mathrm{d_{lim1}} - \mathrm{d_{lim2}}} \right| \tag{7.3}$$

where $\mathrm{d_c}$ is the dpa value of interest and $\mathrm{d_{lim1}}$ and $\mathrm{d_{lim2}}$ are the dpa limits in the range with unavailable data closest to the dpa value of interest.

The steady-state results presented in Section 7.4 are conservative and the conclusions are still valid in the case in which the dpa are considered, since they are based on the assumption that the loads have zero time derivative, which is usually an asymptotic case. On the other hand, the stress limit value of RCC-MR is a transient function, since it is dependent on the amount of dpa, which is time-dependent. Therefore, comparing steady-state results with a transient limit is a very conservative approach.

It can be seen from Figure A.1 and Figure A.3 that the yield strength (R_{p02}) and the tensile strength (R_m) increase with the accumulated irradiation value. These two quantities are the contributors to the stress limit (S_m) value, as presented in Equation (A.12). Therefore, it can be said that the components that passed the level A criteria without considering the dpa will still pass the level A criteria for irradiated materials at the end of the component lifetime, since the stress limit increases with the dpa. The results of this analysis are presented in Appendix C.1. The impact of material swelling and embrittlement has not been considered in this thesis and is left for future works with transient analyses.

7.6 Discussion of the Results

The performance of the DEMO reflectometry system depends on the active cooling, which allows to control the operation temperature of the DSC which hosts the WGs and antennas required for the reflectometry measurements. As shown in the previous section, besides acting as a heat source, neutron irradiation also contributes to change the properties of the materials used for the in-vessel components of DEMO (i.e. BB, DSC, VV, and other diagnostics).

A thermo-mechanical study was performed for a section of the DSC located on the high-field side at the equatorial plane (a location of high neutron flux on the high-field side). This study started with the design of a cooling system with the aim to ensure operation temperatures below the material limits under irradiation. This design was then optimized using steady-state coupled thermal-CFD analyses, performed with ANSYS Workbench. Very high temperatures, up to 1000 °C, were obtained with this preliminary design, well above the temperature limit of EUROFER, with the hot-spots located around the antennas. In a second iteration, the maximum temperature in the DSC module was reduced to 656 °C, which is still 100 °C above the limit for EUROFER (550 °C).

Further iterations on the cooling channel design of the DSC, focused on the hotspots, showed that it is not possible to maintain the operation temperatures below 550 °C when the antennas of the DSC are made of EUROFER. Therefore, tungsten, which will also be used in the 2 mm plasma-facing layer of the DEMO BB, is proposed to replace EUROFER in the antennas (with a thickness of 1.57 mm). This is because tungsten has a higher temperature limit (1300 °C) than EUROFER and, besides, will act as a thermal shield for the EUROFER behind it. By changing the material of the antennas, the maximum operation temperature estimated for the DSC was brought down to 541 °C in EUROFER, 656 °C in the tungsten layer, and 581 °C in the tungsten antennas. These results clearly show the effectiveness of the cooling channel design. With the latest cooling channel design, the maximum velocity of the coolant is just half of the maximum allowable coolant velocity and the outlet temperature of the water coolant is only 2 °C below the desirable outlet water temperature, which is important because the power conversion system of DEMO is optimized for PWR conditions. These results were then extrapolated to the other segments of the DSC across the poloidal plane. With this extrapolation it was found that the maximum temperature of the whole DSC is kept under 550 °C, including in the location with highest nuclear wall loading (gap G4).

Using the temperature maps obtained in the thermal analysis, a structural integrity assessment was performed using a quarter of the previous DSC module and with symmetry boundary conditions, both under normal operation and after long irradiation periods. The thermo-mechanical assessment under normal operation allowed to conclude that the current design already complies with the RCC-MR level A criteria for the P-type damage, which ensures the safety of the DSC under the specified operation condition throughout its lifetime. A thermo-mechanical assessment after cumulative radiation exposure was done in parallel, resorting to the material properties database of DEMO. It should be highlighted that there is still a lack of material properties data related to the dpa values expected for DEMO operational phases. Notwithstanding, approximations for the yield strength and the tensile strength were assumed using the available data. These two quantities increase with the dpa, which means that the current design will also stay below the stress limit at the end of the DEMO operation phases, according to RCC-MR. This assessment was performed for dpa values of 20, 50, and 70, which corresponds to the 1st DEMO operation phase, the 2nd DEMO operation phase, and the entire lifetime of DEMO. In face of these promising results, similar approaches to the cooling system design can be adopted by other diagnostics that consider the DSC as a possible integration approach.

Overall, the results presented in this chapter should be used as guidelines for other diagnostics that consider the DSC as a possible integration solution (i.e. ECE system [204]). These studies provide a thorough analysis process, encompassing CAD design, neutronics simulations, and thermo-mechanical analyses. Even if the cooling system design needs to be adapted in the future due to integration constraints with the DEMO BB, the results quantify the cooling needs of the DSC and illustrate the main challenges to overcome when addressing them. With the current assumptions, the proposed cooling system is able to keep the DSC operations temperatures within the limits without compromising the mechanical integrity of the system. This work should be extended in the future to include material fatigue and cyclic (S-type) loads.

Chapter 8

Integration studies for the Diagnostics Slim Cassette

As mentioned in Section 6.2, there are several considerations to be taken for the integration of the DSC in DEMO. Assuming the designed cooling system can provide sufficient cooling and ensure a reasonable temperature gradient, the integration of the DSC in the DEMO tokamak is still constrained by other factors, which include the design and segmentation of the BB, compatibility with the RH system and the space availability in the UP. Among these, there are different integration approaches for the DSC with respect to the BBs, which condition the integration with the remaining in-vessel systems: the DSC could be (i) handled independently of the BB, (ii) attached to the BB segment, or (iii) integrated with the BB, in which case it would share the FW and the cooling water manifold with the BB.

This chapter discusses the following integration aspects, which affect the design of the DSC:

1. Possible locations.
2. Integration with the UP.
3. Integration with the WCLL blanket.
4. Compatibility with the RM system.

The following section provides an explanation and possible solutions for the integration issues mentioned above.

8.1 DSC integration

8.1.1 Possible locations for the DSC

Two approaches were followed for the integration of the DSC with the DEMO BBs: (a) with the IB and OB sections of the DSC aligned in the same radial plane; (b) with a non-co-planar splitting of the IB and OB sections of the DSC – the IB section inserted (in a radial plane) to the left/right wall of the RIBS/LIBS and the OB section aligned parallel to the lateral parallel walls of the ROBS/COBS/LOBS (see Figure 6.2). The possible locations arising from these two approaches are depicted in Figure 8.1, where the (200 mm wide) DSC is presented in purple, the EP plug is delimited by a yellow line, and the UP aperture on the VV is delimited with a red line.

It was concluded in [205] that the most favourable DSC location follows configuration (6.2) of Figure 8.1. This configuration has The IB and OB sections of the DSC in different vertical planes, and minimizes the number of operations needed to remove the DSC. If the DSC were to be manipulated independently of the blanket, this configuration would allow the removal of OB section of the DSC with all five BB segments still in place and could allow the removal of the IB section of the DSC after removing just the COBS. If the DSC were to be attached to the BB, this configuration would allow the replacement of both sections of the DSC after the removal of just two of the OB BB segments. Splitting the DSC into two poloidal planes also facilitates the avoidance of the EP. Misaligning the IB and OB segments of the DSC does not compromise the performance of reflectometry diagnostic, since the probing Electromagnetic (EM) waves from each antenna cluster are reflected back when they find a layer of the plasma with the same cut-off frequency, as explained in Section 2.1. However, the resulting toroidal shift of the two sections should be taken into account when performing correlation studies between the HFS and the LFS plasma.

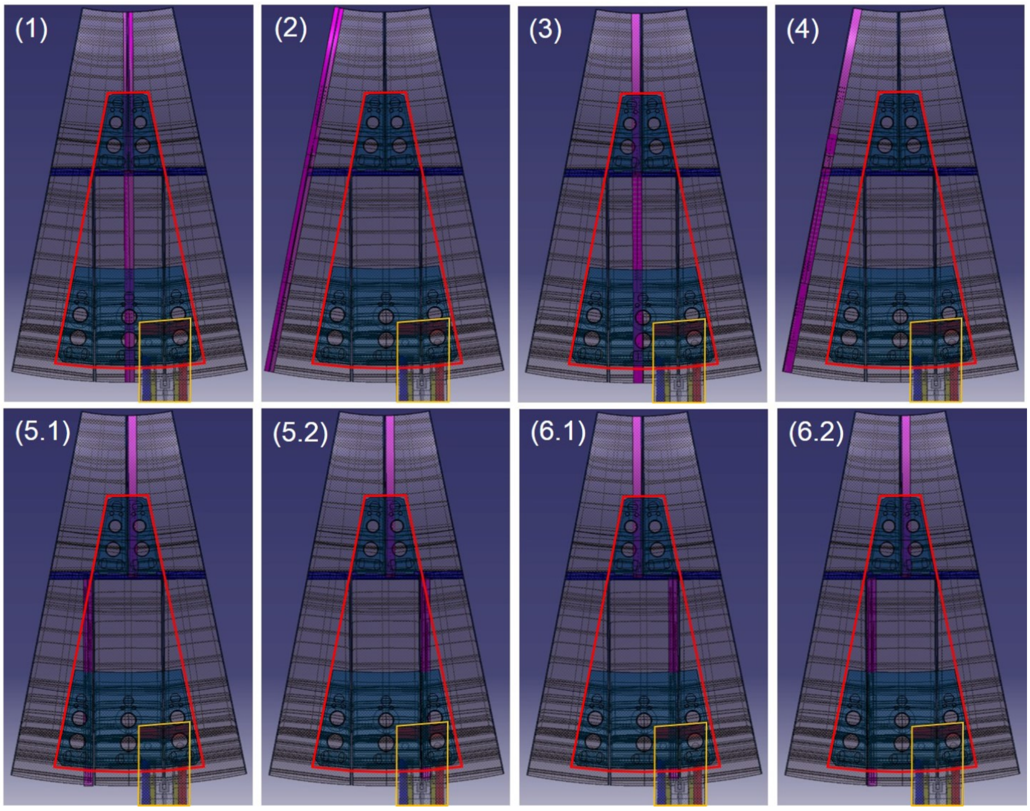

Figure 8.1: Possible locations for the DSC regarding integration with the BB (taken from [205]). The DSC is presented in purple, the EP plug is delimited by a yellow line, and the UP aperture on the VV is delimited with a red line.

8.1.2 DSC Integration with the UP

From the discussion in Section 6.1, the DSC can be divided into three sections: the IB, the OB, and the "keystone", as depicted in Figure 8.2. The DSC is expected to house the front-end components of the reflectometry system, leaving most of its components in the ex-vessel. Therefore, the design of the WG extensions, which route the microwaves between the DSC and ex-vessel components, is mandatory. The routing of these interfaces is affected by the RH operation sequences and by the space availability in the "chimneys', which were not designed with the presence of diagnostic components in mind. A preliminary sketch of the WG extensions that connect the DSC with the ex-vessel, with the WGs grouped inside, is presented in Figure 8.2.

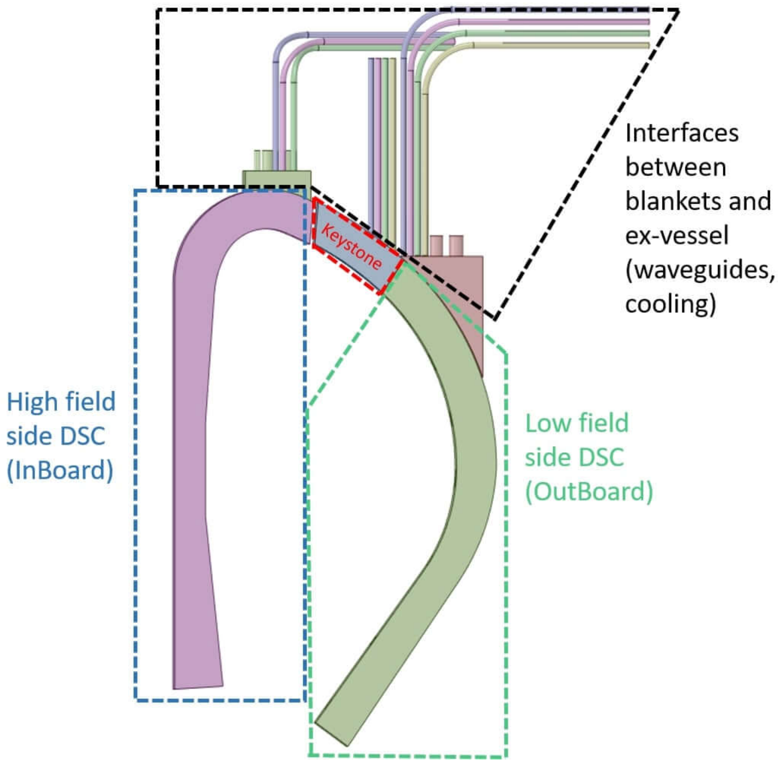

Figure 8.2: The three-section DSC: the IB, the OB, and the keystone, as well as the corresponding WG interfaces with the ex-vessel.

An early concept of a WG connector to the "chimney" in the UP using a male-female socket is presented in Figure 8.3. This concept ordered the WGs in a rectangular grid with a male/female ridge/groove around each WG to reduce crosstalk between WGs. In order to align these pairs of sockets, passive alignment features such as pin/hole arrangements are used. These sockets could be then connected by welding or using a Mechanical Pipe Connection (MPC), depending on the types of interfaces considered for the BB pipes.

The concept described above is presented in more detail in Figure 8.4, where it is illustrated with the HCPB "chimney" in the IB section of the DSC. Note that the inner cross section of the WGs is 19 mm $\times$ 9.5 mm (shown in Figure 6.11), whereas the DSC is 200 mm wide. The WG pipe sockets presented in Figure 8.4 are based on the concept presented in Figure 8.3, and have a diameter of 154 mm, which can accommodate fewer WGs.

A preliminary concept for the WG modules is presented in Figure 8.5 for all three sections of the DSC, illustrated with the HCPB pipes and "chimney" concept. These supporting modules containing the WGs are expected to be integrated with the pipe modules of the BB, which, if designed with space for the WGs in mind, will allow for a much simpler design of the WG-pipe module structures, especially at the IB. It should be noted that the WG extensions (hollow pipes with stiffener plates, to increase the stability of the WGs, and pipe compensators to accommodate the relative displacements between BBs and the VV) at the IB module must be carefully considered, to avoid as much as possible any curvatures in the toroidal direction, which in turn may affect the wave propagation inside the WGs. However, in reality, these curvatures cannot be completely avoided. The reason for this is the requirement to remove the "keystone"

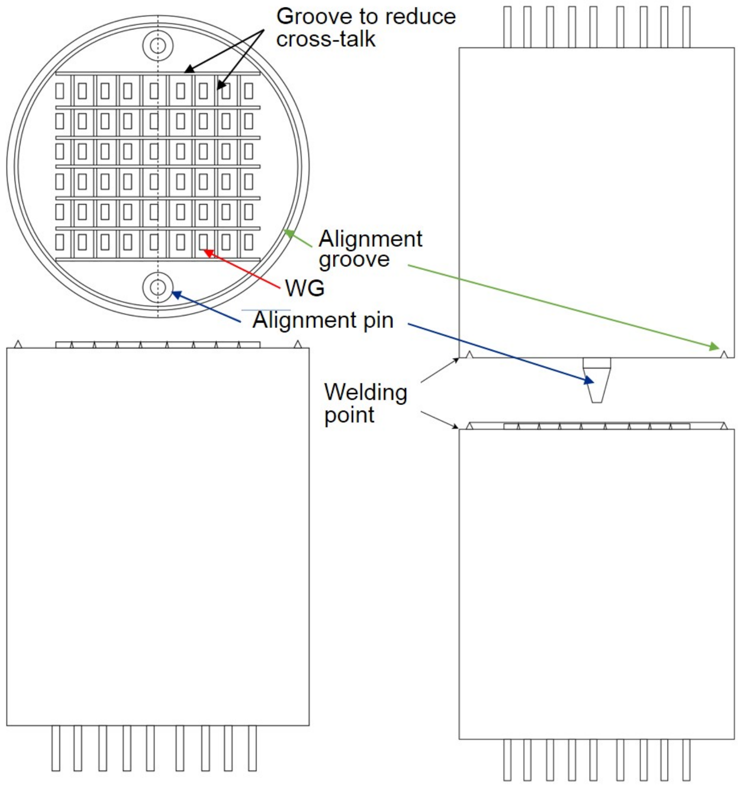

Figure 8.3: Concept of a WG male/female socket arrangement with alignment features.

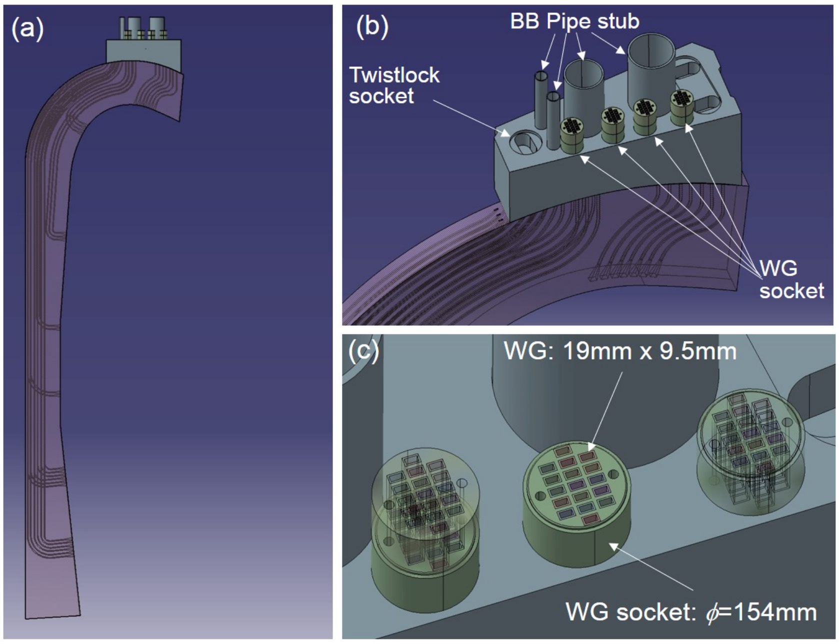

Figure 8.4: DSC with the WG interface on the HCPB RIBS chimney, in which the DSC rectangular WGs are grouped inside pipes.

neutron shield before the removal of the blanket modules and the DSC. This requirement implies that the RH tools' access to this component should not be hindered. Because of that, the design of WG extensions for the IB section of the DSC should not cross the area above the "keystone". Furthermore, in order to minimize the number of RH operations, it is wise to integrate the WG extensions into the existing pipe modules of the BB, especially at the IB. Regarding the WG extensions of the OB, the possibility of independent WG modules is not yet ruled out. The proposed WG connectors in the UP for the OB considering all these aspects are illustrated in Figure 8.6.

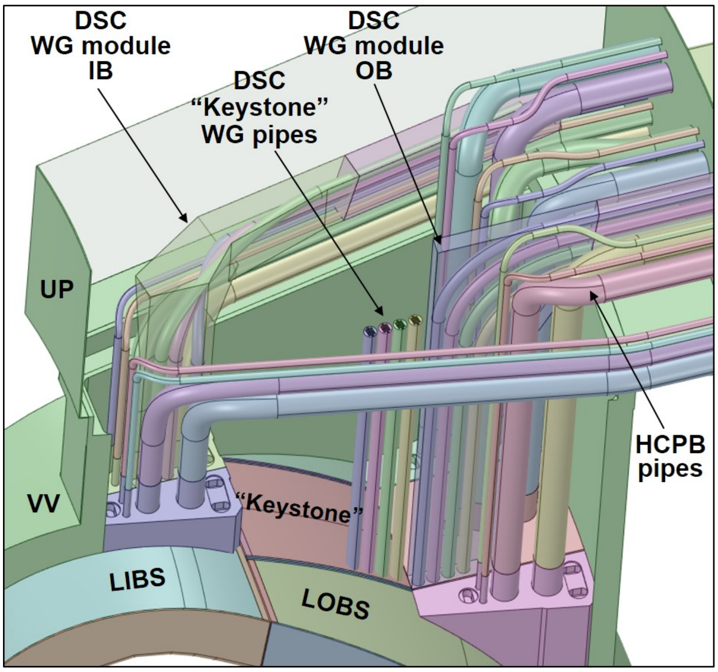

Figure 8.5: The supporting modules concept for the IB and the OB WG extensions of the DSC, including the keystone WG pipes, placed in HCPB chimneys and piping.

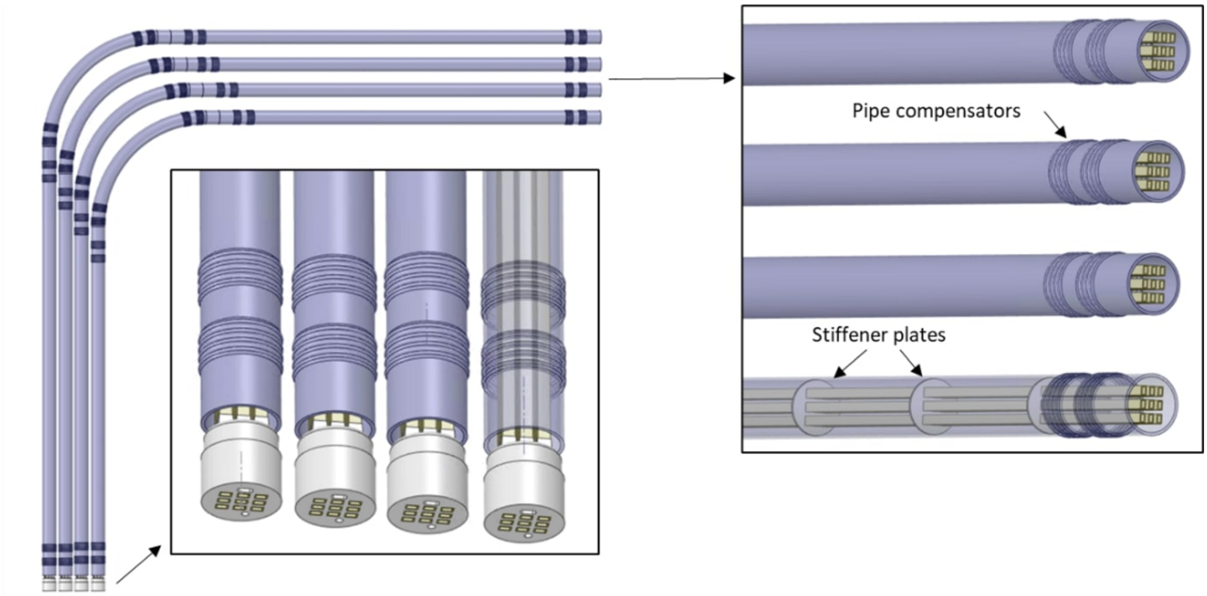

Figure 8.6: Proposed WG extensions and connectors in the UP.

Regarding the WG extension attachments, they affect the available space in the "chimneys". These attachments will require the allocation of some space and the existing "chimney" does not take the diagnostic interface into account. The WG extension attachments proposed in this work are the 154 mm diameter cylindrical pipes presented in Figure 8.4. Though a concept of these interfaces is presented here, further discussions with different work packages (Work Package Breeding Blankets (WPBB) and Work Package Remote Maintenance (WPRM)) are required to define it. The definition of these connector interfaces will also affect the space required for the support structure, since the WG extension pipes shall be integrated into the pipe module.

8.1.3 DSC integration with the WCLL blanket

There are two approaches under consideration for the integration of the DSC with the WCLL blankets, presented for illustrative purposes in Figure 8.7:

1. DSC attached in the front of the BSS (sharing the BSS and the water manifold).
2. DSC attached to the side of the BB (having its own water manifold).

As discussed in Section 6.1.2.2, the WCLL blankets have two independent cooling circuits (one for the FW-SW and the other for BZ) as highlighted in Figure 8.7 in different shades of blue. It should be noted that the current design of the DSC also has two cooling systems, one for the FW-SW (following the dimensions of the BB cooling system), the other for the shielding block FB inside the DSC, in the form of concentric cylinders in which water circulates from the outer cylinder to the inner one [254].

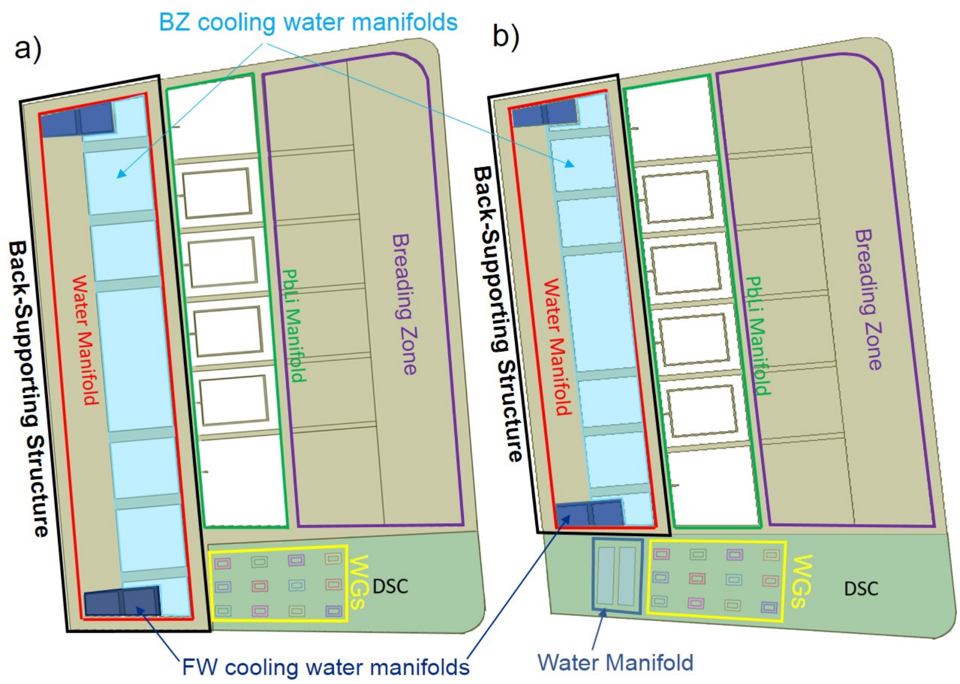

Figure 8.7: Two types of DSC (light green) attachment to the WCLL blanket (light brown), illustrated with an IB segment (cross section view): a) shared BSS; b) DSC attached to the side of BB [205].

In the case of the DSC attached to the front of the BSS, the WGs housed in the DSC will have to sit closer to the plasma, resulting in higher radiation fluxes experienced by these WGs. This approach would allow the cooling system inside the DSC to be supplied via the existing manifold in the BSS, which supplies the inlet/outlet channels to the BB cooling circuit.

Regarding the second approach, the BSS must be reduced in the toroidal direction to accommodate the space for the DSC. This implies a reduction of the BSS water manifold channels. In this case, the

WGs could be placed further back relative to the previous approach. Moreover, the cooling circuit of the DSC could be connected directly to the inlet/outlet channels of the BSS water manifold.

Irrespective of the solution proposed above, the integration of the DSC still has an open issue regarding the design of the attachment between the BB and the DSC, to ensure that both components are installed and removed as one single component compatible with RH operations.

8.1.4 Remote handling compatibility of the DSC

The DSC is expected to be removed/replaced in case of failure and also to be exchanged during routine BB replacement. Therefore, the RH compatibility of the DSC with the BB operations is paramount. Some important factors affecting the RH compatibility of the DSC are:

1. Available RH tools and interface requirements.
2. Stability and deformation of the DSC during RH operations.
3. RH procedure sequence for DSC extraction and installation.
4. Required space to perform the DSC extraction and installation.

8.1.4.1 RH tools and interface requirements

The RH tools should be able to perform the removal and installation operations of the DSC including manoeuvrering the components and the alignment and plug-in of the IB and OB segments of the DSC. Several RH tools have been studied and proposed over the years [212, 216]. It was found that the two best approaches are the HKM and the six-degree of freedom telescopic arm, both sharing the same BB interface design presented in Figure 8.8.

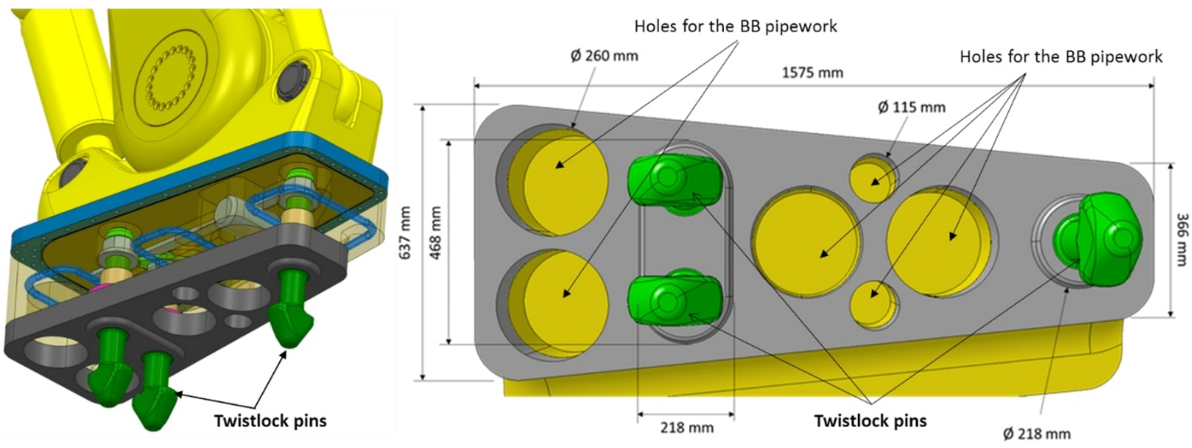

Figure 8.8: BB RM transporter interface (2014 baseline design), showing the three clamping twistlock pins (to lift the BB) and the holes to accommodate the BB pipe stubs (which protrude from the chimneys) [218].

8.1.4.2 Stability and deformation of the DSC during RH operations

A preliminary structural analysis was performed to provide a first estimate of the stability and deformation that might happen during RH operations, if the DSC has to be manipulated independently from the blanket at some point. The analysis considers the DSC as an independent slim cassette, the HKM as the RH tool, and the dimensions of the DSC as space constraints, to consider all the possibilities of RH manoeuvring needed for the DSC. The boundary conditions considered for the analysis are:

- 2 Contact Points (CPs) and 3 CPs (like in the HKM manipulator), as shown in Figure 8.9.
- Fixed support aplied to each point (to model the RH operation).
- Standard earth gravity acceleration applied to each component.

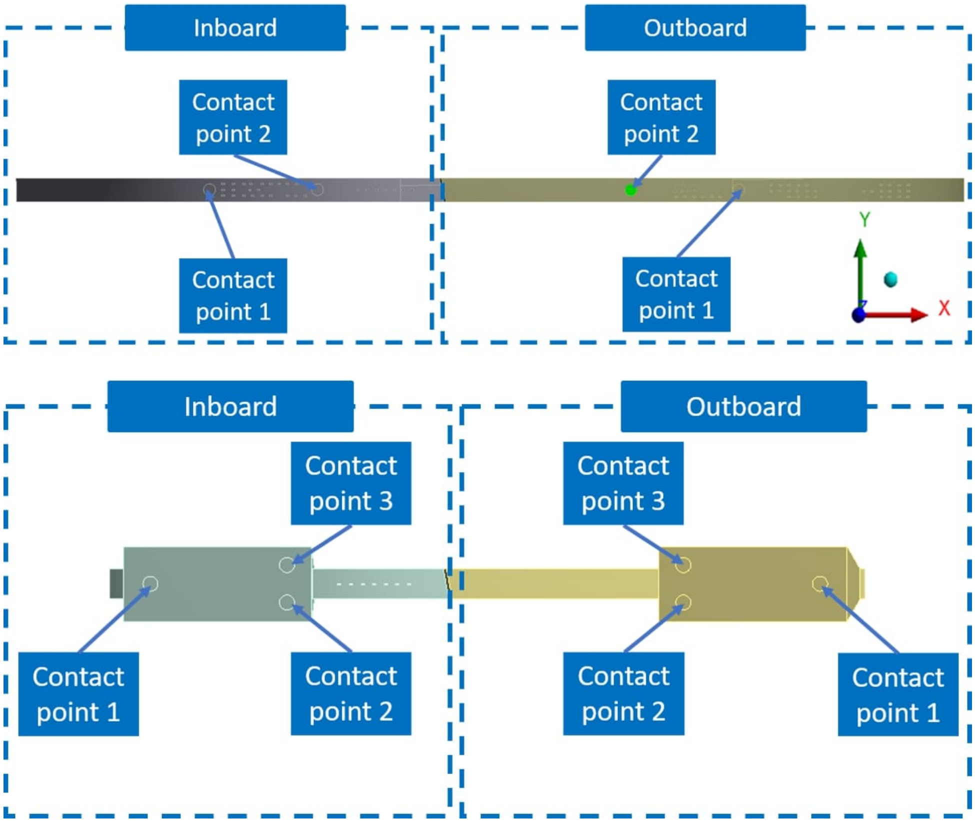

Figure 8.9: Position of the contact points used in the preliminary structural assessment of the DSC (from the Z+ point of view): using two contact points (above) and using three contact points as in the HKM manipulator (below).

The results for the total deformations along the DSC on fixed support by 2 CPs and 3 CPs during the RH operations are depicted in Figure 8.10, whereas the corresponding maximum deformations are presented in Table 8.1. Noting that the OB section of the DSC is a 12 m long component, a maximum deformation of 2.1 mm can be considered negligible, which means that the DSC is able to sustain its own weight. This deformation should occur in the elastic region of the stress-strain diagram of EUROFER; in other words, the deformation will revert back to normal after the load is released. Furthermore, assuming that the gap between neighbouring BB segments to enable RH operations of installation and extraction is 20 mm [216], a maximum deformation of 2.1 mm will not lead to contact with other IVCs. The resulting moments for the DSC presented in Table 8.2 and Table 8.3 show that the 3 CPs configuration has more stability and smaller deformation compared to the 2 CPs configuration. Yet, it has the downside of requiring additional space for the RH interface and supporting modules in the UP, which is unlikely to be granted. In the case of 2 CPs, the need for additional space for the support modules still exists, with the additional drawback that the DSC would require a custom end-effector. In summary, these results are unfavorable to the concept of a DSC independent of the blanket.

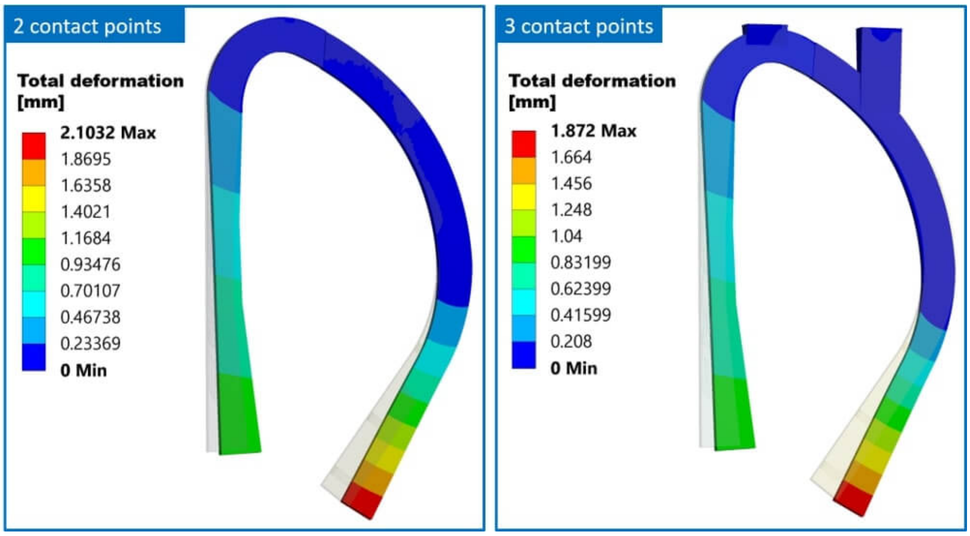

Figure 8.10: Deformation (mm) of the DSC on fixed support by 2 and 3 contact points, scale: 500.

Table 8.1: Maximum deformations (mm) of the DSC on fixed support by 2 and 3 contact points.

	Max. deformations (mm)	
	2 CP	**3 CP**
Inboard	1.12	2.10
Outboard	0.99	1.87

Table 8.2: Moments (N m) of the DSC on fixed support by 2 contact points.

		Moments (N m)		
		X-axis	**Y-axis**	**Z-axis**
Inboard	**CP 1**	-332.48	1030.90	30.78
	CP 2	-80.14	1148.00	-0.49
Outboard	**CP 1**	35.14	-37.62	-12.12
	CP 2	5.76	121.79	-2.55

8.2 New design proposed for the DSC

Based on all the considerations presented up to now, the new design proposed for the DSC is presented in Figure 8.11 (poloidal view). In the current proposal, there are 16 gaps with a variable number of antennas, based on the needs estimated for reflectometry measurements. The distribution of antennas in the FW of the DSC is based on the assumptions presented in Table 8.4, derived from ray-tracing simulations [229]. At positions closer to the equatorial plane, a pair of antennas will be enough to emit and collect the reflectometry signal, while at positions closer to the upper port or the divertor clusters of 3 to 5 antennas will be required. These dispositions will be strongly affected by the space available in the upper ports to route the WGs, especially at the inboard side. Since the WGs need to be grouped into sockets (7 in the current proposal, as shown in Figure 8.11) and routed through the BB pipe chimneys,

Table 8.3: Moments (N m) of the DSC on fixed support by 3 contact points.

		Moments (N m)		
		X-axis	**Y-axis**	**Z-axis**
Inboard	**CP 1**	-101.96	733.69	20.50
	CP 2	-1.20	955.11	31.32
	CP 3	23.08	910.18	-21.54
Outboard	**CP 1**	-7.24	-232.75	2.66
	CP 2	-41.66	-390.68	-19.35
	CP 3	16.77	-396.06	25.03

the disposition of the antennas will be affected by two constraints:

- The need to avoid clashing between WGs from different gaps in the DSC.
- The need to route the WGs through a limited number of sockets in the BB chimneys.
- The possibility of symmetrical WG distribution through the DSC.

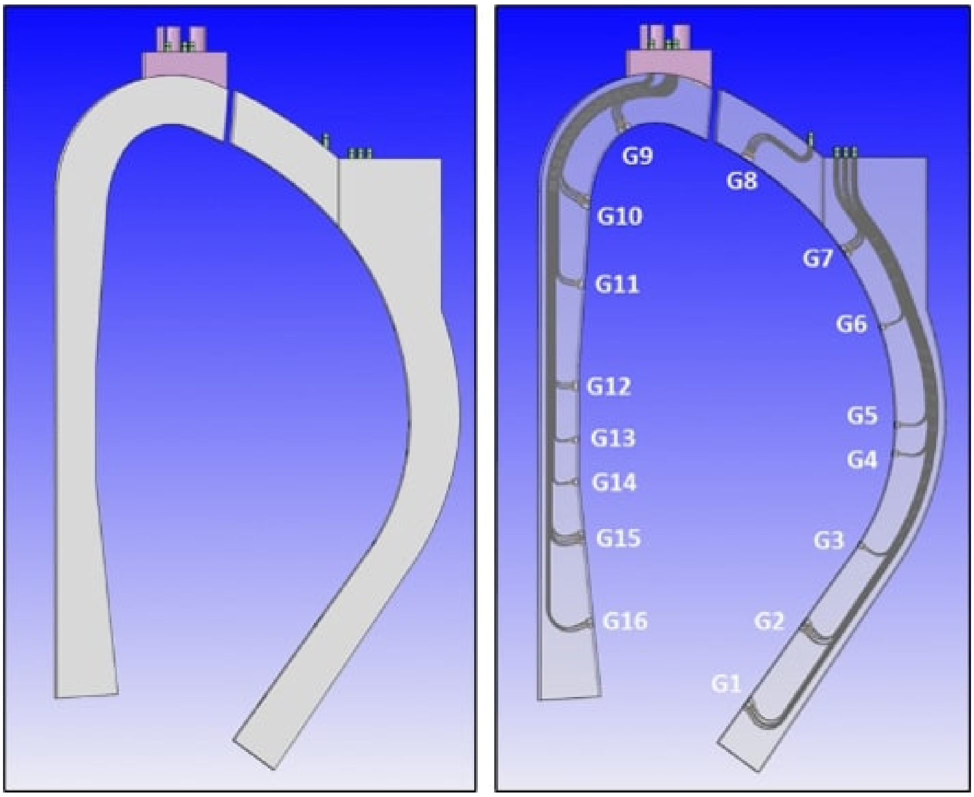

Figure 8.11: Poloidal view of the DSC with (left) and without (right) transparency.

For the work presented in this thesis, it was assumed that each WG socket (see Figure 8.6) would host 9 WGs in order to provide enough space to avoid cross-talking between two or more WGs and to increase the integration flexibility by minimizing the size of each socket. The proposed antenna distribution, based on Table 8.4 and optimized for symmetrical WG placement and to minimize the number of required sockets,

Table 8.4: Desirable antenna configuration for each gap [229].

Gap	Function	IEEE Frequency Band	Antenna configuration
1, 2, 9, 10, 15, 16	Plasma position and shape	K, Ka, U, E (O-mode)	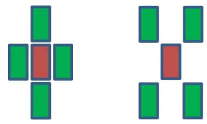
3, 4, 6, 7, 8, 11, 12, 14	Plasma position and shape	K, Ka, U, E (O-mode)	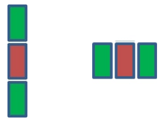
5, 13	Plasma position and shape, density profile	K, Ka, U, E (O-mode) + F (X-mode)	

is presented in Table 8.5.

Based on Table 8.5, a CAD model was developed for the antenna clusters in the FW, aligned perpendicular to the separatrix. The options, illustrated in Figure 8.12, consist of (a) two antennas aligned vertically; (b) two antennas aligned horizontally; (c) a cluster of three antennas aligned horizontally; (d) a T-shape alignment of 4 antennas, with the emitting antenna placed below the receiving antennas (suitable for the divertor region) and e) and f) 5 antennas, in '+' and 'x' shapes, respectively. These two shapes, being complementary, can be used together to maximize the number of WGs that can be routed without clashes.

Table 8.5: Proposed antenna distribution in each gap.

Outboard				**Inboard**			
	Left	Center	Right		Left	Center	Right
Gap 1	1	3	1	Gap 9	2	1	2
Gap 2	2	1	2	Gap 10	2	1	2
Gap 3	1	1	1	Gap 11	0	2	0
Gap 4	1	1	1	Gap 12	0	2	0
Gap 5	1	1	1	Gap 13	1	0	1
Gap 6	1	1	1	Gap 14	1	0	1
Gap 7	2	1	2	Gap 15	2	1	2
Gap 8	0	0	0	Gap 16	1	2	1
Total	9	9	9	**Total**	9	9	9

Using these six alignments, the proposed distribution of antennas in the FW is presented in Figure 8.13. The '+' shape was selected for G1, with the emitting antenna at the bottom and 4 receiving antennas above it, to accommodate the upward bend of the reflected waves in this region. The ’x’ shape configuration is adopted in G2, G7, G9, G10, and G15, following Table 8.4. Clusters of three antennas aligned horizontally were adopted in G3, G4, G5, G6. Though two antennas could be enough in G5 and possibly also in G4, this would mean that some WG positions would not be used in the WG sockets; as such, three antennas were used instead. Two vertically aligned antennas are proposed for G11 and G12, while in G13 and G14 the two antennas are aligned horizontally. It was not possible to adopt 3 antennas in G11, G12 and G14 as suggested in Table 8.4, due to restrictions in the WG routing. However, two antennas might suffice in these regions, as their orientation is almost perpendicular to the separatrix, which is ideal for the reflectometry measurements. In gap G8, which may eventually be placed in the keystone, 9 antennas were assumed in the current design, in order to occupy a full WG socket. If no keystone is required, these WGs will be routed through the BB outboard chimney.

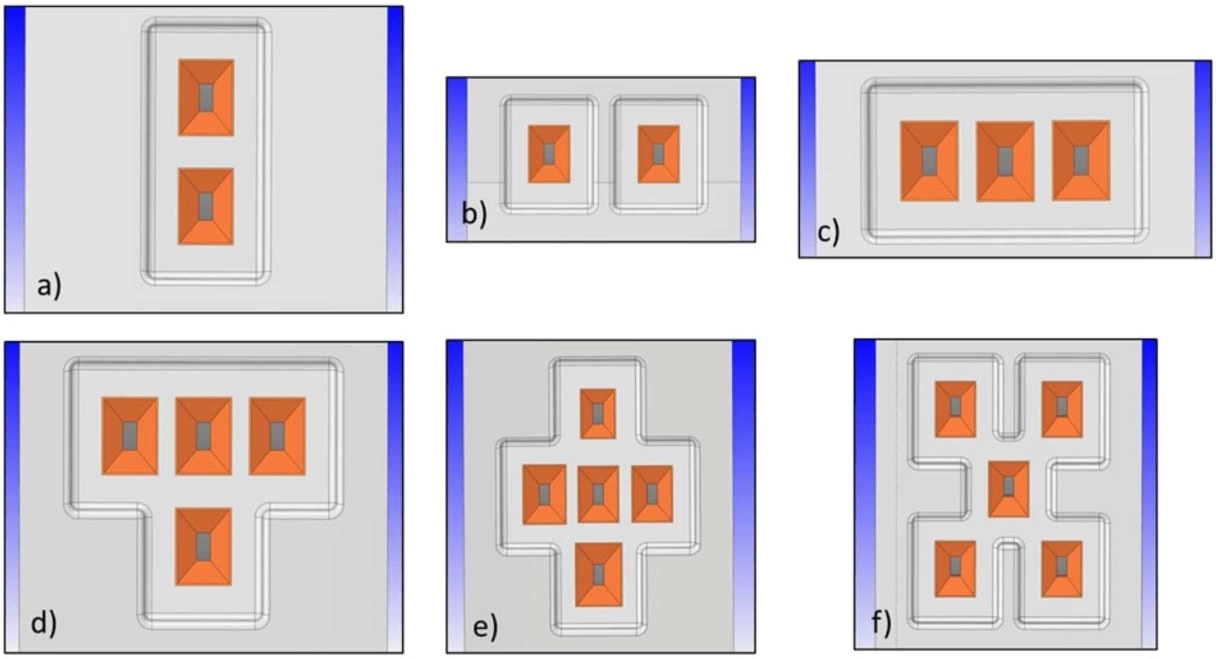

Figure 8.12: Proposed antenna opening configurations in the FW.

The arrangement presented in Figure 8.13 was optimized maximize the number of antennas to receive the microwaves reflected from the plasma, while minimizing the number of sockets needed to route the WGs in the UP. It must be noticed, however, that the WG bends were not yet optimized from the EM point of view.

8.3 Preliminary structural analysis of the COBS

As the reflectometry WGs have a small cross-sectional area (19.05 mm $\times$ 9.525 mm), and since preserving their shape is important to avoid power losses to higher-order modes, an assessment of their thermal expansion is required to evaluate whether their deformation impacts the reflectometry measurements. Ideally, this analysis would be performed using detailed models of the blankets and the DSC, including all the components and the cooling systems. At this stage, however, such analysis is not possible, as the details of the integration of the DSC with the blankets have not been sorted out yet. Furthermore, there is no detailed model for the full DSC segment, and even for the BBs extensive computational resources

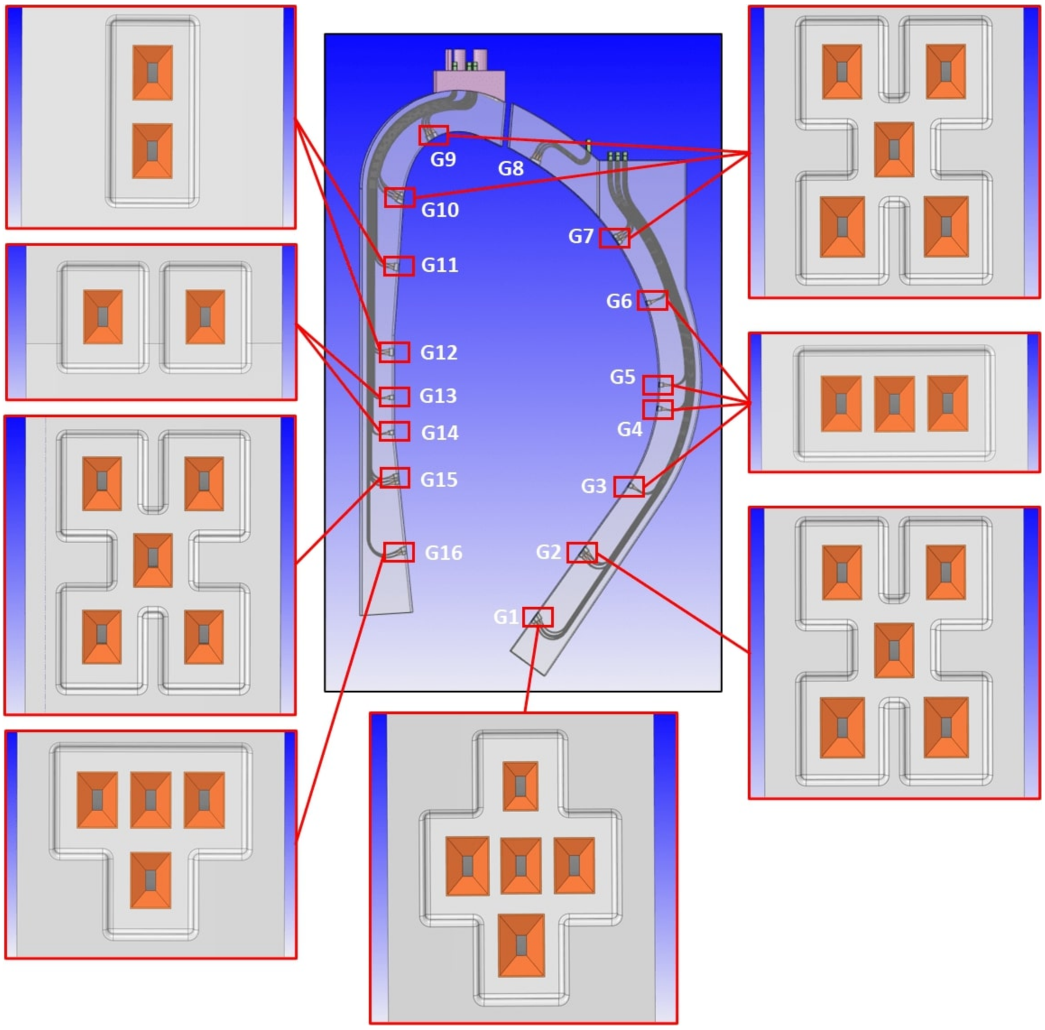

Figure 8.13: First wall openings in the DSC.

would be required to model a full segment with all the details. Nevertheless, a simplified structural assessment has been performed in the past [255] for the back support structure of the WCLL blanket, using simplified models of the blankets and approximate assumptions for the boundary conditions. A more elaborate study for the WCLL COBS was published recently [256], in which the water and the breeder were not modelled but their effect on the thermo-mechanical behaviour was reproduced using simplified loads and boundary conditions. To obtain a preliminary estimation of the WG deformation in the DSC, a basic model of the COBS was created and cut into two parts, one of which is the DSC model presented in Figure 8.13, with 25 cm of toroidal thickness. Figure 8.14 shows the resulting CAD model.

For the simplified thermal analysis, the DSC was assumed to be attached to the left part of the COBS, following the work presented in [205]. Both were modelled as solid EUROFER bodies without cooling channels, to reduce the complexity of the analysis. A temperature boundary condition was applied to the plasma-facing surfaces of the COBS and DSC, averaged from the FW temperatures obtained in the thermal analyses of the DSC presented in the previous chapter (see Table 8.6). Similarly, a boundary condition of 295 °C-–the inlet temperature of the coolant-–was applied to the back surfaces. Although this approach does not consider the hotspots or the effects of the coolant throughout the components, as well as the temperature gradients between the DSC and the COBS, it provides a reasonable first approximation of the thermal gradient in the radial and poloidal directions throughout the DSC, which is the major source

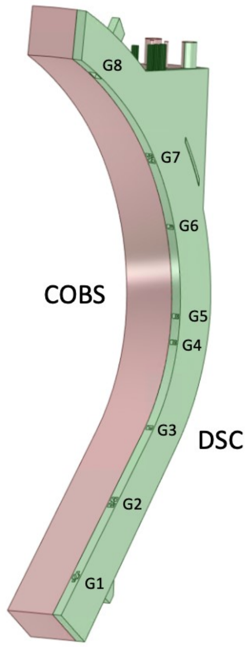

Figure 8.14: Simplified CAD model of the COBS + DSC.

of displacements in the BB [255, 256]. The average temperatures in the EUROFER surfaces behind the antennas (see Table 8.6) were also applied as boundary conditions. At the interfaces between the DSC/COBS and the VV (mechanical supports shown in Figure 8.16) the temperatures were set to 180 °C [218]. The thermal map obtained with these boundary conditions is presented in Figure 8.15.

Table 8.6: Average temperature of the plasma-facing surfaces of the DSC in the COBS.

Gap		G1	G2	G3	G4	G5	G6	G7	G8
EUROFER $\mathbf{T}_{\text{ave}}$(°C)	**Antenna**	425.56	433.70	436.72	436.60	435.70	435.70	433.29	429.47
	FW	425.57	433.45	436.16	436.27	435.32	435.32	433.08	429.59

This thermal map was used as input in a structural analysis. In this analysis, standard earth gravity acceleration (9.8066 m/s^2) was used to model the dead weight of the COBS + DSC. The attachments of the BB to the VV have been designed for DEMO around the concept of keys (set in various places on the BBs' BSS) presented in Figure 6.4, and the corresponding housings (placed on the VV). These mechanical supports are detailed in Figure 8.16. The red faces are the contact areas with the VV, acting in the directions described by the arrows. As prescribed in [256], their action was simulated as spring connections with the stiffness values provided in Table 8.7, obtained from [257]. The maximum transient EM loads and moments, calculated in reference [258] and presented in Table 8.8, were also applied as a boundary condition. Four cases were considered in this structural analysis of the COBS + DSC (see Table 8.9), in order to assess the impact of each load.

The radial displacement results of these four cases are presented in Figure 8.17. A maximum value of 36.7 mm was obtained in the equatorial region in case 2, in which only two loads were applied, namely the gravity acceleration and the thermal load. As expected from the results of references [255] and [256], the thermal expansion clearly dominates the displacement in the radial direction, due to the steep thermal

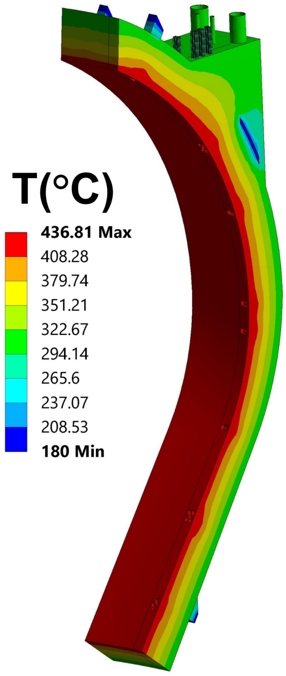

Figure 8.15: Temperature map from the simplified thermal analysis of the COBS + DSC.

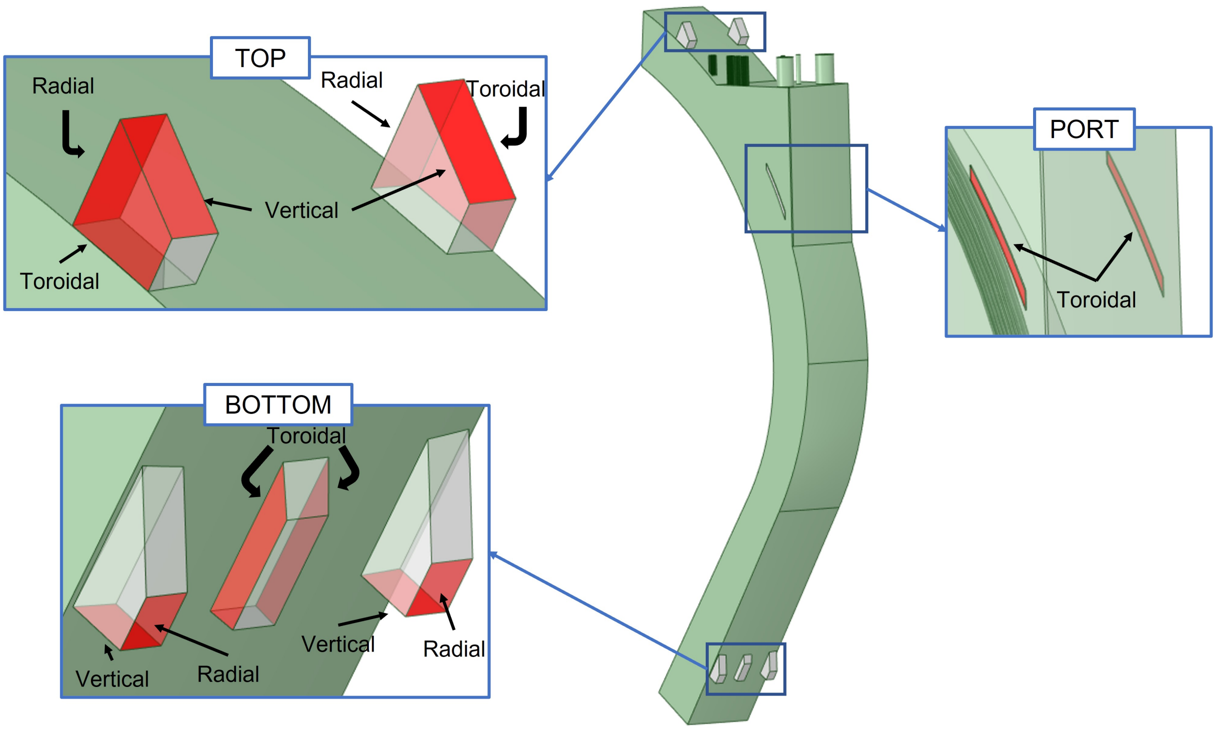

Figure 8.16: COBS structure and its mechanical support (following [256]).

gradient along this direction. The EM loads act in the opposite sense, and therefore the total displacement with the combined loads is slightly smaller than without the EM loads. The poloidal and toroidal displacements, presented in Figure 8.18 and Figure 8.19, are lower than the radial displacements. The maximum deformation value for each case is summarized in Table 8.10.

The expected deformation on the DSC WGs in this preliminary assessment is presented in Figure 8.20.

Table 8.7: Mechanical support stiffness of COBS + DSC (taken from [257]).

Attachment	**Stiffness** (MN/m)
Bottom outer vertical right	2999
Bottom outer vertical left	2999
Bottom outer radial right	3385
Bottom outer radial left	3393
Bottom outer toroidal	398
Port toroidal right	229
Port toroidal left	229
Top radial right	1994
Top radial left	1991
Top vertical right	1139
Top vertical left	1139
Top toroidal right	349
Top toroidal left	349

Table 8.8: WCLL COBS maximum loads - local coordinate system (taken from [258]).

	Total loads (ferromagnetic + Lorentz)	**Lorentz loads**	**Ferromagnetic loads**
F_x (MN)	-3.18	0.00	-3.18
F_y (MN)	0.00	0.00	0.00
F_z (MN)	-0.39	0.00	-0.39
M_x (MN m)	-0.24	0.00	-0.24
M_y (MN m)	3.10	0.00	3.10
M_z (MN m)	-0.03	0.00	-0.03

Table 8.9: Structural analysis boundary condition loads.

Case	**Gravity**	**Thermal map**	**EM load**	**EM moment**
Case 1	✓	✗	✗	✗
Case 2	✓	✓	✗	✗
Case 3	✓	✗	✓	✓
Case 4	✓	✓	✓	✓

The maximum deformation, up to 32 mm, is at the equatorial plane. This is around 15 mm less than estimated for the BB in [256]. This difference may be due to the simplified boundary conditions in

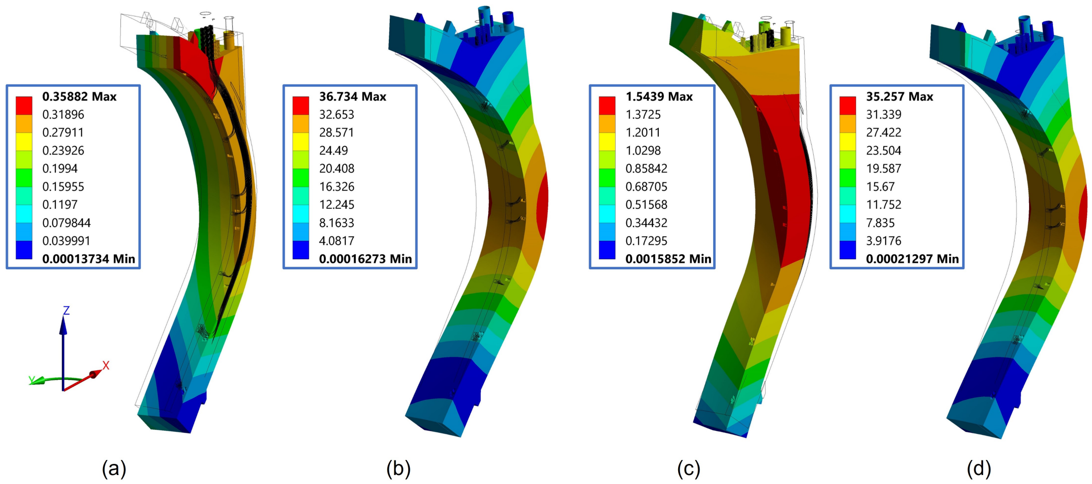

Figure 8.17: The COBS blanket and DSC radial displacement (mm) deformed vs. undeformed shape of:(a) Case 1 (scale: 2000); (b) Case 2 (scale: 19); (c) Case 3 (scale: 450); (d) Case 4 (scale: 20).

Table 8.10: Maximum displacement values in the assessed cases.

Case	$\mathbf{U_r}$ (mm)	$\mathbf{U_p}$ (mm)	$\mathbf{U_t}$ (mm)
Case 1	0.359	0.358	0.347
Case 2	36.73	23.365	10.131
Case 3	1.54	0.993	0.775
Case 4	35.26	23.647	10.866

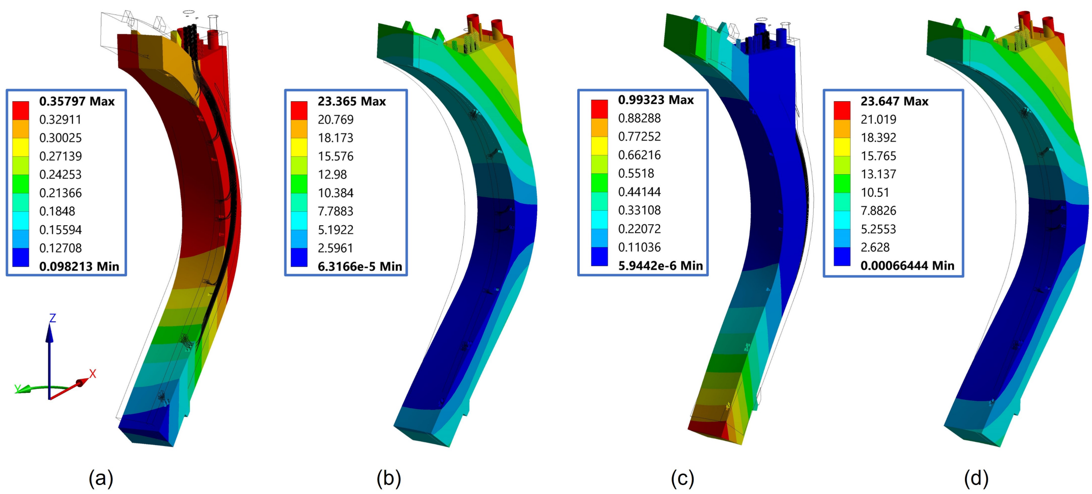

Figure 8.18: The COBS blanket and DSC poloidal displacement (mm) of:(a) Case 1 (scale: 2000); (b) Case 2 (scale: 19); (c) Case 3 (scale: 450); (d) Case 4 (scale: 20).

this work, but also due to the more rigid structure of the DSC when compared to the BB. The deformed geometry of the WGs are used in the next section to estimate the losses in the reflectometry measurements, using ANSYS HFSS [259].

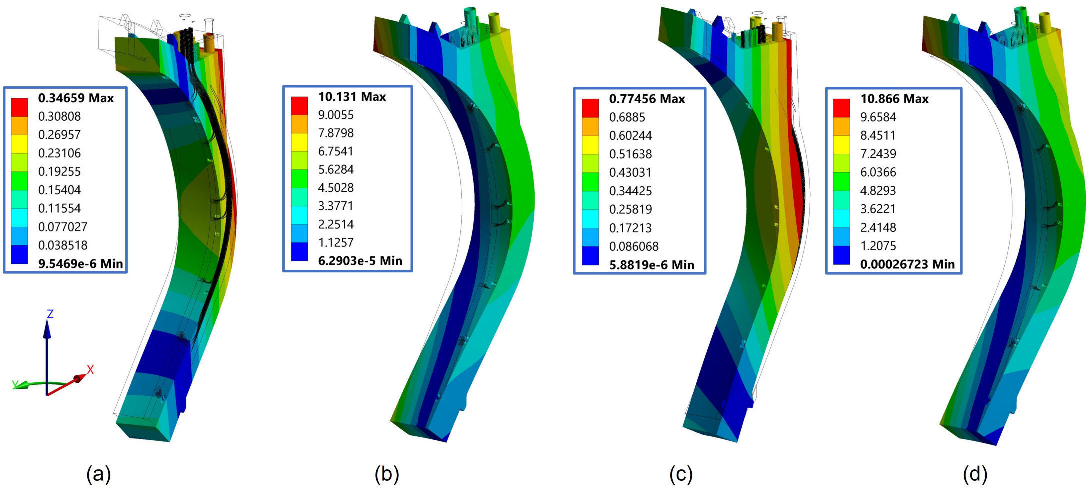

Figure 8.19: The COBS blanket and DSC toroidal displacement (mm) of:(a) Case 1 (scale: 2000); (b) Case 2 (scale: 19); (c) Case 3 (scale: 450); (d) Case 4 (scale: 20).

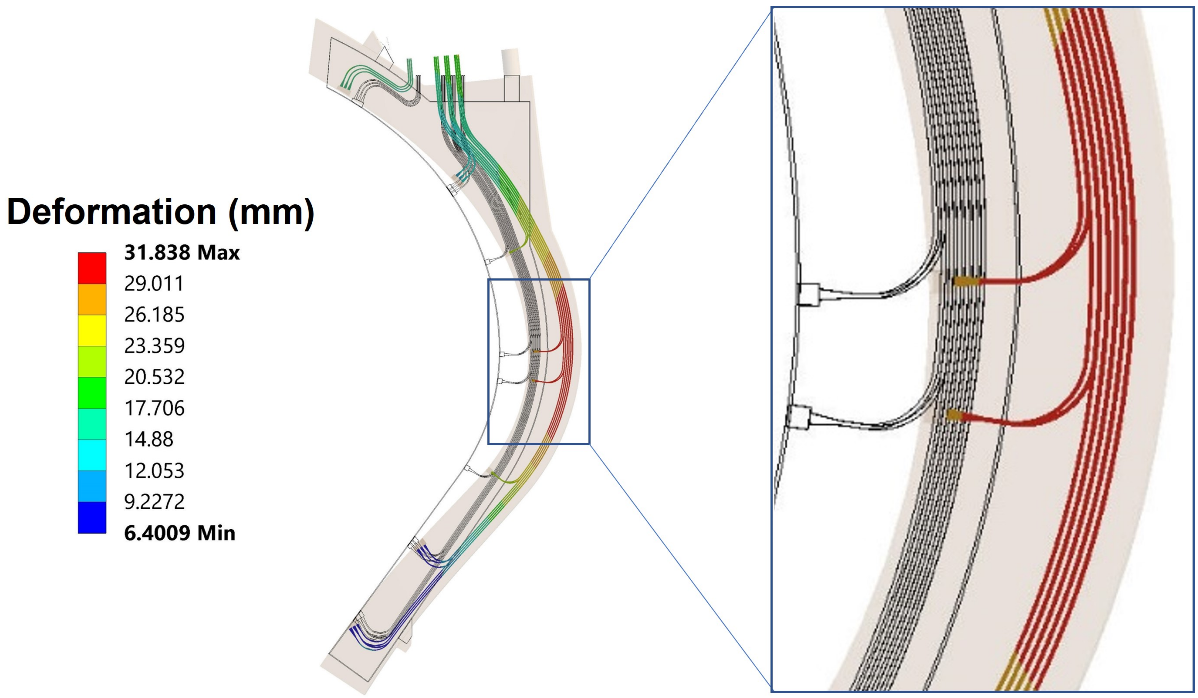

Figure 8.20: Maximum deformation expected for the WGs in the OB DSC.

8.4 Preliminary assessment of the WG extensions

Another important aspect influencing the performance of the reflectometry diagnostic in DEMO is the WG connections between in-vessel and ex-vessel, in which the interface (WG extensions) will experience thermal expansion differences between the BB and VV, as shown in Figure 8.21 [218, 219]. In section Section 8.3 the maximum value of the expected displacement of the DSC with the combined loads is approximately 35.3 mm, with a temperature of 295 °C. The VV, on the other hand, will have an expected relative displacement in the poloidal direction of 15 mm [218], with a temperature of 180 °C [260].

In order to do this assessment, a simplified geometry of the WG extensions was used, consisting of 4 hollow pipes with stiffener plates close to the bend to support the WGs hosted by each pipe (see

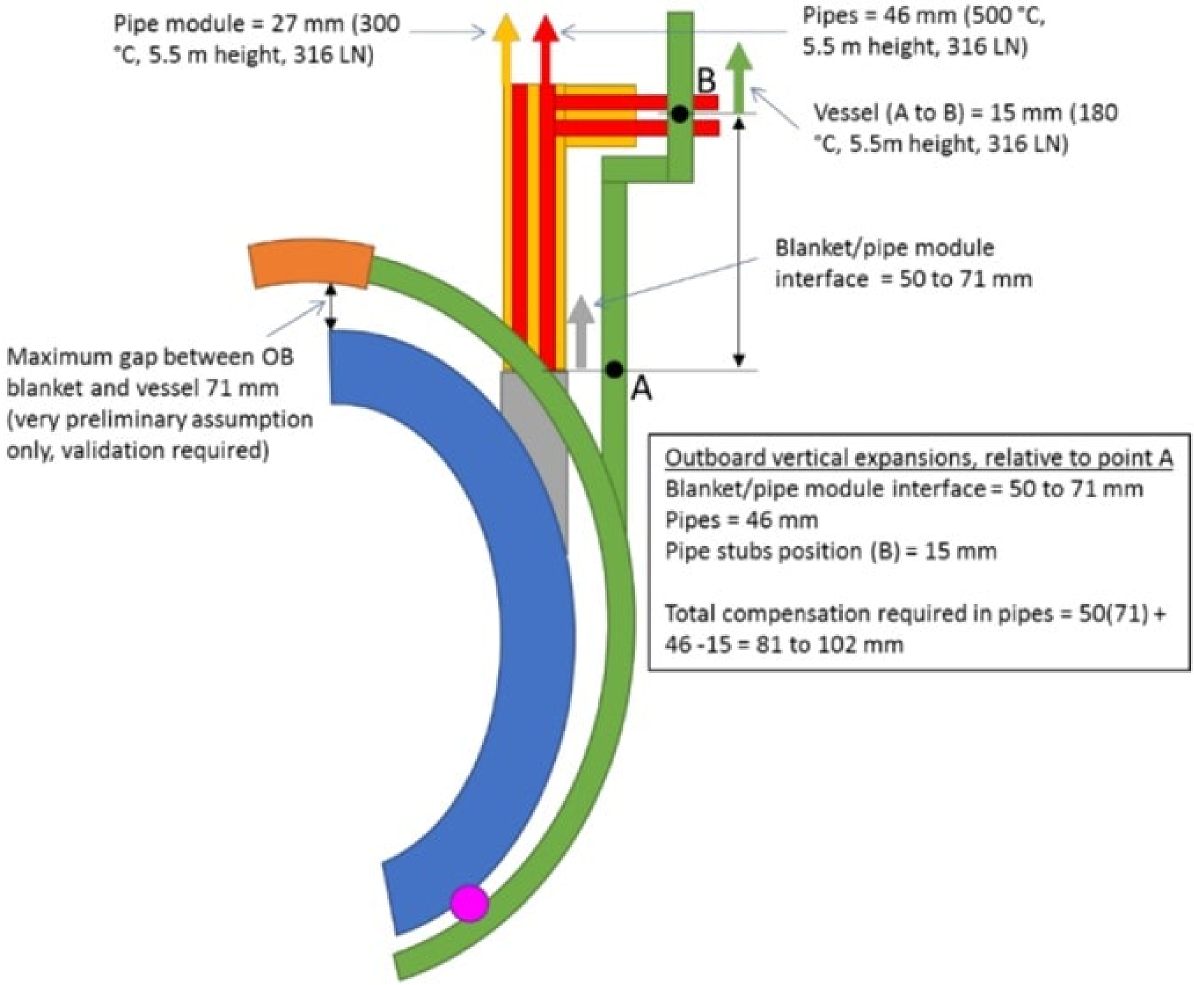

Figure 8.21: Estimated thermal expansion for an pipe module in OB (taken from [218], page 71).

Figure 8.22). In this simplified geometry, the pipe compensator has not been considered. The thickness of each stiffener plate is 5 mm. The displacement boundary condition presented in case 4 of Table 8.10 was imported to each surface connected to the OB DSC. The displacement of the VV, obtained from the latest information available in [218] (15 mm), was modelled using remote displacement applied to the surfaces of the WG extensions on the VV end. A temperature map calculated using two boundary conditions – at the back surface of the DSC, 328 °C, and at the VV, 180 °C, as presented in Figure 8.23a – was applied to model the thermal expansion of the WG extensions. The estimated Von Mises stress of the WG extensions is presented in Figure 8.23b. The maximum stress in concentrated in the contact surfaces between the WG extension and the DSC.

The estimated deformation of the WG extensions is presented in Figures 8.24a–8.24c. The results show that the scale of the deformation is in line with the one estimated in [218], which was done in 2018 based on 2013 baseline blankets. These displacements on the WG extensions are expected to be compensated by pipe compensators, which have not been designed yet. Their design must follow the guidelines of the structural analysis performed for the DSC segment, to guarantee that they can withstand the displacements without compromising the performance of the reflectometry system.

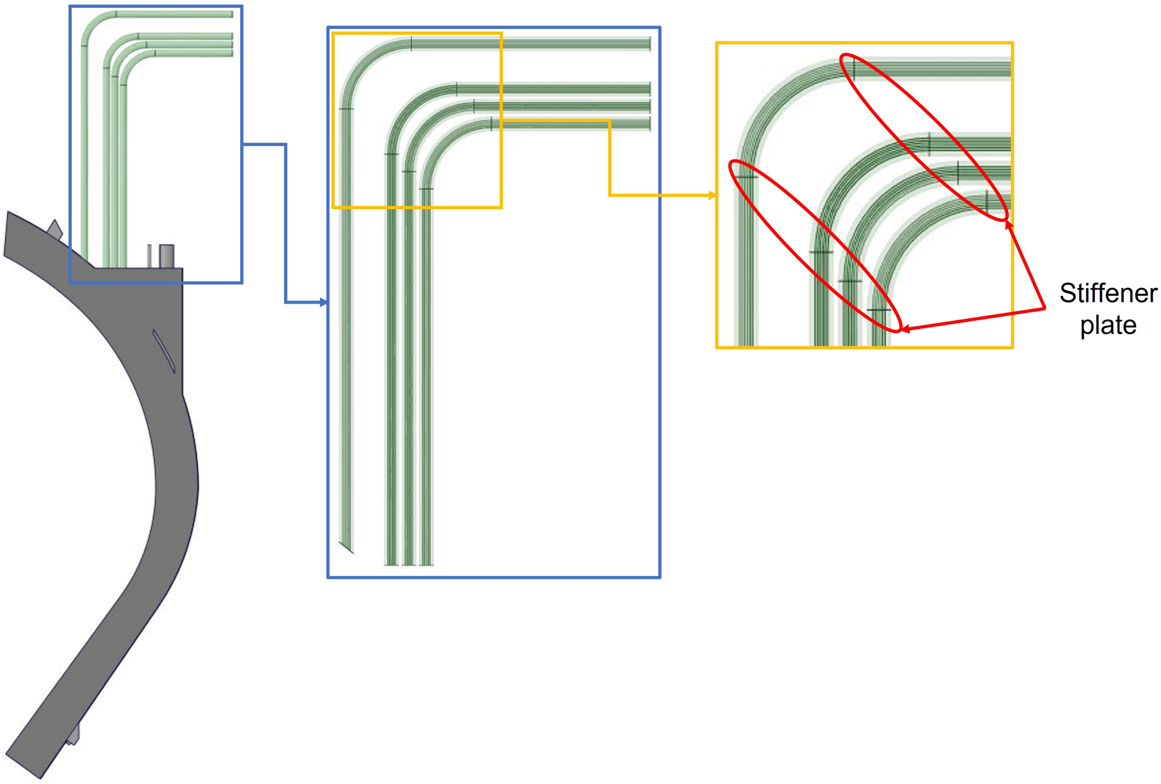

Figure 8.22: Simplified geometry of the WG extensions used in the structural analysis.

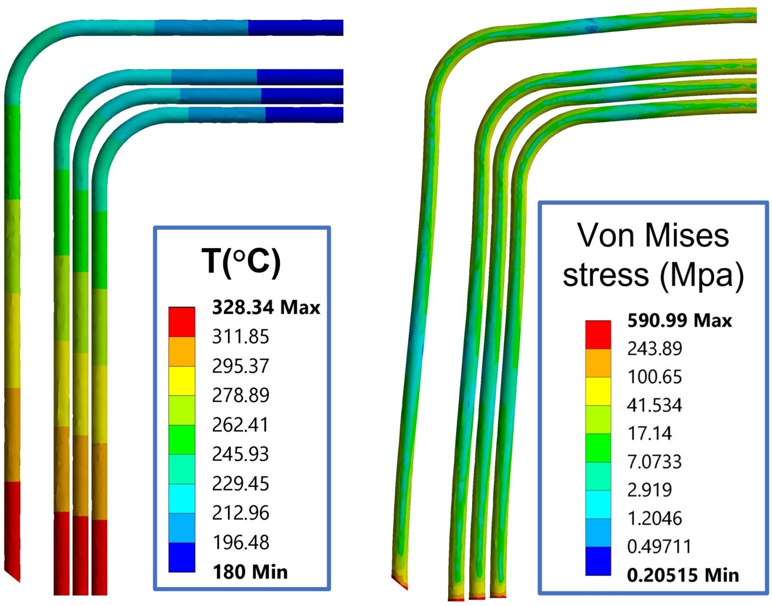

(a) (b)

Figure 8.23: Left: Estimated temperature distributionin the WG extensions. Right: Estimated Von Mises stress in the WG extensions.

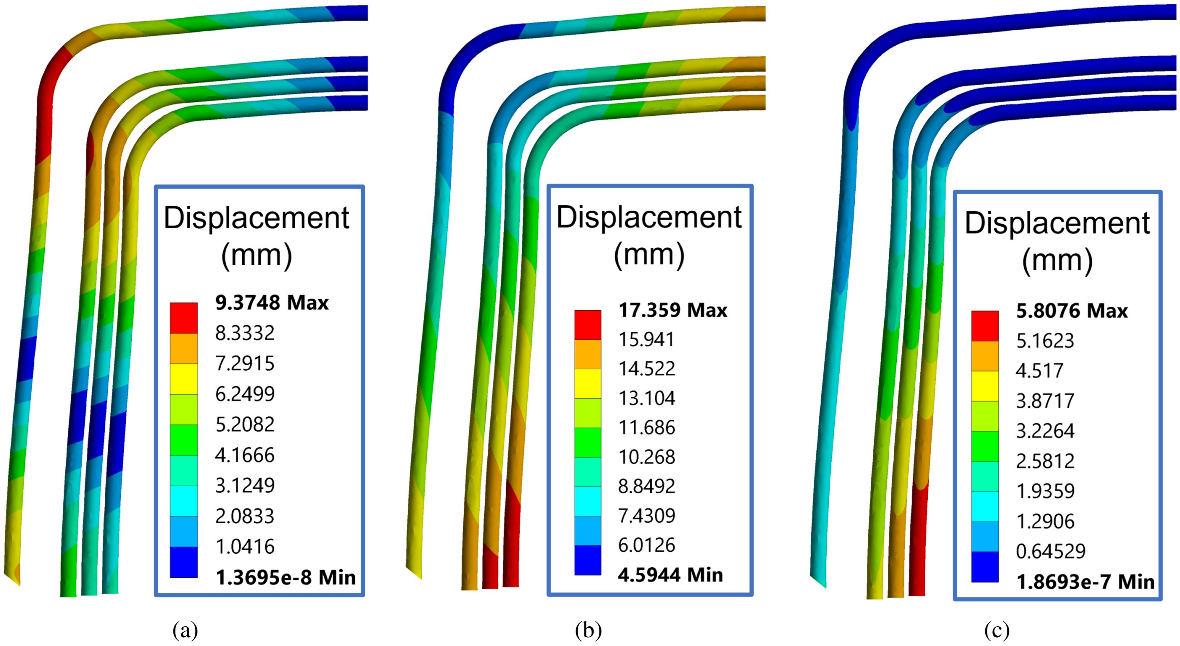

Figure 8.24: The estimated displacement of the WG extensions: (a) in radial direction; (b) in poloidal direction; (c) in toroidal direction;(scale: 20).

8.5 Preliminary electromagnetic analysis of the deformed WG

In order to assess the performance of the reflectometry system, EM analyses are required for the WGs, from their source to the antennas. However, considering that the lengths of the in-vessel parts of the WGs go up to 21 m (including the WG extensions), and the span of frequency bands, simulating the complete WGs would require very extensive computational resources. Therefore, it is wise to select critical parts, containing the worst expected deformations, for a preliminary study.

In this thesis, electromagnetic analyses using ANSYS HFSS[8] were done to estimate the impact of the WG deformation on the wave propagation. These simulations took as input the deformed WG geometries presented in Figure 8.20. These geometries were then cut into smaller components and the pieces with maximum deformation were selected for the simulations. This process resulted in two important WG sections, a “straight” WG section and a “curved” WG section (see Figure 8.25). Symmetry boundary conditions were applied to the mid-section of the WG to reduce the simulation time. The simulations were performed by sweeping the frequency up to 75 GHz according to each frequency band (Ku-band, K-band, Ka-band, U-band, and V-band). The meshes in the simulation were optimized for each band, in order to optimize the computational time and resources. Therefore, discontinuities between the frequency bands are expected. These discontinuities could be eliminated if the simulations used one sweep for the whole range from 15 GHz–75 GHz; this would, however, increase the simulation resources required for the simulations, since the mesh system has to be optimized for the highest frequency for each frequency sweep. Nevertheless, even with all the simplifications mentioned above, it was still impossible to complete the EM analysis for the E-band for frequencies above 75 GHz, using all the available resources.

[8]These simulations were conducted by J.H. Belo at IPFN.

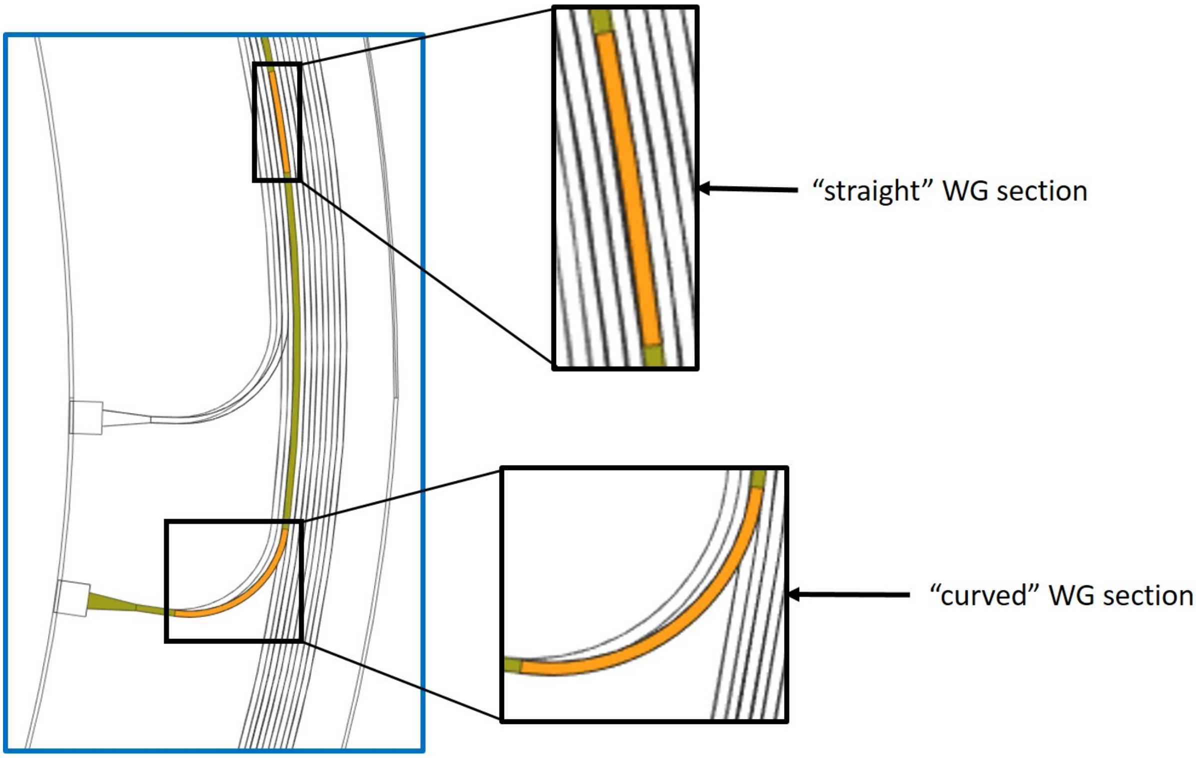

Figure 8.25: Locations of the selected WG sections for the EM analysis.

As explained in [261–263], oversized waveguides have advantages for long-distance signal transmission with low losses [263]. However, the excitation of higher-order modes, which contribute to power losses, cannot be avoided. Therefore, in the following analysis the power losses for mode TE_{10} (the fundamental mode) and other relevant higher-order modes will be presented, and compared for the cases under study (undeformed and deformed WGs).

Regarding the 30 cm “straight” WG section, the undeformed and the deformed geometries are presented in Figure 8.26. The differences between these two geometries might not be apparent from the figure, but the EM waves transmitted inside these WGs behave differently. In order to show these differences, a comparison between the signal transmission power losses and the mode conversion losses is required. The power gain/loss of mode TE_{10} is presented in Figure 8.27, while the conversions from TE_{10} to TE_{20} and TE_{30} are presented in Figure 8.28 and Figure 8.29, respectively.

The results presented in Figure 8.27 show that for lower frequencies, the deformed WG performed better to transmit the fundamental mode, in particular around 35 GHz, in which the losses in the undeformed case exceed 0.1 dB and almost no losses are registered in the deformed case. For frequencies from 50 GHz–75 GHz, the deformed WG has higher losses than the undeformed WG. These power losses are also supported by the results presented in Figures 8.28 and 8.29: for frequencies lower than 50 GHz, the power used to excite higher order modes in the undeformed WG section is higher when compared to the deformed case; for frequencies from 50 GHz–75 GHz, the portion of power converted to higher order modes is larger in the deformed WG section. Therefore, the power loss inside this oversized rectangular WG is due to mode conversion, as mentioned in [263]. The lower losses in the deformed geometry highlight the fact that the current WG design in the DSC is not yet optimized to minimize the losses in the reflectometry measurements, as discussed with more detail below.

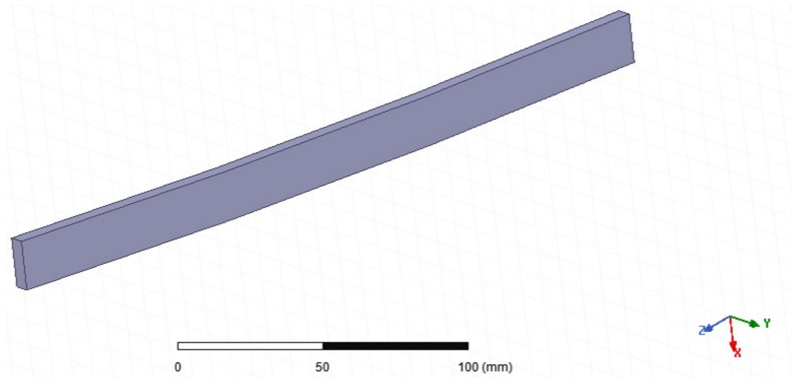

(a)

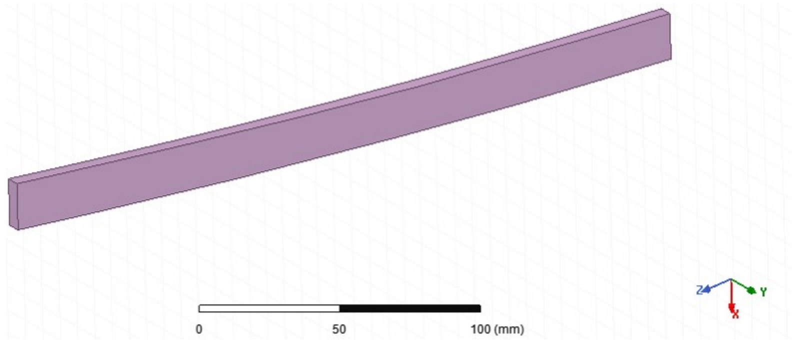

(b)

Figure 8.26: 30 cm “straight” WG section geometry comparison: (a) Undeformed; (b) Deformed.

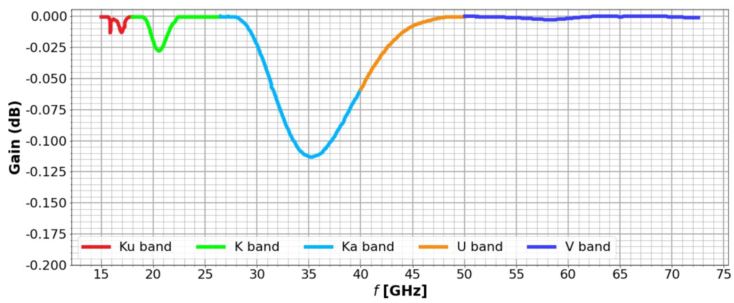

(a)

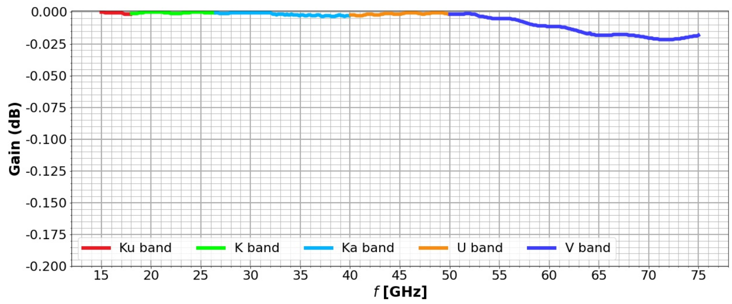

(b)

Figure 8.27: Power gain/loss plot for TE_{10} transmission case: (a) Undeformed WG section; (b) Deformed WG section.

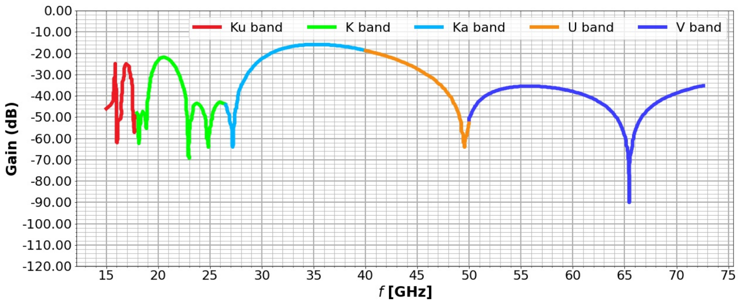

(a)

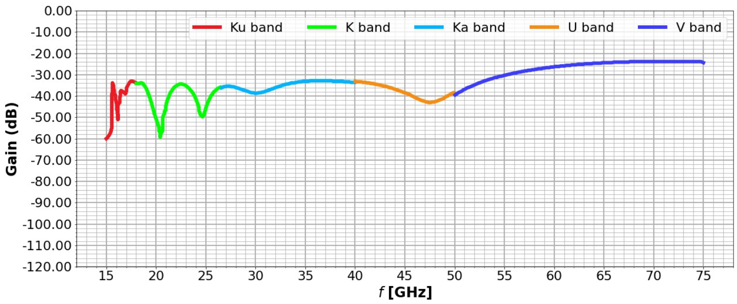

(b)

Figure 8.28: Power gain/loss plot for mode conversion from TE_{10} to TE_{20} transmission case: (a) Undeformed WG section; (b) Deformed WG section.

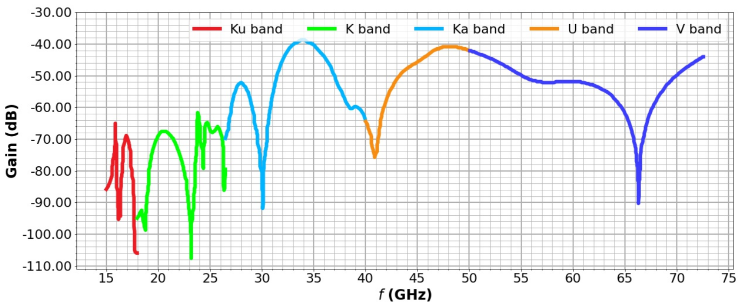

(a)

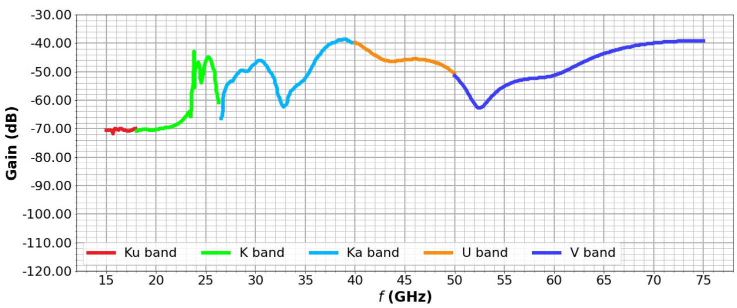

(b)

Figure 8.29: Power gain/loss plot for mode conversion from TE_{10} to TE_{30} transmission case: (a) Undeformed WG section; (b) Deformed WG section.

The geometry of the 45 cm “curved” WG, which includes the whole curve behind the antenna, is presented in Figure 8.30. In order to compare the reflectometry performance between the undeformed and deformed WGs, the power loss during EM wave transmission is presented in Figures 8.31–8.33. In Figure 8.31, the fundamental mode transmission in the undeformed WG section seems to experience more power losses compared to the deformed WG section. Moreover, the frequencies related to the power loss peaks are shifted, due to the change in the WG cross-section dimensions. The trend of power loss due to higher order mode excitation for the “straight” WG section is also observed for the “curved” WG section.

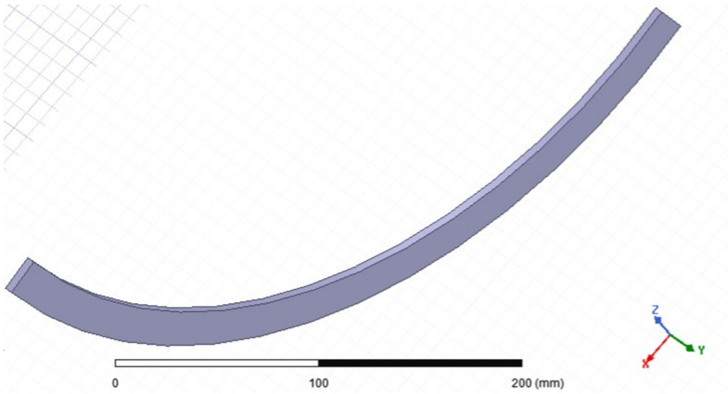

(a)

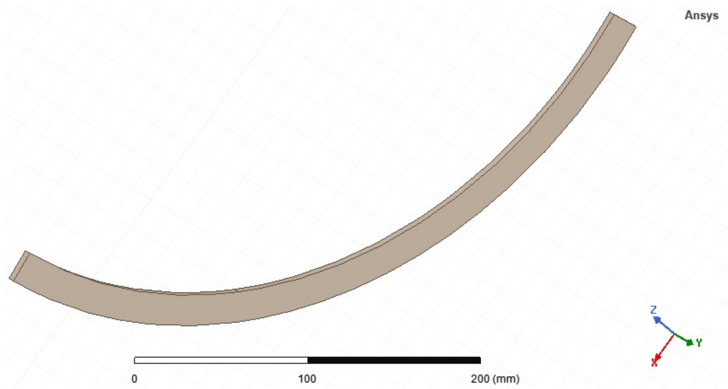

(b)

Figure 8.30: 45 cm curved WG section geometry comparison: (a) Undeformed WG section; (b) Deformed WG section.

Comparing the losses between the “straight” and the “curved” WG sections, in the “straight” case the maximum power loss is –0.1 dB (see Figure 8.27), which means that 98% of the power of the probing signal is being transmitted and around 2% is lost due to higher order mode excitation. This amount of power loss will not affect the performance of reflectometry system. In the “curved” WG section, however, the power loss is –1.1 dB, which means that only 78% of the power is transmitted, which, considering the number of curves between the antennas and the end of the WG extensions, may have a sizable effect on the performance of the reflectometry system. This conclusion is in line with the results of the works presented in [264, 265], which showed that the shape of the oversized WG bends are critical and may lead to significant losses due to higher order mode excitation. In [264], in particular, it was shown through simulation that optimization of 90° WG bends using hyperbolic secant shapes can lead to a reduction in power losses from 1 dB–2 dB to approximately 0.1 dB.

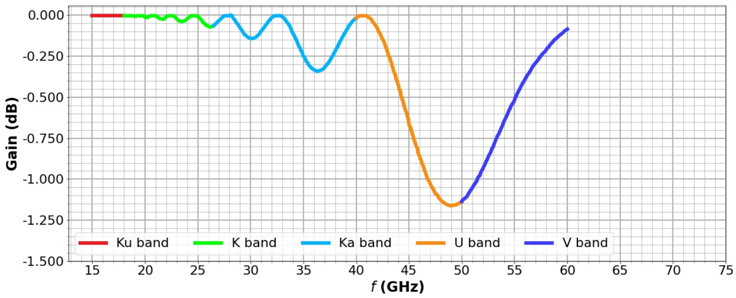

(a)

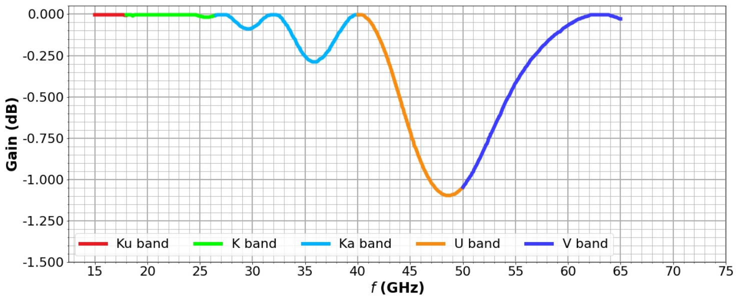

(b)

Figure 8.31: Power gain/loss plot for TE_{10} transmission case: (a) Undeformed; (b) Deformed.

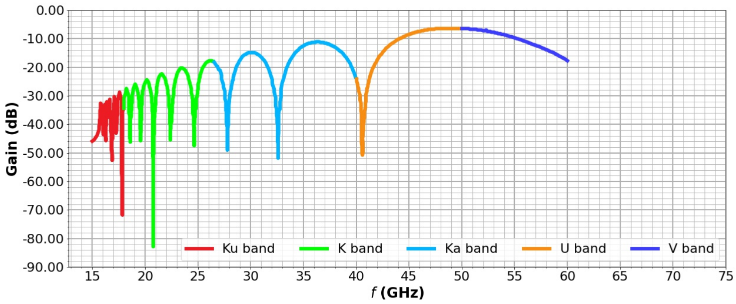

(a)

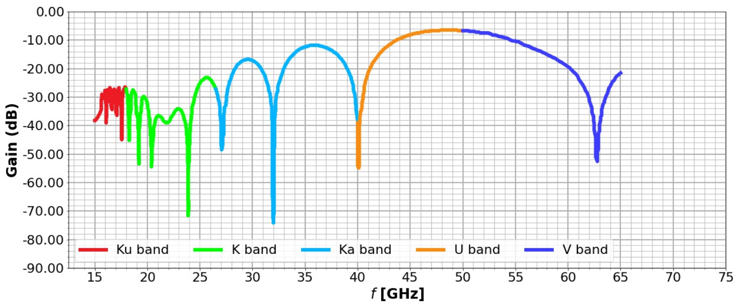

(b)

Figure 8.32: Power gain/loss plot for mode conversion from TE_{10} to TE_{20} transmission case: (a) Undeformed WG section; (b) Deformed WG section.

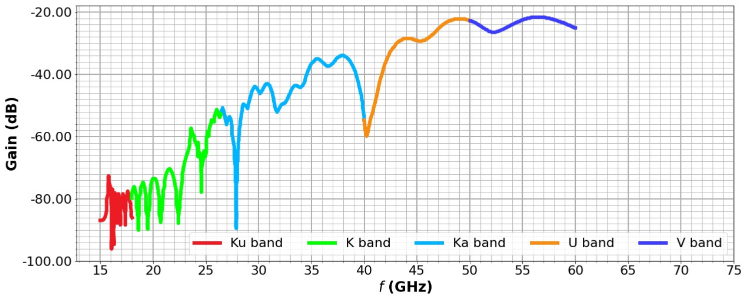

(a)

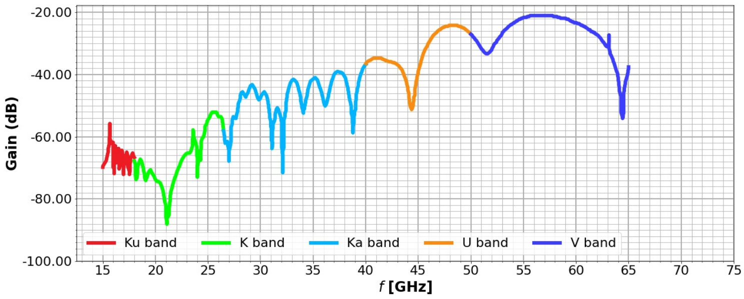

(b)

Figure 8.33: Power gain/loss plot for mode conversion from TE_{10} to TE_{30} transmission case: (a) Undeformed WG section; (b) Deformed WG section.

Therefore, optimizations of the WG bends in the DSC are required to minimize the attenuation. What this work shows is that this tuning needs to take into account the impact of the thermo-mechanical loads on the shape of the WGs, such that the final design is optimized for operation conditions. This consideration, while important for reflectometry, may be crucial for other diagnostics, such as the neutron and gamma cameras in the EP, which foresee thin straight ducts from the plasma to the port cell [266]. In that case, displacements of the magnitude of the ones calculated for the WG bend may compromise the views. Those diagnostics must be designed for operation conditions, to minimize the offsets.

8.6 Summary and discussion

Regarding the integration of the DSC with the BBs, different options have been considered concerning the possible sharing of the FW and the BSS. The possible approaches are: a) DSC integrated with the BB, b) DSC attached to the BB (sharing the cooling system), and c) DSC handled independently of the BB. This work shows that the DSC handled independently of the BB would face numerous difficulties, including the need for 1) independent pipe modules in the UP (which would be virtually impossible at the IB due to lack of space), 2) a non-standardized end-effector for RH manipulation, 3) routing of the cooling pipes through the already overcrowded "chimneys" in the UP area and 4) extra toroidal clearance (20 mm) between the DSC and the corresponding BB (a requirement for RM operations). As such, approaches a) and b) shall be studied in more detail in the near future, in close collaboration with the WPBB and WPRM work packages.

The in-vessel components of the DSC are designed with RH compatibility as a requirement. The

DSC is assumed to be installed and removed similarly to the other in-vessel component of the DEMO tokamak, using RH operation through UP. The UP has limited space constrained by the number of the toroidal width of the TF coils, which limit its span on the toroidal direction, and two upper Poloidal Field (PF) coils, which limit its radial extent. Thus, in order to minimize the number of operations required to replace the DSC, the inboard and outboard sections of the DSC are proposed to be placed on different vertical planes, which are on the left side of the RIBS and the left side of COBS. The other reason behind this consideration is the amount of space for the interfaces to the ex-vessel in the UP area, which should not hinder the existing pipes, and the space for the RM tools to access these in-vessel components.

An interface between the BB and the WG extensions was proposed, a male-female connection socket grouping 9 WGs through the BB pipe "chimneys' and designed to avoid crosstalk between the WGs. The WG extensions are connected to these sockets and grouped inside hollow pipes (to minimize the weight) with stiffener plates (to increase stability) and pipe compensators (to accommodate the relative displacements between the BBs and VV). To minimize the space occupation, these pipes can be integrated with the BB pipe modules, with the caveat that toroidal curvatures should be avoided if possible, to minimize losses in the measurements.

A preliminary structural analysis was performed to assess the expected deformation of the WGs inside the DSC and its impact on the reflectometry measurements. This assessment was done using a simplified geometry of the COBS and a new design proposed for the DSC, from which the OB section was used. The results show that the thermal loads have the main contribution to the deformation of the DSC in the radial, poloidal, and toroidal directions. The maximum deformation value of the WGs – 32 mm – occurs at the equatorial plane. This deformation is around 15 mm less than estimated for the BB in [256]. This difference may be in part explained by the simplified boundary conditions assumed here, but they are also due to the rigid structure of the DSC, compared to the BB.

Preliminary structural simulations were also performed for the WG extensions, to evaluate their deformation. The results show a displacement of 15 mm in the poloidal direction, in line with previous estimations performed in [218]. These displacements are expected to be accommodated using pipe compensators, which have not been studied or designed yet.

The deformed geometry of the WGs were then used in electromagnetic simulations to assess the losses in the reflectometry measurements. The simulations were performed for two different geometries, to compare the reflectometry signal loss between the deformed geometries and the original ones. Indeed, differences were found between the two, which shows that the required tuning of the WG shapes needs to take into account the impact of the thermo-mechanical loads on these components, to optimize the design for operation conditions. This conclusion also applies to other diagnostics, in particular the ones with straight channels from the plasma to the port cell.

To fully assess the performance of the reflectometry diagnostic in DEMO, extensive simulation work is still required, involving CAD design, neutronics, thermo-mechanical analyses, EM simulations, and seismic analyses (response spectrum). The work presented in this thesis is a first step in that direction, involving most of the tools required in the simulation workflow.

Part IV

Conclusions

Chapter 9

Final Discussion and Conclusions

This Doctoral Thesis presents an engineering assessment and design studies for two diagnostics being developed by IPFN/IST: the Plasma Position Reflectometry for ITER and the Multi-reflectometer System for DEMO. Both diagnostics will measure the electron density profile and monitor the plasma position and shape. Since both systems serve an important role in the respective reactors, it is indispensable to ensure that they survive in the harsh radiation environments of ITER and DEMO without serious compromise to their performance. Due to the nature of reflectometry measurements, some front-end components are required to be directly exposed to the plasma, subjected to fluxes of high-energy neutrons (14 MeV) and thermal loads. Thus, complex design studies (involving neutronics, thermo-mechanical studies and EM analyses) are crucial to ensure their ability to operate under a fusion power of 500 MW for ITER and 2000 MW for DEMO. The neutronics and thermo-mechanical studies provide an insight into what needs to be optimized in the design in order to meet certain requirements, while the EM studies provide an understanding on the impact of the thermo-mechanical loads on the ability of the systems to perform reflectometry measurements.

The work here presented combined exhaustive model optimization processes with large and complex simulation workflows and data analyses. The ANSYS Workbench commercial code was the main tool used to perform the thermo-mechanical simulations. Previous to the simulations, CAD designs were developed in CATIA V5 and geometry simplifications were made in ANSYS SpaceClaim, two software tools designed to manipulate 3D geometries. McCad was then used to convert the models from CAD into the MCNP input format, to perform neutronics simulations. Afterwards, Paraview was the preferred tool for data visualisation. Neutronics outcomes, namely particle fluxes and energy deposition, heavily influence the operation temperatures and material properties of the components; therefore, thermo-mechanical analyses were also performed, using ANSYS Workbench. To provide more reliable estimations, coupled steady-state thermal analyses using ANSYS Mechanical and ANSYS CFX were used and the outcomes of these simulations provided the required inputs for steady-state structural analyses using ANSYS Mechanical. Besides guaranteeing that the material temperature limits are not exceeded and ensuring the mechanical integrity of the systems, the mechanical displacements calculated in the structural analyses are used as input in EM simulations, to assess the impact of the thermal and structural loads on the reflectometry measurements. This description of the workflow illustrates the complexity of the simulation process and the range of software tools required to produce reliable results.

9.1 ITER Plasma Position Reflectometry

The PPR system proposed for ITER consisted of four reflectometers distributed poloidally and toroidally in four locations known as gap 3, 4, 5, and 6. The work presented here focused on the in-vessel components of the PPR systems of gaps 4 and 6, both with antennas and part of the transmission lines directly exposed to the plasma. The integrity of these components depend on the temperature distribution and the dpa experienced by the components, since both of these variables could modify the mechanical properties of the materials. Although the dpa in ITER are expected to be low enough not to impact the material properties, for safety reasons the maximum allowable operation temperature is 450 °C for stainless steel 316L(N)-IG, which was the driving limit for the thermal analyses of the PPR in-vessel components.

The PPR system was planned to operate without any active cooling system, relying on the VV as the ultimate heat sink. In this work, two separate studies were performed, one for a WG section between blanket modules and another for the the diagnostic front-ends (antennas and support). Although the WG section is directly exposed to the plasma, steady-state thermal analyses showed that its operation temperature is well below the limit for stainless steel 316L(N)-IG under neutron irradiation (450 °C). However, the operation temperatures of the front-end components of the PPR systems of gaps 4 and 6 are well above 450 °C. Transient thermal analyses (taking into account the ITER plasma pulse duration) showed that the 90° bend supports in both gaps operate below (but very close to) 450 °C. Nevertheless, the antennas are still above the limit, even after several optimization attempts, which aimed to maximize the contact area between the 90° bend support and the VV.

In face of these results, it is suggested that different materials are considered for the front-ends of gaps 4 and 6. A nickel-based superalloy, for example Inconel 718, would be an option, as it is a structural material suitable for high temperature applications, with a maximum working temperature under neutron irradiation above 700 °C [199].

Even though the ITER PPR system was descoped after these studies were finished, they are still relevant as a guideline for the design of the reflectometry system for DEMO, which adopted a similar workflow.

9.2 DEMO multi-reflectometer system

The role of the reflectometry diagnostic in DEMO is twofold: i) to provide the radial edge density profile at several poloidal angles and ii) to provide data for the feedback control for plasma position and shape. The primary integration approach for reflectometry in DEMO has been based on the DSC concept. The first step of this work consisted of an iterative study to define preliminary positions for the antennas in the DSC and the corresponding WGs routing up to the UP. This study resulted in a preliminary design with 73-antennas distributed along 16 poloidal positions.

In order to ensure the performance of the reflectometry system under the harsh irradiation environment of DEMO, an adequate active cooling, which allows to control the operation temperatures in the DSC, is required. A thermo-mechanical study was performed for a section of the DSC located on the high-field side at the equatorial plane (a location of high neutron flux on the high-field side). This study started with the design of a cooling system with the aim to ensure operation temperatures below the material limits under irradiation. This design was then optimized using steady-state coupled thermal-CFD analyses, performed with ANSYS Workbench. Very high temperatures, up to 1000 °C, were obtained with the first design, well above the temperature limit for EUROFER under neutron irradiation (550 °C). Therefore, the next design iterations were focused on eliminating the hotspots around the plasma-facing antennas. After testing several designs, it was concluded that it is not possible to maintain the operation temperatures below 550 °C when the antennas of the DSC are made of EUROFER. Therefore, tungsten, which will also be used in the 2 mm plasma-facing layer of the DEMO BB, is proposed to replace EUROFER in the antennas (with a thickness of 1.57 mm). By changing the material of the antennas, the maximum operation temperature estimated for the DSC was brought down to 541 °C in EUROFER, 656 °C in the tungsten layer, and 581 °C in the antennas. Furthermore, the maximum velocity of the water coolant in the latest cooling channel design is just half of the maximum allowable coolant velocity, and the outlet temperature of the water is only 2 °C below the desirable outlet water temperature. The results obtained in this analysis were then extrapolated to the other segments of the DSC, across the whole poloidal plane. With this extrapolation it was found that the maximum temperature of the whole DSC is kept under 550 °C, including in the locations with the highest nuclear wall loads.

Using the temperature maps obtained in the thermal analysis, a structural integrity assessment was performed using a quarter of the previous DSC module and with symmetry boundary conditions, both under normal operation and after long irradiation periods. The thermo-mechanical assessment under normal operation showed that the current design already complies with the RCC-MR level A criteria for the P-type damage, which ensures the safety of the DSC under the specified operation conditions throughout its lifetime. A thermo-mechanical assessment after cumulative radiation exposure was done in parallel, resorting to the material properties database of DEMO. It should be highlighted that there is still a lack of material data related to the dpa values expected for the DEMO operational phases. Notwithstanding, approximations for the yield strength and the tensile strength were assumed using the available data. These two quantities increase with the dpa, which means that the current design will also stay below the stress limit at the end of the DEMO operation phases, according to RCC-MR. This assessment was performed for dpa values of 20, 50, and 70, which correspond to the 1st DEMO operation phase, the 2nd DEMO operation phase, and the entire lifetime of DEMO, respectively.

In conclusion, the results presented strongly suggest that the DSC concept is feasible and can operate below the temperature limit for each material. The current cooling system has a much simpler design than the ones proposed prior to this work, possible to manufacture using conventional techniques. The results presented here should be used as guidelines for other diagnostics that consider the DSC as a possible integration solution (i.e. ECE system [204]). Even if the cooling system design needs to be adapted in the future due to integration constraints with the DEMO BB, this work quantifies the cooling needs of the DSC and illustrate the main challenges to overcome when addressing them. With the current assumptions, the proposed cooling system is able to keep the DSC operation temperatures within the limits without compromising the mechanical integrity of the system.

9.3 Integration study of the DSC

Regarding the integration of the DSC with the BBs, different options have been considered concerning the possible sharing of the FW and the BSS. The possible approaches are: a) DSC integrated with the BB, b) DSC attached to the BB (sharing the cooling system), and c) DSC handled independently of the BB. This work shows that the DSC handled independently of the BB would face numerous difficulties, including the need for 1) independent pipe modules in the UP (which would be virtually impossible at the

IB due to lack of space), 2) a non-standardized end-effector for RH manipulation, 3) routing of the cooling pipes through the already overcrowded “chimneys” in the UP area and 4) extra toroidal clearance (20 mm) between the DSC and the corresponding BB (a requirement for RM operations). As such, approaches a) and b) shall be studied in more detail in the near future, in close collaboration with the WPBB and WPRM work packages.

The in-vessel components of the reflectometry system of DEMO are designed with RH compatibility as a requirement. The DSC is assumed to be installed and removed similarly to the other in-vessel components of the DEMO tokamak, using RH operations through the UP. In order to minimize the number of operations required to replace the DSC, the inboard and outboard sections of the DSC are proposed to be placed on different vertical planes, on the left side of the RIBS and the left side of COBS. The other reason behind this consideration is the amount of space for the interfaces to the ex-vessel in the UP area, which should not hinder the existing pipes, and the space for the RM tools to access these in-vessel components.

An interface between the BB and the WG extensions was proposed, a male-female connection socket grouping 9 WGs through the BB pipe “chimneys’ and designed to avoid crosstalk between the WGs. The WG extensions are connected to these sockets and grouped inside hollow pipes (to minimize the weight) with stiffener plates (to increase stability) and pipe compensators (to accomodate the relative displacements between the BBs and VV). To minimize the space occupation, these pipes can be integrated with the BB pipe modules, with the caveat that toroidal curvatures should be avoided if possible, to minimize losses in the measurements.

A preliminary structural analysis was performed to assess the expected deformation of the WGs inside the DSC and its impact on the reflectometry measurements. This assessment was done using a simplified geometry of the COBS and a new design proposed for the DSC, from which the OB section was used. The results show that the thermal loads have the the main contribution to the deformation of the DSC in the radial, poloidal, and toroidal directions. The maximum deformation value of the WGs – 32 mm – occurs at the equatorial plane. This deformation is around 15 mm less than estimated for the BB in [256]. This difference may be in part explained by the simplified boundary conditions assumed here, but they are also due to the rigid structure of the DSC, compared to the BB.

The deformed geometry of the WGs were then used in electromagnetic simulations to assess the losses in the reflectometry measurements. The simulations were performed for two different geometries, to compare the reflectometry signal loss between the deformed geometries and the original ones. Indeed, differences were found between the two, which shows that the required tuning of the WG shapes needs to take into account the impact of the thermo-mechanical loads on these components, to optimize the design for operation conditions. This conclusion also applies to other diagnostics, in particular the ones with straight channels from the plasma to the port cell.

9.4 Future work

ITER, under construction, is projected to start operation in 2025, while DEMO is currently in the Conceptual Design Phase and its first plasma is still decades away. The maturity of each project is therefore reflected on the design and development stages of the diagnostics designed for each reactor.

At the start of this work, the ITER PPR system was already at a very developed design stage. The results presented here showed that the design of the PPR system would not comply with the temperature limit for SS-316L(N)-IG under irradiation, and alternative materials were proposed. Similar studies would be required for these alternatives. However, the PPR system was unfortunately descoped and will not be used in ITER. Therefore, the extensive reflectometry and integration work performed in the past will be used to inform the design of reflectometry systems for future tokamaks, including DEMO.

The DEMO reflectometry system is at an early stage of development and a significant amount of work is still required. The cooling system design presented in this work is very efficient to bring down the operation temperatures of the DSC and comply with the limits, and it was shown that the current DSC design is able to fulfill the level A criteria of RCC-MR for IPC, IPI and IPFL. However, this work has not included transient events (i.e. plasma disruption events) nor cyclic damages (fatigue). Furthermore, the design of the DSC may change drastically depending on the type of interface that is chosen for the integration with the BB. Therefore, the analyses presented here, although comprehensive, will have to be updated at each design step. Moreover, to validate the results presented in this work, experimental tests and prototyping activities will be required. These activities might include material irradiation tests in IFMIF [267] and performing measurements with clusters of antennas in existing tokamaks.

Regarding the integration of reflectometry in DEMO, many open issues persist. These are not only dependent on the development of the concept itself, but also on the outcomes of the research work performed by other work packages, such as WPBB and WPRM. Among the open issues are 1) the interface between the DSC and the BB (and respective cooling services), 2) the definition of the antenna configurations in the first wall and the WG routing in the DSC, 3) the interface for attaching/detaching the WG extensions to/from the BB chimneys, 4) the limited space available in the UP (especially at the inboard) and the need to avoid toroidal curvatures in the WGs, 5) the relative displacements between the BB and the VV (which must be accommodated by the WG extensions), and 6) the design of the in-vessel/ex-vessel WG transitions.

To fully assess the performance of the reflectometry diagnostic in DEMO, all these issues have to be tackled. To address them, extensive simulation work is still required, involving CAD design, neutronics, thermo-mechanical analyses, seismic analyses, and EM simulations. The work presented in this thesis is a first step in that direction, involving most of the tools required in the simulation workflow. Similar optimization studies will be required for the development of other DEMO diagnostics, which may be more heavily impacted by deformations from thermo-mechanical loads. These include the neutron and gamma cameras, which foresee long and thin straight ducts from the plasma to the port cell.

It also illustrates the complexity of the challenges that lie ahead before fusion energy can be realized commercially, as an alternative, clean energy source. Addressing these challenges, which go far beyond the development of reliable diagnostics and control systems for the next-generation tokamaks, requires many resources and an effective collaboration between scientists and engineers all across the globe. This thesis is part of that combined effort to build the fusion reactors of the future, essential to address one of the most complex challenges of our time.

Chapter 10

Scientific Outputs from this Thesis

The scientific work presented and discussed in this PhD Thesis resulted in several scientific contributions that are summarised below:

Internal Deliverables for Fusion for Energy

- Technical Report: Y. Nietiadi, R. Luís, P. Varela, ITER Plasma Position Reflectometry System (PPR): Technical Report (**July 2019**)

Internal Deliverables for EUROFusion

- Design Description Document of the reflectometry diagnostic system (**February 2022, submitted**)
- DC-S.03.14-T001-D002 Deliverable: Final report on diagnostic design, integration and engineering studies for DEMO, covering the technical specifications of this task specification (**February 2022, submitted**)
- CAD Model: Diagnostics Slim Cassette (2021) (**November 2021, submitted**)
- DC-S.03.14-T001-D001 Deliverable: Intermediate report on diagnostic, integration and engineering studies for DEMO, covering the technical specifications of this task specification (**November 2021, submitted and approved**)
- Design description Document of the reflectometry diagnostic system (**September 2021, submitted and approved**)
- DC-2-T025 Deliverable: Final Report DEMO WPDC system engineering and design integration (**March 2021, submitted and approved**)
- CAD Model: Diagnostics Slim Cassette module with cooling (2020) (**February 2021, submitted**)
- DC-2-T022 Deliverable: Final Report DEMO WPDC system engineering and design integration – detailed neutronics studies for spectroscopic diagnostics on DEMO (**February 2021, submitted and approved**)
- DC-2-T019 Deliverable: Final Report DEMO WPDC system engineering and design integration (**January 2020, submitted and approved**)
- DC-2-T015 Deliverable: Final Report DEMO WPDC system engineering and design integration (**January 2020, submitted and approved**)
- DC-2-T010 Deliverable: Final Report DEMO WPDC system engineering and design integration (**February 2019, submitted and approved**)

Peer-reviewed Papers

- R. Luís, Y. Nietiadi, J. H. Belo, A. Silva, A. Vale, A. Malaquias, B. Gonçalves, F. da Silva, J. Santos, E. Ricardo, T. Franke, A. Krimmer, W. Biel, *A Diagnostics Slim Cassette for Reflectometry Measurements in DEMO: design and simulation studies*, Fusion Engineering and Design (**2022, submitted**)
- Y. Nietiadi, R. Luís, A. Silva, J.H. Belo, A. Vale, A. Malaquias, B. Gonçalves, F. da Silva, J. Santos, E. Ricardo, W. Biel, *Thermomechanical Analysis of a Multi-Reflectometer System for DEMO*, Fusion Engineering and Design (**2022, submitted**)
- J. H. Belo, Y. Nietiadi, R. Luís, A. Silva, A. Vale, B. Gonçalves, T. Franke, A. Krimmer, W. Biel, *Design and integration studies of a diagnostics slim cassette concept for DEMO*, Nuclear Fusion (**2021, published**), DOI: 10.1088/1741-4326/ac24d3
- Y. Nietiadi, R. Luís, A. Silva, E. Ricardo, B. Gonçalves, T. Franke, and W. Biel, *Nuclear and thermal analysis of a multi-reflectometer system for DEMO*, Fusion Engineering and Design (**2021, published**), DOI: 10.1016/j.fusengdes.2021.112349
- Y. Nietiadi, C. Vidal, R. Luís, P. Varela, *Thermal analysis of the in-vessel frontends of the ITER plasma position reflectometry system*, Fusion Engineering and Design (**2020, published**), DOI: 10.1016/j.fusengdes.2020.111599
- C. Vidal, R. Luís, Y. Nietiadi, N. Velez, P. Varela, *Thermal analysis of a waveguide section of the ITER plasma position reflectometry system on the high-field side*, Fusion Engineering and Design (**2019, published**), DOI: 10.1016/j.fusengdes.2019.03.197

Presentations at Conferences/Meetings

- R. Luís, J. H. Belo, Y. Nietiadi, A. Silva, A. Vale, A. Malaquias, B. Gonçalves, F. da Silva, J. Santos, E. Ricardo, T. Franke, A. Krimmer, W. Biel, *A Diagnostics Slim Cassette Concept for Reflectometry Measurements in DEMO*, 32nd Symposium on Fusion Technology (SOFT 2022) hybrid edition (**September 2022**)
- A. Malaquias (Speaker), R. Luís, A. Silva, Y. Nietiadi, J. Belo, A. Vale, D. Rechena, W. Biel, J. Santos, F. Silva, E. Ricardo, *Diagnostic integration concepts for DEMO - The reflectometry example*, International Conference on Diagnostics For Fusion Reactors (ICFRD2020), Varenna, Italy (**September 2021**)
- W. Biel, E. Alessi, R. Ambrosino, M. Ariola, I. Bolshakova, K.J. Brunner, M. Cecconello, S. Conroy, D. Dezman, I. Duran, S. Entler, E. Fable, D. Farina, T. Franke, L. Giacomelli, L. Giannone, R. Gomes, B. Gonçalves, S. Heuraux, A. Hjalmarsson, M. Hron, F. Janky, A. Jesenko, A. Krimmer, O. Kudlacek, R. Luís, O. Marchuk, G. Marchiori, M. Mattei, F. Maviglia, G. de Masi, D. Mazon, P. Muscente, Y. Nietiadi, S. Nowak, A. Pironti, A. Quercia, E. Ricardo, N. Rispoli, G. Sergienko, G. Schramm, S. El Shawish, M. Siccinio, A. Silva, F. da Silva, C. Sozzi, M. Tardocchi, D. Testa, W. Treutterer, A. Vale, O. Vasyliev, S. Wiesen, H. Zohm, *Disruption avoidance strategies for DEMO*, 28th European Fusion Programme Workshop, virtual edition (**December 2020**)
- Y. Nietiadi (Speaker), C. Vidal, R. Luís, P. Varela, *Thermal analysis of the in-vessel frontends of the ITER plasma position reflectometry system*, International Conference on Advancement in Nuclear Instrumentation Measurement Methods and their Applications (ANIMMA) 2019, Portoroz, Slovenia (**June 2019**)

- R. Luís (Speaker), A. Lopes, Y. Nietiadi, F. Mourão, B. Gonçalves, A. Vale, E. Ricardo, A. Silva, A. Malaquias, *Neutron shielding assessment of a multi-reflectometer system for DEMO*, 3rd European Conference on Plasma Diagnostics (ECPD) 2019, Portugal (**May 2019**)

Posters at Conferences/Meetings

- Y. Nietiadi, R. Luís, A. Silva, J.H. Belo, A. Vale, A. Malaquias, B. Gonçalves, F. da Silva, J. Santos, E. Ricardo, W. Biel, *Thermomechanical Analysis of a Multi-Reflectometer System for DEMO*, 32nd Symposium on Fusion Technology (SOFT 2022), hybrid edition (**September 2022**)
- Y. Nietiadi, R. Luís, A. Silva, and B. Gonçalves, *Structural Analysis of a Diagnostics Slim Cassette for DEMO*, European Conference on Plasma Diagnostics (ECPD 2021), virtual edition (**June 2021**)
- Y. Nietiadi, R. Luís, A. Silva, E. Ricardo, B. Gonçalves, T. Franke, and W. Biel, *Nuclear and thermal analysis of a multi-reflectometer system for DEMO*, 31st Symposium on Fusion Technology (SOFT 2020), virtual edition (**September 2020**)
- W. Biel, E. Alessi, R. Ambrosino, M. Ariola, I. Bolshakova, K.J. Brunner, M. Cecconello, S. Conroy, D. Dezman, I. Duran, S. Entler, E. Fable, D. Farina, T. Franke, L. Giacomelli, L. Giannone, R. Gomer, B. Gonçalves, S. Heuraux, A. Hjalmarsson, M. Hron, F. Janky, A. Jesenko, A. Krimmer, O. Kudlacek, R. Luís, O. Marchuk, G. Marchiori, M. Mattei, F. Maviglia, G. de Masi, D. Mazon, P. Muscente, Y. Nietiadi, S. Nowak, A. Pironti, A. Quercia, E. Ricardo, N. Rispoli, G. Sergienko, R. Schramm, S. El Shawish, M. Siccinio, A. Silva, C. Sozzi, M. Tardocchi, D. Testa, W. Treutterer, A. Vale, O. Vasyliev, S. Wiesen, H. Zohm, F. da Silva, *Overview on the development of the DEMO diagnostic and control system*, 31st Symposium on Fusion Technology (SOFT 2020), virtual edition (**September 2020**)

The scientific contributions of the author to several projects outside the work presented and discussed in this PhD Thesis are summarised below:

Peer-reviewed Papers

- S.B. Korsholm, A. Chambon, B. Gonçalves, V. Infante, T. Jensen, E. Klinkby, A. Larsen, R. Luís, Y. Nietiadi, E. Nonbøl, J. Rasmussen, D. Rechena, M. Salewski, A. Taormina, A. Vale, P. Varela, L. Sanchez, R. Ballester, V. Udintsev, Y. Liu, *ITER Collective Thomson Scattering – preparing to diagnose fusion-born alpha particles*, Review of Scientific Instruments (**2022, published**)
- A.Chambon, R. Luís, E. Klinkby, Y. Nietiadi, D. Rechena, B. Gonçalves, M. Jessen, S.B. Korsholm, A.W. Larsen, B. Lauritzen, J. Rasmussen, M. Salewski, M. Fabbri, C. Morillo, *Assessment of shutdown dose rates in the ITER collective Thomson Scattering system and in equatorial port plug 12*, Journal of Instrumentation (**2021, published**), DOI: 10.1088/1748-0221/16/12/C12001
- R. Luís, Y. Nietiadi, A. Silva, B. Gonçalves, T. Franke, and W. Biel, *Nuclear analysis of the DEMO divertor survey visible high-resolution spectrometer*, Fusion Engineering and Design (**2021, published**), DOI: 10.1016/j.fusengdes.2021.112460
- A. Lopes, R. Luís, E. Klinkby, Y. Nietiadi, A. Chambon, E. Nonbøl, B. Gonçalves, M. Jessen, S.B. Korsholm, A.W. Larsen, B. Lauritzen, J. Rasmussen, and M. Salewski, *Shielding Analysis of the ITER Collective Thomson Scattering system*, Fusion Engineering and Design (**2020, published**), DOI: 10.1016/j.fusengdes.2020.111994

Presentations at Conferences/Meetings

- A. Chambon (Speaker), R. Luís, E. Klinkby, Y. Nietiadi, D. Rechena, B. Gonçalves, M. Jessen, S.B. Korsholm, A.W. Larsen, B. Lauritzen, J. Rasmussen, M. Salewski, *Assessment of Shutdown Dose Rates in the ITER Collective Thomson Scattering System and in Equatorial Port Plug 12*, 4th European Conference on Plasma Diagnostics 2021 (**June 2021**)
- A. Lopes (Speaker), R. Luís, E. Klinkby, E. Nonbøl, B. Gonçalves, M. Jessen, S.B. Korsholm, A.W. Larsen, B. Lauritzen, Y. Nietiadi, J. Rasmussen, M. Salewski, *Nuclear Analysis and Neutron Activation Assessment for the ITER Collective Thomson Scattering system*, International Conference on Advancement in Nuclear Instrumentation Measurement Methods and their Applications (ANIMMA) 2019, Portoroz, Slovenia (**June 2019**)
- A. Lopes(Speaker), R. Luís, E. Klinkby, E. Nonbøl, C. Vidal, Y. Nietiadi, *Nuclear analysis of the ITER Collective Thomson Scattering diagnostic*, 13th ITER Neutronics Meeting, Cadarache, France (**November 2018**)

Posters at Conferences/Meetings

- R. Luís, Y. Nietiadi, A. Silva, B. Gonçalves, T. Franke, and W. Biel, *Nuclear analysis of the DEMO divertor survey visible high-resolution spectrometer*, 31st Symposium on Fusion Technology (SOFT 2020), virtual edition (**September 2020**)
- A. Lopes, R. Luís, E. Klinkby, E. Nonbøl, M. Jessen, R. Moutinho, M. Salewski, J. Rasmussen, B. B. Gonçalves Lauritzen, S.B. Korsholm, A.W. Larsen, C. Vidal, Y. Nietiadi, *Nuclear analysis of the collective Thomson Scattering system for ITER*, 30th Symposium of Fusion Technology (SOFT 2018), Italy (**September 2018**)
- A. Lopes, R. Luís, E. Klinkby, E. Nonbøl, B. Gonçalves, M. Jessen, S.B. Korsholm, A.W. Larsen, B. Lauritzen, Y. Nietiadi, J. Rasmussen, M. Salewski, *Nuclear analysis of the collective Thomson Scattering system*, 3rd European Conference on Plasma Diagnostics (ECPD), Portugal (**May 2018**)

Bibliography

[1] C. Zou, Q. Zhao, G. Zhang, and B. Xiong, "Energy revolution: From a fossil energy era to a new energy era," *Natural Gas Industry B*, vol. 3, no. 1, pp. 1–11, 2016. DOI:10.1016/j.ngib.2016.02.001.

[2] J. Tollefson, "Carbon's future in black and white: There are reasons to be optimistic that the world will break its addiction to fossil fuels. But time is running out," *Nature*, vol. 556, pp. 422–425, 2018. DOI: 10.1038/d41586-018-04931-6.

[3] IEA, "Global energy-related CO2 emissions, 1900-2020 – Charts – Data & Statistics." https://www.iea.org/data-and-statistics/charts/global-energy-related-co2-emissions-1900-2020.

[4] BP, "BP Statistical Review of World Energy." https://www.bp.com/content/dam/bp/business-sites/en/global/corporate/pdfs/energy-economics/statistical-review/bp-stats-review-2021-full-report.pdf, 2021.

[5] H. Ritchie and M. Roser, "CO_2 and Greenhouse Gas Emissions," *Our World in Data*, 2020. DOI:10.1002/2014GL061957.

[6] European Environment Agency (EEA, "Trends in atmospheric concentrations of CO2 (ppm), CH4 (ppb) and N2O (ppb), between 1800 and 2017." https://www.eea.europa.eu/data-and-maps/data/external/agage-measurements, 2017.

[7] Population Division of United Nations, "World Urbanization Prospects." https://population.un.org/wup/DataQuery/.

[8] D. Castelvecchi, "Neutrinos reveal final secret of Sun's nuclear fusion," *Nature*, vol. 583, pp. 20–21, Jul 2020. DOI:10.1038/d41586-020-01908-2.

[9] H. Hora, G. H. Miley, and F. Osman, "Boltzmann equilibrium of endothermic heavy nuclear synthesis in the universe and a quark relation to the magic numbers," *Astrophysics and Space Science*, vol. 298, no. 1, pp. 247–253, 2005.

[10] N. Ghahramany, S. Gharaati, and M. Ghanaatian, "New approach to nuclear binding energy in integrated nuclear model," *J. Theor. Appl. Phys.*, vol. 6, p. 3, Jul 2012. DOI:10.1186/2251-7235-6-3.

[11] M. Kikuchi, K. Lackner, and M. Quang, *Fusion Physics*. International Atomic Energy Agency, 2012.

[12] D.A. Brown et al., "ENDF/B-VIII.0: The 8th Major Release of the Nuclear Reaction Data Library with CIELO-project Cross Sections, New Standards and Thermal Scattering Data," *Nuclear Data Sheets*, vol. 148, pp. 1–142, 2018. DOI:10.1016/j.nds.2018.02.001.

[13] J. R. McNally Jr., K. E. Rothe, and R. D. Sharp, "Fusion reactivity graphs and tables for charged particle reactions," tech. rep., Oak Ridge national Laboratory, Oak Ridge, TN (United States), Aug 1979.

[14] J.P. Freidberg, *Plasma physics and fusion energy*. Cambridge University Press, 2007.

[15] G. R. Blumenthal and R. J. Gould, "Bremsstrahlung, Synchrotron Radiation, and Compton Scattering of High-Energy Electrons Traversing Dilute Gases," *Rev. Mod. Phys.*, vol. 42, pp. 237–270, Apr 1970. DOI: 10.1103/RevModPhys.42.237.

[16] J. D. Lawson, "Some criteria for a power producing thermonuclear reactor," *Proc. Phys. Soc. Sect. B*, vol. 70, pp. 6–10, Jan 1957. DOI:10.1088/0370-1301/70/1/303.

[17] P. H. Rebut, "ITER: the first experimental fusion reactor," *Fusion Eng. Des.*, vol. 27, pp. 3–16, Mar 1995. DOI:10.1016/0920-3796(95)90113-2.

[18] ITER Organization, "What is ITER?." https://www.iter.org/proj/inafewlines.

[19] E. A. Azizov, "Tokamaks: from A D Sakharov to the present (the 60-year history of tokamaks)," *Physics-Uspekhi*, vol. 55, pp. 190–203, Feb 2012. DOI: 10.3367/ufne.0182.201202j.0202.

[20] A. E. Costley, "Towards diagnostics for a fusion reactor," *IEEE Trans. Plasma Sci.*, vol. 38, no. 10 PART 2, pp. 2934–2943, 2010. DOI: 10.1109/TPS.2010.2064182.

[21] N. Mitchell et al., "The ITER magnets: Design and construction status," *IEEE Trans. Appl. Supercond.*, vol. 22, pp. 4200809–4200809, Jun 2012. DOI: 10.1109/TASC.2011.2174560.

[22] G. De Tommasi, "Plasma Magnetic Control in Tokamak Devices," *J. Fusion Energy*, vol. 38, no. 3-4, pp. 406–436, 2019. DOI:10.1007/s10894-018-0162-5.

[23] A. R. Christopherson et al., "Theory of alpha heating in inertial fusion: Alpha-heating metrics and the onset of the burning-plasma regime," *Phys. Plasmas*, vol. 25, p. 072704, Jul 2018. DOI: 10.1063/1.5030337.

[24] K. Ioki et al., "ITER-FEAT vacuum vessel and blanket design features and implications for the r&d programme," *Nuclear Fusion*, vol. 41, pp. 265–275, Mar 2001. DOI:10.1088/0029-5515/41/3/303.

[25] C.R. Rudy and K.C. Jordan, "Tritium half-life," tech. rep., Mound Lab., 1977.

[26] M. Rubel, "Fusion Neutrons: Tritium Breeding and Impact on Wall Materials and Components of Diagnostic Systems," *Journal of Fusion Energy*, vol. 38, pp. 315–329, Aug 2019. DOI:10.1007/s10894-018-0182-1.

[27] D. Stork, "DEMO and the Route to Fusion Power." 3^{rd} Karlsruhe International School on Fusion Technology, 2009.

[28] H. Zohm, "DEMO demonstration power plant." http://www.ipp.mpg.de/16355/demo.

[29] "ITER ... and then what?." http://www.iter.org/mag/3/22.

[30] W. Biel et al., "Controlling a DEMO reactor with a sparse set of diagnostics," 18th International Congress on Plasma Physics (ICPP 2016), Kaohsiung (Taiwan), 27 Jun 2016 - 1 Jul 2016, 2016.

[31] EUROfusion, "Roadmap." https://www.euro-fusion.org/eurofusion/roadmap/.

[32] G. Federici et al., "European DEMO design strategy and consequences for materials," *Nucl. Fusion*, vol. 57, no. 9, 2017. DOI:10.1088/1741-4326/57/9/092002.

[33] D. Stork et al., "Assessment of the EU R & D Programme on DEMO Structural and High-Heat Flux Materials," Tech. Rep. December, Culham Centre for Fusion Energy (CCFE), 2012.

[34] G. Federici et al., "Overview of the DEMO staged design approach in Europe," *Nuclear Fusion*, vol. 59, p. 066013, Apr 2019. DOI: 10.1088/1741-4326/ab1178.

[35] A. Costley et al., "ITER Diagnostics: design choices and solutions," in *Proc. 19th IAEA Fusion Energy Conf.*, 2002.

[36] A. E. Costley, T. Sugie, G. Vayakis, and C. I. Walker, "Technological challenges of ITER diagnostics," *Fusion Eng. Des.*, vol. 74, pp. 109–119, 2005. DOI:10.1016/j.fusengdes.2005.08.026.

[37] A. J.H. Donné, A. E. Costley, and A. W. Morris, "Diagnostics for plasma control on DEMO: Challenges of implementation," *Nucl. Fusion*, vol. 52, p. 074015, Jul 2012. DOI:10.1088/0029-5515/52/7/074015.

[38] G. Federici et al., "An overview of the EU breeding blanket design strategy as an integral part of the DEMO design effort," *Fusion Engineering and Design*, vol. 141, pp. 30–42, 2019. DOI:10.1016/j.fusengdes.2019.01.141.

[39] J. Linke et al., "Challenges for plasma-facing components in nuclear fusion," *Matter and Radiation at Extremes*, vol. 4, no. 5, p. 056201, 2019. DOI:10.1063/1.5090100.

[40] International Atomic Energy Agency (IAEA), *Development of Radiation Resistant Reactor Core Structural Materials*. Vienna, 2007.

[41] D.R. Olander, *Fundamental aspects of nuclear reactor fuel elements*. Technical Information Center, Office of Public Affairs Energy Research and Development Administration, Jan 1976.

[42] T. N. Todd, "Diagnostic systems in DEMO: Engineering design issues," *AIP Conference Proceedings*, vol. 1612, pp. 9–16, 2014. DOI:10.1063/1.4894017.

[43] J. M. Linke, T. Hirai, M. Rödig, and L. A. Singheiser, "Performance of plasma-facing materials under intense thermal loads in tokamaks and stellarators," *Fusion Science and Technology*, vol. 46, pp. 142–151, 2004. DOI:10.13182/FST04-A550.

[44] S. J. Zinkle, "Fusion and Spallation Irradiation Conditions." International Workshop on Advanced Computational Science: Application to Fusion and Feneration-IV Fission Reactors, 2004.

[45] F. A. Garner and L. R. Greenwood, “Neutron irradiation effects in fusion or spallation structural materials: Some recent insights related to neutron spectra,” *Radiat. Eff. Defects Solids*, vol. 144, no. 1-4, pp. 251–286, 1998. DOI:10.1080/10420159808229678.

[46] A. Möslang et al., “Towards reduced activation structural materials data for fusion DEMO reactors,” *Nucl. Fusion*, vol. 45, pp. 649–655, Jul 2005. DOI:10.1088/0029-5515/45/7/013.

[47] V. Barabash, “In-vessel Component, SDC-IC IDM: ITER_D_222RHC v.3.0,” tech. rep., ITER Organization, 2012.

[48] M. L. Grossbeck F. W. Wiffen, P. J. Maziasz, E. E. Bloom, J. O. Stieglar, “the Behavior of Type 316 Stainless Steel Undersimulated Fusion Reactor Irradiation,” in *Proc. Symp. t he Met. Phys. Stainl. Steels.*, Historical Energy Database, AIME, May 1978. DOI:10.2172/6750137.

[49] R. Luís et al., “Neutronics analysis of the in-vessel components of the ITER plasma-position reflectometry system on the low-field side,” *Fusion Engineering and Design*, vol. 123, pp. 847–851, 2017. DOI:10.1016/j.fusengdes.2017.03.141.

[50] R. Luís et al., “Neutronics Analysis of the In-Vessel Components of the ITER Plasma-Position Reflectometry System on the High-Field Side,” *IEEE Transactions on Nuclear Science*, vol. 65, no. 9, pp. 2404–2411, 2018. DOI:10.1109/TNS.2018.2810950.

[51] R. Luís et al., “Nuclear and thermal analysis of a reflectometry diagnostics concept for demo,” *IEEE Transactions on Plasma Science*, vol. 46, no. 5, pp. 1247–1253, 2018. DOI:10.1109/TPS.2017.2780922.

[52] L. Prior, *Design and Mechanical of an Integrated Reflectometry System Module for the DEMO Project*. Master’s thesis, Instituto Superior Técnico, 2018.

[53] A. Malaquias et al., “Integration Concept of the Reflectometry Diagnostic for the Main Plasma in DEMO,” *IEEE Transactions on Plasma Science*, vol. 46, no. 2, pp. 451–457, 2018. DOI:10.1109/TPS.2017.2784785.

[54] W. Biel et al., “Diagnostics for plasma control – From ITER to DEMO,” *Fusion Engineering and Design*, vol. 146, pp. 465–472, 2019. DOI:10.1016/j.fusengdes.2018.12.092.

[55] Y. Nietiadi et al., “Nuclear and thermal analysis of a multi-reflectometer system for DEMO,” *Fusion Engineering and Design*, vol. 167, p. 112349, 2021. DOI:10.1016/j.fusengdes.2021.112349.

[56] A.I. Anisimov, N.I. Vinogradov, V.E. Golant, and B.P. Konstantinov, “Method of investigating electron spatial distribution in a plasma,” *Soviet Physics-Technical Physics*, vol. 5, no. 9, pp. 939–948, 1961.

[57] G.D. Conway et al., “Plasma rotation profile measurements using Doppler reflectometry,” *Plasma Physics and Controlled Fusion*, vol. 46, no. 6, p. 951, 2004. DOI:10.1088/0741-3335/46/6/003.

[58] J. Santos et al., “Reflectometry-based plasma position feedback control demonstration at ASDEX Upgrade,” *Nuclear Fusion*, vol. 52, no. 3, p. 032003, 2012. DOI:10.1088/0029-5515/52/3/032003.

[59] J. Santos, L. Guimarais, M. Manso, and ASDEX Upgrade Team, “Real-time reflectometry measurement validation in H-mode regimes for plasma position control,” *Review of Scientific Instruments*, vol. 81, no. 10, p. 10D926, 2010. DOI:10.1063/1.3499640.

[60] A. Silva et al., “Ultrafast broadband frequency modulation of a continuous wave reflectometry system to measure density profiles on ASDEX Upgrade,” *Review of Scientific Instruments*, vol. 67, no. 12, pp. 4138–4145, 1996. DOI:10.1063/1.1147517.

[61] M. E. Manso et al., “Reflectometry in conventional and advanced plasma scenarios on ASDEX Upgrade and perspectives for ITER,” *Plasma physics and controlled fusion*, vol. 43, no. 12A, p. A73, 2001. DOI:10.1088/0741-3335/43/12A/306.

[62] Antonio Silva, *The ASDEX Upgrade broadband microwave reflectometry system*. PhD thesis, Instituto Superior Técnico, 2006.

[63] L. Zeng et al., “Application of fast reflectometer density profile measurements to investigate plasma instabilities in DIII-D,” *Review of scientific instruments*, vol. 74, no. 3, pp. 1530–1533, 2003. DOI:10.1063/1.1527250.

[64] L. Zeng et al., “Fast automated analysis of high-resolution reflectometer density profiles on DIII-D,” *Nuclear fusion*, vol. 46, no. 9, p. S677, 2006. DOI:10.1088/0029-5515/46/9/S03.

[65] G. Wang et al., “High-resolution dual-polarization frequency modulated reflectometer density profile measurements on DIII-D,” *Review of scientific instruments*, vol. 75, no. 10, pp. 3800–3803, 2004. DOI:10.1063/1.1788849.

[66] A.E. Hubbard, A. E. Costley, and C.W. Gowers, “A simple fixed-frequency reflectometer for plasma density profile measurements on JET,” *Journal of Physics E: Scientific Instruments*, vol. 20, no. 4, p. 423, 1987. DOI:10.1088/0022-3735/20/4/016.

[67] L. Meneses et al., “New reflectometer design for density profile measurements on JET,” *Review of scientific instruments*, vol. 77, no. 10, p. 10E927, 2006. DOI:10.1063/1.2338308.

[68] L. Cupido et al., “New millimeter-wave access for JET reflectometry and ECE,” *Fusion Engineering and Design*, vol. 74, no. 1-4, pp. 707–713, 2005. DOI:10.1016/j.fusengdes.2005.06.312.

[69] F. Clairet, C. Bottereau, J.-M. Chareau, and R. Sabot, “Advances of the density profile reflectometry on TORE SUPRA,” *Review of scientific instruments*, vol. 74, no. 3, pp. 1481–1484, 2003. DOI:10.1063/1.1530359.

[70] F. Clairet et al., “Fast sweeping reflectometry upgrade on Tore Supra,” *Review of Scientific Instruments*, vol. 81, no. 10, p. 10D903, 2010. DOI:10.1063/1.3460624.

[71] R. Sabot et al., “Single sideband modulator, a key component of Tore-Supra heterodyne reflectometers,” *Review of scientific instruments*, vol. 75, no. 8, pp. 2656–2659, 2004. DOI:10.1063/1.1777379.

[72] J.C. Maxwell, “VIII. A dynamical theory of the electromagnetic field,” *Philosophical transactions of the Royal Society of London*, no. 155, pp. 459–512, 1865. DOI:10.1098/rstl.1865.0008.

[73] M. Taylor, "The appleton-hartree formula and dispersion curves for the propagation of electromagnetic waves through an ionized medium in the presence of an external magnetic field part 1: curves for zero absorption," *Proceedings of the Physical Society*, vol. 45, p. 245, mar 1933.

[74] H. P. Hugon, *Study and optimisation of the antennas for the ITER plasma-position reflectometry diagnostics system*. Master's thesis, Instituto Superior Técnico, 2014.

[75] V.L. Ginzburg, J. B. Sykes, and R.J. Tayler, *The Propagation of Electromagnetic Waves in Plasmas*. Commonwealth and International Library, Pergamon Press, 1970.

[76] K. G. Budden, *Radio Waves in the Ionosphere*. Cambridge University Press, 1961.

[77] I. H. Hutchinson, *Principles of Plasma Diagnostics*. Cambridge University Press, 2 ed., 2002.

[78] F. Simonet, "Measurement of electron density profile by microwave reflectometry on tokamaks," *Review of Scientific Instruments*, vol. 56, no. 5, pp. 664–669, 1985. DOI:10.1063/1.1138200.

[79] I. Nunes et al., "Characterization of the density profile collapse of type I ELMs in ASDEX Upgrade with high temporal and spatial resolution reflectometry," *Nuclear Fusion*, vol. 44, pp. 883–891, Jul 2004. DOI:10.1088/0029-5515/44/8/007.

[80] A. Bock et al., "Advanced tokamak investigations in full-tungsten asdex upgrade," *Physics of Plasmas*, vol. 25, no. 5, p. 056115, 2018. DOI:10.1063/1.5024320.

[81] A. Kallenbach, "ASDEX Upgrade." https://www.ipp.mpg.de/16195/asdex.

[82] I. Milch, "30years of ASDEX Upgrade." https://www.euro-fusion.org/news/2021/march/30-years-of-asdex-upgrade/.

[83] V. Udintsev, M.F. Direz, and F. S. Arcos, *Design Description Document (DDD) for 55.F3 Plasma Position Reflectometry IDM: ITER_D_76MW26_v.1.9*. ITER Organization, Marseille, 2012.

[84] General Atomics, "DIII-D National Fusion Facility." https://www.ga.com/magnetic-fusion/diii-d.

[85] L. Zeng et al., "Performance and data analysis aspects of the new DIII-D monostatic profile reflectometer system," *Review of Scientific Instruments*, vol. 85, no. 11, p. 11D843, 2014. DOI:10.1063/1.4889775.

[86] D. Clery, "JET fusion reactor passes 30 and plunges into midlife crisis," *Science*, vol. 341, p. 121, 2013. DOI:10.1126/SCIENCE.341.6142.121.

[87] P.H. Rebut, "The jet preliminary tritium experiment," *Plasma Physics and Controlled Fusion*, vol. 34, no. 13, p. 1749, 1992. DOI:10.1088/0741-3335/34/13/002.

[88] E. Gibney, "Nuclear-fusion reactor smashes energy record," *Nature*, Feb 2022. DOI:10.1038/D41586-022-00391-1.

[89] A. Sirinelli and B. Alper and C. Bottereau and F. Clairet and L. Cupido and J. Fessey and C. Hogben and L. Meneses and G. Sandford and M. J. Walsh and JET-EFDA Contributors, "Multiband reflectometry system for density profile measurement with high temporal resolution on JET tokamak," *Review of Scientific Instruments*, vol. 81, no. 10, p. 10D939, 2010. DOI:10.1063/1.3502329.

[90] ITER Organization, "On the road to iter: milestones." https://www.iter.org/proj/itermilestones#18.

[91] F. Clairet et al., "X-mode heterodyne reflectometer for edge density profile measurements on tore supra," *Review of Scientific Instruments*, vol. 72, no. 1, pp. 340–343, 2001. DOI:10.1063/1.1319865.

[92] T. Gerbaud et al., "Comparison of density fluctuation measurements between O-mode and X-mode reflectometry on Tore Supra," *Review of Scientific Instruments*, vol. 77, no. 10, p. 10E928, 2006. DOI:10.1063/1.2354310.

[93] Ph. Moreau et al., "Ultrafast frequency sweep heterodyne reflectometer on the Tore Supra tokamak," *Review of Scientific Instruments*, vol. 71, no. 1, pp. 74–81, 2000. DOI:10.1063/1.1150164.

[94] J. Chadwick, "The existence of a neutron," *Proc. R. Soc. London. Ser. A, Contain. Pap. a Math. Phys. Character*, vol. 136, pp. 692–708, Jun 1932. DOI:10.1098/rspa.1932.0112.

[95] J. Chadwick, "Possible existence of a neutron," *Nature*, vol. 129, no. 3252, p. 312, 1932. DOI:10.1038/129312a0.

[96] K.S. Krane, *Introductory Nuclear Physics*. John Wiley & Sons, Inc, 1987.

[97] D. Reilly et al., *Passive Nondestructive Assay of Nuclear Materials*. United States Nuclear Regulatory Comission, 1991.

[98] A.L. Nichols, D.L. Aldama, and M. Verpelli, *Handbook of Nulcear data for safeguards database extensions*. IAEA, 2008.

[99] G. Breit and E. Wigner, "Capture of slow neutrons," *Phys. Rev.*, vol. 49, pp. 519–531, Apr 1936. DOI:10.1103/PhysRev.49.519.

[100] A. J.M. Plompen et al., "The joint evaluated fission and fusion nuclear data library, JEFF-3.3," *Eur. Phys. J. A*, vol. 56, p. 181, Jul 2020. DOI:10.1140/epja/s10050-020-00141-9.

[101] W. M. Stacey, *Nuclear Reactor Physics: Second Edition*. Wiley, Feb 2007.

[102] J.R. Lamarsh and A.J. Baratta, *Introduction to Nuclear Engineering Third Edition*. Prentics Hall, Inc, 2001.

[103] L. Dobrzynski, K. Blinowski, and M. Copper, *Neutrons and Solid State Physics*. Ellis Horwood Ltd., 1994.

[104] N. Metropolis and S. Ulam, "The Monte Carlo Method," *Journal of the American Statistical Association*, vol. 44, pp. 335–341, Sep 1949. DOI:10.1080/01621459.1949.10483310.

[105] J. M. Perlado, "The monte carlo method," in *Systems Reliability Assessment* (A. G. Colombo and A. S. de Bustamante, eds.), (Dordrecht), pp. 23–43, Springer Netherlands, 1990.

[106] N. Metropolis, *The Beginning of the Monte Carlo Method*, 1987.

[107] Jasmina L Vujic, "Monte Carlo Sampling Methods," *Monte Carlo*, p. 25, 2008.

[108] D. P. Kroese, T. Brereton, T. Taimre, and Z. I. Botev, "Why the Monte Carlo method is so important today," *WIREs Comput Stat*, vol. 6, pp. 386–392, 2014.

[109] A. Badano and J. Kanicki, "Monte Carlo analysis of the spectral photon emission and extraction efficiency of organic light-emitting devices," *Journal of Applied Physics*, vol. 90, pp. 1827–1830, Aug 2001. DOI:10.1063/1.1385571.

[110] M. Mesta et al., "Molecular-scale simulation of electroluminescence in a multilayer white organic light-emitting diode," *Nature Materials*, vol. 12, pp. 652–658, Apr 2013. DOI:10.1038/nmat3622.

[111] X-5 Monte Carlo Team, *MCNP - A General Monte Carlo N-Particle Transport Code, version 5 - Volume I: Overview and Theory*. Los Alamos National Security, LLC, 2003.

[112] R. A. Forster and T. N. K. Godfrey, "MCNP - a general Monte Carlo code for neutron and photon transport," in *Monte-Carlo Methods and Applications in Neutronics, Photonics and Statistical Physics* (Raymond Alcouffe et al., eds.), vol. 240, pp. 33–55, Berlin/Heidelberg: Springer-Verlag, 1985. Series Title: Lecture Notes in Physics.

[113] S. Ghali, *Constructive Solid Geometry*, pp. 277–283. London: Springer London, 2008. DOI:10.1007/978-1-84800-115-2_30.

[114] C. R Sonawane and G. Sujit, "Design Intent for CAD Modeling Features Using Boolean Operations," *IOP Conference Series: Materials Science and Engineering*, vol. 197, p. 012047, May 2017. DOI:10.1088/1757-899x/197/1/012047.

[115] G. H. Kinchin and R. S. Pease, "The Displacement of Atoms in Solids by Radiation," *Reports on Progress in Physics*, vol. 18, pp. 1–51, Jan 1955. DOI:10.1088/0034-4885/18/1/301.

[116] J.K. Shultis and R.E. Faw, *An MCNP Primer*. Kansas State University, Manhattan, 2011.

[117] J. S. Hendricks and T. E. Booth, "MCNP variance reduction overview," in *Monte-Carlo Methods and Applications in Neutronics, Photonics and Statistical Physics* (R. Alcouffe et al., eds.), (Berlin, Heidelberg), pp. 83–92, Springer Berlin Heidelberg, 1985.

[118] R.A. Forrest et al., "FENDL-3 Library - Summary documentation," tech. rep., International Atomic Energy Agency (IAEA), Vienna International Centre, P.O. Box 100, 1400 Vienna, Austria, Dec 2012.

[119] Nuclear Energy Agency, "Index to the JEF-1 Nuclear Data Library, volume 1," tech. rep., Nuclear Energy Agency (NEA), Vienna International Centre, P.O. Box 100, 1400 Vienna, Austria, 1985.

[120] U. Fischer, "PMI-3.3-T014-D001 - Guidelines for neutronics analyses," 2017. IDM: EFDA_D_2L8TR9_v.1.5.

[121] R. Kinsey, "Data Formats and Procedures for the Evaluated Nuclear Data File, ENDF," tech. rep., Brookhaven National Laboratory, 1979.

[122] A. J. Koning et al., "The JEFF evaluated nuclear data project," in *Proceedings of the ND 2007 International Conference on Nuclear Data for Science and Technology*, pp. 721–726, Jan 2007.

[123] K. Shibata et al., "JENDL-4.0: A New Library for Nuclear Science and Engineering," *Journal of Nuclear Science and Technology*, vol. 48, no. 1, pp. 1–30, 2011. DOI:10.1080/18811248.2011.9711675.

[124] A.I. Blokhin et al., "Current Status of Russian Evaluated Neutron Data Libraries," in *Proc. of International Conference on Nuclear Data for Science and Technology*, p. 695, May 1994.

[125] International Atomic Energy Agency, "FENDL-2.1." https://www-nds.iaea.org/fendl21/.

[126] M. Martone, M. Angelone, and M. Pillon, "The 14 MeV Frascati neutron generator," *Journal of Nuclear Materials*, vol. 212-215, pp. 1661–1664, 1994. DOI:10.1016/0022311594911096.

[127] P. Batistoni et al., "Validation of FENDL-2.1 nuclear data library for use in ITER nuclear analysis," in *ND2007*, (Nice, France), p. 257, EDP Sciences, 2007. DOI:10.1051/ndata:07700.

[128] U. Fischer, D. Leichtle, and A. Serikov, "FENDL-2.1 Benchmark Analyses," tech. rep., NEA Data Bank, 2006.

[129] K. Seidel et al., "Benchmark experiments to validate the nuclear data of tungsten," *Fusion Engineering and Design*, vol. 81, no. 8, pp. 1211–1217, 2006. DOI:10.1016/j.fusengdes.2005.09.050.

[130] P. Batistoni et al., "Neutronics experiment on a helium cooled pebble bed (HCPB) breeder blanket mock-up," *Fusion Engineering and Design*, vol. 82, no. 15, pp. 2095–2104, 2007. DOI:10.1016/j.fusengdes.2007.04.009.

[131] D. Leichtle et al., "Sensitivity and uncertainty analyses of the tritium production in the hcpb breeder blanket mock-up experiment," *Fusion Engineering and Design*, vol. 82, no. 15, pp. 2406–2412, 2007. DOI:10.1016/j.fusengdes.2007.08.007.

[132] K. Seidel et al., "Measurement and analysis of neutron and gamma-ray flux spectra in a neutronics mock-up of the HCPB Test Blanket Module," *Fusion Engineering and Design*, vol. 82, no. 15, pp. 2212–2216, 2007. DOI:10.1016/j.fusengdes.2007.05.043.

[133] International Atomic Energy Agency, "FENDL–3.0." https://www-nds.iaea.org/fendl30/.

[134] U. Fischer et al., "Benchmarking of the FENDL-3 Neutron Cross-Section Data Library for Fusion Applications," Mar 2014.

[135] C. Konno et al., "FENDL-3.0 benchmark test with shielding experiments at JAEA/TIARA," tech. rep., JAEA, 2015.

[136] K. Kondo, U. Fischer, P. Pereslavtsev, and A. Serikov, "Analyses of shielding benchmark experiments using FENDL-3 cross-section data starter library for ITER and IFMIF applications," *Progress in Nuclear Science and Technology*, vol. 4, pp. 322–326, Jan 2014. DOI:10.15669/pnst.4.322.

[137] A. Lopes, *Collective Thomson Scattering and Plasma Position Reflectometry systems for ITER and DEMO: Neutronics performance assessment and optimisation*. PhD thesis, Instituto Superior Técnico, 2020.

[138] R. C. Little, “New Photon Library from ENDF Data,” tech. rep., Los Alamos National Laboratory, 2003.

[139] M. C. White, “Photoatomic data library MCPLIB04: a new photoatomic library based on data from ENDF/B-VI release 8,” tech. rep., Los Alamos National Laboratory, 2003.

[140] B. C. Kiedrowski and F. B. Brown and M. C. White and D. K. Parsons and MCNP Documentation, “Testing for the photon doppler broadening data sampling bug in MCNP5/X,” tech. rep., Los Alamos National Laboratory, 2012.

[141] M.C. White, “Further notes on MCPLIB03/04 and new MCPLIB63/84 Compton broadening data for all versions of MCNP 5,” tech. rep., Los Alamos National Laboratory, 2012.

[142] Bethany Colling, I Kodeli, S Lilley, and LW Packer, “Benchmarking comparison and validation of mcnp photon interaction data,” in *EPJ Web of Conferences*, vol. 146, p. 06024, EDP Sciences, 2017.

[143] Chinese Academy of Sciences (CAS) Frontier Development of Science Team of the Institute of Nuclear Energy Safety Technology (INEST). http://www.fds.org.cn/en/other/fds.asp.

[144] Y. Li et al., “Benchmarking of MCAM 4.0 with the ITER 3D model,” *Fusion Engineering and Design*, vol. 82, no. 15, pp. 2861–2866, 2007. DOI:10.1016/j.fusengdes.2007.02.022.

[145] Y. Wu, “CAD-based interface programs for fusion neutron transport simulation,” *Fusion Engineering and Design*, vol. 84, no. 7, pp. 1987–1992, 2009. DOI:10.1016/j.fusengdes.2008.12.041.

[146] E. Brun et al., “TRIPOLI-4®, CEA, EDF and AREVA reference Monte Carlo code,” *Annals of Nuclear Energy*, vol. 82, pp. 151–160, 2015. DOI:10.1016/j.anucene.2014.07.053.

[147] S. Agostinelli et al., “Geant4—a simulation toolkit,” *Nuclear Instruments and Methods in Physics Research Section A: Accelerators, Spectrometers, Detectors and Associated Equipment*, vol. 506, no. 3, pp. 250–303, 2003. DOI:10.1016/S0168-9002(03)01368-8.

[148] G. Battistoni et al., “Overview of the FLUKA code,” *Annals of Nuclear Energy*, vol. 82, pp. 10–18, 2015. DOI:10.1016/j.anucene.2014.11.007.

[149] Y. Wu et al., “CAD-based Monte Carlo program for integrated simulation of nuclear system SuperMC,” *Annals of Nuclear Energy*, vol. 82, pp. 161–168, 2015. DOI:10.1016/j.anucene.2014.08.058.

[150] H. Tsige-Tamirat, U. Fischer, A. Serikov, and S. Stickel, “Use of McCad for the conversion of ITER CAD data to MCNP geometry,” *Fusion Engineering and Design*, vol. 83, no. 10, pp. 1771–1773, 2008. DOI:10.1016/j.fusengdes.2008.07.040.

[151] L. Lu, Y. Qiu, and U. Fischer, “Improved solid decomposition algorithms for the CAD-to-MC conversion tool McCad,” *Fusion Engineering and Design*, vol. 124, pp. 1269–1272, 2017. DOI:10.1016/j.fusengdes.2017.02.040.

[152] A. Ribes and C. Caremoli, "Salomé platform component model for numerical simulation," in *31st Annual International Computer Software and Applications Conference (COMPSAC 2007)*, vol. 2, pp. 553–564, 2007. DOI:10.1109/COMPSAC.2007.185.

[153] Electricité de France, "Finite element *code_aster*, Analysis of Structures and Thermomechanics for Studies and Research." Open source on www.code-aster.org, 1989–2017.

[154] F. Archambeau, N. Méchitoua, and M. Sakiz, "Code Saturne: A Finite Volume Code for the computation of turbulent incompressible flows - Industrial Applications," *International Journal on Finite Volumes*, vol. 1, pp. http://www.latp.univ–mrs.fr/IJFV/spip.php?article3, Feb. 2004.

[155] G. Sannazzaro et al., "Development of design Criteria for ITER In-vessel Components," *Fusion Engineering and Design*, vol. 88, no. 9, pp. 2138–2141, 2013. DOI:10.1016/j.fusengdes.2013.01.019.

[156] J. Guirao, "Building Good Load Specifications," Mar 2017.

[157] ASME Boiler, "Pressure vessel code section viii division 1," *American Society of Mechanical Engineers Press. New York, NY*, 2007.

[158] ASME BPVC, "Asme boiler and pressure vessel code, section viii, division 2, rules for construction of pressure vessels, alternative rules," *American Society of Mechanical Engineers (ASME), New York, USA*, 2011.

[159] ASME Boiler, Pressure Vessel Committee, et al., *Qualification Standard for Welding and Brazing Procedures, Welders, Brazers, and Welding and Brazing Operators*. American Society of Mechanical Engineers, 2007.

[160] *Presentation of RCC-MR Code 2007 for High Temperature Reactor and ITER Projects: General Overview*, vol. Volume 1: Codes and Standards of *Pressure Vessels and Piping Conference*, Jul 2009. DOI:10.1115/PVP2009-77118.

[161] Domenico De Meis, "RCC-MRx design code for nuclear components," Dec 2015.

[162] C. A. de J. Miranda, A. A. Faloppa, M. M. Neto, and G. Fainer, "ASME stress linearization and classification – a discussion based on a case study," in *Proc. of International Nuclear Atlantic Conference*, Oct 2011.

[163] G. Ferenc, E. Gaganidze, and I. Szenthe, "Material Property Handbook on EUROFER97 (2016-MTA)," 2020. IDM: EFDA_D_2MT9X8.

[164] G. Slagis, "ASME Section III Design-by-Analysis Criteria Concepts and Stress Limits," *Journal of Pressure Vessel Technology-transactions of The Asme - J PRESSURE VESSEL TECHNOL*, vol. 128, Feb 2006. DOI:10.1115/1.2140797.

[165] S. Timoshenko and J. N. Goodier, *Theory of elasticity*. McGraw-Hill Book Company, Inc, 1951.

[166] S. M. A. Kazimi, *Solid Mechanics*. Tata McGraw-Hill, 2006.

[167] F.P. Incropera, D. P. Dewitt, T. L. Bergman, and A. S. Lavine, *Fundamentals of Heat and Mass Transfer*. John Wiley & Sons, 2007.

[168] J. B. J. Fourier, *The analytical theory of heat*. Cambridge University Press, 1878.

[169] J. H. Lienhard IV and J. H. Lienhard V, *A Heat Transfer Textbook*. Phlogiston Press, 2019.

[170] K. C. Cheng and T. Fujii, "heat in history Isaac Newton and Heat Transfer," *Heat Transfer Engineering*, vol. 19, no. 4, pp. 9–21, 1998. DOI:10.1080/01457639808939932.

[171] S.A. Alameri and A.K. Alkaabi, "1 - Fundamentals of nuclear reactors," in *Nuclear Reactor Technology Development and Utilization* (Salah Ud-Din Khan and Alexander Nakhabov, eds.), Woodhead Publishing Series in Energy, pp. 27–60, Woodhead Publishing, 2020.

[172] M. Planck and M. Masius, *The Theory of Heat Radiation*. The Maple Press, 1914.

[173] ANSYS®, *Theory Reference for the Mechanical APDL and Mechanical Applications*. Canonsburg, PA, USA, 2009.

[174] J. Walker, D. Halliday, and R. Resnick, *Fundamental of Physics*. John Wiley & Sons, Inc, 2013.

[175] A. E. Tekkaya and C. Soyarslan, *Finite Element Method*, pp. 508–514. Berlin, Heidelberg: Springer Berlin Heidelberg, 2014. DOI:10.1007/978-3-642-20617-7_16699.

[176] G. P. Nikishkov, "Introduction to the Finite Element Method," Jan 2004.

[177] J. N. Reddy, *An introduction to the finite element method*, vol. 1221. McGraw-Hill New York, 2004.

[178] R. D. Cook, D. S. Malkus, M. E. Plesha, and R. J. Witt, *Concepts and applications of finite element analysis*. John wiley & sons, 2007.

[179] H. K. Versteeg and W. Malalasekera, *An introduction to computational fluid dynamics - the finite volume method.* Addison-Wesley-Longman, 1995.

[180] H. Hattori et al., "DNS, LES and RANS of turbulent heat transfer in boundary layer with suddenly changing wall thermal conditions," *International Journal of Heat and Fluid Flow*, vol. 41, pp. 34–44, 2013. DOI:10.1016/j.ijheatfluidflow.2013.03.014.

[181] ANSYS®, *ANSYS CFX-Solver Theory Guide*. Canonsburg, PA, USA, 2011.

[182] F. Menter, M. Kuntz, and R. B. Langtry, "Ten years of industrial experience with the SST turbulence model," *Heat and Mass Transfer*, vol. 4, Jan 2003.

[183] F.C. Lockwood and N.G. Shah, "A new radiation solution method for incorporation in general combustion prediction procedures," *Symposium (International) on Combustion*, vol. 18, no. 1, pp. 1405–1414, 1981. DOI:10.1016/S0082-0784(81)80144-0.

[184] H. Knaus et al., *Comparison of different radiative heat transfer models and their applicability in coal-fired utility boiler simulations*. Universität Stuttgart, Fakultät Energietechnik, 1997.

[185] A.N. Elmekawy, "Module 01:CoreSkills." `https://drahmednagib.com/CAD_2018/Lecture_2_Meshing_1.pdf`, 2018. Accessed: 30-01-2022.

[186] ANSYS®, *Meshing User's Guide, Release 13.0*. Canonsburg, PA, USA, 2010.

[187] F. da Silva and S. Heuraux, "Study of ITER plasma position reflectometer using a two-dimensional full-wave finite-difference time domain code," *Review of Scientific Instruments*, vol. 79, no. 10, p. 10F104, 2008. DOI:10.1063/1.2955568.

[188] H. Policarpo et al., "Optimum design of the ITER in-vessel plasma-position reflectometry antenna coverage," *Fusion Engineering and Design*, vol. 123, pp. 654–658, 2017. DOI:10.1016/j.fusengdes.2017.05.075.

[189] P.B. Quental, H. Policarpo, R. Luís, and P. Varela, "Thermal analysis of the in-vessel components of the ITER plasma-position reflectometry," *Review of Scientific Instruments*, vol. 87, no. 11, p. 11E720, 2016. DOI:10.1063/1.4960493.

[190] C. Vacas and J. Guirao, *55.F3 – PPR: Load Specification for In-Vessel components*. ITER Organization, Marseille, 2015.

[191] C. Vidal et al., "Thermal analysis of a waveguide section of the ITER plasma-position reflectometry system on the high-field side," *Fusion Engineering and Design*, vol. 146, pp. 2389–2392, 2019. DOI:10.1016/j.fusengdes.2019.03.197.

[192] V. Barabash, "Historical baseline document: Appendix A, materials design limit data," tech. rep., ITER Organization, 2013.

[193] Y. Nietiadi, C. Vidal, R. Luís, and P. Varela, "Thermal analyses of the in-vessel frontends of the ITER plasma position reflectometry system," *Fusion Engineering and Design*, vol. 156, p. 111599, 2020. DOI:10.1016/j.fusengdes.2020.111599.

[194] ENOVIA Database. https://www.3ds.com/products-services/enovia/disciplines/.

[195] ENOVIA Database for ITER. https://www.iter.org/newsline/118/1718.

[196] CATIA®V5. https://www.3ds.com/products-services/catia/disciplines/.

[197] ANSYS®, *Academic Research Mechanical, Release 19.1*. Canonsburg, PA, USA, 2018.

[198] G. W. Mckinney et al., "MCNP 6.1.1 - New Features Demonstrated," in *Proceedings IEEE Nuclear Scientific Symposium*, Nov 2014.

[199] TS Byun and K Farrell, "Tensile properties of Inconel 718 after low temperature neutron irradiation," *Journal of Nuclear Materials*, vol. 318, pp. 292–299, 2003.

[200] W. Biel et al., "Development of a concept and basis for the demo diagnostic and control system," *Fusion Engineering and Design*, vol. 179, p. 113122, 2022. DOI:10.1016/j.fusengdes.2022.113122.

[201] O. Crofts et al., "Overview of progress on the european demo remote maintenance strategy," *Fusion Engineering and Design*, vol. 109, pp. 1392–1398, 2016. DOI:10.1016/j.fusengdes.2015.12.013.

[202] A. Jesenko et al., "DEMO Diagnostics and Control System Requirement Document," Mar 2020. IDM:EFDA_D_2MNK4R_v3.0.

[203] G. Renko, "DC-2-T026-D001, DC-2-T026-D002, DC-2-T026-D003, DC-2-T026-D004 Final Report On Collection and structuring of requirements for DEMO diagnostics and control and Initial CAD Studies and Engineering Analysis, including Diagnostic Integration on DEMO and List of Ex-Vessel Diagnostic Components on DEMO, their Locations and Estimated Space Consumption (input to KDII6) and Contribution to the development of a concept for the ex-vessel diagnostic layout, and specific investigations of the correlation of diagnostics and control signals (Industry)," Feb 2021. IDM:EFDA_D_2PJN3V_v1.2.

[204] M. Zerbini, "WPDC_Final review meeting_ECE diagnostic design_Marco Zerbini_18Jan2022," Jan 2022. IDM:EFDA_D_2PKXA7_v1.0.

[205] J. H. Belo et al., "Design and integration studies of a diagnostics slim cassette concept for DEMO," *Nuclear Fusion*, vol. 61, p. 116046, Oct 2021. DOI:10.1088/1741-4326/ac24d3.

[206] L.V. Boccaccini et al., "Objectives and status of EUROfusion DEMO blanket studies," *Fusion Engineering and Design*, vol. 109-111, pp. 1199–1206, 2016. DOI:10.1016/j.fusengdes.2015.12.054.

[207] S. Jimenez, "Upper Port RM CAD Model," Feb 2018. IDM:EFDA_D_2N8JKE_v1.0.

[208] F. Cismondi et al., "Progress in eu breeding blanket design and integration," *Fusion Engineering and Design*, vol. 136, pp. 782–792, 2018. DOI:10.1016/j.fusengdes.2018.04.009.

[209] A. Del Nevo et al., "Recent progress in developing a feasible and integrated conceptual design of the WCLL BB in EUROfusion project," *Fusion Engineering and Design*, vol. 146, pp. 1805–1809, 2019. DOI:10.1016/j.fusengdes.2019.03.040.

[210] A. Tassone, G. Caruso, and A. Del Nevo, "Influence of pbli hydraulic path and integration layout on mhd pressure losses," *Fusion Engineering and Design*, vol. 155, p. 111517, 2020. DOI:10.1016/j.fusengdes.2020.111517.

[211] A. Del Nevo and P. Arena, "BB.WCLL-JUS-2-CD1-BB WCLL Design Description Document (DDD)," Apr 2021. IDM:EFDA_D_2NGB4U.

[212] S. Budden and J. Keep, "RM-3.1.2-T001 PD10-Concept Design Description for Blanket transporter," Jun 2019. IDM:EFDA_D_2MRZLG.

[213] WCLL development team (2020).

[214] C. Gliss, "CAD Model Blanket Supports Study," Oct 2017. IDM:EFDA_D_2NF6D9.

[215] HCPB development team (2020).

[216] J. Keep et al., "Remote handling of DEMO breeder blanket segments: Blanket transporter conceptual studies," *Fusion Engineering and Design*, vol. 124, pp. 420–425, 2017. DOI:10.1016/j.fusengdes.2017.02.016.

[217] S. Budden et al., "Rescue and recovery studies for the DEMO blanket transporter," *Fusion Engineering and Design*, vol. 146, pp. 2494–2497, 2019. DOI:10.1016/j.fusengdes.2019.04.026.

[218] A. Wilde, “Concept Design Description for The DEMO Upper Port Maintenance System,” Jul 2018. IDM:EFDA_D_2MMR6P_v3.1.

[219] R. Luís et al., “Final report on diagnostic design, integration and engineering studies for DEMO, covering the technical specifications of this task specification,” Feb 2022. IDM:EFDA_D_2PAPE2.

[220] Z. Vizvary et al., “European DEMO first wall shaping and limiters design and analysis status,” *Fusion Engineering and Design*, vol. 158, p. 111676, 2020. DOI:10.1016/j.fusengdes.2020.111676.

[221] F. Maviglia et al., “Impact of plasma thermal transients on the design of the EU DEMO first wall protection,” *Fusion Engineering and Design*, vol. 158, p. 111713, 2020. DOI:10.1016/j.fusengdes.2020.111713.

[222] T. Franke et al., “The EU DEMO equatorial outboard limiter — Design and port integration concept,” *Fusion Engineering and Design*, vol. 158, p. 111647, 2020. DOI:10.1016/j.fusengdes.2020.111647.

[223] C. Bachmann et al., “Key design integration issues addressed in the EU DEMO pre-concept design phase,” *Fusion Engineering and Design*, vol. 156, p. 111595, 2020. DOI:10.1016/j.fusengdes.2020.111595.

[224] T. Steinbacher, “DEMO For Study CAD Model,” Jul 2019. IDM:EFDA_D_2NR3DB.

[225] C. Vorpahl, R. Mozzillo, C. Bachmann, and G. Di Gironimo, “Initial configuration studies of the upper vertical port of the european demo,” *Fusion Engineering and Design*, vol. 146, pp. 2469–2473, 2019. DOI:10.1016/j.fusengdes.2019.04.021.

[226] D. Iglesias, “Final Report on Deliverable MMS Blanket Handling Assessment,” May 2015. IDM:EFDA_D_2HD4JD.

[227] B. Caiffi, “Neutron shielding study of the DEMO upper vertical port,” Des 2014. IDM:EFDA_D_2APSUF_v1.0.

[228] D. Cooper, “RH compatible baseline segmentation in VV with shifted port,” Jan 2015. IDM:EFDA_D_2MEDGC.

[229] R. Luís et al., “Design Description Document of the Reflectometry System,” Sep 2021. IDM:EFDA_D_2NFMG8.

[230] E. Ricardo, F. da Silva, S. Heuraux, and A. Silva, “Assessment of a multi-reflectometers positioning system for DEMO plasmas,” *Journal of Instrumentation*, vol. 14, pp. C08010–C08010, Aug 2019. DOI:10.1088/1748-0221/14/08/c08010.

[231] A. Malaquias and R. Moutinho, “2017 reflectometry diagnostic slim cassette and WGs port extensions,” Jun 2017. IDM:EFDA_D_2MJKQ3_v1.0.

[232] G.W Wille, K.T Slattery, D.E Driemeyer, and G.D Morgan, “Development of 316L(N)-IG stainless steel fabrication approaches for ITER divertor and limiter applications,” *Fusion Engineering and Design*, vol. 39-40, pp. 499–504, 1998. DOI:10.1016/S0920-3796(98)00138-0.

[233] J.M. Gentzbittel, I. Chu, and H. Burlet, "The effect of hot isostatic pressing parameters on microstructure and mechanical properties of Eurofer powder HIPed material," *Journal of Nuclear Materials*, vol. 307-311, pp. 540–543, 2002. DOI:10.1016/S0022-3115(02)00972-8.

[234] R. Luís et al., "DC-2-T025-D001 -D002 -D003 -D004 DC-2-T022-D002 Complete list of all diagnostic penetrations components and their space occupations within the vertical port area (input to KDI#4) (2020) (DC-2-T025-D001) Complete list of all diagnostic penetrations components and their space occupations within the blanket and slim cassette area including the eq. ports (input to KDI#2) (2020) (DC-2-T025-D002) CATIA drawings of diagnostic components and slim cassettes routing and interfaces (blanket to port door) and RH compatibility (2020) (DC-2-T025-D003) Radiation map in diagnostic components and affected machine systems (2020) (DC-2-T025-D004) EXTRA-Remote handling studies in support of DEMO diagnostic design (2019) (DC-2-T019-D002) EXTRA-Remote handling studies for DEMO diagnostics: Systems level analysis and development of RH requirements (2020) (DC-2-T022-D002)," Mar 2021. IDM:EFDA_D_2N7MQB_v1.6.

[235] J. Aubert et al., "Status of the eu demo hcll breeding blanket design development," *Fusion Engineering and Design*, vol. 136, pp. 1428–1432, 2018. DOI:10.1016/j.fusengdes.2018.04.133.

[236] R. Lindau et al., "Present development status of EUROFER and ODS-EUROFER for application in blanket concepts," *Fusion Engineering and Design*, vol. 75-79, pp. 989–996, 2005. DOI:10.1016/j.fusengdes.2005.06.186.

[237] R. Coppola and M. Klimenkov, "Dose Dependence of Micro-Voids Distributions in Low-Temperature Neutron Irradiated Eurofer97 Steel," *Metals*, vol. 9, no. 5, 2019. DOI:10.3390/met9050552.

[238] M. Roldán et al., "Nanoindentation and TEM to Study the Cavity Fate after Post-Irradiation Annealing of He Implanted EUROFER97 and EU-ODS EUROFER," *Micromachines*, vol. 9, no. 12, 2018. DOI:10.3390/mi9120633.

[239] G. Stornelli et al., "Grain Refinement and Improved Mechanical Properties of EUROFER97 by Thermo-Mechanical Treatments," *Applied Sciences*, vol. 11, no. 22, 2021. DOI:10.3390/app112210598.

[240] B. Weinhorst et al., "Comparative assessment of different approaches for the use of CAD geometry in Monte Carlo transport calculations," *Fusion Engineering and Design*, vol. 98-99, pp. 2094–2097, 2015. DOI:10.1016/j.fusengdes.2015.06.042.

[241] D. Flammini, "2017 Generic DEMO MCNP model at 22.5 degree v1.3," May 2019. IDM: EFDA_D_2MCJ69.

[242] A. Del Nevo, "WCLL design report 2017," Jul 2018. IDM:EFDA_D_2MYHNE_v1.1.

[243] J. Ahrens, B. Geveci, and C. Law, *ParaView: An End-User Tool for Large-Data Visualization*. Burlington, 2005. DOI:10.1016/B978-012387582-2/50038-1.

[244] U. Ayachit, *The ParaView Guide: A Parallel Visualization Application*, 2015.

[245] F. A. Hernandez and M. Oron-Carl, "Internal Deliverable BB-1.2.1-T004-D001: HCPB Design Report 2017," Des 2018. IDM:EFDA_D_2N66T5.

[246] F. Giannetti, A. Del Nevo, M. Oron-Carl, and C. Schweier, "BOP-2.2-T006-D006 WCLL BB DEMO Configuration without IHTS+ESS: BB/DIV/VV PHTS and Power Conversion System (PCS) Preliminary Design (DDD)," Jan 2020. IDM:EFDA_D_2N9MAE.

[247] A. Del Nevo, M. Oron-Carl, and P.Arena, "WCLL BB design and Integration studies 2019 activities," Feb 2020. IDM:EFDA_D_2P5NE5.

[248] F. Hernandez and M. Oron-Carl, "Internal Deliverable BB-1.2.1-T002-D001: HCPB Design Report 2015," Jun 2016. IDM:EFDA_D_2MNBH9.

[249] C. Bachmann et al., "Mechanical support concept of the demo breeding blanket," *Fusion Engineering and Design*, vol. 173, p. 112840, 2021. DOI:10.1016/j.fusengdes.2021.112840.

[250] M. Utili and A. Venturini, "TER.WCLL-JUS-2-CD1-TER WCLL Load Specification Document," Apr 2020. IDM:EFDA_D_2P86SX.

[251] G. A. Spagnuolo et al., "Development of load specifications for the design of the breeding blanket system," *Fusion Engineering and Design*, vol. 157, p. 111657, 2020. DOI:10.1016/j.fusengdes.2020.111657.

[252] AFCEN, *RCC-MRx: Design and construction rules for mechanical components of nuclear installations, Addenda Included (2013)*. Paris, France, 2013.

[253] R. Luís et al., "DC-2-T010-D001,-D002,-D003,-D004 Final Report on Deliverable(s): Complete list of all diagnostic penetrations, components and their space occupations within the vertical port area (input to KDI#4); Complete list of all diagnostic penetrations, components and their space occupations within the blanket and slim cassette area, including the eq. ports (input to KDI#2); CATIA drawings of diagnostic components and slim cassettes, routing and interfaces (blanket to port door) and RH compatibility; Radiation map in diagnostic components and affected machine systems," Mar 2021. IDM:EFDA_D_2MM2KJ_v1.1.

[254] R. Luís et al., "DC-2-T015-D001-D002-D003-D004, DC-2-T019-D001 (EXTRA) Final Report on Deliverable(s) Complete list of all diagnostic penetrations, components and their space occupations within the vertical port area (input to KDI#4) Complete list of all diagnostic penetrations, components and their space occupations within the blanket and slim cassette area, including the eq. ports (input to KDI#2) CATIA drawings of diagnostic components and slim cassettes, routing and interfaces (blanket to port door) and RH compatibility Radiation map in diagnostic components and affected machine systems EXTRA - Detailed neutronics studies for spectroscopic diagnostics on DEMO," Feb 2020. IDM:EFDA_D_2NYUJD.

[255] P.A. Di Maio et al., "Structural analysis of the back supporting structure of the DEMO WCLL outboard blanket," *Fusion Engineering and Design*, vol. 124, pp. 944–947, 2017. DOI:10.1016/j.fusengdes.2016.12.018.

[256] I. Catanzaro et al., "Structural assessment of the EU-DEMO WCLL Central Outboard Blanket segment under normal and off-normal operating conditions," *Fusion Engineering and Design*, vol. 167, p. 112350, 2021. DOI:10.1016/j.fusengdes.2021.112350.

[257] C. Bachmann, "IDD - Blanket Mechanical Supports," Jan 2019. IDM:EFDA_D_2NHC86.

[258] I. A. Maione, "BB-9.3.1-T005-D002: Assessment of EM results - 2018," Sep 2019. IDM:EFDA_D_2NUFTN.

[259] ANSYS®, *ANSYS HFSS 2020R1*. Canonsburg, PA, USA, 2020.

[260] C. Bachmann, "DEMO vacuum vessel load specification," Jul 2020. IDM:EFDA_D_2MBPN6_v1.8.

[261] A.P. King and E.A. Marcatili, "Transmission loss due to resonance of loosely-coupled modes in a multi-mode system," *The Bell System Technical Journal*, vol. 35, no. 4, pp. 899–906, 1956.

[262] H.J. Butterweck and F.C. de Ronde, "Oversized rectangular waveguide components for millimetre waves," *Philips Tech. Rev.*, vol. 29, pp. 86–101, 1968.

[263] F.J. Tischer, "Oversized waveguides and resonators for millimeter waves," *International journal of infrared and millimeter waves*, vol. 9, no. 1, pp. 15–27, 1988.

[264] E. Ricardo, P. Varela, A. Silva, and B. Gonçalves, "Assessment and performance optimization of the ITER plasma position reflectometry in-vessel oversized waveguide bends," *Fusion Engineering and Design*, vol. 98-99, pp. 1593–1596, 2015. DOI:10.1016/j.fusengdes.2015.06.169.

[265] S. Meschino et al., "Bends in oversized rectangular waveguide," *Fusion engineering and design*, vol. 86, no. 6-8, pp. 746–749, 2011.

[266] M. Cecconello et al., "Pre-conceptual study of the european demo neutron diagnostics," *Journal of Instrumentation*, vol. 14, no. 09, p. C09001, 2019. DOI:10.1088/1748-0221/14/09/C09001.

[267] W. Królas et al., "The IFMIF-DONES fusion oriented neutron source: evolution of the design," *Nuclear Fusion*, vol. 61, p. 125002, Dec 2021. DOI:10.1088/1741-4326/ac318f.

[268] E. Gaganidze, "DEMO-DEF-1-CD1 - Materials Properties Handbook - EUROFER97," Feb 2020. IDM:EFDA_D_2NZHBS.

[269] T. Hirose et al., "Physical properties of F82H for fusion blanket design," *Fusion Engineering and Design*, vol. 89, no. 7, pp. 1595–1599, 2014. [DOI:10.1016/j.fusengdes.2013.12.005].

[270] E. Gaganidze, "DEMO-DEF-1-CD1 - Materials Properties Handbook - Tungsten," Feb 2020. IDM:EFDA_D_2P3SPL.

Part V

Appendices

Appendix A

Material Definitions

This Appendix provides the material definitions for some of the materials used in the models of the ITER PPR system and the multi-reflectometer system of DEMO.

A.1 Stainless-Steel (SS316L(N)-IG)

Stainless-Steel (SS316L(N)-IG) material definition taken from [192].

A.1.1 Chemical composition

Table A.1: Chemical composition of Stainless-Steel (SS316L(N)-IG).

Element	Isotope	Abundance(%)	Volume Fraction (%)
B	^{10}B	19.90	0.002
	^{11}B	80.10	
N	^{14}N	99.63	0.070
	^{15}N	0.37	
Si	^{28}Si	92.23	0.500
	^{29}Si	4.68	
	^{30}Si	3.09	
P	^{31}P	100.00	0.025
Ti	^{46}Ti	8.25	0.100
	^{47}Si	7.44	
	^{48}Si	73.72	
	^{49}Si	5.41	
	^{50}Si	5.18	

Continued on next page

Table A.1 – continued from previous page

Element	Isotope	Abundance(%)	Volume Fraction (%)
Cr	^{50}Cr ^{52}Cr ^{53}Cr ^{54}Cr	4.34 83.79 9.50 2.37	17.500
Fe	^{54}Fe ^{56}Fe ^{57}Fe ^{58}Fe	5.84 91.75 2.12 0.28	64.750
Mn	^{55}Mn	100.00	1.800
Co	^{59}Co	100.00	0.050
Ni	^{58}Ni ^{60}Ni ^{61}Ni ^{62}Ni ^{64}Ni	68.08 26.22 1.14 3.63 0.93	12.250
Cu	^{63}Cu ^{65}Cu	69.17 30.83	0.300
Nb	^{93}Nb	100.00	0.100
Mo	^{92}Mo ^{94}Mo ^{95}Mo ^{96}Mo ^{97}Mo ^{98}Mo ^{100}Mo	14.84 9.25 15.92 16.68 9.55 24.13 9.63	2.500
Ta	^{181}Ta	100.00	0.010

A.1.2 Coefficient of thermal expansion

A.1.2.1 Unirradiated conditions

The equations describing the variations of the mean coefficient of thermal expansion α_m and the instantaneous coefficient of thermal expansion α_i as a function of temperature are:

$$\alpha_m = 15.13 + 7.93 \times 10^{-3}\, T - 3.33 \times 10^{-6}\, T^2 \tag{A.1}$$

and

$$\alpha_i = 14.97 + 1.599 \times 10^{-2}\, T - 9.99 \times 10^{-6}\, T^2 \tag{A.2}$$

with α_m and αi in 10^{-6} /K and T in °C. Equation (A.1) and Equation (A.2) are valid for the temperature range presented in Table A.2.

Table A.2: Mean α_m (reference temperature - 20 °C) and instantaneous α_i coefficients of linear thermal expansion.

T, °C	**20**	**50**	**100**	**150**	**200**	**250**	**300**	**350**	**400**	**450**	**500**
$\alpha_{\mathbf{m}}$,10^{-6}**/K**	15.3	15.5	15.9	16.2	16.6	16.9	17.2	17.5	17.8	18.0	18.3
$\alpha_{\mathbf{i}}$,10^{-6}**/K**	15.3	15.7	16.5	17.1	17.8	18.3	18.9	19.3	19.8	20.1	20.5

T, °C	**550**	**600**	**650**	**700**	**750**	**800**	**850**	**900**	**950**	**1000**
$\alpha_{\mathbf{m}}$,10^{-6}**/K**	18.5	18.7	18.9	19.0	19.2	19.3	19.5	19.6	19.7	19.7
$\alpha_{\mathbf{i}}$,10^{-6}**/K**	20.7	21.0	21.1	21.3	21.3	21.4	21.3	21.3		

A.1.2.2 Irradiation effects

The unirradiated values shall be used for irradiated conditions.

A.1.3 Young's modulus

A.1.3.1 Unirradiated conditions

Young's modulus, E, is given as a function of the temperature, T, by the following equation:

$$E = (201660 - 84.8T)/1000 \tag{A.3}$$

with E in GPa and T in °C. Equation (A.3) is valid for T values from 20 °C to 700 °C, as presented in Table A.3.

Table A.3: Values of Young's modulus from room temperature to 700 °C.

T, °C	**20**	**100**	**150**	**200**	**250**	**300**	**350**	**400**	**450**	**500**	**550**	**600**	**650**	**700**
E, GPa	200	193	189	185	180	176	172	168	164	159	155	151	147	142

A.1.3.2 Irradiation effects

The unirradiated values of E shall be used for irradiated conditions.

A.1.4 Poisson's ratio

The value 0.3 shall be used for elastic calculations.

Table A.4: Values of mass density from room temperature to 800 °C.

T, °C	20	50	100	150	200	250	300	350	400
ρ,kg/m^3	7930	7919	7899	7879	7858	7837	7815	7793	7770

T, °C	450	500	550	600	650	700	750	800
ρ,kg/m^3	7747	7724	7701	7677	7654	7630	7606	7582

A.1.5 Mass density

A.1.5.1 Unirradiated conditions

A.1.5.2 Irradiation effects

The effect of irradiation on the density is expressed through the swelling law. For irradiation temperatures below 450 °C and displacement doses below 10 dpa, swelling (and density changes) of stainless steel can be neglected.

A.1.6 Thermal conductivity

A.1.6.1 Unirradiated conditions

The thermal conductivity variation, λ, is given as a function of the temperature, T, by the following equation:

$$\lambda = 1.502 \times 10^{-2}\, T + 13.98 \tag{A.4}$$

with λ in W/(mK) and T in °C. Equation (A.4) is valid for T values from 20 °C to 800 °C, as presented in Table A.5.

Table A.5: Values of thermal conductivity from room temperature to 800 °C.

T, °C	20	50	100	150	200	250	300	350	400
λ,W/(m K)	14.28	14.73	15.48	16.23	16.98	17.74	18.49	19.24	19.99

T, °C	450	500	550	600	650	700	750	800
λ,W/(m K)	20.74	21.49	22.24	22.99	23.74	24.49	25.25	26.00

A.1.6.2 Irradiation effects

The thermal conductivity changes due to irradiation can be neglected for design analyses, if the displacement dose (fusion spectrum) does not exceed 3 dpa at temperatures from 20 °C to 450 °C.

A.1.7 Specific Heat

The specific heat, C_p, as a function of temperature is given by the following equation:

$$C_p = 462.69 + 0.520265T - 1.7117 \times 10^{-3}T^2 + 3.3658 \times 10^{-6}T^3 - 2.1958 \times 10^{-9}T^4 \tag{A.5}$$

with C_p in J/(kgK) and T in °C. Equation (A.5) is valid for T values from 20 °C to 800 °C, as presented in Table A.6.

Table A.6: Values of specific heat from room temperature to 500 °C.

T, °C	**20**	**50**	**100**	**150**	**200**	**250**	**300**	**350**	**400**	**450**	**500**
C_p,J/(kgK)	472	485	501	512	522	530	538	546	556	567	578

A.2 EUROFER

EUROFER material definition taken from [268].

A.2.1 Chemical composition

Table A.7: Chemical composition of EUROFER.

Element	**Isotope**	**Abundance(%)**	**Volume Fraction (%)**
B	^{10}B ^{11}B	19.90 80.10	0.001
C	^{12}C	100	0.105
N	^{14}N ^{15}N	99.63 0.37	0.040
O	^{16}O ^{17}O	99.96 0.04	0.001
Al	^{27}Al	100	0.004
Si	^{28}Si ^{29}Si ^{30}Si	92.23 4.68 3.09	0.026
P	^{31}P	100.00	0.020
S	^{32}S ^{33}S ^{34}S ^{36}S	94.89 0.77 4.33 0.02	0.003
Ti	^{46}Ti ^{47}Ti ^{48}Ti ^{49}Ti ^{50}Ti	8.25 7.44 73.68 5.45 5.18	0.001
			Continued on next page

Table A.7: Continued from previous page.

Element	Isotope	Abundance(%)	Volume Fraction (%)
V	^{51}V	100	0.200
Cr	^{50}Cr	4.35	9.000
	^{52}Cr	83.79	
	^{53}Cr	9.50	
	^{54}Cr	2.37	
Fe	^{54}Fe	5.85	88.821
	^{56}Fe	91.75	
	^{57}Fe	2.12	
	^{58}Fe	0.28	
Mn	^{55}Mn	100.00	0.550
Co	^{59}Co	100.00	0.005
Ni	^{58}Ni	68.08	0.010
	^{60}Ni	26.22	
	^{61}Ni	1.14	
	^{62}Ni	3.63	
	^{64}Ni	0.93	
Cu	^{63}Cu	69.17	0.003
	^{65}Cu	30.83	
Nb	^{93}Nb	100.00	0.005
Mo	^{92}Mo	14.81	0.003
	^{94}Mo	9.30	
	^{95}Mo	15.87	
	^{96}Mo	16.77	
	^{97}Mo	9.60	
	^{98}Mo	24.05	
	^{100}Mo	9.60	
Ta	^{181}Ta	100.00	0.120
W	^{182}W	26.53	1.100
	^{183}W	14.33	
	^{184}W	30.68	
	^{186}W	28.46	

Table A.8: Mean α_m (reference temperature - 20 °C) and instantaneous α_i coefficients of linear thermal expansion.

T, °C	**20**	**50**	**100**	**200**	**300**	**400**	**500**
$\alpha_{\mathbf{m}}$,10^{-6}/K	10.3	10.5	10.7	11.2	11.6	11.9	12.2
$\alpha_{\mathbf{i}}$,10^{-6}/K	10.3	10.6	11.1	11.9	12.6	13.2	13.5

A.2.2 Coefficient of thermal expansion

A.2.2.1 Unirradiated conditions

Irradiated conditions

The irradiated thermal expansion data for EUROFER is not available presently [268]. In reference [269], irradiation of FH82 at 588 K to a dose of 2.7 dpa has a small effect on the coefficient of thermal expansion, but it is suggested that higher fluences may affect the values.

A.2.3 Young's modulus

A.2.3.1 Unirradiated conditions

Table A.9: Values of Young's modulus from room temperature to 700 °C.

T, °C	**20**	**50**	**100**	**200**	**300**	**400**	**500**	**600**	**700**
E, GPa	217	215	212	207	202	196	190	170	162

A.2.3.2 Irradiated conditions

Presently values measured on aged EUROFER are not available.

A.2.4 Poisson's ratio

No exact measurement of Poisson's ratio exists for EUROFER. As a good approach, 0.3 can be used. This value is valid for most metals [268].

A.2.5 Mass density

A.2.5.1 Unirradiated conditions

Table A.10: Values of mass density from room temperature to 800 °C.

T, °C	**20**	**50**	**100**	**200**	**300**	**400**	**500**	**600**	**700**
ρ,kg/m^3	7744	7750	7740	7723	7691	7657	7625	7592	7559

A.2.5.2 Irradiation effects

High dose irradiation may cause swelling and consequently changes in the density. At low temperatures EUROFER shows a very long incubation time, with swelling starts at over 70 dpa. The aged EUROFER density value is not presently available.

A.2.6 Thermal conductivity

A.2.6.1 Unirradiated conditions

Table A.11: Values of thermal conductivity from room temperature to 800 °C.

T, °C	20	50	100	200	300	400	500	600
λ,W/(m K)	28.08	28.86	29.78	30.38	30.01	29.47	29.58	31.12

For practical applications, the thermal conductivity least squares fitted empirical equations for EUROFER are

$$\lambda = \begin{cases} 27.41997 + 0.0351\mathrm{T} - 1.2827 \times 10^{-4}\mathrm{T}^2 + 1.334\,27 \times 10^{-7}\mathrm{T}^3 & \text{if T in °C} \\ \\ 5.56254 + 0.134\,97\mathrm{T} - 2.375\,65 \times 10^{-4}\mathrm{T}^2 + 1.334\,27 \times 10^{-7}\mathrm{T}^3 & \text{if T in K} \end{cases} \tag{A.6}$$

A.2.6.2 Irradiation effects

The thermal conductivity values on aged EUROFER are not available.

A.2.7 Specific Heat

A.2.7.1 Unirradiated condition

The specific heat of EUROFER can be described by the following formula:

$$C_p = 2.6996\mathrm{T} - 0.004\,96\mathrm{T}^2 + 3.335 \times 10^{-6}\mathrm{T}^3 \tag{A.7}$$

with C_p in J/(kgK) and T in K.

Table A.12: Values of specific heat from room temperature to 500 °C.

T, °C	20	50	100	200	300	400	500	600
C_p,J/(kgK)	439	462	490	523	546	584	660	800

A.2.7.2 Irradiation effects

The specific heat values on aged EUROFER are not available.

A.2.8 Stress limit

For practical applications, the yield strength and ultimate tensile strength least squares fitted empirical equations for EUROFER are:

$$R_{p02,ave} = 542.69 - 0.692T + 0.005\,12T^2 - 1.926 \times 10^{-5}T^3 + 2.96 \times 10^{-8}T^4 - 1.755 \times 10^{-11}T^5, \quad (A.8)$$

$$R_{p02,min} = 491.5 - 0.627T + 0.004\,64T^2 - 1.744 \times 10^{-5}T^3 + 2.68 \times 10^{-8}T^4 - 1.59 \times 10^{-11}T^5, \quad (A.9)$$

and

$$R_{m,ave} = 670.1 - 0.904T + 0.004\,01T^2 - 1.091 \times 10^{-5}T^3 + 1.115 \times 10^{-8}T^4 - 4.75 \times 10^{-12}T^5 \quad (A.10)$$

The stress limit of EUROFER can be calculated according to [160] as

$$S = \min\left[\frac{2}{3}R_{p02,min}\,(20\,°C)\,\frac{2}{3}R_{p02,min}\,(\vartheta)\,,\,\frac{1}{4}R_{m,min}\,(20\,°C)\,,\,\frac{1}{3.6}R_{m,min}\,(\vartheta)\right] \quad (A.11)$$

$$S_m = \min\left[\frac{2}{3}R_{p02,min}\,(20\,°C)\,\frac{2}{3}R_{p02,min}\,(\vartheta)\,,\,\frac{1}{3}R_{m,min}\,(20\,°C)\,,\,\frac{1}{2.7}R_{m,min}\,(\vartheta)\right] \quad (A.12)$$

$$S_{mB} = \min\left[\frac{1}{3}R_{p02,min}\,(20\,°C)\,\frac{1}{3}R_{p02,min}\,(\vartheta)\right] \quad (A.13)$$

where S,S_m, and S_{mB} are in MPa and T is in °C

Table A.13 shows some values of the yield strength, ultimate tensile strength and allowable stress values for unirradiated EUROFER.

A.2.8.1 Unirradiated condition

Table A.13: Average and minimum yield strength values for unirradiated EUROFER and allowable stress values.

T (°C)	$R_{p02,ave}$ (MPa)	$R_{p02,min}$ (MPa)	$R_{m,ave}$ (MPa)	$R_{m,min}$ (MPa)	S_m (MPa)	S (MPa)	S_{mB} (MPa)
-200	1093	990	1118	1060			
-150	843	764	939	890			
-100	685	621	813	770			
-50	593	537	727	689			
0	543	492	670	635			
20	531	481	654	619	206	155	160

Continued on next page

Table A.13 – continued from previous page

T (°C)	$R_{p02,ave}$ (MPa)	$R_{p02,min}$ (MPa)	$R_{m,ave}$ (MPa)	$R_{m,min}$ (MPa)	S_m (MPa)	S (MPa)	S_{mB} (MPa)
50	519	470	634	601	206	155	157
100	508	460	610	578	206	155	153
150	503	455	593	562	206	155	152
200	497	450	579	549	203	152	150
250	487	441	563	534	198	148	147
300	473	428	544	516	191	143	143
350	454	411	519	492	182	137	137
400	430	390	489	463	172	129	130
450	403	365	451	427	158	119	122
500	371	336	405	384	142	107	112
550	332	300	352	334	124	93	100
600	282	255	291	276	102	77	85
700	118	107	140	132			

A.2.8.2 Irradiation effects

The yield strength curves of irradiated EUROFER, taken from [268], for low irradiation temperatures are presented in Figure A.1, while the ones for high irradiation temperatures and 16 to 18 dpa are presented in Figure A.2. The polynomial function to approximate the value of the EUROFER yield strength is summarized in Table A.14.

Table A.14: Yield strength trend curves for irradiated EUROFER.

Ageing conditions	**Polynom to calculate the yield strength** (MPa)
<3 dpa, <350 °C	$800.0\text{-}0.94T\text{+}0.0025T^2\text{-}4.128\times10^{-6}T^3$
7 to 15 dpa, <350 °C	$1070.015\,38\text{-}0.992\,01T\text{+}0.001\,14T^2$
30 to 42 dpa, <350 °C	1157.9-0.644T
70 to 78 dpa, <350 °C	1240.3-0.72T
16 to 18 dpa, ≥350 °C	1651.1-2.884T

On the other hand, the tensile strength trend curves of irradiated EUROFER taken from [268] for low irradiation temperature is presented in Figure A.3 while for high irradiation temperature for 16 to 18 dpa

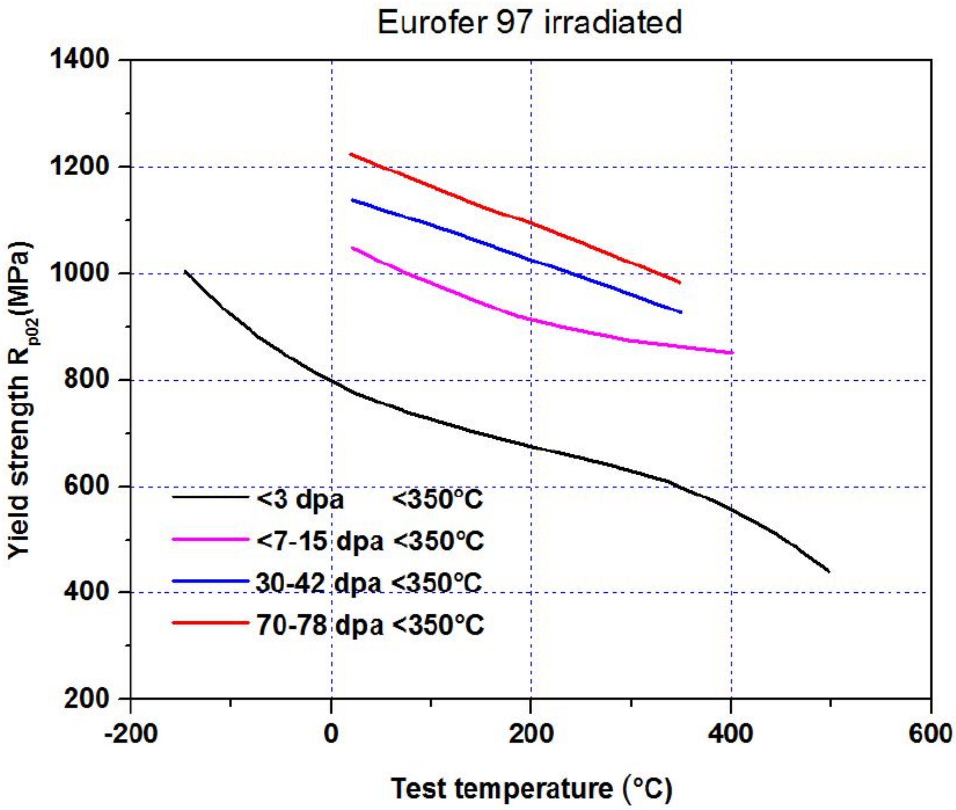

Figure A.1: Effect of the irradiation on the yield strength of EUROFER, for irradiation temperatures below 350 °C (taken from [268]).

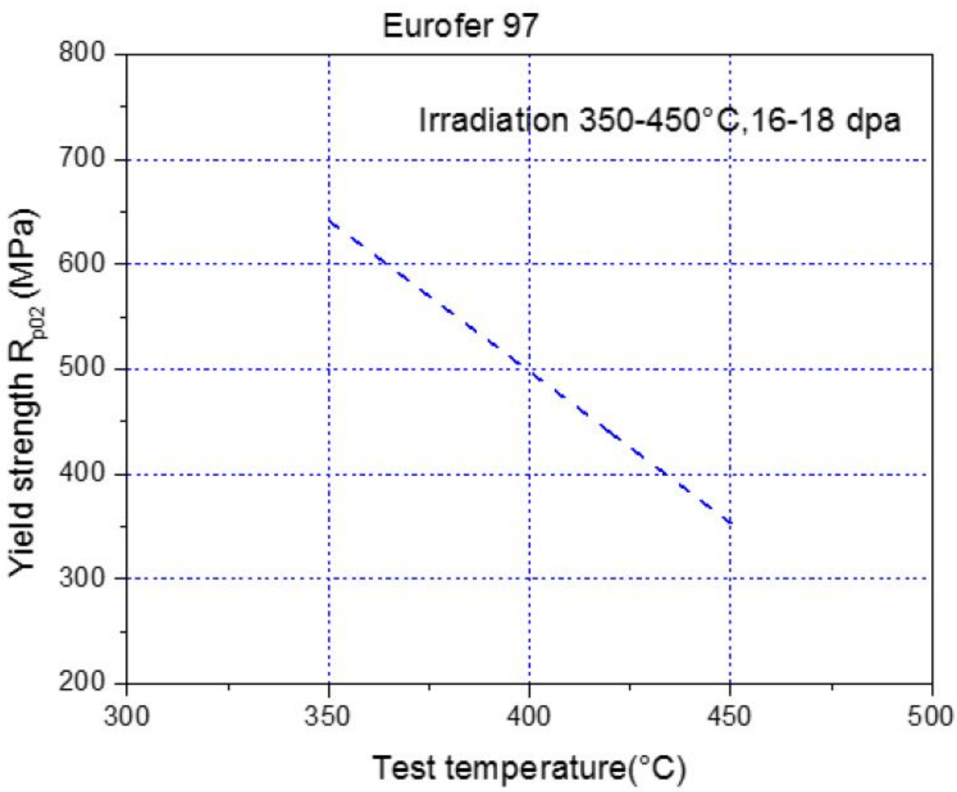

Figure A.2: Effect of the irradiation on the yield strength of EUROFER, at irradiation temperatures from 350 °C to 450 °C, 16 to 18 dpa. (taken from [268]).

is presented in Figure A.4, and the polynomial function to approximate the value of EUROFER yield strength is summarized in Table A.15

Table A.15: Ultimate tensile strength trend curves for irradiated EUROFER.

Ageing conditions	**Polynom to calculate the ultimate tensile strength** (MPa)
<3 dpa, <350 °C	$845.4\text{-}1.033T+0.0021T^2\text{-}2.5217\times10^{-6}T^3$
7 to 15 dpa, <350 °C	$1071.1\text{-}0.987T+0.001\,19T^2$
30 to 42 dpa, <350 °C	1170.5-0.675T
70 to 78 dpa, <350 °C	1251-0.7332T
16 to 18 dpa, ≥350 °C	1478.2-2.373T

A.3 Tungsten

Tungsten material definition taken from [270].

A.3.1 Chemical composition

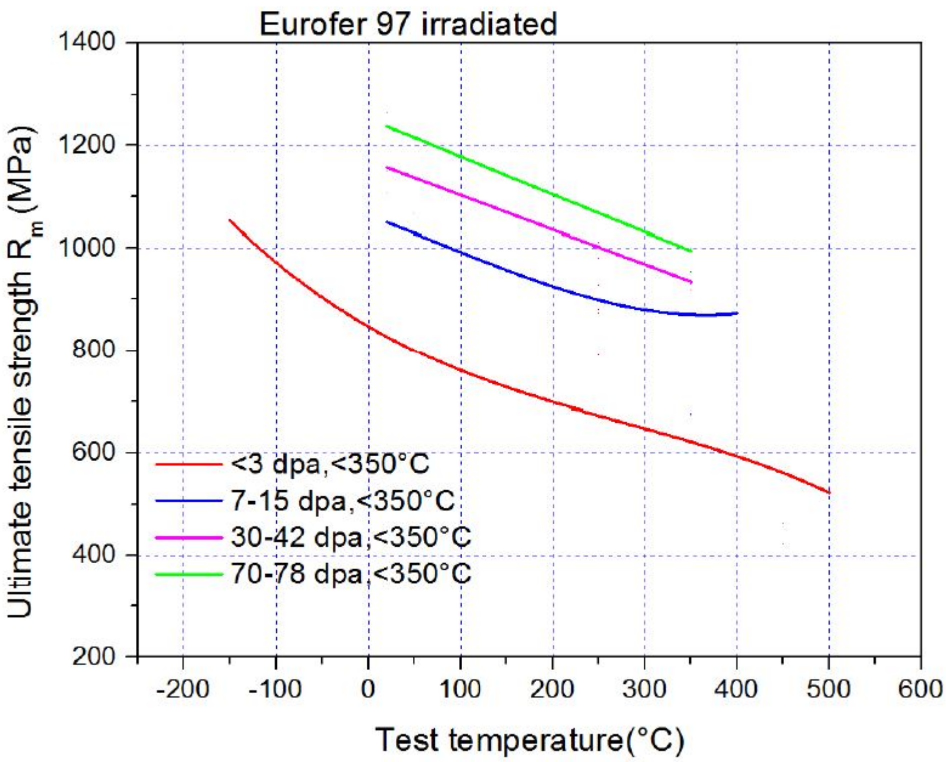

Figure A.3: Effect of the irradiation on the yield strength of EUROFER, for irradiation temperatures below 350 °C (taken from [268]).

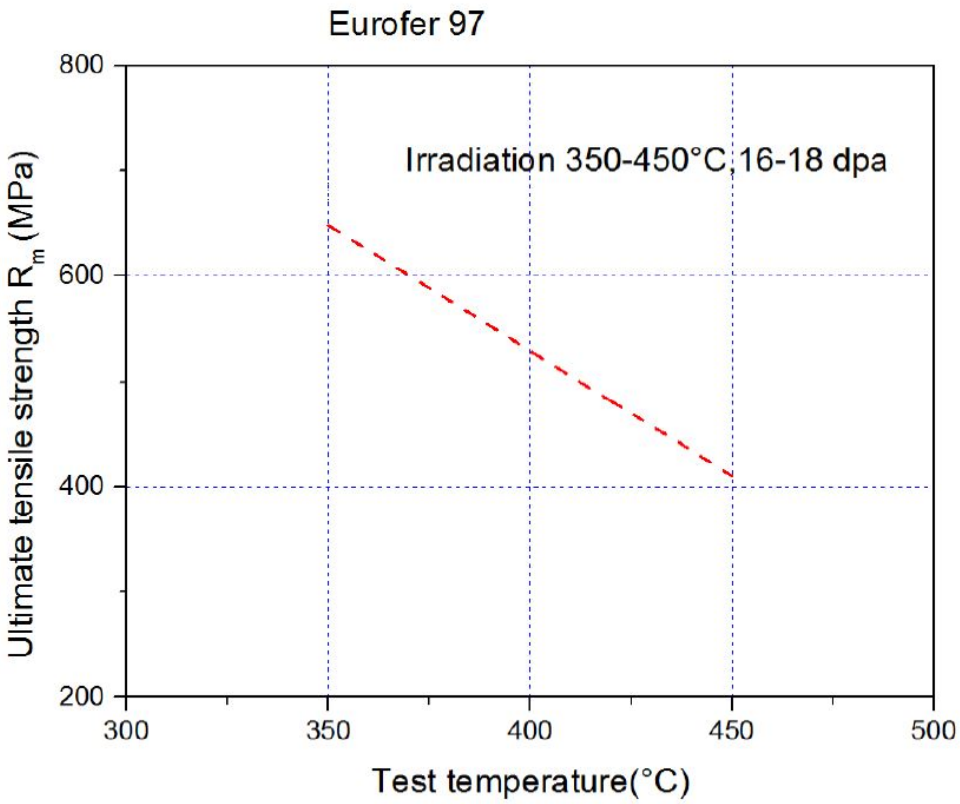

Figure A.4: Effect of the irradiation on the yield strength of EUROFER, at irradiation temperatures from 350 °C to 450 °C, 16 to 18 dpa (taken from [268]).

Table A.16: Chemical composition of Tungsten.

Element	Isotope	Abundance(%)	Volume Fraction (%)
W	^{182}W	26.53	100
	^{183}W	14.33	
	^{184}W	30.68	
	^{186}W	28.46	

A.3.2 Coefficient of thermal expansion

A.3.2.1 Unirradiated conditions

Table A.17: Mean α_m (reference temperature - 20 °C) and instantaneous α_i coefficients of linear thermal expansion.

T, °C	20	50	100	150	200	250	300	350
α_m, 10^{-6}/K	4.40229	4.40459	4.40937	4.41533	4.42248	4.43082	4.44034	4.45105
α_i, 10^{-6}/K	4.25943	4.25975	4.26346	4.27112	4.28273	4.29829	4.31780	4.34126

T, °C	400	450	500	550	600	650	700
α_m, 10^{-6}/K	4.46295	4.47603	4.49031	4.50576	4.52241	4.54024	4.55926
α_i, 10^{-6}/K	4.36868	4.40004	4.43536	4.47463	4.51785	4.56502	4.61615

A.3.2.2 Irradiated conditions

The unirradiated values shall be used for irradiated conditions.

A.3.3 Young's modulus

A.3.3.1 Unirradiated conditions

Table A.18: Values of Young's modulus from room temperature to 700 °C.

T, °C	20	50	100	150	200	250	300	350
E, GPa	395.97	395.74	395.24	394.60	393.82	392.91	391.86	390.67

T, °C	400	450	500	550	600	650	700
E, GPa	389.34	387.88	386.27	384.53	382.66	380.64	378.49

A.3.3.2 Irradiated conditions

The unirradiated values of E shall be used for irradiated conditions.

A.3.4 Poisson's ratio

Table A.19: Values of Poisson's ratio from room temperature to 700 °C.

T, °C	20	50	100	150	200	250	300	350
ν	0.2802	0.2804	0.2807	0.2810	0.2814	0.2818	0.2823	0.2827

T, °C	400	450	500	550	600	650	700
ν	0.2832	0.2837	0.2843	0.2848	0.2854	0.2861	0.2867

A.3.5 Mass density

A.3.5.1 Unirradiated conditions

Table A.20: Estimated density of tungsten based on the average density and the fitted average thermal expansion coefficient from room temperature to 700 °C.

T, °C	20	50	100	150	200	250	300	350
ρ,kg/m^3	19281.1	19273.7	19261.3	19248.9	19236.4	19223.8	19211.2	19198.4

T, °C	400	450	500	550	600	650	700
ρ,kg/m^3	19185.6	19172.6	19159.5	19146.3	19132.9	19119.5	19105.8

A.3.5.2 Irradiation effects

The effect of irradiation on the density is expressed through the swelling law. For irradiation temperatures below 450 °C and displacement doses below 10 dpa swelling (and density changes) in tungsten can be neglected.

A.3.6 Thermal conductivity

A.3.6.1 Unirradiated conditions

Table A.21: Values of thermal conductivity from room temperature to 800 °C.

T, °C	**20**	**50**	**100**	**150**	**200**	**250**	**300**	**350**	**400**
λ,W/(m K)	14.28	14.73	15.48	16.23	16.98	17.74	18.49	19.24	19.99

T, °C	**450**	**500**	**550**	**600**	**650**	**700**	**750**	**800**
λ,W/(m K)	20.74	21.49	22.24	22.99	23.74	24.49	25.25	26.00

A.3.6.2 Irradiation effects

The thermal conductivity changes due to irradiation can be neglected for design analyses, if displacement dose (fusion spectrum) does not exceed 3 dpa at temperatures from 20 °C to 450 °C.

A.3.7 Specific Heat

Table A.22: Values of specific heat from room temperature to 500 °C.

T, °C	**20**	**50**	**100**	**150**	**200**	**250**	**300**	**350**	**400**	**450**	**500**
$\mathbf{C_p}$,J/(kgK)	472	485	501	512	522	530	538	546	556	567	578

A.4 Water

A.4.1 Chemical composition

Table A.23: Chemical composition of Water.

Element	**Isotope**	**Abundance(%)**	**Volume Fraction (%)**
H	^{1}H	99.99	66.67
	^{2}H	0.01	
O	^{16}O	99.96	33.33
	^{17}O	0.04	

A.4.2 Physical properties

Table A.24: Physical properties of Water at 15.5 MPa.

Temperature T (°C)	**Density** ρ (kg/m^3)	**Heat Capacity** C_p (J kg^{-1} K^{-1})	**Thermal Conductivity** λ (W m^{-1} K^{-1})	**Viscosity** μ (10^{-6} kg m^{-1} s^{-1})
200	875	4404	0.676	137.0
210	863	4443	0.670	130.0
220	852	4489	0.662	124.0
230	839	4542	0.653	119.0
240	825	4606	0.643	114.0
250	812	4684	0.633	110.0
260	797	4778	0.621	106.0
270	782	4895	0.607	102.0
280	765	5043	0.593	98.2
290	747	5232	0.577	94.9
300	727	5481	0.559	91.7
310	705	5818	0.539	88.3
320	680	6290	0.516	84.5

Appendix B

APDL macro

This Appendix provides the APDL macro for calculating view factors from the plasma to the PPR in-vessel front-end surfaces.

```
FINISH
/CLEAR,START

!CONSTANTS

Working_Folder = ''
Model      = 'ANTENNA_SURF_ENOVIA'
CaseName     = 'VF_RUN'
Type_Analysis = 'VF_CALC'
Heat_Flux    = 0.35E6 ![W/m^2]

!CHECKPOINT NUMBER 1

  !CHECKPOINT NUMBER 1
  !Set the working directory
  /CWD,      '%Working_Folder%'
  /CWD,      '.\%Type_Analysis%\%CaseName%'

!FILENAME, OUTPUT FILE AND TITLE

!Set filename

  /FILNAME,'%CaseName%',1
  !/TITLE,'BSM:%CaseName%'

!PRE-PROCESSING
  /PREP7
  SHPP,off
  CDREAD, DB, '../../MODEL/%Model%','cdb', ,'', ''

  !Selection of the relevant components
  CMSEL, S, PLASMA
  CMSEL, A, ANTENNA
  CMSEL, A, FIRST_WALL
  CMSEL, A, VACUUM_VESSEL
```

```
  !Compress node and element numbers
  NUMCMP, NODES
  NUMCMP, ELEM

  !Determination of the model size and storage of the list of selected elements
  *GET, nE, ELEM, 0, COUNT
  *DIM, eids, , nE
  *VGET, eids, ELEM, 0, ELIST

  !Definition of emissivities for surface-to-surface radiation

  ALLSEL, ALL
  SFE, ALL,        2, RDSF, 1, 1   !Unitary emissivity
  SFE, PLASMA,     2, RDSF, 2, -1      !For enclosure number 1
  SFE, ANTENNA,      2, RDSF, 2, 1     !For enclosure number 1
  SFE, FIRST_WALL,  2, RDSF, 2, 1      !For enclosure number 1
  SFE, VACUUM_VESSEL, 2, RDSF, 2, 1      !For enclosure number 1

FINISH

!SOLUTION
 /SOLU
 ALLSEL, ALL
 STEF, 5.67E-8  !Stefan-Boltzmann constant
 TOFFST, 100    !Temperature offset from absolute zero to zero
 HEMIOPT, 1000    !Hemicube resolution
 SPCTEMP, 1, 0    !Free-space ambient temperature for radiation (0 for enclosure
    1)
 /AUX12
 VTYPE,0,1000
 VFOPT, NEW,,,,BINA,1   !Calculate view factors and write them to a binary file

 SAVE


VFOPT,READ,VF_RUN,vf,

  *CFOPEN, '..\VF_OUTPUT\HEAT_FLUXES_ANTENNA_SURF_ENOVIA',txt
 *VWRITE, '!HEAT FLUXES'
%C
  *CFCLOSE

    *CFOPEN, '..\VF_OUTPUT\VIEW_FACTORS_ANTENNA_SURF_ENOVIA',txt
 *VWRITE, '!Eid, VF'
%C
  *CFCLOSE

  !CMSEL, S, WAVEGUIDE
  CMSEL, S, ANTENNA
  *GET, nE, ELEM, 0, COUNT
  *DIM, vf, , nE
```

```
 *DIM, HEAT_LOAD,ARRAY,nE,4
  iE=0
  *DO, i, 1, nE

     iE=ELNEXT(iE)   !Consult view factors of each element with respect to the
    plasma
     VFQUERY, iE, PLASMA,
     *GET, vf(i), RAD, , VFAVG
     *GET, HEAT_LOAD(i,1),ELEM,iE,CENT,X
     *GET, HEAT_LOAD(i,2),ELEM,iE,CENT,Y
     *GET, HEAT_LOAD(i,3),ELEM,iE,CENT,Z
       viewFact = vf(i)
       hf = viewFact*Heat_Flux !Elemental heat fluxes are determined as the
    elemental view factors times the constant fluxes
       HEAT_LOAD(i,4)=hf
       eid = eids(i)

  !Write elemental view factors to the corresponding output file
  *CFOPEN, '..\VF_OUTPUT\VIEW_FACTORS_ANTENNA_SURF_ENOVIA', txt, , APPEND
     *VWRITE,'SFE,', iE, ',1,','PRES,,',viewFact
   %C %8I %C %C %12.5E
     *CFCLOSE

  *ENDDO

  !Write elemental heat fluxes to output file
  *CFOPEN, '..\VF_OUTPUT\HEAT_FLUXES_ANTENNA_SURF_ENOVIA', txt, , APPEND
    *VWRITE,HEAT_LOAD(1,1),HEAT_LOAD(1,2),HEAT_LOAD(1,3),HEAT_LOAD(1,4)
  %12.5E %12.5E %12.5E %12.5E
      *CFCLOSE


  !Information confirming that the process has been finished is written

  /OUTPUT,  ,TXT, , APPEND

  *VWRITE, 'Number of elements processed;', nE, nE
%s %i of %i (Finished)

FINISH

!MODEL SAVING

SAVE
```

Appendix C

Tabulated stress linearization results

This Appendix provides the tabulated results of the stress linearization taking into account the impact of irradiation accumulated during the 1st DEMO operation phase, the 2nd DEMO operation phase, and the whole DEMO lifetime (see Chapter 7and Figure 7.36 for more details).

C.1 1st DEMO operation phase (20 dpa)

Table C.1: Results of stress linearization of critical region with 20 dpa compared with RCC-MR level A.

Path	T_{avg} (°C)	IPC			IPI			IPFL		
		Value (MPa)	**Limit** (MPa)	**Ratio over limit**	**Value** (MPa)	**Limit** (MPa)	**Ratio over limit**	**Value** (MPa)	**Limit** (MPa)	**Ratio over limit**
P-1	451.5	20.4	143.2	0.14	37.5	214.8	0.17	411.3	429.6	0.96
P-2	429.5	22.7	165.9	0.14	37.0	248.9	0.15	401.6	497.8	0.81
P-3	381.4	19.1	211.8	0.09	31.4	317.7	0.10	430.4	635.4	0.68
P-4	382.6	20.2	210.7	0.10	34.6	316.0	0.11	434.2	632.0	0.69
P-5	377.9	26.4	214.9	0.12	41.6	322.4	0.13	402.4	644.8	0.62
P-6	395.4	31.0	198.9	0.16	45.3	298.4	0.15	389.9	596.8	0.65
P-7	397.0	30.3	197.5	0.15	44.2	296.2	0.15	371.5	592.4	0.63
P-8	380.2	30.5	212.8	0.14	47.6	319.3	0.15	374.0	638.5	0.59

C.2 2nd DEMO operation phase (50 dpa)

Table C.2: Results of stress linearization of critical region with 50 dpa compared with RCC-MR level A.

Path	T_{avg} (°C)	IPC			IPI			IPFL		
		Value (MPa)	Limit (MPa)	Ratio over limit	Value (MPa)	Limit (MPa)	Ratio over limit	Value (MPa)	Limit (MPa)	Ratio over limit
P-1	451.5	20.4	309.6	0.07	37.5	464.4	0.08	411.3	928.7	0.44
P-2	429.5	22.7	315.5	0.07	37.0	473.2	0.08	401.6	946.4	0.42
P-3	381.4	19.1	328.1	0.06	31.4	492.1	0.06	430.4	984.2	0.44
P-4	382.6	20.2	327.8	0.06	34.6	491.6	0.07	434.2	983.3	0.44
P-5	377.9	26.4	329.0	0.08	41.6	493.5	0.08	402.4	986.9	0.41
P-6	395.4	31.0	324.5	0.10	45.3	486.7	0.09	389.9	973.4	0.40
P-7	397.0	30.3	324.1	0.09	44.2	486.1	0.09	371.5	972.2	0.38
P-8	380.2	30.5	328.4	0.09	47.6	492.6	0.10	374.0	985.1	0.38

C.3 DEMO lifetime (70 dpa)

Table C.3: Results of stress linearization of critical region with 70 dpa compared with RCC-MR level A.

Path	T_{avg} (°C)	IPC			IPI			IPFL		
		Value (MPa)	Limit (MPa)	Ratio over limit	Value (MPa)	Limit (MPa)	Ratio over limit	Value (MPa)	Limit (MPa)	Ratio over limit
P-1	451.5	20.4	323.2	0.06	37.5	484.8	0.08	411.3	969.5	0.42
P-2	429.5	22.7	329.4	0.07	37.0	494.1	0.07	401.6	988.3	0.41
P-3	381.4	19.1	342.8	0.06	31.4	514.2	0.06	430.4	1028.4	0.42
P-4	382.6	20.2	342.5	0.06	34.6	513.7	0.07	434.2	1027.4	0.42
P-5	377.9	26.4	343.8	0.08	41.6	515.6	0.08	402.4	1031.3	0.39
P-6	395.4	31.0	339.0	0.09	45.3	508.5	0.09	389.9	1016.9	0.38
P-7	397.0	30.3	338.5	0.09	44.2	507.8	0.09	371.5	1015.6	0.37
P-8	380.2	30.5	343.1	0.09	47.6	514.7	0.09	374.0	1029.4	0.36